

ISSN: 2349-6495(P) | 2456-1908 (O)



International Journal of Advanced Engineering Research and Science

(IJAERS)

An Open Access Peer Reviewed International Journal



Journal DOI: [10.22161/ijaers](https://doi.org/10.22161/ijaers)

Issue DOI: [10.22161/ijaers.4.11](https://doi.org/10.22161/ijaers.4.11)

AI PUBLICATIONS

Vol.- 4 | Issue - 11 | Nov, 2017
editor@ijaers.com | <http://www.ijaers.com/>

FOREWORD

I am pleased to put into the hands of readers Volume-4; Issue-11: 2017 (Nov, 2017) of “**International Journal of Advanced Engineering Research and Science (IJAERS) (ISSN: 2349-6495(P)| 2456-1908(O)**”, an international journal which publishes peer reviewed quality research papers on a wide variety of topics related to Science, Technology, Management and Humanities. Looking to the keen interest shown by the authors and readers, the editorial board has decided to release print issue also, but this decision the journal issue will be available in various library also in print and online version. This will motivate authors for quick publication of their research papers. Even with these changes our objective remains the same, that is, to encourage young researchers and academicians to think innovatively and share their research findings with others for the betterment of mankind. This journal has DOI (Digital Object Identifier) also, this will improve citation of research papers.

I thank all the authors of the research papers for contributing their scholarly articles. Despite many challenges, the entire editorial board has worked tirelessly and helped me to bring out this issue of the journal well in time. They all deserve my heartfelt thanks.

Finally, I hope the readers will make good use of this valuable research material and continue to contribute their research finding for publication in this journal. Constructive comments and suggestions from our readers are welcome for further improvement of the quality and usefulness of the journal.

With warm regards.

Dr. Swapnesh Taterh

Editor-in-Chief

Date: Dec, 2017

Editorial/ Reviewer Board

Dr. Shuai Li

Computer Science and Engineering, University of Cambridge, England, Great Britain

Behrouz Takabi

Mechanical Engineering Department 3123 TAMU, College Station, TX, 77843

Dr. C.M. Singh

BE., MS(USA), PhD(USA), Post-Doctoral fellow at NASA (USA), Professor, Department of Electrical & Electronics Engineering, INDIA

Dr. Gamal Abd El-Nasser Ahmed Mohamed Said

Computer Lecturer, Department of Computer and Information Technology, Port Training Institute (PTI), Arab Academy For Science, Technology and Maritime Transport, Egypt

Dr. Ram Karan Singh

BE.(Civil Engineering), M.Tech.(Hydraulics Engineering), PhD(Hydraulics & Water Resources Engineering),BITS- Pilani, Professor, Department of Civil Engineering, King Khalid University, Saudi Arabia.

Dr. Asheesh Kumar Shah

*IIM Calcutta, Wharton School of Business, DAVV INDORE, SGSITS, Indore
Country Head at CrafsOL Technology Pvt.Ltd, Country Coordinator at French Embassy, Project Coordinator at IIT Delhi, INDIA*

Dr. A. Heidari

Faculty of Chemistry, California South University (CSU), Irvine, California, USA

Dr. Swapnesh Taterh

Ph.d with Specialization in Information System Security, Associate Professor, Department of Computer Science Engineering, Amity University, INDIA

Dr. Ebrahim Nohani

Ph.D.(hydraulic Structures), Department of hydraulic Structures, Islamic Azad University, Dezful, IRAN.

Dr. Dinh Tran Ngoc Huy

Specialization Banking and Finance, Professor, Department Banking and Finance, Viet Nam

Dr. Sameh El-Sayed Mohamed Yehia

Assistant Professor, Civil Engineering (Structural), Higher Institute of Engineering -El-Shorouk Academy, Cairo, Egypt

Dr. Ahmadad Nabih Zaki Rashed

Specialization Optical Communication System, Professor, Department of Electronic Engineering, Menoufia University

Dr. Alok Kumar Bharadwaj

BE(AMU), ME(IIT, Roorkee), Ph.D (AMU), Professor, Department of Electrical Engineering, INDIA

Dr. M. Kannan

*Specialization in Software Engineering and Data mining
Ph.D, Professor, Computer Science, SCSVMV University, Kanchipuram, India*

Dr. Sambit Kumar Mishra

*Specialization Database Management Systems, BE, ME, Ph.D, Professor, Computer Science Engineering
Gandhi Institute for Education and Technology, Baniatangi, Khordha, India*

Dr. M. Venkata Ramana

*Specialization in Nano Crystal Technology
Ph. D, Professor, Physics, Andhara Pradesh, INDIA*

DR. C. M. Velu

Prof. & HOD, CSE, Datta Kala Group of Institutions, Pune, India

Dr. Rabindra Kayastha

Associate Professor, Department of Natural Sciences, School of Science, Kathmandu University, Nepal

Dr. P. Suresh

*Specialization in Grid Computing and Networking, Associate Professor, Department of Information
Technology, Engineering College, Erode, Tamil Nadu ,INDIA*

Dr. Uma Choudhary

*Specialization in Software Engineering Associate Professor, Department of Computer Science Mody
University, Lakshmanagarh, India*

Dr. Varun Gupta

Network Engineer, National Informatics Center , Delhi ,India

Dr. Hanuman Prasad Agrawal

*Specialization in Power Systems Engineering Department of Electrical Engineering, JK Lakshmi Pat
University, Jaipur, India*

Dr. Hou, Cheng-I

*Specialization in Software Engineering, Artificial Intelligence, Wisdom Tourism, Leisure Agriculture and
Farm Planning, Associate Professor, Department of Tourism and MICE, Chung Hua University, Hsinchu
Taiwan*

Dr. Anil Trimbakrao Gaikwad

Associate Professor at Bharati Vidyapeeth University, Institute of Management , Kolhapur, India

Dr. Ahmed Kadhim Hussein

Department of Mechanical Engineering, College of Engineering, University of Babylon, Republic of Iraq









Mr. T. Rajkiran Reddy

Specialization in Networking and Telecom, Research Database Specialist, Quantile Analytics, India

M. Hadi Amini




Carnegie Mellon University, USA

Vol-4, Issue-11, November 2017

Sr No.	Detail with DOI
1	<p><u>3D Reservoir Study for Yamama Formation in Nasirya Oil field in Southern of Iraq</u> Author: Salman Z. Khorshid, Ghazi H. Al-Sharaa, Maha Fadel Mohammed  DOI: 10.22161/ijaers.4.11.1 Page No: 001-007</p>
2	<p><u>BER Performance of OFDM System in Rayleigh Fading Channel Using Cyclic Prefix</u> Author: Miss. Sneha Kumari Singh, Mr Ankit Tripathi  DOI: 10.22161/ijaers.4.11.2 Page No: 008-013</p>
3	<p><u>Interactive effect of tillage and wood ash on heavy metal content of soil, castor shoot and seed</u> Author: Nweke I A, Ijearu S I, Dambaba N  DOI: 10.22161/ijaers.4.11.3 Page No: 014-027</p>
4	<p><u>Study of Mechanical Properties of Stabilized Lateritic Soil with Additives.</u> Author: Elijah O. Abe, Ezekiel A. Adetoro  DOI: 10.22161/ijaers.4.11.4 Page No: 028-032</p>
5	<p><u>Assessment of Performance Properties of Stabilized Lateritic Soil for Road Construction in Ekiti State.</u> Author: Elijah O. Abe, Ezekiel A. Adetoro  DOI: 10.22161/ijaers.4.11.5 Page No: 033-039</p>
6	<p><u>Some aspects of Cold Deformation studies of Al-ZrB₂ composites</u> Author: C. Venkatesh, B. Chaitanya, K S M Yadav  DOI: 10.22161/ijaers.4.11.6 Page No: 040-048</p>
7	<p><u>Study of Irrigation Water Supply Efficiency to Support the Productivity of Farmers (Case Study at Kobisonta North Seram Central Maluku District)</u> Author: Hengky Jhony Soumokil, Obednego Dominggus Nara  DOI: 10.22161/ijaers.4.11.7 Page No: 049-057</p>
8	<p><u>The Air Flow Analysis of Coffee Plantation Based on Crops Planting Pattern of the Triangular Grid and Shackle of Wheel graphs by using a Finite Volume Method</u> Author: Dafik, Muhammad Nurrohim, Arif Fatahillah, Moch. Avel Romanza P, Susanto  DOI: 10.22161/ijaers.4.11.8 Page No: 058-061</p>

9	<p><u>Seismic Study at Subba Oil Field Applying Seismic Velocity Analysis</u> <i>Author:</i> Nawal Abed Al-Ridha, Zahraa Shakir Jassim  DOI: 10.22161/ijaers.4.11.9</p>	Page No: 062-069
10	<p><u>Peculiarities of a Colloidal Polysaccharide of Newly Isolated Iron Oxidizing Bacteria in Armenia</u> <i>Author:</i> Levon Markosyan, Hamlet Badalyan, Arevik Vardanyan, Narine Vardanyan  DOI: 10.22161/ijaers.4.11.10</p>	Page No: 070-076
11	<p><u>Daylight Performance of Middle-rise Wide Span Building in Surabaya (Case Study: G-building ITATS)</u> <i>Author:</i> Dian P.E. Laksmiyanti, Poppy F Nilasari  DOI: 10.22161/ijaers.4.11.11</p>	Page No: 077-083
12	<p><u>Application of Cubic Spline Interpolation to Fit the Stress-Strain Curve to SAE 1020 Steel</u> <i>Author:</i> Otávio Cardoso Duarte, Pedro Américo Almeida Magalhães Junior  DOI: 10.22161/ijaers.4.11.12</p>	Page No: 084-086
13	<p><u>Tensile Test: Comparison Experimental, Analytical and Numerical Methods</u> <i>Author:</i> Tatiana Lima Andrade, Pedro Américo Almeida Magalhães Júnior, Wagner Andrade de Paula  DOI: 10.22161/ijaers.4.11.13</p>	Page No: 087-090
14	<p><u>Review on Exhaust Heat Recovery Systems in Diesel Engine</u> <i>Author:</i> Mohamed Shedid, Moses Sashi Kumar  DOI: 10.22161/ijaers.4.11.14</p>	Page No: 091-097
15	<p><u>Estimation of Reservoir Storage Capacity and Maximum Potential Head for Hydro-Power Generation of Propose Gizab Reservoir, Afghanistan, Using Mass Curve Method</u> <i>Author:</i> Khan Mohammad Takal, Abdul Rahman Sorgul, Abdul Tawab Balakarzai  DOI: 10.22161/ijaers.4.11.15</p>	Page No: 098-104
16	<p><u>Pronunciation Remedy of Scientific Plants Names with Pair Exercise Using Flash card Media at Students Plant Taxonomy Course</u> <i>Author:</i> Pujiastuti, Imam mudakir, Iis Nur Asyiah, Siti Murdiyah, Ika Lia Novenda, Vendi Eko Susilo  DOI: 10.22161/ijaers.4.11.16</p>	Page No: 105-110
17	<p><u>The Effect Analysis of Traffic Volume, Velocity and Density in Dr.Siwabessy Salobar Road</u> <i>Author:</i> Selviana Walsen, La Mohamat Saleh  DOI: 10.22161/ijaers.4.11.17</p>	Page No: 111-119

18	<u><i>Flexure and Shear Study of Deep Beams using Metakaolin Added Polypropylene Fibre Reinforced Concrete</i></u> <i>Author:</i> S. Vijayabaskaran, M. Rajiv, A. Anandraj  DOI: <u>10.22161/ijaers.4.11.18</u>	<i>Page No:</i> 120-125
19	<u><i>Design and Analysis of RCA and CLA using CMOS, GDI, TG and ECRL Technology</i></u> <i>Author:</i> Kuldeep Singh Sekhawat, Gajendra Sujediya  DOI: <u>10.22161/ijaers.4.11.19</u>	<i>Page No:</i> 126-129
20	<u><i>Autoregressive Integrated Moving Average (ARIMA) Model for Forecasting Cryptocurrency Exchange Rate in High Volatility Environment: A New Insight of Bitcoin Transaction</i></u> <i>Author:</i> Nashirah Abu Bakar, Sofian Rosbi  DOI: <u>10.22161/ijaers.4.11.20</u>	<i>Page No:</i> 130-137
21	<u><i>Design of Tuning Mechanism of PID Controller for Application in three Phase Induction Motor Speed Control</i></u> <i>Author:</i> Alfred A. Idoko, Iliya. T. Thuku, S. Y. Musa, Chinda Amos  DOI: <u>10.22161/ijaers.4.11.21</u>	<i>Page No:</i> 138-147
22	<u><i>Experimental analysis of the operation of a solar adsorption refrigerator under Sahelian climatic conditions: case of Burkina Faso</i></u> <i>Author:</i> Guy Christian Tubreoumya, Eloi Salmwendé Tiendrebeogo, Ousmane Coulibaly, Issoufou Ouarma, Kayaba Haro, Charles Didace Konseibo, Alfa Oumar Dissa, Belkacem Zeghmati  DOI: <u>10.22161/ijaers.4.11.22</u>	<i>Page No:</i> 148-156
23	<u><i>General Pattern Search Applied to the Optimization of the Shell and Tube Heat Exchanger</i></u> <i>Author:</i> Wagner H. Saldanha, Pedro A. A. M. Junior  DOI: <u>10.22161/ijaers.4.11.23</u>	<i>Page No:</i> 157-159
24	<u><i>Study the Dynamic Response of the Stiffened Shallow Shell Subjected to Multiple Layers of Shock Waves</i></u> <i>Author:</i> Le Xuan Thuy  DOI: <u>10.22161/ijaers.4.11.24</u>	<i>Page No:</i> 160-165
25	<u><i>Theoretical investigation of series of diaza²⁻,uorene-functionalized TTFs by using density functional method</i></u> <i>Author:</i> Tahar Abbaz, Amel Bendjeddou, Didier Villemin  DOI: <u>10.22161/ijaers.4.11.25</u>	<i>Page No:</i> 166-177

26	<p><u>Is the EM-Drive a Closed System?</u> <i>Author:</i> Carmine Cataldo  DOI: 10.22161/ijaers.4.11.26</p> <p style="text-align: right;"><i>Page No:</i> 178-181</p>
27	<p><u>3D Seismic Study to Investigate the Structural and Stratigraphy of Mishrif Formation in Kumiya Oil Field Southern Eastern Iraq</u> <i>Author:</i> Kamal K. Ali, Ghazi H. Alsharaa, Ansam H. Rasheed  DOI: 10.22161/ijaers.4.11.27</p> <p style="text-align: right;"><i>Page No:</i> 182-187</p>
28	<p><u>Hydraulic jump on smooth and uneven bottom</u> <i>Author:</i> A. Mammadov  DOI: 10.22161/ijaers.4.11.28</p> <p style="text-align: right;"><i>Page No:</i> 188-198</p>

3D Reservoir Study for Yamama Formation in Nasriya Oil field in Southern of Iraq

Salman Z. Khorshid¹, Ghazi H. Al-Sharaa², Maha Fadel Mohammed³

¹ Department of Geology, College of Science, University of Baghdad, Baghdad, Iraq.

² Ministry of petroleum, Oil Exploration Company, Baghdad, Iraq.

Abstract— Nasriya oil field is located at the Southern part of Iraq, this field is a giant and prolific, so it take a special are from the Oil Exploration Company for development purposes by using 3D seismic reflection.

The primary objective of this thesis is to obtain reservoir properties and enhance the method of getting precise information about subsurface reservoir characterizations by improving the estimation of petrophysical properties (effective porosity, P-wave, water saturation and poisson's ratio).

There are five wells in the study area penetrated the required reservoirs within Yamama Formation. The Synthetic seismogram of Nasriya wells were created to conduct well tie with seismic data. These well tie was very good matching with seismic section using best average statistical wavelet. Five main horizons were picked from the reflectors by using synthetic seismogram for wells then converted to structural maps in depth domain by using average velocity of five wells.

By using petrel program TWT maps have been constructed from the picked horizons, Average velocity maps calculated from the wells velocities survey data and the sonic log information and Depth maps construction was drawn using Direct time-depth conversion and the general trend of these map was NW-SE. The model of low frequency was created from the low frequency contents from well data and the five main horizons were picked.

The seismic inversion technique was performed on post-stack three dimensions (3D) seismic data in Nasriya oil field.

Keywords— Seismic Inversion , Synthetic seismogram, Check Shot correction, The wavelet, Synthetic trace, Structural pictures of the picked horizons, Low frequency model LFM (Initial model), Inversion results.

I. INTRODUCTION

Nasriya structure was discovered in 1975 through a seismic investigations covered partially the southern part of Iraq by (I.P.C.) groups [1].

Nasriya oil field is located in southern of Iraq within the Dhi Qar governorate about 38 km north-west from the Nasriya city figurer (1)

This research is dedicated to study of the Yamama Formation and study reservoir characterization such as (effective porosity) of Yamama Formation by using software, specifically Hampson- Russell and petrel programs.

Because of the good prospects of the oil in the rocks of Cretaceous generally in Yamama Formation specially in the Nasriya oil field and in view of the economic importance of Yamama Formation, which is considered as important formation that contains hydrocarbon accumulation, this formation is of the one most important oil production reservoirs in southern Iraq.

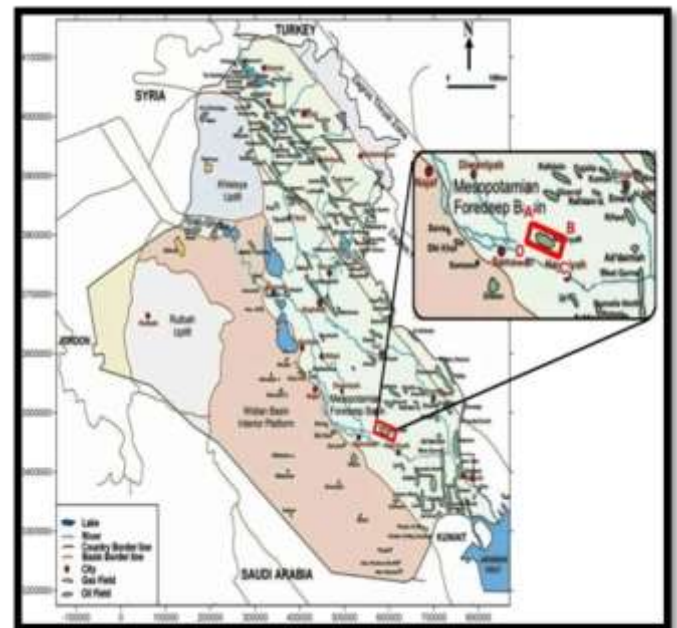


Fig.1: Location map of the study area [2].

II. SEISMIC INVERSION

Seismic inversion is the extracting and calculation process of the earth's structure (underlying geology that gave rise to that seismic) and physical properties from some sets of observed seismic data. The output of the seismic inversion can be P-wave and S-wave velocities, density, Poisson's ratio, acoustic impedance and S-impedance volumes [3],[4],[5]. The flow chart shown in figure (2) to explain the main steps of the work process.

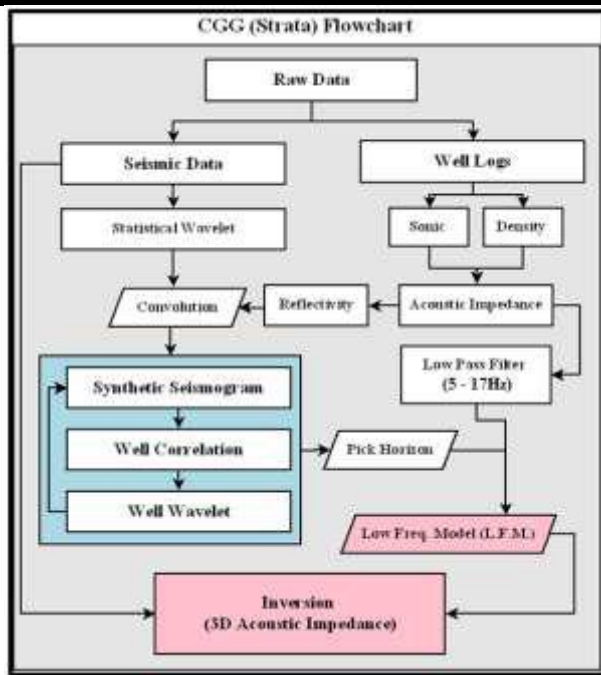


Fig. 2: Flow chart summarized the main steps of inversion process [6].

III. THE WORK FLOW

Inversion is a process of extraction from seismic data that utilized in the post stack and aim of to extract the acoustic impedance volumes, this allows to compute the porosity of fluids and water saturation, seismic inversion is used to transform the seismic effect into acoustic log and density log.

So the inversion helps to delete small wavelets and then contributes the determine of reservoir properties with better dispersion capacity of waves, and that the acoustic impedance requires the integration of the data of the log of the well so the inversion is a step integrated data and the output data connects the wells and also matches the seismic data. The process of description the reservoir regularly using seismic data is not sufficient to simulate the reservoir, and the field seismic data and the processing of these data provide excellent side coverage of the reservoir.

But seismology requires calculating the characteristics of the bottom of the surface by sending controlled seismic energy into the earth and watching the reflected waves at the receiving stations. Synthetic seismogram synthetics allows you to utilize all the well logs, geologic markers, 2D and 3D seismic, check shot data and structural interpretations [7].

3.1 CHEC SHOT CORRECTION

This is basically true for vertical wells, small offset of the source to the well, and little or no formation dip [8]. in the study area all wells are vertical and check shot times measured in these wells are vertical (one way time) OWT.

Figure (3) shows check shot correction have been applied for one wells in study area (Ns-1), in well diagram there are three track, the left track represent relation between true vertical depth (TVD) and TWT which contain two curves, input time in black color and corrected time in red color, middle track represent drift curve and right track represent original velocity from sonic log in black color and corrected velocity in orange color.

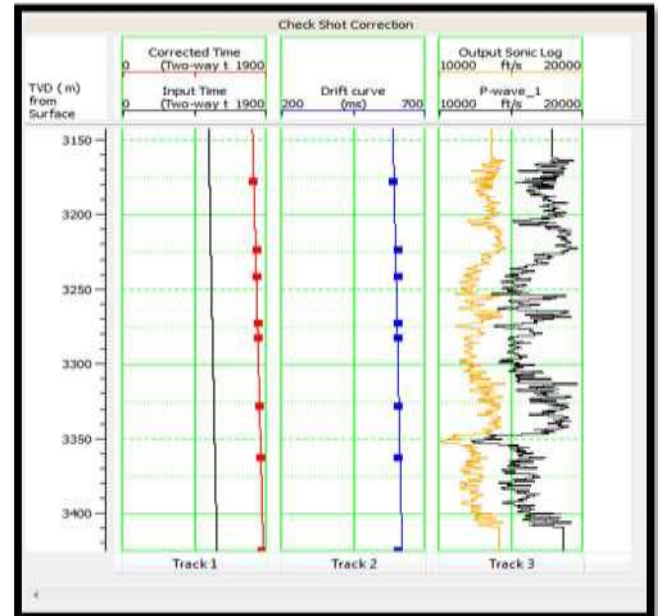


Fig.3: Check shot correction for well Ns-1 in the study area.

3.2 THE WAVELET

The wavelet is a wave pulse approximation for a seismic source which contains many frequencies and is time limited. By correlating reflection events across the wells, an estimated cross-section of the geologic structure can be interpreted [9]. Amplitude spectrum of the wavelet is extracted by analyzing the auto-correlation process of a set of traces over a selected time window [10]. The best average wavelet that match the synthetic trace of the wells of (Ns-1, Ns-2, Ns-3, Ns-4, and Ns-5) figure (4).

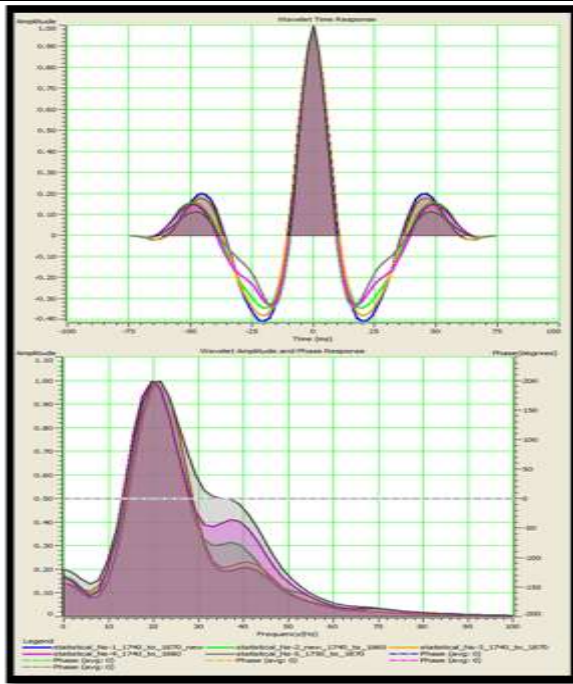


Fig.4: The average statistical wavelet of wells Ns-1, 2, 3, 4, and 5.

3.3 SYNTHETIC TRACE

The synthetic trace in this study is created by convolution process between reflectivity calculated from well data and statistical extracted wavelet in first step, after gate proper correlation between synthetic trace and seismic trace at well location see the figure (5). The corrected synthetic seismogram is displayed in seismic data through wells Ns-1 and Ns-3 with picked main horizons in the study area figure (6).

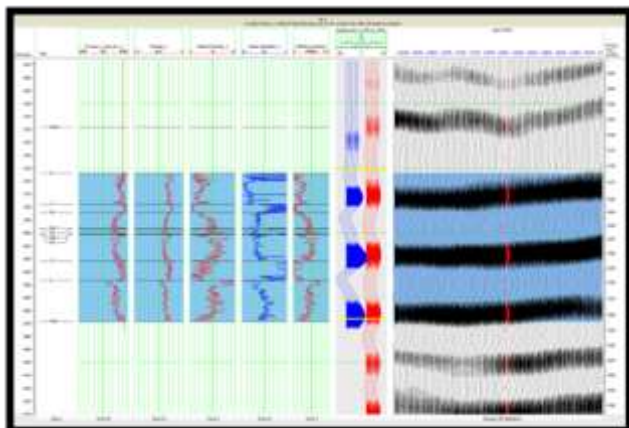


Figure (5): Synthetic seismogram of well Ns-1 with statistical wavelet max. coeff. = 89%.

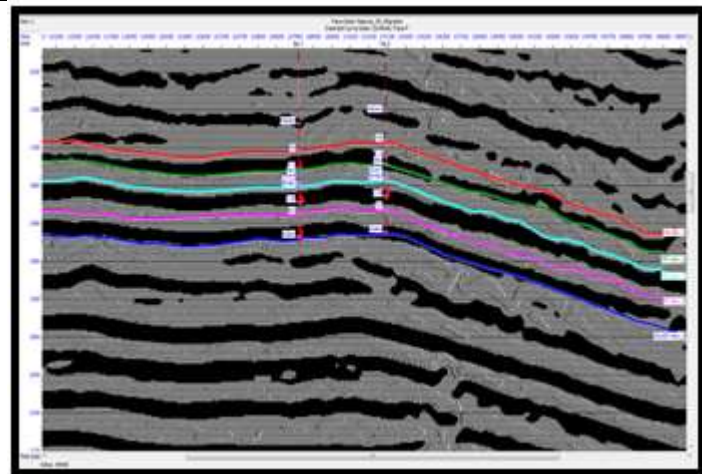


Fig.6: Inline section from 3D seismic data pass through wells Ns-1 and Ns-3 with synthetic seismogram.

IV. STRUCTURAL PICTURES OF THE PICKED HORIZONS

The studied reflectors were defined by using synthetic seismogram for wells (Ns-1,2,3,4 and 5). These reflectors were picked over all seismic cube and mapped to Top of Yamama Formation (YA) , YB1, YB3, YC, and Top of Sulaiy Formation in time domain, then converted to structural maps in depth domain by using average velocity of five wells.

By using petrel program, TWT maps have been constructed from the picked horizons (Yamama) respectively using sea level surface as a datum plane TWT maps shows in general three enclosure domes with a NW-SE axis in the middle of Nasriya Oil field, also show these layers covered all study area with general dip toward NE figure (7) and (8).

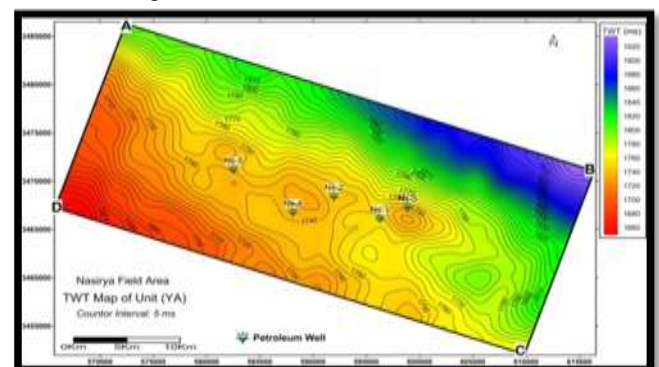


Fig.7: Show TWT map to the top of Yamama Formation (unit YA).

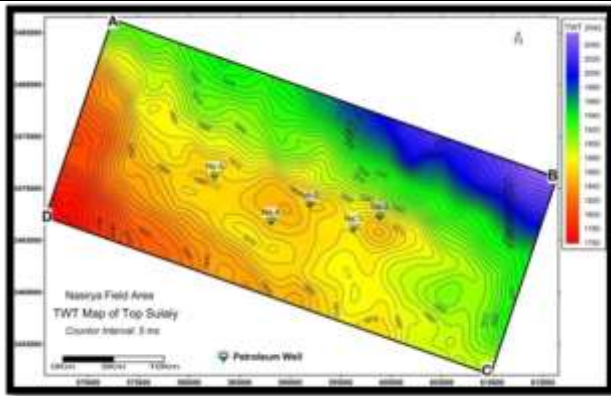


Fig.8: Show TWT map to the top of Sulaiy Formation. (Bottom Yamama Formation).

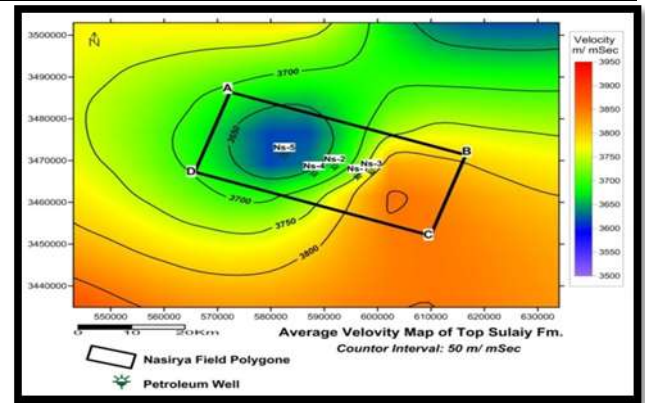


Fig.10: Average velocity map of top of Sulaiy Formation.

The average velocity was calculated from the wells velocity survey data for the five previously well of Nasirya oil field and the Sonic Log information through which the cumulative time (TWT) was calculated for the formation after the measurement conversions from (Micro) Second to millisecond and feet to meter and its compatibility with the inverter, thus obtaining the inverter speed from the output of the depth distribution of the configuration on the double-measured time. The RMS was not adopted to convert to the depths because of uneven differences with the values of average velocity of the wells and is so accurate that the correction process is inaccurate

The maps shows generally a gradual increase from the center of the domal shape to the all directions approximately figures (9 and 10). In the Nasirya Oilfield there is a relatively small decrease in the velocity values.

Generally, depth estimation can be done wide range of existing methods, but which can be separated into two broad categories [11], In the current study, we have used Direct time-depth conversion by using petrel program In general, the depth maps revealed three major enclosure domes where the first dome is located at the location of the two wells (Ns-1, 3). The second dome is located near the two wells (Ns-2, 4) and the third dome northwest of the well (Ns-5) figure (11 and 12).

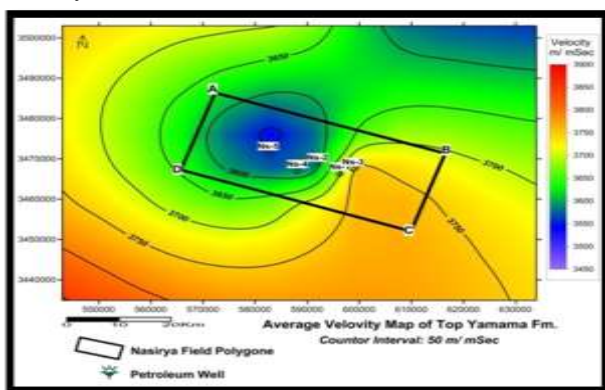


Fig.9: Average velocity map of top of Yamama Formation.

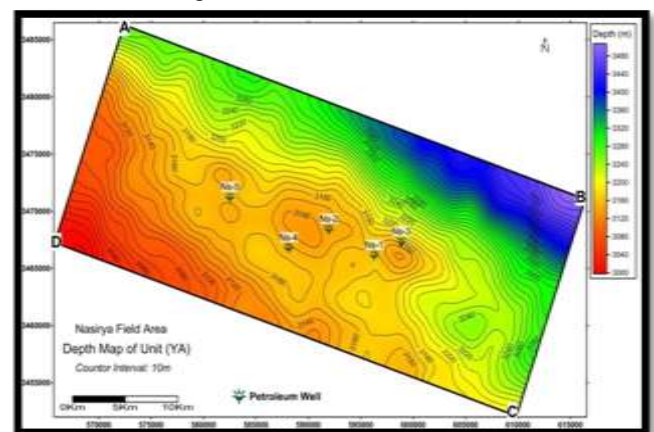


Fig.11: Shows depth map to the top of Yamama Formation (unit YA).

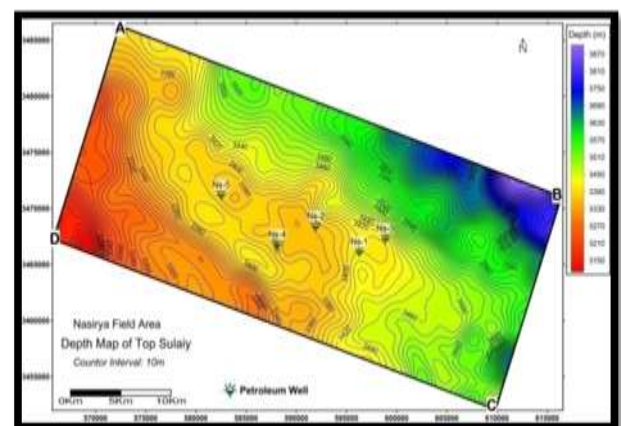


Fig.12: Show depth map to the top of (Sulaiy Formation)
 (Bottom of Yamama Formation).

V. CLOW FREQUENCY MODEL LFM (INITIAL MODEL)

In amplitude seismic data, the common occurrence is the absence of low-frequency content, that lost during acquisition and processing of seismic data by the effect of band limited wavelet of seismic sources and applied band-pass filter to eliminate low-frequency ground-roll and coherent high frequency noise [12]. Inversion of seismic data alone leads to band-limited Acoustic Impedance estimation [13], therefore, in seismic inversion process, the low frequency content must be compensated by build 3D geologic model of (AI) from well logs to obtain absolute rather than relative (band-limited) inverted property values [14], [15] figure (13) shows Initial model.

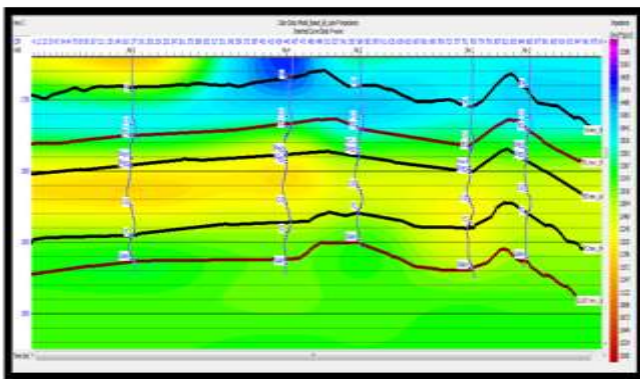


Fig.13: Arbitrary line section passed through 3D volume
 of low frequency model.

VI. INVERSION RESULTS

The Model Based Inversion (MBI) is a type of post stack inversion to compute acoustic impedance from the seismic datasets. The model based inversion technique is also known as blocky inversion which was used in an attempt to better define stratigraphic features and contacts of interest. The final step of the inversion process is run through all 3D seismic volume to create 3D acoustic impedance between wells and cover all study area figure (14). The final results of acoustic impedance (AI) inversion and used four wells (Ns-1,2,3, and 5) to the inverted seismic data and blind well (Ns-4) to quality control inverted data as shown in figure (15). Acoustic impedance (AI) from wells data were posted on vertical sections passed through wells in the study area which shows very good correlation between original and calculated acoustic impedance (AI), in figures the low acoustic impedance shows the good porosity and promising areas in the oil field.

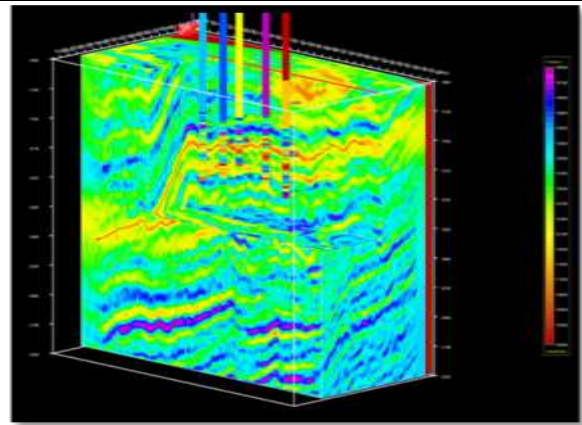


Fig.14: 3D inverted acoustic impedance volume resulted
 from post stack inversion.

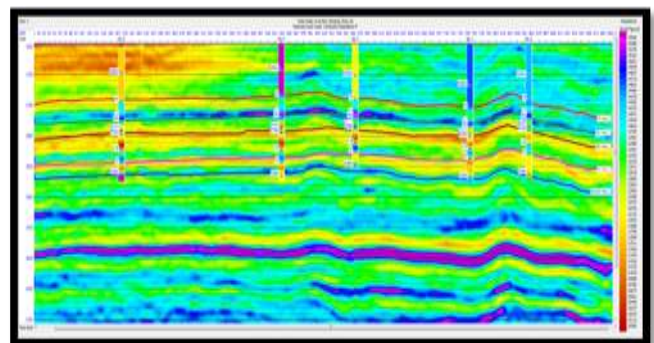


Fig.15: Arbitrary line from 3D all data pass through
 well locations and shows matching between AI from
 wells and calculated from seismic data.

The final results of acoustic impedance (AI) inversion, a horizon slices of all units reservoir (Yb1, Yb3, and Yc) centered window beneath Yamama horizon has been out of the (AI) inverted cube indicated a quality reservoir units tend to be enhancement at the crest, NW-SE and eastern sides of the anticline as shown in figure (16) shows the low (AI) in the crest, NW and eastern side of the fold, indicated high porosity. figure (17) shows the low AI in the crest, NW-SE and eastern side of the fold, indicated high porosity. and in figure (18) shows the low (AI) in the crest and NW-SE side of the fold, indicated high porosity.).

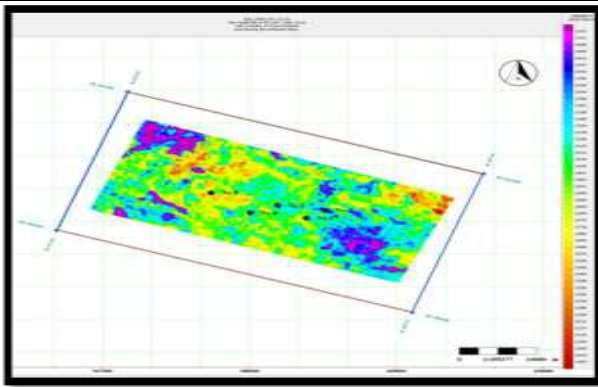


Fig.16: shows the low(AI) horizon slice of unit Yb1

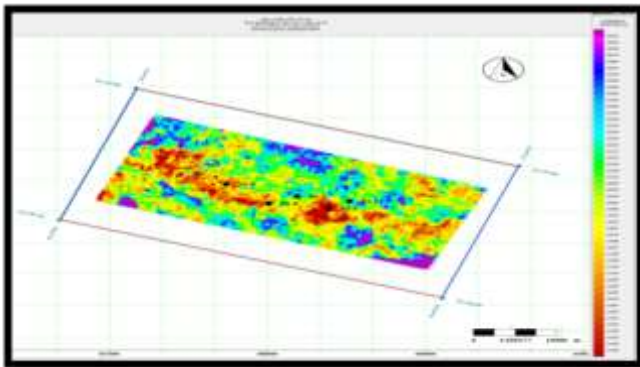


Fig.17: shows (AI) horizon slice of unit Yb.

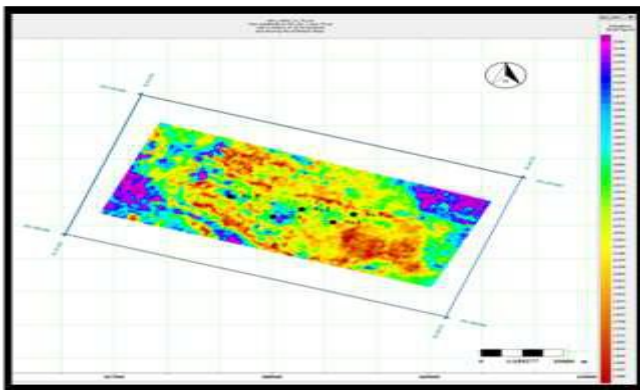


Fig.18: shows (AI) horizon slice of unit Yc in the crest and NW-SE side of the fold.

VII. CONCLUSIONS

- 1- The Synthetic seismogram of Nasiriya wells were created to conduct well tie with seismic data. These well tie was good matching with seismic section.
- 2- There is a good match of the average statistical wavelet with the synthetic seismogram of the wells of (Ns-1, Ns-2, Ns-3, Ns-4, and Ns-5).
- 3- By using petrel program, TWT maps: have been constructed from the picked horizon (tops of Yamama and Sulaiy). The result of study TWT maps appear in general three enclosure domes with a NW-SE axis in

the middle of Nasriya Oil field with general dip toward the NE.

- 4- Average velocity maps calculated from the wells velocity survey data and the sonic log information. The result of maps was generally a gradual increase from the center of the domal shape to the all direction approximately.

- 5- Depth maps construction in the current study, was drawn using Direct time-depth conversion,

Depth maps were appeared general direction of the study area is NW-SE, and the southwestern side is structurally higher than the northeastern side. In general, the depth maps revealed three major enclosure domes where the first dome is located at two wells (Ns-1and Ns-3). The second dome is located near the two wells (Ns-2 and Ns-4) and the third dome was on the northwest of the well (Ns-5).

6-The seismic inversion technique was performed on post-stack three dimensions (3D) seismic data in Nasriya oil field. The final results of acoustic impedance (AI) inversion were used for four wells (Ns-1,2,3, and 5) to the inverted seismic data and wildcat well (Ns-4) to quality control inverted data. Horizon slices of all units reservoir indicated a quality reservoir units tend to be enhanced at the crest and eastern sides of the NW-SE anticline. The result of inverted slices of Yb1,Yb3 and Yc in directional mentioned later low acoustic impedance indicated to the high effective porosity.

ACKNOWLEDGEMENTS

The words are racing and the phrases are crowded to organize the thanksgiving which is only worthy of you Praise be to God in the heavens and the earth , Praise be to God and thank you the number of atoms of the universe and beyond and beyond. Prayer and peace be upon the prophet of Muhammad and his household.

I would like to express my special appreciation and thank To my supervisor (Dr. Salman Z. Khorshid) for all his patience, guidance and continuous support of my MSc. study and related research.

My best thanks to the dean of the college of science, head of geology department, and postgraduate unit of department tin Baghdad University. Thanks are due to all the staff of Oil Exploration Company, and I would like to thanks (Dr.Ghazi H. Al- Sharaa) for helping me and providing all the facilities and information that contributed to the completion of this research. Especially I would like to thank the coordinator (Mr. Ammar Ahmed) to help me and supporting me. Also I will not forget I give my thanks and gratitude to those who were able to consummation the march of my life from the depths of my heart, thank you my parents ,my brother and sister and my husband and all family .

And I thank all my colleagues in the Department of Geology-University of Baghdad, and my friends, and my gratitude to all who read this research.

REFERENCES

- [1] O.E.C., (2007), Integrated reservoir study updating of Nasriya field , oil exploration company, unpublished study.
- [2] Al-Ameri, T. K., (2010), Petroleum systems in Iraqi oil field lectures presented in department of geology, University of Baghdad, (Extended Abstract).
- [3] Hampson-Russell, (1999), 2D and 3D Post-Stack Seismic Modeling, Processing and Inversion.
- [4] Hampson, D. P., Schuelke, J.S., Quirein, J.A., (2001), Use of multiattribute transforms to predict log properties from seismic data, *Geophysics*, January-February, vol. 66, no. 1, PP. 220-236.
- [5] Hampson-Russell, (2007), pre and post stack Seismic Inversion Workshop.
- [6] Al-Rahim, Ali, M. and Hashem, H., A., (2016), Subsurface 3D Prediction Porosity Model from Converted Seismic and Well Data Using Model Based Inversion Technique, *Iraqi Journal of Science*, Vol. 57, No.1A, pp: 163-174.
- [7] Brown, A. R., (1999), Interpretation of three dimensional seismic data, AAPG Memoir 42: AAPG, Tulsa, SEG Investigations in Geophysics No. 9, 514 p.
- [8] Geotz, J.F., Dupal, L. and Bowler, J. (1979), An investigation into discrepancies between sonic log and seismic check shot velocities. *Journal of the Australian Petroleum Exploration Association*, 19, 131141.
- [9] Liner, C., C-F. Li, A. Gersztenkorn, and J. Smythe, (2004), SPICE: A new general seismic attribute: 72 Annual International Meeting of the Society of Exploration, Geophysicists Expanded Abstracts, PP.433-436.
- [10] Cariolaro, G., (2011), *Unified Signal Theory*, Springer, 927 P.
- [11] Etris, E. L., Crabtree, N. J. and Dewar, J., (2001), True Depth Conversion, *Canada Society of Exploration Geophysicists*, pp. 11-22.
- [12] Russell, B., and Hampson, D., (2006), The old and the new in seismic inversion, *CSEG RECORDER* 5.
- [13] Lindseth, R., (1979), Synthetic sonic logs – a process for stratigraphic interpretation: *Geophysics*, vol. 44, pp. 3-36.
- [14] Barclay, F., Bruun, A., Rasmussen, K. B., Alfaro, J. C., Cooke, A., Cooke, D., Salter, D., Godfrey, R., Lowden, D., McHugo, S., Ozdemir, H., Pickering, S., Pineda, F. G., Herwanger, J., Volterrani, S., Murineddu, A., Rasmussen, A., and Roperts, R., (2008), Seismic inversion reading between lines, Spring.
- [15] Latimer, R.B., Davison, r., Van Ril, p., (2000), *An Interpreters Guide to Understanding and Working with Seismic-Derived Acoustic Impedance Data*, The Leading Edge, 19#3, 242 P.

BER Performance of OFDM System in Rayleigh Fading Channel Using Cyclic Prefix

Miss. Sneha Kumari Singh, Mr Ankit Tripathi

Post Graduate Student, Electronics Department, Scope College of Engineering, Bhopal, RGPV Bhopal, Madhya Pradesh, India
Assistant Professor, Electronics Department, Scope College of Engineering, Bhopal, RGPV Bhopal, Madhya Pradesh, India

Abstract— In this research paper, we will focused on the bit error rate (BER) performance of Orthogonal-frequency division multiplexing (OFDM) of various modulation techniques. The Orthogonal Frequency Division Multiplexing (OFDM) is the popular modulation technique for the many wireless communication systems. In the wireless system, the signal transmitted into channel bounces off from the various surfaces resulting in the multiple delayed versions of the transmitted signal arriving to the receiver. The OFDM has trusted to be very effective in mitigating adverse multi-path effects of a broadband channel. The multiple signals are obtained due to the diffraction and reflection of electromagnetic waves around objects. The bit error rate (BER) performance of this type of systems are evaluated in the additive white Gaussian noise (AWGN) channel. The BER performance of the transmission modes are calculated by calculating the bit error rate (BER) versus signal to the noise ratio (SNR) under the Additive white Gaussian noise (AWGN), channel.

Keywords—BER, UWB, SNR, AWGN, OFDM, QPSK, BPSK, QAM, Rayleigh fading.

I. INTRODUCTION

It is very important to calculate the performance of the wireless systems by considering the transmission characteristics, parameters of the wireless channel and the device structure. The Bit Error Rate Ratio (BER) is considered to be one of the most extensively used performance measures for wireless communication systems and hence it has been extensively studied. In our research paper, we proposed a novel approach to calculate the average probability of error by using OFDM modulation techniques and by considering an approximation of the spatial filter.

In present time, ULTRA WIDE BAND (UWB) communication technology is an emerging as a popular standard for high-data-rate applications over wireless communication networks. Due to the use of its high-frequency bandwidth, the UWB can achieve very high data

rates over the wireless connections of multiple system devices at a low transmission power close to the noise floor. Since the power level required for the UWB transmissions is low, so UWB devices will not generate significantly harmful interference to the other communication standards. A major difference between conventional radio transmissions and the UWB is that – the conventional systems sends information by changing the power level, frequency, and/or phase of a sinusoidal wave whereas in the UWB transmissions information is transmitted by generating radio energy at the specific time intervals and covering a large bandwidth, thus enabling pulse-position or time modulation. In the wireless channels, several models have been introduced and investigated to calculate SNR. Every models are a function of the distance between the transceiver, the path loss exponent and the channel gain. The Several probability distributed functions are also available to model a time-variant parameter i.e. channel gain.

It is highly believed that the OFDM results in an improved multimedia download services requiring high data rates communications, but this condition is significantly controlled by inter-symbol interference (ISI) due to the existence of the multiple paths. The Multicarrier modulation techniques, including OFDM modulation are considered as the most depending technique to overcome this problem. The OFDM technique is a multi-carrier wireless transmission technique which is being considered as an excellent method for the high speed bi-directional wireless communication of data.

II. OFDM TECHNIQUE

The Orthogonal frequency division multiplexing (OFDM) is a wireless communications technique that breaks a communications channel into a number of equally spaced frequency bands. A sub-carrier having a portion of the user information is sended in each band. Each sub-carrier is the orthogonal (i.e. independent of each other) with other sub-carrier; distinguishing OFDM from the commonly used

frequency division multiplexing (FDM) technique. The FDM is a modulation technique that transmits multiple signals simultaneously over a single transmission path.

The Orthogonal frequency-division multiplexing (OFDM) is the modulation technique for the European standards such as the Digital Audio Broadcasting (DAB) and the Digital Video Broadcasting (DVB) systems. The Orthogonal frequency-division multiplexing (OFDM) is a process of encoding digital data on the multiple carrier frequencies. The data are transmit over parallel sub-channels with each sub-channel modulated by the modulation scheme such as BPSK, QPSK, QAM etc. The benefit of the OFDM is its ability to cope with severe channel conditions compared to a single carrier modulation scheme but still maintain the data rates of a conventional scheme with the same bandwidth. The Orthogonal Frequency Division Multiplexing has become one of the main physical layer techniques used in the modern communication systems.

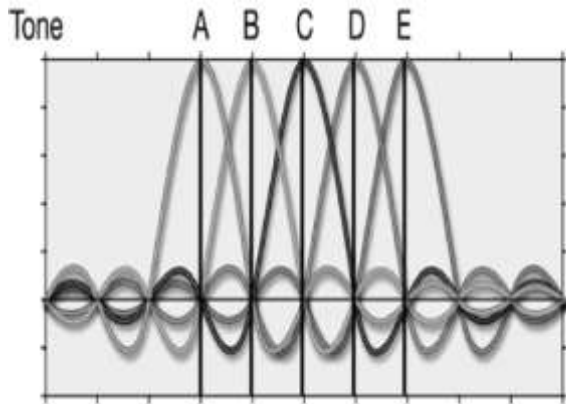


Fig.1: OFDM Tones

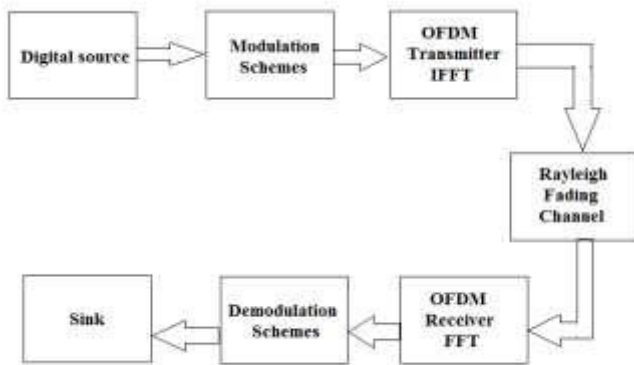


Fig.2: Block diagram of OFDM Transmitter and Receiver

III. CHANNEL MODEL

1. AWGN Channel :When the impaired communication channel are linear addition of wide band or the white noise consisting constant spectral density over infinite period and

the amplitude is Gaussian distribution then such a channel model is known as AWGN channel [1].

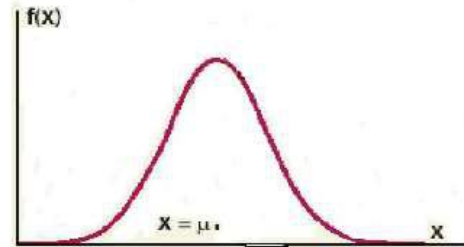


Fig.3:Gaussian distribution of white noise

The High data rate communication over the additive white Gaussian noise channel (AWGN) is limited by the white noise. The received signal in the interval range $0 \leq t \leq T$ may be given as $r(t) = s_m(t) + n(t)$

Where $n(t)$ represents the sample function of additive white Gaussian noise (AWGN) process with power- spectral density.

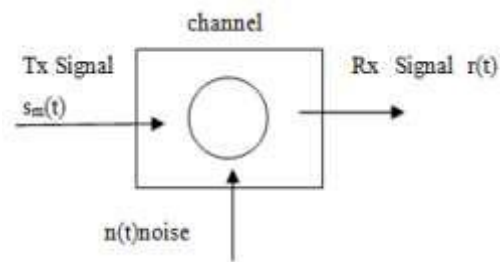


Fig.4: Model for received signal passed through AWGN channel

2. Rayleigh channel model:The Rayleigh fading environment is described by the many multipath components, each having relatively similar signal magnitude, and uniformly distributed phase, that means there is no line of sight (LOS) path between transmitter and receiver. The channel in which the signal takes various path to reach the receiver after getting reflect from various objects in the environment. The signal receiving at receiver is sum of the reflected signal and the main signal. The signal in the environment get diffracted or reflected from the objects like tree, building, moving vehicle etc and imposes problem when the envelope of the individual signal is added up [2].



Fig.5: Rayleigh Fading Scenario

3. Rician channel model: When the line of sight propagation path exists between transmitter and receiver, then the dominant stationary signal component persists, the fading of the channel is called as Rician channel. The white noise which occurs because of Rician channel is explained as Rician distribution. The Random multipath components arriving at the receiver side comes from the different angles superimposing on a stationary signal [3].

IV. MODULATION SCHEMES

(i). Binary Phase Shift Keying (BPSK)

The PSK uses a finite number of phases; each are assigned with a unique pattern of binary digits. Generally, each phase encodes an equal number of the bits. Each pattern of the bits generates the symbol that is denoted by the particular phase. The BPSK is the simplest type of phase shift keying (PSK). It consists of two phases which are separated by 180° and so they can also be named as 2-PSK. It does not matter exactly that where the constellation points are positioned, and in the below figure they are represented on the real axis, at 0° and 180°.

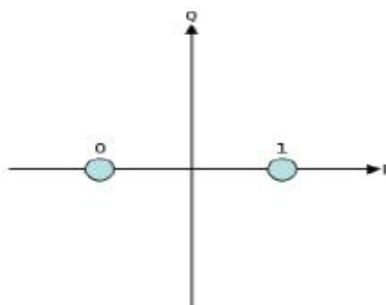


Fig.6: Constellations for BPSK

(ii) Quadrature Phase Shift Keying (QPSK)

The QPSK have four points on the constellation diagram, and are equispaced around a circle. With four phases, QPSK can encode the two bits per symbol, shown in the figure with gray coding to reduce the bit error rate (BER) — some

times it misperceived as twice the BER of the BPSK. The mathematical studies shows that QPSK can used either to double the data rate when compared with a BPSK system while maintaining the same bandwidth of the signal, or to maintain the BPSK data rate but halving the needed bandwidth.

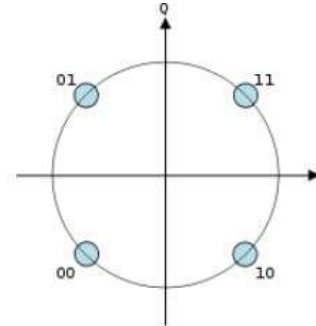


Fig.7: Constellation for QPSK

(iii). Quadrature amplitude modulation (QAM)

The QAM is the modulation scheme which encode the information into a carrier wave by varying the amplitude of both the carrier wave and a - quadrature carrier that is 90° out of phase with the main carrier wave in accordance with the two input signals. It means that, the amplitude and the phase of the carrier wave are simultaneously varied in accordance to the information we want to transmit. The symbol rate is one fourth of the bit rate. So this modulation format produces a more spectrally efficient transmission. It is more efficient than BPSK, QPSK.

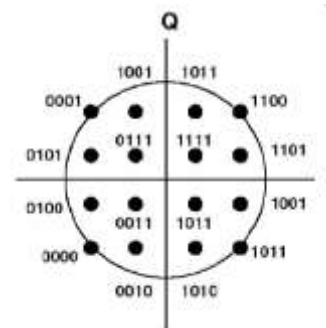


Fig.8: Constellation for QAM

V. RESULTS AND ANALYSIS

The software MATLAB R2010a has been used to program and simulate the complete environment. The various parameters that have been initialized and various built in functions have been used to implement the complete design of the system. For this research work, Communication Systems Toolbox has been used along with standard MATLAB mathematics and graphics functions. The various simulation parameters used in this research work are shown in below table-

Table.1: Simulation Parameters

Parameter	Value
Number of Subcarriers	512
FFT Length	512
Bandwidth	5×10^6
Sampling Frequency	2xBW
Cyclic Pad Length	64 bits
Modulation Technique	BPSK, QPSK, 16QAM, 64 QAM

Simulation Results and Graphs

MATLAB software has been used to simulate the OFDM scheme with different modulation schemes and the performance is plotted in the form of Bit Error Rate (BER) vs Signal to Noise Ratio(SNR) plots, as shown in the below figures. The probability of error has also been computed and plotted against the SNR. Figure 12 shows the power spectral density plot against the sampling frequency, which shows the orthogonality of the OFDM signals.

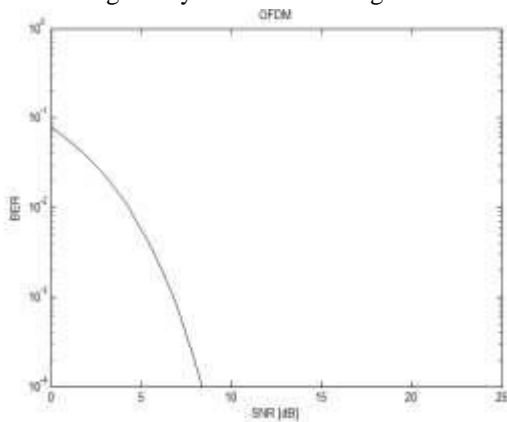


Fig.9: BPSK BER vs SNR curve

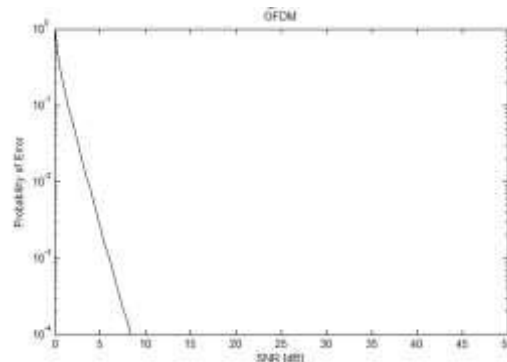


Fig.10: Probability of error for BPSK

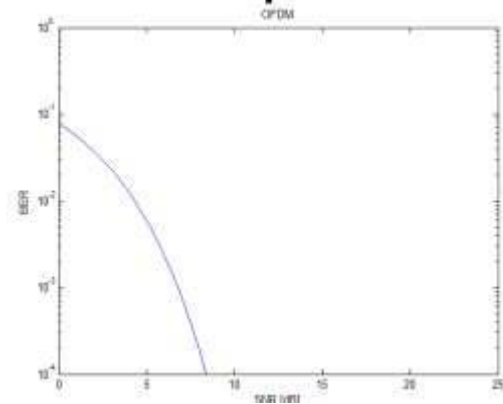


Fig.11: BER vs SNR for QPSK

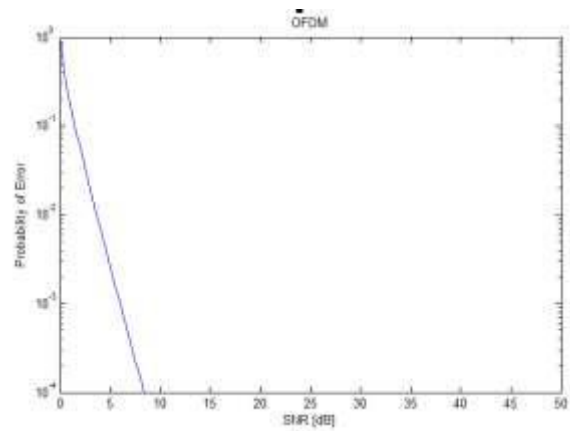


Fig.12: Probability of Error QPSK

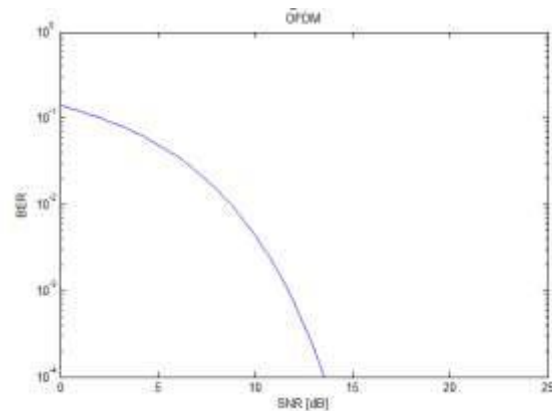


Fig.13: BER vs SNR for 16-QAM

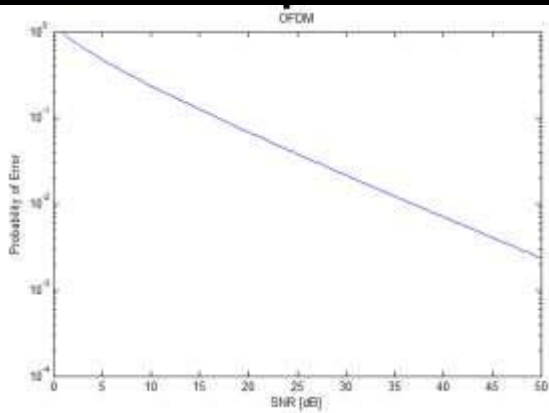


Fig.14: Probability of Error for 16 QAM

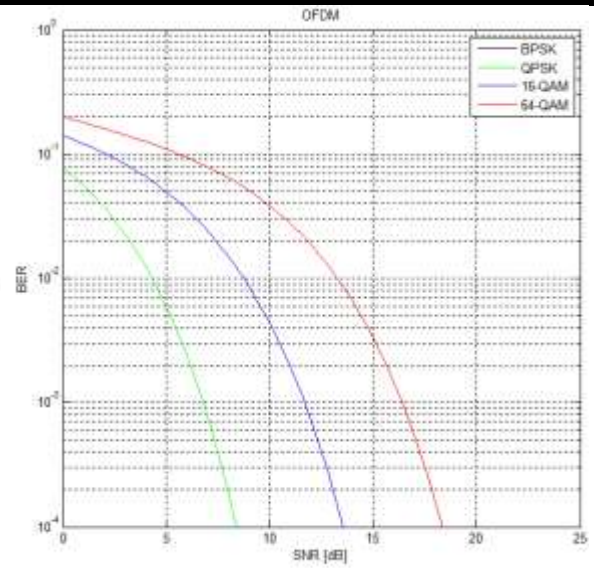


Fig. 17: BER vs SNR plot

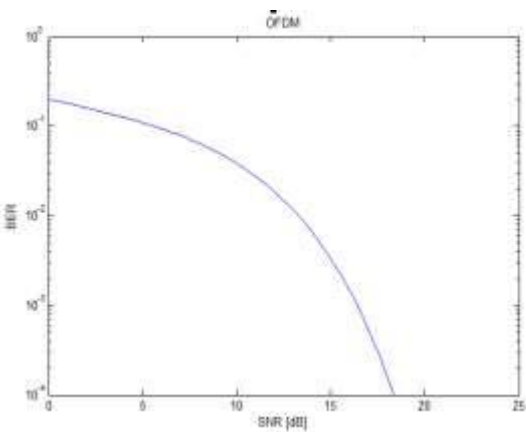


Fig.15: BER vs SNR for 64 QAM

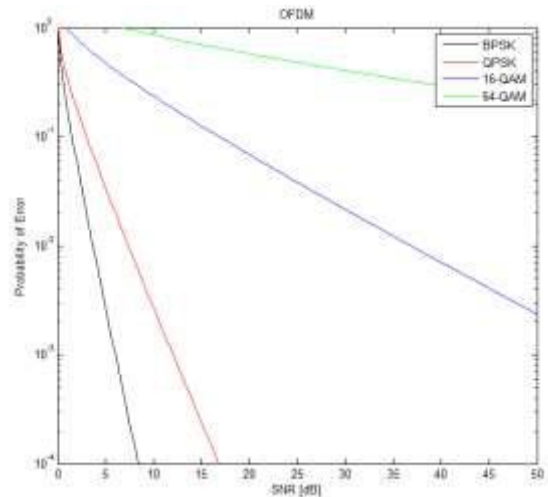


Fig.18: Probability vs SNR

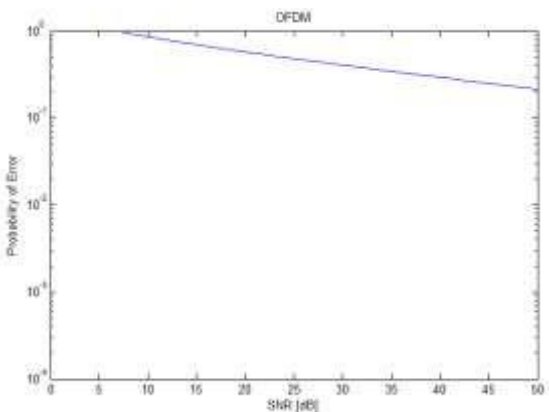


Fig.16: Probability of Error for 16 QAM

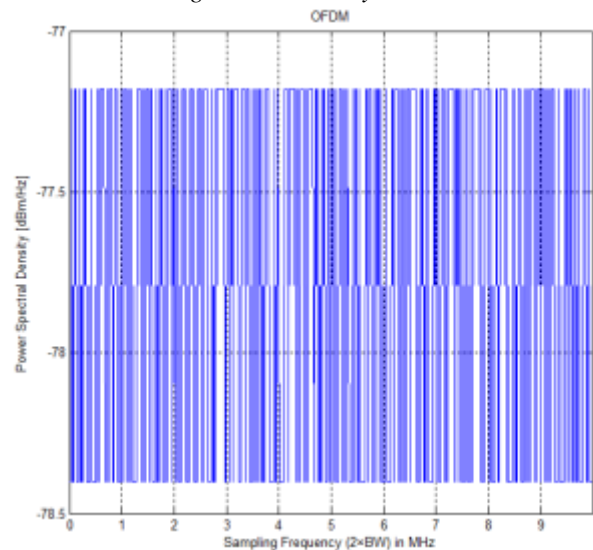


Fig.19: PSD vs Sampling frequency

VI. CONCLUSION

In this research work, the OFDM model of Wireless Communication is implemented and a number of modulation schemes are used viz. BPSK, QAM, QPSK, 16PSK, etc. The various performance parameters like BER, SNR etc. are to be evaluated. The channel used is Rayleigh fading Channel, for this research. The research work is intended to study and analyse the performance of OFDM technique under various modulation schemes.

REFERENCES

- [1] Nilesh Chide, ShreyasDeshmukh, Prof. P.B. Borole, "Implementation of OFDM System using IFFT and FFT", *International Journal of Engineering Research and Applications (IJERA)*, Vol. 3, Issue 1, pp.2009-2014, January -February 2013
- [2] Vidhya, R.Shankarkumar, "Ber Performance of AWGN, Rayleigh and Rician Channel", *International Journal of Advanced Research in Computer and Communication Engineering* Vol. 2, Issue 5, pp.308-314, May 2013.
- [3] V. Hindumathi, K. Rama Linga Reddy, K. Prabhakara Rao, "Performance Analysis of OFDM by using different Modulation Techniques", *International Journal of Research and Development*, Volume 3, Issue 7, PP. 07-10, September 2012
- [4] Mohammed S. Akhoirshida and Mustafa M. Matalgah- BER Performance Analysis of Interference-Limited BPSK Cooperative Communication Systems with Cochannel Interference in Nakagami-m Fading Channels, PAWR 2013, IEEE.
- [5] Jun Lu, ThiangTjhung, Fumiyuki Adachi and Cheng Li Huang, —BER performance of OFDM-MDPSK system in Frequency –Selective Rician Fading with Diversity Reception, || IEEE Trans. On Vehicular Technology, vol. 49, no. 4, pp. 1216-1225, July 2000.
- [6] Young Jae Ryu and Dong Seog Han, —Timing phase estimator overcoming Rayleigh Fading For OFDM systems, || IEEE Proc., pp. 66- 67.
- [7] M. Nakagami, —The m-distribution—A general formula of intensity distribution of rapid fading, || in Statistical Methods in Radio Wave Propagation, W. C. Hoffman, Ed. Elmsford, NY: Pergamon, 1960.
- [8] Zheingjiu Kang, Kung Yao, Flavio Lorenzelli, —Nakagami-m Fading Modeling in the Frequency Domain for OFDM system analysis, || IEEE Communication letters, vol. 7, no.10, pp. 484-486, Oct.2003.

Interactive effect of tillage and wood ash on heavy metal content of soil, castor shoot and seed

Nweke I A¹, Ijearu S I², Dambaba N³

^{1,2}Department of Soil Science Chukwuemeka Odumegwu Ojukwu University, Anambra State

³National Cereal Research Institute, Baddagi, Bida, Niger State

Abstract— Organic waste when used as soil amendment improves the fertility status of soil and crop yield, but unrestricted application on soil could lead to accumulation of heavy metals to a level, toxic to plants themselves and the animals that consumes them. Thus a field experiment was conducted in three (3) different planting seasons using three tillage methods (mound, ridge, flat) and four different rates (0t/ha, 2t/ha, 4t/ha, 6t/ha) of wood ash to evaluate the effect of tillage and wood ash on heavy metal; copper (Cu), boron (B) and lead (Pb) content of soil and uptake by castor shoot and seed. Data generated from the study was analyzed using crop start version 7.2 and mean separation was done using least significant difference (LSD0.05). The findings from the study showed that the interactive effect of tillage and wood ash on heavy metals content of soil, castor shoot and seed were significant ($P < 0.05$). The values obtained decreased as the planting season increased, while the amount was found to increase as the rates of wood ash application increased. For soil heavy metal contents it was observed that tillage methods had no effect on virtually all the parameters assessed. The values obtained from ridge and flat were higher when compared to the value of mound with regard to soil and castor shoot heavy metal contents. The result of the shoot also show that interaction of flat and wood ash at the rates of 2t/ha, 4t/ha, and 6t/ha (Ft2, Ft4, Ft6) show statistically similar results. The result of heavy metal content of seed indicated that tillage method had no effect in most of the heavy metal contents of the castor seed, while Cu in 3rd year planting season were not significant among the rates of wood ash applied. The interaction effect of ridge and wood ash at the rates of 2t/ha, 4t/ha and 6t/ha (Rd2, Rd4, Rd6) on Cu, 1st and 2nd season were statistically similar, while the result from mound method was found to increase the seed up take of most of the tested parameters. The observed values of these tested parameters (Cu, B, Pb) in wood ash amended plots in the three planting seasons were within acceptable limits.

Keywords— Heavy metal, castor shoot, castor seed, tillage, wood ash.

I. INTRODUCTION

Soil has been bequeathed by nature a natural medium for waste disposal and filter to many contaminants and toxic elements that might be harmful to crops, animals and man. However, continuous disposal or the use of waste as soil amendment can lead to the accumulation of the toxic metals to a critical level where they become phototoxic to plants and ecto-toxic to animals and man that will directly and indirectly depend on plants for their livelihood. There are increases in incurable diseases such as cancer; kidney problems etc and most of these diseases are traced to our food and water. One of the hopeless situations of pollution of the soil with heavy metals according to Lone et al., (2008) and Jing et al., (2007) is that they cannot be biologically degraded; they can only be transformed from one oxidation state or organic complex to another. Moolenaar and Lexmond (1999) found out that lead (Pb) and cadmium (Cd) is cumulative toxins that are indestructible and can only be eliminated through excretion. When accumulate in human body according to Wildlife, (2000) they cause health hazards that include but not limited to central nervous system, reduce intellectual capabilities and hypertension (Stassen, 2002).

Though most of the trace elements are found naturally in soil inform of their complexes or bound form their accumulation in the environment are intensified by human activities. According to the works of Okoronkwo et al., (2005); Jing et al., (2007) Lone et al., (2008) and Umeoguaju (2009) mining and purification of lead, zinc and cadmium, steel production, burning of wastes, and coal burning, discharges from industrial effluents as well as excessive use of fertilizers, pesticides application and use of sewage and other organic wastes in farming operations are man's activities on soil that are capable of creating good condition for heavy metals to enter and accumulate in the soil environment.

However, from the agricultural point of view, most of the organic wastes are applied in agricultural lands with a view to improve the fertility status of the soil. Basically many

tropical soils like southeastern soils of Nigeria have low organic matter content, plant nutrient deficiency resulting from high rainfall and temperature. Consequently these soils lack the strength and ability to sustain crop production at optimum level, hence the need for organic waste as soil amendment to increase soil nutrients and crop yield. The work of Pierzynstic et al., (2002) have portrayed that lack of effective waste management can have substantial negative effects to plants and animals including man through the introduction of pollutants into the soil environment. In Nigeria, the efficiency of wood ash as well as tillage systems in improving soil productivity and crop yield has been documented in the works of Agbede et al., (2008), Mbah et al., (2010), Ojeniyi et al., (2012), Omoju and Ojeniyi, (2012), and Nwachukwu et al., (2012). However, no attention has been given to contents of heavy metals of wood ash as soil amendment. Thus the present study tend to report on the uptake of selected heavy metals like Cu, B, Pb, by castor shoot and seed and their accumulation in soil following four different rates of wood ash application and three tillage methods.

The work is intended to recommend an appropriate rates of wood ash and frequency of application with appropriate tillage method, all with a view to avoid excessive soil accumulation and up take by castor plant, because oil from the seed is very useful to man medically and industrially.

II. MATERIALS AND METHODS

Location of Experiment

This study was carried out in three different cropping seasons at Teaching and Research Farm of Faculty of Agriculture and National Resources Management Ebonyi State University, Abakaliki. The area of the study is located within latitude 06°19' N and Longitude 08°06' of the southeast in the derived savannah agro-ecological zone of Nigeria. The rainfall distribution is bimodal with wet season from April to July and peak in June and September to November. It has an average annual rainfall range of 1700 – 1800mm. The temperature of the area ranges from 27°C – 31°C. The relative humidity of the study area is between 60 – 80% and the soil is ultisol and classified as Typic Haplustult by FDALR (1985).

Land preparation and Treatment Application

A land area measuring 41m x 15m (0.0615ha) was mapped out and used for the study. The experimental site was cleared of the natural vegetation using cutlass and the debris removed. Tillage operation was done manually using hoe. The tillage treatments are mound (Md), ridge (Rd) and flat (Ft). Wood ash of different levels was spread uniformly on

the soil surface and buried in their respective plots immediately after cultivation. The details of treatments used are as follows:

1. Md0 – Mound without wood ash (Md0)
2. Rd0 - Ridge without wood ash (Rd0)
3. Ft0 - Flat without wood ash (Ft0)
4. Md + 2 t/ha of wood ash (Md2)
5. Md + 4 t/ha of wood ash (Md4)
6. Md + 6t/ha of wood ash (Md6)
7. Rd + 2t/ha of wood ash (Rd2)
8. Rd + 4t/ha of wood ash (Rd4)
9. Rd + 6t/ha of wood ash (Rd6)
10. Ft + 2t/ha of wood ash (Ft2)
11. Ft + 4t/ha of wood ash (Ft4)
12. Ft + 6t/ha of wood ash (Ft6)

Two castor seeds per hole were planted at a spacing of 0.9m between rows and 0.45m within rows at a depth of 8cm. There was basal application of NPK fertilizer to all plots two weeks after planting. The seedlings were thinned down to one plant per stand two weeks after germination. Weeding was done manually with hoe at 3-weeks interval till harvest. Harvesting was done when the capsules containing the seed turn brown. The harvested spikes was dried in the sun 2-3 days and then threshed to release the seeds used for heavy metal content determination. The shoot was also harvested for heavy metal studies. The same procedure was repeated in the 2nd and 3rd year of the experiment but without application of wood ash in the 3rd year to test the residual effect.

Experimental Design

The total land area used for the study was 0.0615ha. The experiment was laid out as split plot in a randomized complete block design (RCBD), with 12 treatments replicated 3 times to give a total of 36 plots each measuring 3m x 4m (12m²). A plot was separated by 0.5m alley and each replicate was 1m apart. Four (4) rates of wood ash viz control (0tha⁻¹); wood ash (WA) at the rate of 2tha⁻¹ equivalent to 2.4kg/plot, WA at 4tha⁻¹ equivalent to 4.8kg/plot and WA at 6tha⁻¹ equivalent to 7.2kg/plot was used for the study. Each treatment was replicated 3 times along with the three tillage methods (Mound, Ridge and Flat) used for the study.

Soil Sample Collection

Auger soil samples were randomly taken from ten (10) observational points in the experimental area at the depth of 0 – 20cm prior to planting. The auger soil samples were mixed thoroughly to form a composite soil sample and used for pre-planting soil analysis of which the result is shown in Table I. Also the wood ash treatment used was analyzed for

determination of its heavy metal values, quantity and chemical composition. The result is presented in Table 2. At the end of each cropping season that is after crop harvest, auger soil samples were collected from three observational points in each plot, the soil samples were air dried, sieved and used for the determination of soil heavy metal content.

Laboratory Method

Heavy Metals (trace elements)

Heavy metals otherwise known as trace elements (metals) are plant essential micro-nutrient elements but adversely become toxic to plants and animals and indirectly to humans in excess quantities. Hence they are inorganic pollutant particles in soil.

Determination of Heavy Metals

The determination of heavy metals (Cu, B, and Pb) was by using the method outlined by Miller et al., (1986).

Table.1: Initial soil parameters before treatment application

Test Parameter	Value
Lead (Pb)	48.60 mgkg ⁻¹
Copper (Cu)	26.50 ‘‘
Boron (B)	5.60 ‘‘

Table.2: Chemical composition of the wood ash before application

Test Parameter	Value
Lead (Pb)	52.28 mgkg ⁻¹
Copper (Cu)	148.00 ‘‘
Boron (B)	54.60 ‘‘

Effect of Tillage and Wood ash on soil heavy metals (Cu, B, Pb mgkg⁻¹)

The result of the effect of TM on heavy metals of the soil studied (Cu, B and Pb) is presented in Table 3. The result obtained showed that tillage methods had statistical significant ($P < 0.05$) effect in all the parameters tested. Although non-significant differences in the values of B (1st year), and 2nd year values of Cu, B and Pb were observed. The result of Mound showed that the value of Cu decreased in the 2nd year planting, but increased rapidly in the residual year to the extent that the fractional differences in value of the 1st and 2nd year value from 3rd year result were large with 35.128mgkg⁻¹ and 44.55mgkg⁻¹ respectively. The

Data Analysis

The data obtained from the study were subjected to an analysis of variance test based on RCBD using CropStat software version of 7.0, while statistically significant difference among treatment means was estimated using the least significant difference ($LSD < 0.05$).

III. RESULTS

Initial properties of the soil of the study site and wood ash before the beginning of the study

The heavy metal content of the soil show medium values in lead (Pb) and copper (Cu) and lower value in boron (B). The order of their increase in the soil was $Pb > Cu > B$ (Table 1). The ash showed higher values in the tested heavy metal contents, the order of their increase in the ash were $Cu > B > Pb$ (Table 2). There were high level content of lead, copper and boron in ash visa-vies their content in soil.

result of Boron (B) from Mound indicated decrease in value as the planting year increased. There was a radical decrease in value of B in the residual year when compared to the 1st year result as the percentage decrease in value was 98.75%. The result of lead (Pb) showed gradual decrease in value as the year of planting increased. The result order was 1st year result $>$ 2nd year result $>$ 3rd year result. The result of Ridge for Cu showed an order of 3rd year result $>$ 1st year result $>$ 2nd year result. The percentage decrease in value of Cu in the 2nd year relative to the 3rd year planting result was 78.04%, this value showed that there was a rapid decrease in the value of Cu in the 2nd year planting period.

Table.3: Effect of Tillage and Wood ash on Soil heavy Metals (Cu, B, Pb, mgkg⁻¹)

Treatment	1 st Year			2 nd Year			3 rd Year		
	Cu	B	Pb	Cu	B	Pb	Cu	B	Pb
Md0	4.440	96.340	157.800	4.800	116.000	7.200	7.900	0.940	24.400
Md2	17.900	204.600	48.220	8.950	147.400	58.600	96.450	1.940	85.080
Md4	28.000	136.300	76.400	16.600	108.300	109.500	95.800	2.000	95.110
Md6	56.200	94.800	240.400	38.500	106.600	246.100	46.900	1.750	95.380
Mean	26.635	133.010	130.705	17.213	119.575	105.350	61.763	1.658	74.993
Rd0	9.600	37.200	10.400	2.440	98.700	8.860	11.080	0.750	113.700
Rd2	12.000	248.100	88.200	18.100	144.500	56.200	88.400	2.370	79.967
Rd4	84.400	158.700	54.116	9.600	113.800	148.100	116.400	7.500	94.200
Rd6	65.400	266.800	116.700	42.200	122.600	202.900	114.500	17.600	129.000
Mean	42.850	177.700	67.354	18.085	119.900	104.015	82.595	7.055	104.217
Ft0	3.840	140.300	8.540	2.350	96.200	5.400	6.540	0.550	33.990
Ft2	5.790	133.467	170.400	3.800	100.500	206.400	14.100	2.370	63.760
Ft4	24.100	204.000	46.600	9.600	156.400	124.500	33.950	2.450	46.410
Ft6	60.233	142.800	10.240	32.100	240.200	235.800	48.200	8.810	96.640
Mean	18.491	155.142	58.945	11.963	148.325	143.025	25.697	3.545	60.198

LSD 0.05

TM	20.37	NS	53.88	NS	NS	NS	29.49	3.66	24.17
WA	15.27	51.55	65.37	4.09	34.35	56.60	30.56	3.54	28.75
TM x WA	0.70	14.09	0.14	0.23	0.44	85.27	0.19	0.28	28.11

TM= Tillage method; WA= Wood ash; Md0 = Mound without wood ash (WA); Md2 =Mound +2t/ha WA; Md4 = Mound + 4t/ha WA; Md6 = Mound + 6t/ha WA; Rd0 = Ridge without WA ; Rd2 = Ridge +2t/ha WA; Rd4 = Ridge + 4t/ha WA; Rd6 = Ridge + 6t/ha WA; Ft0 = Flat without WA; Ft2 = Flat + 2t/ha WA; Ft4 = Flat + 4t/ha WA; Ft6 = Flat + 6t/ha WA

The results of B showed an increased value as the years of planting increased, but the residual year result presented drastic reduction in the value of B. The reduction in value of B in 3rd year planting relative to 1st and 2nd year planting were 96.03% and 94.12% respectively. Lead (Pb) for Ridge showed a rapid increase in value as the planting year increased, though the value of Pb in 2nd and 3rd year planting are relatively similar as their difference in value was merely 0.202mgkg⁻¹. However, its decrease in value in 1st planting year was 35.37% relative to the 3rd year planting. The result of Cu in Flat method indicated decrease in value as planting year increased, though the value which increased in the 3rd year planting was higher than the 1st and 2nd year planting result. The result of B showed reduction in value as the planting year increased with drastic reduction in value in residual year. The result of Pb from Flat showed rapid increase in value in the 2nd year planting result when compared to the 1st year planting result however, this value decreased rapidly in the 3rd year result. When the tillage methods are compared, it showed that for 1st planting period, the result order was Ridge > Mound > Flat for Cu result. Boron showed an order of

Ridge > Flat > Mound and for Pb Mound > Ridge > Flat. The same result scenario of 1st year was observed in 2nd year result for Cu, but B had a contrary order as the values of Mound and Ridge are the same with the highest value observed in Flat. The 2nd year result of Pb showed highest value in Flat, hence the order Flat > Mound > Ridge though the value of Ridge and Mound are relatively alike as the fractional difference in their values is 1.335mgkg⁻¹. The residual year result presents an order of result for Cu as Ridge > Mound > Flat. The observed value of Cu in Flat when compared to the other methods was relatively very low. The result order of B showed that highest value of B was observed in Ridge, next in rank was Flat, while the least value was observed in Mound. The order of Pb result was Ridge > Mound > Flat. The Ridge result showed very much increased value when compared to value obtained from Mound and Flat.

The changes in soil heavy metals contents following the application of wood ash on the soil are shown in Table 3 for the three cropping years. The soil heavy metal contents (Cu, B and Pb) were significantly (P<0.05) different among the rates of wood ash applied. The effect of wood ash

application on Mound, showed that the value of Cu in 1st and 2nd year result was dependent on the quantity of ash applied, as the value increased with attendant increase in WA applied hence the result order for 1st and 2nd year was Md6 > Md4 > Md2 > Md0. The 3rd year result depicts Md2 as having the highest content of Cu the next in rank was Md4 among all the other rates. For the 3 years' study Md0 consistently showed lowest value of Cu. The result of B showed that Md2 recorded the highest value in 1st and 2nd year planting, the next in rank was Md4 hence the result order Md2 > Md4 > Md0 > Md6 (1st and 2nd year planting result). The residual year presented a different order of result whereby the highest of 2.0mgkg⁻¹B was observed in Md4 and the least value (0.94mgkg⁻¹) was recorded in Md0 relative to other rates of WA applied. The result of Pb in 1st year planting indicated non-dependent of values on the quantity of ash applied. The 1st year planting showed highest value of Pb was recorded in Md6, next in rank was Md0 and the least value was obtained in Md2. The 2nd and 3rd year result of Pb showed that values obtained are dependent on the quantity of ash applied, because the values observed increased with increase in the rates of ash applied. The result variation of 1st and 2nd year present an order of Md6 > Md4 > Md2 > Md0 for the two cropping years, the value recorded in Md6 and Md4 were higher compared to the other two rates of WA. The effect of ash on Ridge indicated that higher value of Cu was observed in Rd4 relative to other rates in 1st year planting, the next closest value in rank was obtained in Rd6. The 2nd year result showed Rd6 to have recorded the highest value (42.20mgkg⁻¹) and the least value (2.440mgkg⁻¹) from Rd0, while the 3rd year present an order of Rd4 > Rd6 > Rd2 > Rd0. For the 3 years' under study, the lowest values of Cu were observed in Rd0s' rate of which the lowest among them is from 2nd year result. The result of B showed an increased value on the rates in 1st and 2nd year planting, but these values decreased drastically in the residual year. The 1st year result of B showed an order of Rd6 > Rd2 > Rd4 > Rd0 and 2nd year Rd2 > Rd6 > Rd4 > Rd0. The residual year showed dependency of value on the rates of WA applied. An increased value was observed in Rd6, compared to the values recorded in the other rates. The result variation was Rd6 > Rd4 > Rd2 > Rd0. The lowest value of Pb (10.4mgkg⁻¹) was recorded in Rd0 and the highest from Rd6 (116.700mgkg⁻¹) relative to the values obtained from the other rates in the 1st year planting. The 2nd year result showed an increased value in the recorded value of Rd6 and Rd4, though the result order showed Rd6 > Rd4 > Rd2 > Rd0. The 3rd year result scenario changed as the Rd0 which

consistently recorded the lowest value of Pb in 1st and 2nd planting turned out to record the next in rank to the highest value that was obtained from Rd6, hence the order Rd6 > Rd0 > Rd4 > Rd2. The effect of rates of WA on Flat for Cu follows a particular order. The 1st, 2nd and 3rd year planting result indicated increase in value as the rate of WA applied increased and decreased in value as the planting year increased especially when the 1st year and 2nd year planting result values are compared. Therefore, the result order for Cu 1st, 2nd and 3rd year results were Ft6 > Ft4 > Ft2 > Ft0. The result of B showed an increased value in all the rates in 1st and 2nd year results but these values decreased rapidly in the residual year. The 1st year result however showed Ft4 to record the highest value, next to Ft4 in value was Ft6 and the least value obtained in Ft2. The 2nd year and 3rd year result showed that value of B obtained was dependent on the quantity of ash applied, hence result order was Ft6 > Ft4 > Ft2 > Ft0. For the 3 years' of study the lowest value of 0.55mgkg⁻¹ B was observed in Rd0 of 3rd year planting result. The 1st year planting result of Pb showed that very low values were obtained in Ft0 and Ft6 compared to the values of Ft2 and Ft4. Among these rates the highest value of Pb was recorded in Ft2 and next in rank was Ft4. In 2nd year planting result an increased value of Pb was observed in all the rates except for Ft0 were very low value was recorded compared to the values of the other rates of WA, the result order is Ft6 > Ft2 > Ft4 > Ft0. The 3rd year result showed decreased values relative to the values of 2nd year result except for Ft0 that showed rapid increase in value in the 3rd year result. The 3rd year result show a result variation of Ft6 > Ft2 > Ft4 > Ft0.

The effect of tillage and wood ash presented in Table 3 showed significant differences among the tillage methods and rates of WA applied. The result indicated that the combination of tillage and WA has great effect on the amount and quantity of soil heavy metals contents obtained. The results also showed that the values of the soil heavy metals (Cu, B and Pb) increased as the rates of WA applied increased in the entire TM. Their values were observed to be higher in the 1st and 2nd year planting and decreased in the 3rd year planting period. The values observed in 4tha⁻¹ (Md4, Rd4, Ft4) and 6tha⁻¹ (Md6, Rd6, Ft6) rates of WA and TM were relatively similar, but higher in value compared to the values obtained from 2tha⁻¹ (Md2, Rd2, Ft2) and 0tha⁻¹ (Md0, Rd0, Ft0) rates of WA. The result equally showed that the value of Cu obtained from Mound and Ridge in 1st and 3rd year planting results was statistically similar. The values of these parameters observed in Ridge and Flat for the 3 years' study were

relatively similar and higher in value when compared to the values of rates of WA in Mound. Significantly, higher values of B > Pb > Cu were observed in 1st and 2nd year planting period. However, these values decreased much at 3rd year planting period, while the value of Cu which was relatively small in the 1st and 2nd year planting increased sharply in the 3rd year planting, though the increase was not greater than the value of Pb. The results obtained also attest that the values of these heavy metals obtained from the control soils (Md0, Rd0, Ft0) significantly were small when compared with values obtained from the other rates of WA applied which are the ash amended soils. The results of Cu, B (1st year), B (2nd year) and Cu (3rd year) in 4tha⁻¹ (Md4, Rd4, Ft4) and 6tha⁻¹ (Md6, Rd6, Ft6) were statistically similar but significantly different with control plots. Also the values of B (1st and 2nd year), and Cu, Pb (3rd year) obtained from 2tha⁻¹ and 4tha⁻¹ WA respectively were statistically similar but significantly better than the values of control plots.

Effect of Tillage and Wood ash on the Heavy Metal content of Shoot of Castor (Cu, B, Pb mgkg⁻¹)

The effect of tillage methods on the heavy metal contents (Cu, B, Pb) of castor shoot shown in the Table 4 showed significant differences (P<0.05) among the tillage methods studied. The result of Mound showed that for 3 years' planting the value of Cu was observed to be highest in the 1st year planting of which decreased as the year of planting increased. B and Pb result also show the same result scenario of increased value in 1st year planting result with attendant decrease in value as planting year increased and there was a rapid decrease in value of the 3rd year result when compared to the 1st and 2nd year values. The result of Ridge and Flat for the three (Cu B and Pb) parameters for the years of study showed decreased value as planting year increased hence the order 1st > 2nd > 3rd year results. The 3rd year results for the tested parameters in the two tillage methods (Ridge and Flat) showed very sharp reduction in value when compared to their values recorded in 1st and 2nd year result. In comparison of the TM in 1st year planting Mound showed higher value of Cu than the Ridge and the least value from Flat while B showed an order of Ridge > Mound > Flat.

Table.4: Effect of Tillage and Wood ash on the heavy metal content of Shoot of Castor (Cu, B, Pb mgkg⁻¹)

Treatment	1 st Year			2 nd Year			3 rd Year		
	Cu	B	Pb	Cu	B	Pb	Cu	B	Pb
Md0	1.010	20.250	1.030	0.060	19.300	0.080	0.000	1.150	0.017
Md2	1.320	12.650	1.170	0.370	11.700	0.220	0.018	1.270	0.055
Md4	1.060	23.950	1.830	0.110	23.000	0.880	0.011	1.250	0.028
Md6	0.650	32.050	1.430	0.700	21.100	0.480	0.016	1.080	0.034
Mean	1.260	22.225	1.365	0.310	18.775	0.415	0.011	1.188	0.034
Rd0	0.980	32.350	1.280	0.030	31.400	0.930	0.012	0.950	0.022
Rd2	1.120	21.850	1.200	0.170	20.900	0.250	0.035	1.250	0.031
Rd4	1.370	33.950	2.110	0.420	33.000	1.160	0.030	1.510	0.028
Rd6	1.260	43.650	1.230	0.310	42.700	0.280	0.028	1.350	0.033
Mean	1.183	32.950	1.455	0.233	32.000	0.505	0.026	1.265	0.029
Ft0	1.030	21.750	1.150	0.080	20.800	0.200	0.013	1.750	0.016
Ft2	1.090	15.450	1.060	0.140	14.500	0.110	0.011	1.500	0.011
Ft4	1.100	16.010	1.070	0.150	15.060	0.120	0.016	1.680	0.024
Ft6	1.150	6.040	1.130	0.200	5.090	0.180	0.019	1.640	0.040
Mean	1.093	14.813	1.103	0.143	13.863	0.153	0.015	1.643	0.023

LSD 0.05

TM	0.15	5.93	0.25	0.14	5.27	0.24	0.01	0.13	0.01
WA	0.14	9.46	0.24	0.15	9.34	0.23	0.01	0.24	0.01
TM x WA	0.04	0.17	0.08	0.10	1.04	0.03	0.003	0.10	0.003

TM= Tillage method; WA= Wood ash; Md0 = Mound without wood ash (WA); Md2 =Mound +2t/ha WA; Md4 = Mound + 4t/ha WA; Md6 = Mound + 6t/ha WA; Rd0 = Ridge without WA ; Rd2 = Ridge +2t/ha WA; Rd4 = Ridge

+ 4t/ha WA; Rd6 = Ridge + 6t/ha WA; Ft0 = Flat without WA; Ft2 = Flat + 2t/ha WA; Ft4 = Flat + 4t/ha WA; Ft6 = Flat + 6t/ha WA

The reduction in the value of B recorded in Flat relative to the Ridge value is of much value 55.04%. The variation in the result of Pb indicates an order of Ridge > Mound > Flat, the reduction in value in Flat was 24.19% relative to the value obtained from Ridge. The 2nd year result showed Cu to be higher in Mound of which the decreased value in Ridge and Flat were 24.84% and 53.87% respectively. Boron (B) showed increased value in Ridge, this value decreased in Mound but lowest in Flat. Pb result presents an order of Ridge > Mound > Flat. The result of the 3rd year for Cu and B present a variation of Ridge > Flat > Mound, while Pb present a contrary result order of Mound > Ridge > Flat. For the 3 years' of study the lowest value of Cu and B was observed in Mound in the 3rd year planting, while that of Pb was observed in Flat in 3rd year planting.

The rates of WA application showed decrease in value as the year of planting increased in the entire TM and lowest values were recorded in the 3rd year planting. The result variation in Mound in 1st year for Cu, show Rd2 to be higher in value compared to the other rates while the lowest value of 0.65mgkg⁻¹ Cu was recorded in Md6. B result presented Md6 as the highest, next in rank was Md4 and least value of 12.65mgkg⁻¹ B was obtained in Md2. For Pb result the highest value was observed in Md4 and its decreased value in Md0 was 43.72%. The 2nd year result variation for Cu, B and Pb showed a variation of Md6 > Md4 > Md2 > Md0 (Cu), for B, Md4 > Md6 > Md0 > Md2 and Pb, Md4 > Md6 > Md2 > Md0. The result of Mound showed non-presence of Cu in the shoot of castor from Md0 plots an indication that tend to suggest that Mound method without soil amendment and continuous cultivation can drastically reduce or remove entirely heavy metals from the soil, thereby making it impossible for the growing plants to pick them up. The other rates however showed increased value of Cu. B showed an order of Md2 > Md4 > Md0 > Md6 and Pb, Md2 > Md6 > Md4 > Md0. The result variation indicated that higher value of B and Pb were observed in Md2 respectively. The rate of ash on Ridge indicated higher Cu content in Rd4 and the least in Rd0 compared to the other rates. The B result indicated an increased value from Rd2-Rd6, but the value of Rd0 was higher than the Rd2 values. For Pb higher value was recorded in Rd4 and the next closed value was obtained in Rd0. The 2nd year result for the three elements was of the same scenario with the 1st year result, only that lower values were obtained in the rates compared of their values in the 1st year result. The 3rd year result of Cu and B showed increased value as rate of ash applied increased, though a decreased value for the elements were observed in Rd₆ respectively, but higher than

their values in Rd0. The Flat result for Cu showed that the value of Cu in 1st and 2nd year was dependent on the rate of ash applied, hence result order of Ft6 > Ft4 > Ft2 > Ft0. Its 3rd year result presents a contrary order of Ft6 > Ft4 > Ft0 > Ft2, but in the 3 years' study higher value was shown to be observed in Ft6 relative to other rates. The 1st year result of B indicated an increased value in Ft0 of which its decreased value in Ft6 was of much value 72.23% while for Pb higher value was still observed in Ft0 and its decreased value in Ft2 the least value was merely 7.83%. The 2nd year result of B and Pb was in line with the result variation obtained from the 1st year result only that lower values were obtained compared to their values in the rates of 1st year result. The 3rd year planting present a result order of Ft0 > Ft4 > Ft6 > Ft2 for B and Pb, Ft0 > Ft6 > Ft4 > Ft2 the two results indicated higher values to have been obtained in Ft0 while the values of Ft4 and Ft6 were relatively alike.

The result presented in Table 4 showed that the effect of tillage methods and rates of wood ash (TM x WA) on the heavy metal content of the shoot were significantly different ($P < 0.05$) among the rates of WA and tillage methods studied. The values of the tested elements (Cu, B and Pb) decreased as the years of planting period increased. The values obtained for these parameters (Cu, B and Pb) from 4th^a and 6th^a rates of WA among the tillage methods were found to be relatively higher than the values obtained from 0th^a and 2th^a rates. Continuous cultivation and non-application of wastes can even lead to exhaustion or non-uptake of some of these heavy metals as was found in Cu in the third year planting. Tillage (Flat) and WA at the rate of 2th^a, 4th^a and 6th^a (Ft2, Ft4, Ft6) showed statistically similar results for Pb and Cu in 1st and 2nd year planting periods respectively. The yield values obtained in Ridge and Flat were relatively higher than the values obtained from Mound. The ash application also influences changes in the values obtained for the parameters and the trend of changes was observed to be in consistent. For instance, the values of Cu in 1st and 2nd years planting were found to increase as the rate of WA applied increased, while the values of B and Pb decreased as the rates of WA increased to 2th^a and then increased in 4th^a and decreased again in 6th^a rates of WA. Also the values of Cu, B and Pb in 3rd year planting obtained from 2th^a, 4th^a and 6th^a respectively were not significantly different among the rates. The value trend for the 3 years of study from the rates of WA applied showed B > Pb > Cu.

Effect of Tillage and Wood ash on heavy metal content of Castor seed (Cu, B, Pb mgkg⁻¹)

The effect of tillage methods on the heavy metal contents of seed presented in Table 5 indicated non-significant differences for B 1st and 2nd year planting and Pb for the 3 years of study. However, significant differences in Cu were observed among the tillage methods for the years under study. The result obtained from Mound method in 1st year planting indicated that highest values of Cu, B and Pb were observed in the 1st planting year of which decreased in value as the planting year increased, with sharp reduction in the 3rd year planting. The result of the parameters from Ridge and Flat follow the same result order of Mound, whereby the 1st year recorded the highest value and the value decreased as planting year increased with greatest decrease in value in the 3rd year planting. The result of B in Ridge 1st and 2nd year planting however, are close as its percentage decrease in 2nd year planting was relatively small with a value of 3.17%. When the TM are compared, Ridge method showed higher content of Cu, compared to Flat and Mound that made least value. The reduction in Cu content of Mound in the 1st year planting result was observed to be 35.04% relative to the Ridge value. The variation in B and Pb result for 1st and 2nd year planting among the tillage methods were not much, though result order showed Mound > Ridge > Flat. The residual (3rd) year result showed that higher value of Cu content was obtained in Mound with a value of 0.098mgkg⁻¹ and the least value 0.045mgkg⁻¹ obtained in Flat method. The result of B presents a different order of Ridge > Mound > Flat while Pb showed that Mound > Flat > Ridge.

The rates of WA application in Table 5 showed significant differences ($P < 0.05$) for the tested elements except for residual year result of Cu. The result of its application on Mound methods in 1st year planting indicated that highest values of Cu, B and Pb were observed in Md2, Md4 and Md6 respectively. For Cu the least values were obtained in Md6 of which its percentage decreased value relative to Md2 was 85.95%. This value showed greater reduction of Cu value in Md6 while B showed 76.27% value reduction in Md0 relative to Md4. Pb value showed dependence of value on the rate of ash applied as order was Md6 > Md4 > Md2 > Md0. It showed much reduction in value in Md0 with a value of 49.746% relative to the Md6 value. The 2nd year planting result indicated that Md2 was higher in Cu content compared to the other rates of WA the next in rank was Md6 and the least value from Md0. B showed least value in Md0 and the highest value from Md4. The value of Pb showed dependent on the rate of ash as the result order was Md6 > Md4 > Md2 > Md0 but greater reduction in Md0 with 96.078% relative to Md6 value. The 3rd year result

showed the Cu content to be high in Md6 the closest in rank was the value of Md2, but the Cu value decreased in Md0 with 32.20% relative to Md6 value. The result of B showed a result order of Md2 > Md6 > Md0 > Md4. However, the values of Md2 and Md6 as well as Md0 and Md4 did not vary much from the other as the fractional difference in their values were 0.017mgkg⁻¹ and 0.005mgkg⁻¹ respectively. The result from Mound in the residual year for lead (Pb) indicated non-uptake of the element by the castor seed in Md0 and Md6 plots, but its uptake in Md2 and Md4 showed that among the two rates, much of Pb content was observed in Md4 relative to Md2. The rate of ash on Ridge in 1st year planting indicated that higher content of Cu was obtained from Rd2 plots, the next in rank was observed in Rd6 plots, but the value decreased in Rd0 plots with a value of 32.97% relative to the Rd2 plots. The B content indicated a variation of Rd6 > Rd4 > Rd0 > Rd2 of which the percentage decrease in value of the element in Rd2 was 45.80% relative to the plots that recorded the highest B value. The content of Pb increased as the rate of ash increased. Although a decreased value was observed in Rd6 of which was higher in value than the Rd0 value the percentage difference in value between the Rd6 and Rd0 plots was 22%. The 2nd year planting result showed a decrease in value from the 1st year planting result. The result of Cu in this 2nd year result showed that Rd2 and Rd6 had the same value of Cu, while there was a greater decrease in the value of Rd0 relative to the Rd6 and Rd2 values. The value of B content in this 2nd year result still observed the scenario of 1st year result whereby the higher content of B was obtained from Rd6 of which is greater than the value of Rd4 and Rd0. While the least value was observed in Rd2 of which is 46.93% decreased compared to the value from Rd6 plots. When compared to its 1st year results, it means that the content of B decreased with a value of 1.13% in 2nd year planting result. The result of Pb showed increased value as the rate of ash applied increased to

Rd4, but decreased in Rd6. Though the observed value of Pb in the Rd6 was decreased, it was still higher than the value obtained in the Rd0 plots. The residual year result for the parameter showed sharp decrease in values obtained. The Cu content showed much decreased value in Rd4 with a value of 76.77% relative to the value of Cu obtained from Rd0 plots. The result of B increased in Rd4 relative to other rates of ash applied, the next increased value was observed in Rd0. Pb result, however, showed a variation of Rd4 > Rd2 > Rd0 > Rd6. The values obtained for Pb also show that there was much decreased value in Rd6 with 60.98%

relative to the value from Rd4. The result of ash on Flat showed higher value of Cu in Ft6 and the next in rank from Ft2 while the least value was obtained in Ft0 from the 1st year planting result. The B and Pb content showed a variation result order of Ft4 > Ft2 > Ft6 > Ft0 and Ft4 > Ft6 > Ft2 > Ft0 respectively. The values of the tested parameters in 2nd year planting result showed decrease in value when compared to the 1st year result. The value of Cu showed decreased value in Ft4 when compared to the value Ft6, while the B content showed decreased value in Ft0 relative to the value of Ft4. The Pb value showed higher value in Ft6 with much decreased value in Ft0 with a value of 86.96%. The residual year result showed a greater decrease in value of the elements when compared to the 1st and 2nd year results. The result of Cu showed an increased value in

Ft0 though the value did not vary much from the value obtained in Ft4 as the fractional difference in their values was merely 0.001mgkg⁻¹. The B content showed higher value in Ft2 with very much decreased value in Ft4 which was 96.66% showing greater reduction of B in Ft4 relative to Ft2 value. While Pb result indicated decrease in value as the rate of ash applied increased, hence the result order of Ft0 > Ft2 > Ft4 > Ft6.

The effect of tillage methods and rates of WA application were significant (Table 5). However, the effect of Ridge and WA at the rates of 2tha⁻¹ (Rd2), 4tha⁻¹ (Rd4) and 6tha⁻¹ (Rd6) on Cu 1st and 2nd year planting were statistically similar. The same kind of result was observed for B in the 3rd year where the Mound and the four different rates of WA (Md0, Md2, Md4 and Md6) were statistically similar.

Table.5: Effect of Tillage and wood ash on heavy Metal Content of Castor Seed (Cu, B, Pb mgkg⁻¹)

Treatment	1 st Year			2 nd Year			3 rd Year		
	Cu	B	Pb	Cu	B	Pb	Cu	B	Pb
Md0	1.040	11.150	0.990	0.090	10.200	0.040	0.080	0.250	0.000
Md2	1.210	24.550	1.170	0.260	23.600	0.220	0.100	0.350	0.086
Md4	1.070	46.990	1.210	0.120	46.040	0.260	0.095	0.245	0.099
Md6	0.170	39.850	1.970	0.220	38.900	1.020	0.118	0.333	0.000
Mean	1.123	30.635	1.335	0.173	29.685	0.385	0.098	0.295	0.046
Rd0	0.990	27.910	1.180	0.040	26.960	0.230	0.095	0.270	0.020
Rd2	1.477	21.430	1.200	0.520	20.480	0.250	0.066	0.650	0.022
Rd4	1.440	30.960	1.510	0.490	30.010	0.560	0.019	0.830	0.041
Rd6	1.470	39.540	1.400	0.520	38.590	0.450	0.030	0.460	0.016
Mean	1.344	29.960	1.323	0.393	29.010	0.373	0.043	0.553	0.025
Ft0	1.040	13.850	1.013	0.090	12.900	0.060	0.065	0.176	0.054
Ft2	1.100	32.150	1.180	0.150	31.200	0.230	0.013	0.510	0.050
Ft4	1.030	40.750	1.500	0.080	39.800	0.200	0.064	0.017	0.038
Ft6	1.130	27.850	1.410	0.180	26.900	0.460	0.040	0.075	0.016
Mean	1.075	28.650	1.188	0.125	27.700	0.237	0.046	0.195	0.040

LSD 0.05

TM	0.11	NS	NS	0.10	NS	NS	0.02	0.14	NS
WA	0.15	0.22	0.17	0.14	0.21	0.16	NS	0.20	0.02
TM x WA	0.04	0.41	0.06	0.02	0.14	0.03	0.03	0.13	0.002

Md0 = Mound without wood ash (WA); Md2 =Mound +2t/ha WA; Md4 = Mound + 4t/ha WA; Md6 = Mound + 6t/ha WA; Rd0 = Ridge without WA ; Rd2 = Ridge +2t/ha WA; Rd4 = Ridge + 4t/ha WA; Rd6 = Ridge + 6t/ha WA; Ft0 = Flat without WA; Ft2 = Flat + 2t/ha WA; Ft4 = Flat + 4t/ha WA; Ft6 = Flat + 6t/ha WA

It was also observed that tillage methods, especially Mound and Non-application of organic waste like WA influence greatly the uptake of heavy metals like Pb as can be seen from the presented result in Table 5. From the obtained values, it was observed that the effect of tillage and WA increased the seed uptake of B relative to the other

elements. Though these obtained values of the heavy metals (Cu, B and Pb) content of seed decreased as the years of planting increased. The tillage methods increased the uptake of B by the castor seed. Statistically similar results were obtained from Ridge and Flat for Cu in 3rd year planting as well as Mound and Flat for Cu in the 2nd year

and B in the 3rd year planting period. Among the tillage methods Mound was found out to increase the uptake of tested parameters, followed by Ridge method. The WA application showed that the values obtained from 4tha⁻¹ and 6tha⁻¹ rates of WA for the parameters tested were found to be statistically similar, but significantly different from the control plots. Examples are Cu, B (1st and 2nd year planting) and B (3rd year) planting periods. It was equally observed that the values of heavy metal contents (Cu, B and Pb) of seed in each rate of WA applied decreased as the year of planting increased and in some cases increasing the rates of WA application increased the uptake of these heavy metals.

IV. DISCUSSION

Soil Heavy Metals

The result of soil heavy metals after 3 years' of study showed that higher values are observed in 1st and 2nd year planting compared to the 3rd year planting values in all the tillage methods studied. The values of these parameters observed in the Ridge and Flat for the 3 years planting were relatively similar and higher in value when compared to their values obtained from Mound. The value of Cu obtained from Mound and Ridge in 1st and 3rd year plantings were statistically similar. The yield of these parameters could be dependent on the soil type, climate and drainage. Griffith *et al.*, (1993) noted that effect of tillage systems on yield and soil parameters are highly dependent upon soil type, drainage and climate. The nature of the results obtained could also be attributed to the tillage depth and rooting depth of castor plant as tillage methods affect the sustainable use of soil resources through its influence on soil properties. Strudley *et al.*, (2008) found out that tillage depth and intensity alter soil physical and chemical properties that affect plant growth and yield. The management effect of tillage methods and organic waste application on a near-soil surface is vitally important considering the effect of soil surface on water infiltration, nutrient conservation, trace metals distribution and erosion control. Thus, good soil quality not only produces good crop yield, but also maintains environmental quality and consequently plant, animal and human health (Action and Gregorich, 1995; Franzluebbers, 2002).

The wood ash application for the 3 years study showed that the result of Cu, B, (1st year), B (2nd year) and Cu (3rd year) in 4tha⁻¹ and 6tha⁻¹ were statistically similar but significantly different with control plot. Also the values of B (1st year), B (2nd year) and Cu, Pb (3rd year) obtained from 2tha⁻¹ and 4tha⁻¹ WA respectively were statistically similar

but significantly better than the control plots. The values of B decreased as planting years increased and among the soil heavy metals tested it was B that decreased most in value in the 3rd year planting season. Heavy metals concentrations in soils are always a guide to the potential redevelopment of the field sites. The nature of the result obtained may have been influenced by the pH, cation exchange, organic matter and to some extent the available P content of the soil. The result of the 3 years study also show that the soil heavy metals vary with the rate of WA application. The heavy metals obtained from 0tha⁻¹ significantly were small when compared with the values obtained from the other rates of WA applied. Alloway (1996) put the normal range of Cu to be from 2 – 250 mgkg⁻¹, while Malcon (1991) put Cu range to be from 2 – 100 mgkg⁻¹ the values obtained for the element is within the range. Anthropogenic activities such as amendment of soils with agricultural wastes increased soil heavy metals concentration. The following authors: Asadu *et al.*, (2008), Nwite *et al.*, (2008), LASEPA (2005) and WHO (1996) reported significant increases in these soil heavy metals in organic waste amended soils compared to the control plots. Lead, (Pb) in its own case, is believed to be absorbed by the soil and is highly insoluble. The values obtained for these heavy metals differed greatly with that of the results of Mba *et al.*, (2006), (2009) and (2011) which could be associated with the type of organic waste applied, test crop used, planting period observed and the state of climate and precipitation at the time of study. Tillage and WA effect showed that the values of the soil heavy metals (Cu, B, Pb) increased as the rate of WA applied increased irrespective of the tillage method the ash was applied. The effect on the values were observed to be higher in the 1st and 2nd years planting and decreased in the 3rd year planting season. Also their values obtained from 4tha⁻¹ and 6tha⁻¹ irrespective of the TM the WA was applied were found to be relatively similar, but higher in value compared to their values obtained from 2tha⁻¹ and 0tha⁻¹ rate of WA. The result obtained could be associated with the type of tillage method, waste applied and water content and infiltration rate of the soil. Soil water content is affected by tillage because of changes produced in infiltration, surface run-off and evaporation. These factors are capable of influencing the soil heavy metal contents, as some of them can be soluble and transformed in the soil into their carbonate or hydroxyl content which might be of help to soil nutrient distribution and plant growth, while in water stress situation some of them can become insoluble and adsorbed by soil particles. Tillage methods influenced soil water storage

more than the degree of canopy formed by the different crop varieties, according to Fabrizzi *et al.*, (2006).

Heavy Metal Content of Shoot of Castor

The effect of tillage methods on the heavy metal contents of castor shoot showed significant difference at $P < 0.05$ among the TM studied (Table 4). The values obtained in each of the TM decreased as the planting years increased. Their recorded values in Ridge and Flat were relatively higher than the values obtained from the Mound. In most of the parameters such as Cu and Pb (3rd year) their values in Ridge and Flat were statistically similar. The same statistical similarity applies to the values obtained from Mound and Ridge with regard to the values of Cu, Pb (1st and 2nd) years planting and B, Pb in the 3rd year planting periods. The result obtained for the parameters could be attributed to some factors such as tillage method used, waste applied, root development and soil aggregation. For instance, when soil is annually cultivated, roots develop more extensively below 10 cm than with no-till systems while intermediate root distribution occurs with minimum tillage system and when residues are removed, there is greater root growth in the 15 cm soil surface (Larson, 1999). This affected the yield contents of these parameters much on the 3rd year planting period where their values decreased remarkably, probably due to non-application of WA. Also, the ability of Ridge and Mound to conserve limited soil moisture might have influenced the statistical similarity in values of the parameters observed. Rowland (1993) observed that the traditional system of Ridge and Mound cultivation improve aeration for roots and facilitates the growth and development of crops. Continuous cultivation reduces aggregate size, because small aggregates are less stable than large ones (Nweke and Nnabude, 2014, 2015) and soils with small aggregates are more prone to compaction, crusting, soil erosion and reduced yield. All these invariably may have influenced the uptake of heavy metals by the castor plant.

The trend of change in these parameters was observed to be inconsistent irrespective of the TM. For example the values of Cu in 1st and 2nd years planting were found to increase as the rates of WA applied increased. While the values of B and Pb decreased as the rates of WA increased to 2tha⁻¹ and then increased in 4tha⁻¹ and decreased again in 6tha⁻¹ rates of WA. The value of the parameters Cu, Pb and B are within the tolerable limits and, therefore, may not cause toxicity problems to the crop nor cause any injury to humans. Comparison of the rates of WA on TM indicated that the rates of WA on Ridge show relatively higher values in these parameters compared to Mound and Flat values.

Though the tested parameters are within the tolerable range, they have the potential to build up rapidly to critical levels in the soil due to continuous application of wastes in the soil. Increasing the heavy metal contents of soil may not only be deleterious to soil productivity but harmful to humans and animals that invariably will depend on soil for their livelihood. Thus, Naidu *et al.*, (1997) stressed that continuous application of organic waste amendment were the greatest threat to the environment as a result of surface input to soil system of heavy metals.

The values obtained for the parameters (Cu, B, Pb) from 4tha⁻¹ and 6tha⁻¹ rates WA among the tillage methods were found to be relatively higher than the values obtained from 0tha⁻¹ and 2tha⁻¹ rates. Continuous cultivation and non-application of wastes can even lead to exhaustion or non-uptake of some of these heavy metals as was found in Cu in the 3rd year planting. The effect of tillage (Flat) and WA at the rate of 2tha⁻¹, 4tha⁻¹ and 6tha⁻¹ showed statistically similar results for Pb and Cu in 1st and 2nd year planting periods respectively. Soil disturbance and subsequent changes in soil organic matter strongly affect the stability of soil aggregates and other soil properties (Boivin *et al.*, 2001; Nweke, 2015). These changes in turn will have feedback effect on the uptake ability of the heavy metals by the castor plant.

Heavy Metal contents of Seed

Statistically similar results were obtained from Ridge and Flat for Cu in 3rd year planting as well as Mound and Flat for Cu in the 2nd year and B in 3rd year planting result. Among the TM, Mound was found out to increase the uptake of most of the tested parameters followed by the Ridge method and the least is Flat. Tillage is an integral part of the crop production system that influences plant nutrients and heavy metal uptake by plants. According to Arshad *et al.*, (1999), tillage is crucial for optimising productivity by alleviating physico-chemical and biological constraints of soil. Hence, nature of the result obtained from the three tillage methods collaborated with the findings of Dick *et al.*, (1991) and Okpoku *et al.*, (1997) who postulated that yield reduction have often been observed in no-tillage compared to other methods, especially when used in poorly drained fine textured soils. Also, it should be noted that crop responses to tillage methods depend upon the number of years a tillage system has been established, amendment used and the history of the field.

The values obtained from 4tha⁻¹ (Md4, Rd4, and Ft6) and 6tha⁻¹ (Md6, Rd6, Ft6) rates were found to be statistically similar but significantly different from the control plots. Heavy metal contents of seed in each rate of WA applied

decreased as the year of planting increased. The observed remarkable decrease in the uptake of these heavy metals in third year planting by the castor seed could be due to non-application of WA, which tend to portray that organic waste application on agricultural soils can be one of the common sources of soil contamination as the crops source out the nutrients from the soil. Thus, Jones *et al.*, (1991) reported that heavy metals were absorbed at particle surface, bound to carbonates or occluded in iron or manganese hydroxides, organic matter and sulphide. The value of rates of WA on Mound was observed to be relatively higher compared to the values of rate of WA on Ridge and Flat.

From the obtained values it was equally observed that the combined effect of tillage methods and rates of WA increased the uptake of heavy metal like B. The observed variations in the tested parameters among the tillage methods and rates of WA and the three years of study collaborated with the findings of Vousta and Samara (1996) who reported that harvested crops show large variations in heavy metal concentration from year to year in the same field. This they attributed to plant uptake, variable emission rates, deposition process and atmospheric transport. The values obtained from Pb uptake by castor seed is in line with the findings of Miller and Miller (2000) who observed that Pb is not taken by plants to any degree. This observation particularly with the present study can equally be associated with the result of Cu.

V. CONCLUSION

Results of the study show that tillage methods and rates of wood ash application as soil amendments increase the heavy metal contents of soil, castor shoot and seed to non-toxic level, the values of heavy metal increased as the rates of wood ash increased and decreased as the planting seasons increased. The values obtained from Ridge and Flat were higher than the values obtained from Mound method though Mound method was found to increase the uptake of heavy metal contents of seed. Based on the results of the study the use of wood ash as soil amendment on continuous basis especially at higher rates should not exceed three consecutive years on the same piece of land in order not to constitute pollution problems at the near future.

REFERENCES

[1] Action, D.F. and Gregorich, L.J. (1995). The health of our soils: Toward sustainable agriculture in Canada, Agriculture and Agricultural food, Canada, CDR, 960 Carlingn.

- [2] Agbede, F.M., Ojeniyi, S.O. and Awodun, M.M (2008). Effect of tillage methods on growth grain yield. Northeastern Thailand J. 34:197-200.
- [3] Alloway, B.J. (1996). Heavy metals in soil. Halsted Press, John Wiley and Sons Inc. London, pp. 230 – 239.
- [4] Arshad, M.A., Franzuebbers, A.J. and Azooz, R.H. (1999). Components of surface soil structure under conventional and no-tillage in North Western Canada. Soil Till. Res. 53:41 – 47.
- [5] Asadu, C.L.A., Ucheonye Oliobi, C. and Agada, C. (2008). Assessment of sewage application in south-western Nigeria. part I, impact on selected soil morphological and physical properties. Outlook on Agriculture, 37(1):57 – 62.
- [6] Awodun M.A. (2007). Effect of saw dust ash on soil chemical properties and cowpea performance in south western Nigeria IJSC 2(1): 78-81.
- [7] Boivin, H.B., Bummer; G. W. Horn, R; Randeler, E., Kogel Knabner, I.; Kretschmar, R.; Stabr, K. and Wike, B.M. (2009). Lehrbuch der Bodkunde. Spektrum, 500pp.
- [8] Dick, W.A., McCoy, E.L., Edwards, W.M. and Lal, R. (1991). Continuous application of no-tillage to Ohio soils. Agron. J. 83:65-73.
- [9] Fabrizzi, K.P., Garcia, F.O., Costa, J.I. and Picone, L.I. (2006). Soil water dynamics, physical properties and corn and wheat responses to minimum and no-tillage systems in the southern pampas of Argentina, soil and Tillage Research, 81:57 – 69.
- [10] Federal Department of Agriculture and Land Resources (1985). Reconnaissance soil survey of Anambra State of Nigeria soil report 1985, Federal department of Agriculture and Land Resources Lagos Nigeria.
- [11] Franzluebbers, A.J. (2002). Soil organic matter stratification ratio as an indicator of soil quality, Soil and Tillage research 66:95 – 106.
- [12] Gallardo-Lara, F., Robles, J., Esteban, E., Azeon, M. and Nogales, R. (1984). Poder fertilizant de un compost de fey Zn: In proceeding of J. Congreso Nacional de la Ciencia del silo. Vol. I, SECs, Madrid, 393 – 403.
- [13] Griffith, D.R., Mannering, J.V., Galloway, H.M., Parson, S.D. and Richey, C.B. (1993). Effect of eight tillage planting systems on soil temperature, percent stand, plant growth and yield of corn on five Indiana soils Agron. J. 65:321 – 326.
- [14] Islam, E.U., Yang, X., HE, Z and Mahmood, Q. (2007). Assessing potential dietary toxicity of heavy

- metals in selected vegetables and food crops, J. Zhejiang Univ. Sci. B. 8:1-13.
- [15]Jing, Y. He, Z., and Yang, X. (2007). Role of soil rhizobacteria in phytoremediation of heavy metal contaminated soils. J Zhejiang Univ. Sci. B. 8, 192-207.
- [16]Jones, A.S., Suter, H.G.W. and Hull, R.N. (1991). Toxicological benchmark for screening potential contaminants of concern for effects on sediment-Associated Biota. Oak Ridge National Laboratory, Tenn.
- [17]Kos, B., Greman, H. and Lestan, D. (2003). Phyto-extraction of lead, zinc and cadmium from soil by selected plants. Plant Soil Environ. 49:548 – 563.
- [18]Lagos State Environmental Protection Agency (LASEPA) (2005). Lagos State Environmental Report 3:28 – 33.
- [19]Lal, R. (1993). Soil erosion and conservation in West Africa, P.7 -26. In D. Pimentel (ed), world soil erosion and conservation. Int union for conservation of nature and natural resources, Switzerland
- [20]Larson, W.E. (1999). Soil Parameters for evaluating tillage needs and operations, Soil and water management and conservation. Soil Science and Society Proceedings, 118-122
- [21]Lone, M. I. He, Z., Stoffela, P. J. and Yang, X. (2008). Phytoremediation of heavy metal polluted soils and water, progress and perspectives. J. Zhejiang Univ. Sci. B. 9, 210-220.
- [22]Malcon, E.S. (1999). Bioavailability of nutrients: In Handbook of Soil Science, CRC Press Boca Raton NY Washington DC, pp. 73.
- [23]Mbah, C.N., Idike, F.I. and Njoku, C. (2011). Accumulation of pollutants in an ultisol amended with burnt and unburnt rice mill wastes. J. Agric. Bul. Sci. 2(2):043 – 047.
- [24]Mbah, C.N., Nwite .J.N., Njoku, C. and Nweke, I.A. (2010). Response of maize (*Zea mays* L.) to different rates of wood ash Application in acid ultisol in south east Nigeria. Afri. J. Agric. Res. 5(7) pp 580-583.
- [25]Mbah, C.N., Nwite, J.N., Ogbodo, E.N., Okonkwo, C.I., Mbagwu, J.S.C. and Anikwe, M.A.N. (2006). Trace elements in maize (*zea mays*) as influenced by incorporation of animal wastes in dystric leptosol in south-eastern Nigeria. J.Sci. Agric. Food Tech. Environ. 6:33 – 39.
- [26]Mbah, C.N., Orji, A. and Nweke, I.A. (2009). Effect of organic inputs on soil properties of heavy metal content and maize root yield on engine oil polluted soil. J. Agric. Rural. Dev. 11(2):94 – 99.
- [27]Miller, D.M. and Miller, W.P. (2000). Land application of wastes, In: Summer M.E. (eds). Handbook of Soil Science CRC Books New York.
- [28]Moolenaar, S. W and Lexmond, T. M. (1999). General aspect of cadmium, copper, zinc and lead balance studies in agro-ecosystems. Heavy metal balances, part 1 J Indust. Ecol. 2: 4-8.
- [29]Naidu, R., Kookana, R.S., Summer, M.E., Harter, K.D. and Tiller, K.G. (1997). Calcium sorption and transport in variation change in soils. A review. J. Environ. Qual. 26:608 – 617.
- [30]Nwachukwu, O. I., Nyong, A. E. and Opara, U. D. (2012) . Effect of manures on soil properties, yield and nutrient uptake in an ultisol of southeast, Nigeria, Nig. J. Soil Sci. 22(2):70-78.
- [31]Nweke, I. A. (2015). Effect of land use on organic matter concentration of aggregate fractions of fallow and cultivated soils. Indian J. Appl. Res. 5(3): 507- 511.
- [32]Nweke, I. A., and Nnabude, P. C. (2014). Organic C, TN, and available P concentration in aggregate fraction of four soils under two land use systems. J. Res. Appl. Nat. Soci. Sci. 2(5): 273-288.
- [33]Nweke, I. A., and Nnabude, P. C. (2015). Aggregates stability of four soils as evaluated by different indices. J. Expt. Biol. Agric. Sci. 3(3): 246-252.
- [34]Nwite, J.N., Ekpe, I.I. and Ibeh, L.M. (2008). Assessment of selected heavy metals in spent lubricant oil contaminated and uncontaminated soil amended with organic wastes in Abakaliki: In Proceedings of 42nd Annual Conference, Agricultural Society of Nigeria (ASN), October 19th – 22nd 2000, Ebonyi State University, Abakaliki, Nigeria, 556 pp.
- [35]Ojeniyi, S. O. Adekiya, A. O. and Amusan, O. A. (2012). Three year influence of tillage and poultry manure on soil physical properties and yield of cocoyam, Nig. J. Soil Sci. 22(2): 119-127.
- [36]Okoronkwo, N.E., Igwe, J.C. and Onwuchekwa, E.C. (2005). Risk and health implication of polluted soils for crop production, Afr. J. Biotechnol. 4:1521 – 1524.
- [37]Okpoku, G., Vyn, T.J. and Shanton, G. J. (1997). Modified no-till system for corn following wheat on clay soils, Agron. J. 85:549 – 556.
- [38]Omoju, O. J. and Ojeniyi, S. O. (2012) Effect of tillage methods on soil properties and performance of

- sweet potato (*Ipomoea Batatas* L) in Akure Nigeria, Nig. J. Soil Sci. 22(2): 128-131.
- [39] Pierzynski, G M Sims, J T and George, F (2002) Soils and environmental quality, CRC Press, Boca, Raton.
- [40] Rowland, K.R.J. (1993). Dry land farming in Africa. C.T.A, The Hague, Netherlands, 249 PP.
- [41] Stassen, S. W. (2002). A study on how to prevent toxic effect of cadmium in the population at large, KUL, UL Gasthuisberg, Klinisch lab. Hypertensie, Inwendige, Geneeskunde-Cardio, Herestratt 49, 3000 Leuven.
- [42] Strudley M.W., Green, T.R. and Ascough, J.C. (2008). Tillage effects on soil. Soil Till. Res. 99:4 – 98.
- [43] Umeoguaju F U (2009) Conventional and new ways of remediating soils polluted with heavy metals, Scholars (<http://scholars.ufumes.com>) 1-4pp.
- [44] Vousta, D.A. and Samara, C. (1996). Trace elements in vegetables grown in an industrial area in relation to soil and air particulate matter. Environ. Pollut. 94:125 – 145.
- [45] Wildlife News (2000). Researchers work to reduce lead poisoning of children in Chicago's west town, Chicago USA.
- [46] World Health Organisation (WHO) (1996). Guideline for drinking quality water, 2nd edition, Switzerland 1(3): 50-57.

Study of Mechanical Properties of Stabilized Lateritic Soil with Additives.

Elijah O. Abe¹, Ezekiel A. Adetoro²

^{1,2}Department of Civil Engineering, the Federal Polytechnic, PMB 5351, Ado – Ekiti, Nigeria

Abstract—The overdependence on the usage of industrially manufactured soil improved or conventional additives have resulted in unaffordable cost of construction of better infrastructure in Third World and poor countries which are mostly agriculturally dependent across Globe. This study is aimed at studying the mechanical properties of lateritic soil stabilized with mixture of conventional and locally available additives. Soil samples collected from the study area were subjected to laboratory tests (i.e. Grain Size and Atterberg Limits tests) after stabilized with cement, ESA and RHA additives at proportion of 2% to 10% by sample weight. It is observed that the LL, PL and PI values varied from 30.1% to 35.5%, 9.9% to 12.5% and 20.1% to 23.2% respectively for sample A. While LL, PL and PI values varied from 35.2% to 41.5%, 10.8% to 14.5% and 24.4% to 27.1% respectively for sample B. It could be generally observed that PI values reduced while PL values increased for the soil samples after increase in addition of cement additive from 6% to 8%. All the LL, PL and PI values also reduced as the percentage of RHA additive added increased. Soil sample A has group classifications of A – 2 – 6 while soil sample B has A – 7 and tend towards A – 2 - 6 and A - 6 after stabilization. The stabilization process using local additives as partial replacement of conventional one generally improved the soils Engineering properties. Though it is more felt in ESA than RHA. Further research work should be carried out.

Keywords—Atterberg Limits, Grain Size Analysis, Mechanical Properties, Soil, Stabilization.

I. INTRODUCTION

As necessity is mother of all inventions, there is need for local alternative materials (i.e. local additives) to be used as partial or total replacement to conventional ones as stabilizing agents in order to cut or reduce cost of construction in Third World countries like Nigeria. Cement and lime have been the two main materials used for stabilizing soils for many years and have rapidly increase in prices due to the sudden increase in energy cost since almost half of a century. The over dependence on the usage of industrially manufactured soil improved or conventional additives (cement, lime, etc.) have resulted in rise in construction cost of roads and structures. This has

continue to act as barrier for the Third World and poor countries across Globe to have access to good or better infrastructural amenities such roads and safe structures. Though, these countries are mostly agriculturally dependent ([3]).

Since all structures are built on soil for stability, thus Soil stabilization is a significance aspect of Civil Engineering practices. Any deficiencies in soil characteristics will make it unsuitable for structure to be built on it – thus the need to either excavate the soil or improve its Engineering properties for maximum use. Excavation / replacement of soil is expensive and requires the use of heavy equipment. While Soil stabilization which has to do with improvement of Engineering properties of soil could be carried out through stabilizing agents / additives usage. Locally available additives such as Rice Husk Ash (RHA) and Egg Shell Ash (ESA) in partial replacement of Cement could be used. The overall cost of improving Engineering properties of soil using complete conventional additives (i.e. cement) in stabilization process could be high and unaffordable, but if partially replaced with locally available additives and are found suitable for stabilizing soil, this will reduce the cost of improving the Engineering properties of soil. These locally available additives could be agricultural wastes, industrial wastes, domestic wastes etc. Most of these wastes are hazardous to man and environment. Even burning them can deplete the ozone layer ([5]).

The study area is along Ado Ekiti – Ijan road, Ado – Ekiti Local Government Area (LGA), Ekiti State as shown in Fig. 1 - a state in western Nigeria declared as a state on 1st October, 1996 alongside five others by the military under the dictatorship of General Sani Abacha. The state, carved out of the territory of old Ondo State, covers the former twelve local government areas that made up the Ekiti Zone of old Ondo State. On creation, it had sixteen Local Government Areas (LGAs), having had an additional four carved out of the old ones. One of these sixteen LGAs is Ado – Ekiti LGA. Ado - Ekiti is surrounded by Irepodun / Ifelodun LGA in the North, Gbonyin LGA in the East, Ekiti Southwest / Ikere LGAs in the West and Ise / Orun LGA in the South. The City itself is the Capital of Ekiti State and headquarters of Ado-Ekiti LGA ([9], [15]).

Distribution and Atterberg limits. The results were compared to the standard specified values and grouped in accordance with [7] and [11].

III. RESULTS AND DISCUSSION

Table 1 showed Grain size analysis test results for the natural soil samples. From Table 1, the results showed that soil sample A has percentages finer than 0.075mm fractions less than 35% (i.e. < 35%), which is 27.1%. Hence, general rating as sub-grade in accordance with [7] is excellent to good materials. The average percentages of sand and gravel were 16.7% and 56.2% respectively.

These results implied that the soil has large content of granular materials. It is likely to have significant constituent materials of silty / clayey gravel and sand soils. While soil sample B has percentages finer than 0.075mm fractions greater than 35% (i.e. > 35%), which is 40.8%. Hence, general rating as sub-grade in accordance with [7] is fair to poor materials. The average percentages of sand and gravel were 29.6% and 29.6% respectively. These results implied that the soil has large content of clay materials. It is likely to have significant constituent materials of mainly silty / clayey soils.

Table 1: Grain Size Analysis Test Results for the Natural Soil Samples

SIEVE No. (mm)	% PASSING		LIMITS		SOIL CLASSN.		SOIL TYPE
	SAMPLE A	SAMPLE B	LOWER	UPPER	SAMPLE A	SAMPLE B	
12.5	100.0	100.0	100.0	100.0			
9.5	77.9	94.9	87.0	97.0	34.1	24.5	GRAVEL
4.25	52.4	82.0	65.0	82.0			
2.36	43.8	70.4	50.0	65.0			
1.18	40.1	64.5	36.0	51.0			
0.60	36.6	59.6	26.0	40.0	16.7	29.6	SAND
0.30	32.1	52.6	18.0	30.0			
0.15	28.9	45.5	13.0	24.0			
0.075	27.1	40.8	7.0	14.0	27.1	40.8	SILT/CLAY

It could also be seen that values of fine sand (i.e. 0.075 - 0.60mm) were within the specified limits, while values of coarse sand (i.e. 0.60 - 2.36mm) and gravel (i.e. 2.36 - 9.50mm) were lesser than lower specified limits for soil sample A. These implied that the soil sample has required fine sand, but have lesser coarse sand and gravel than required. For the soil sample B, values of fine sand (i.e. 0.075 - 0.60mm) and coarse sand (i.e. 0.60 - 2.36mm) were greater than the specified limits, while values of gravel (i.e. 2.36 - 9.50mm) were within the specified limits for soil sample B. These implied that the soil sample has more fine and coarse sands than required with required gravel.

Table 2 showed Atterberg Limits tests results for the soil samples stabilized with RHA. From Table 2, it is observed that the Liquid Limit (LL), Plastic Limit (PL) and Plasticity Index (PI) values varied from 30.1% to 35.5%, 9.9% to 12.5% and 20.1% to 23.2% respectively for sample A. While LL, PL and PI values varied from 35.2% to 41.5%, 10.8% to 14.5% and 24.4% to 27.1% respectively for sample B. It could be generally observed that PI values reduced while PL values increased for the

soil samples after increase in addition of cement additive from 6% to 8%. All the LL, PL and PI values also reduced as the percentage of RHA additive added increased.

These portrayed that the additives have effects of reducing the quantities of fine particles in the soil samples. And as the additives were being increased, the cementation process of the particles of the soil samples was being increased. It also showed that the percentages of finer particles than 0.075mm of the soil samples have reduced and cohesive qualities of the binder resulting from the clay or fine contents which make the soil samples better as explained by [14]. As the percentage of additive added increases, the soil samples tends towards meeting the required specification for subgrade course materials (i.e. $LL \leq 80\%$ and $PI \leq 55\%$), base and subbase course materials (i.e. $LL \leq 35\%$ and $PI \leq 12\%$). Thus, they could be suitable for subgrade course materials. Generally, soil sample A can be grouped as A-2-6 even after stabilization process, while soil sample B can initially be grouped as A-7 and later metamorphosed into A-6 and tends towards A - 2 - 6 in accordance with [7] classification system.

Table 2: Atterberg Limit Tests Results for the Stabilized Soil Samples (RHA)

ADDITIVE (%)	ADDITION OF 6% CEMENT						ADDITION OF 8% CEMENT							
	LL (%)		PL (%)		PI (%)		LL (%)		PL (%)		PI (%)			
	SAMP	LE A	SAMP	LE B	SAMP	LE A	SAMP	LE A	SAMP	LE B	SAMP	LE A	SAMP	LE B
0	35.5	41.5	12.3	14.4	23.2	27.1	35.5	41.5	12.5	14.5	23	27		
2	34.9	40.3	11.8	13.2	23.1	27.1	33.8	39.5	12	12.8	21.8	26.7		
4	33	39.5	11	12.5	22	27	32.9	38.4	11.8	12.1	21.1	26.3		
6	32.9	38.9	10.3	11.8	22.6	27.1	32.8	36.4	11	11.8	21.8	24.6		
8	31.8	37.8	10	11.3	21.8	26.5	31.8	36.3	10.5	11.3	21.3	25		
10	30.9	36.5	9.9	10.9	21	25.6	30.1	35.2	10	10.8	20.1	24.4		

Table 3 showed Atterberg Limits tests results for the soil samples stabilized with ESA. From Table 3, it is observed that the Liquid Limit (LL), Plastic Limit (PL) and Plasticity Index (PI) values varied from 28.8% to 35.5%, 9.7% to 12.3% and 19.1% to 23.2% respectively for sample A. While LL, PL and PI values varied from 33.8%

to 41.5%, 9.5% to 13.4% and 19.1% to 29.4% respectively for sample B. It could be generally observed that PI and PL values reduced for the soil samples after increase in addition of cement additive from 6% to 8%. All the LL, PL and PI values also reduced as the percentage of ESA additive added increased.

Table 3: Atterberg Limit Tests Results for the Stabilized Soil Samples (ESA)

ADDITIVE (%)	ADDITION OF 6% CEMENT						ADDITION OF 8% CEMENT					
	LL (%)		PL (%)		PI (%)		LL (%)		PL (%)		PI (%)	
	SAMPLE A	SAMPLE B	SAMPLE A	SAMPLE B	SAMPLE A	SAMPLE B	SAMPLE A	SAMPLE B	SAMPLE A	SAMPLE B	SAMPLE A	SAMPLE B
0	35.5	41.5	12.3	13.4	23.2	28.1	35.5	41.5	12.3	12.1	23.2	29.4
2	34	39.4	11.5	12.6	22.5	26.8	32.9	39.7	11.2	11.4	21.7	28.3
4	33.6	38.6	10.4	12	23.2	26.6	31.1	38.7	10.5	11	20.6	27.7
6	32.5	37.7	10.1	11.4	22.4	26.3	30	36.4	10	10.9	20	25.5
8	31.5	36.9	10	10.8	21.5	26.1	29.8	34.9	9.9	10.5	19.9	24.4
10	30.8	35.8	9.8	9.5	21	26.3	28.8	33.8	9.7	9.7	19.1	24.1

These portrayed that the additives have effects of reducing the quantities of fine particles in the soil samples. And as the additives were being increased, the cementation process of the particles of the soil samples was being increased. It also showed that the percentages of finer particles than 0.075mm of the soil samples have reduced and cohesive qualities of the binder resulting from the clay or fine contents which make the soil samples better as explained [14]. As the percentage of additive added increases, the soil samples tends towards meeting the required specification for subgrade course materials (i.e. $LL \leq 80\%$ and $PI \leq 55\%$), base and subbase course materials (i.e. $LL \leq 35\%$ and $PI \leq 12\%$). Thus, they could be suitable for subgrade course materials. Generally, soil sample A can be grouped as A-2-6 even after stabilization process, while soil sample B can initially be grouped as A-7 and later metamorphosed into A-6 or A-2-6 after stabilization in accordance with [7] classification system.

Generally, from comparative analyses of effects of the additives (i.e. cement, RHA and ESA) on the soil samples, it could be observed that the addition of cement additive + ESA is more effective than addition of cement + RHA. Though it appears that of RHA is more effective at initial stage (i.e. from 6% to 8% cement).

IV. CONCLUSION

From the results of the above study, it could be concluded that:

- The soil sample A was generally classified as granular soil material with mainly silty / clayey gravel and sand constituent materials with some stone fragments. While soil sample B was generally classified as clay material with mainly silty / clayey constituent materials.
- Soil sample A has group classifications of A – 2 – 6 while soil sample B has A – 7 and tend towards A – 2 – 6 and A - 6 after stabilization.

- The general rating as sub-grade materials of soil sample A is excellent to good while that of soil sample B is fair to poor.
- The stabilization process using local additives as partial replacement of conventional one generally improved the soils Engineering properties. Though it is more felt in ESA than RHA.

Further research work should be carried out on this study at large scale. This will help in ascertaining it as one of the means of waste to wealth policy.

REFERENCES

- [1] J. O. Adams and A. E. Adetoro (2014). Quality Assessments of Water in Selected Waste – Dumping Site Areas. *International Journal of Scientific Research and Education*, vol. 2(11), pg. 2399-2404.
- [2] A. E. Adetoro and J.O. Adams (2014). Analysis of Influences of Waste – Dumping Sites on the Quality of Water. *IOSR Journal of Mechanical and Civil Engineering (IOSR-JMCE)*, vol. 11(6 ver.IV), pg. 27-30.
- [3] A. E. Adetoro and S.A. Oladapo (2015). Effects of Sawdust and Palm Kernel Shell Ashes on Geotechnical Properties of Emure / Ise-orun Local Government Areas Soil, Nigeria. *Scientific Research Journal (SCIRJ)*, vol.III (VII), pg. 35 – 38.
- [4] A. E. Adetoro, J.S. Adekanmi and M. O. Dada (2015). Comparative Analyses of Soil Stabilized with Different Additives. *Proceeding of 10th Engineering Forum of School of Engineering of the Federal Polytechnic Ado-Ekiti, Nigeria*, vol.1, pg. 94-100.
- [5] A. E. Adetoro and I. S. Ayeni (2015). Effects of Locally Available Additives on Geotechnical Properties of Ijero Local Government Soil, Ekiti State, Nigeria. *Journal of Multidisciplinary Engineering Science and Technology (JMEST)*, vol. 2(11), pg. 2994-2997.
- [6] A. E. Adetoro and O. M. Dada (2017). Comparative Analyses of Mechanical Properties of Ekiti State Soil, Nigeria. *Journal of Multidisciplinary Engineering Science and Technology (JMEST)*, vol. 4(5), pg. 7272 – 7276.
- [7] American Association of State Highway and Transportation Officials (AASHTO) (1986). *Standard Specification for Transportation Materials and Methods of Sampling and Testing (14th ed.)*. USA: Washington DC, AASHTO.
- [8] British Standard 1377 (BS 1377) (1990). *British Standard Methods of Test for Soils for Civil Engineering Purposes*. UK: London, British Standards Institution.
- [9] Ekiti State Directorate of ICT (2017). *The Official Website of the Government of Ekiti State, Nigeria*. Available: <https://ekitistate.gov.ng/administration/local-govt/ido-osi-lga/>.
- [10] Europa Technologies (2017). *Google Earth*. Available: <http://earth.google.com/>, 2017.
- [11] Federal Ministry of Works and Housing (FMWH) (1997). *General Specification (Roads and Bridges) – Revised Edition (Volume II)*, Nigeria. Abuja: Federal Ministry of Works.
- [12] G.R. Otoko, and B.K. Honest (2014). Stabilization of Nigerian Deltaic Laterites with Saw Dust Ash. *International Journal of Scientific Research and Management*. Vol. 2, no. 8, pp. 1287 – 1292.
- [13] K. R. Thanki and N. V. Gajera (2015). Stabilization Analysis of Black Cotton Soil by using Groundnut Shell Ash. *International Journal of Innovative Research in Science and Technology (IJIRST)*, vol. 2(1).
- [14] E. I. Ugwu and D. A. Famuyibo (2014). Analysis of the Effect of Blending Nigeria Pure Clay with Rice Husk: A Case Study of Ekulu Clay in Enugu State. *American Journal of Materials Engineering and Technology*, 2(3), pg. 34-37.
- [15] Wikimedia Foundation Inc. (2017). *Ekiti State*. Available: https://en.wikipedia.org/wiki/Ekiti_State.

Assessment of Performance Properties of Stabilized Lateritic Soil for Road Construction in Ekiti State.

Elijah O. Abe¹, Ezekiel A. Adetoro²

^{1,2}Department of Civil Engineering, the Federal Polytechnic, PMB 5351, Ado – Ekiti, Nigeria

Abstract—Soil Stabilization usually enhances performance properties of soil. This can foster waste to wealth policy in country like Nigeria. The aim of this study is to assess performance properties of a stabilized lateritic soil with a view to obtain a cheap and more effective additive. Soil samples were collected from the study area and subjected to Compaction and California Bearing Ratio (CBR) laboratory tests with the addition of 2%, 4%, 6%, 8% and 10% Rice Husk Ash (RHA) and Egg Shell Ash (ESA). Results showed that MDD, OMC and CBR values varied from 1575Kg/m³ to 1930Kg/m³, 7.55% to 18.50% and 20% to 131% respectively for sample A. And 1566Kg/m³ to 1896Kg/m³, 7.53% to 16.90% and 16% to 98% respectively for sample B. The MDD values decrease with increase in the additives contents due to the replacement of soil by the additives in the mixture, coating of the soil by additives which resulted in large particles with larger voids and density; and addition of the additives which decreased the quality of free silt, clay fraction and coarse materials with large surface areas formed. OMC values also increase as the additives increase, though, that of RHA increases more than that of ESA. This is due to the increase in additives which resulted to increase in the amount of water required in the system to adequately lubricate all the particles in the mixture equally increase. Generally, CBR values also increase with increase in the additives contents. This could be attributed to gradual formation of cementitious compound between the additives and Calcium Hydroxide (Ca(OH)₂) present in the soil, thus increase in coarse particles of the soil through cementation.

Keywords—California Bearing Ratio, Compaction, Lateritic Soil, Moisture Content, Soil, Performance Properties, Stabilization.

I. INTRODUCTION

Wherever there is deficiency in properties of soil or expansive soil is encountered, it is usually accompanied by awkward problems in Civil Engineering works. Greater part of expansive or problematic soil properties

could be improved through soil stabilization processes. The main reason for Soil Stabilization is to enhance mechanical and performance properties of the soil e.g. Strength, stability, water resistance etc. Soil Stabilization has been in existence for long time and is of different processes. Though, its usage is not so common in developing world. The use of Stabilization in Third World Countries like Nigeria will assist in maximization of “Waste to Wealth Policy”. Therefore help in proper waste disposal and management and rise of standard of living. This will also serve as source of job opportunities ([1]).

The condition of any Civil Engineering structures greatly depends on the soil underneath its substructure. Almost all the soil within some significant Civil Engineering structures are not suitable for their construction purpose, thus cut to spoil. The end result is acquisition of borrow pit materials which are always costly at the end of the day. Most often, stabilization process could also be very expensive when engaged in this kind of situation. Whereas, waste materials are lying fallow within our vicinity waiting for its management and disposal. These materials could be used as replacement and serve the purpose (s) of expensive / imported materials such as Cement and Lime that are being used as stabilization agents in unsuitable soil. When the waste materials are being recycled or reused as stabilized materials, it would help a lot in construction industries and thus, improve the standard of living of people. The taste for imported materials in Third World countries is very high and one of the reasons the poor countries remains poorer. Waste recycling or reusing has been a great means of fame to many First World countries of the world ([2]).

[12] Expressed that though soil stabilization techniques were used for road construction in most parts of the world, the conditions and purposes of stabilization vary greatly from one place to another. In developed world, the need for aggregates has become issue of profound conflict between agricultural and environmental interests. While in developing world, availability of good aggregates of persistent quality and cheap prices may not be available.

The above stated cases usually results in escalation in costs of aggregates and maintenance. The upgrading by stabilization of materials thus comes up as an attractive option, which will help in actualizing the dreams of the Federal Government of Nigeria at long term in scouting for already available cheap construction materials.

The study area is along Ado Ekiti – Ijan road, Ado – Ekiti Local Government Area (LGA), Ekiti State as shown in Fig. 1 - a state in western Nigeria declared as a state on 1st October, 1996 alongside five others by the military under the dictatorship of General Sani Abacha. The state, carved out of the territory of old Ondo State, covers the former twelve local government areas that made up the Ekiti Zone of old Ondo State. On creation, it had sixteen Local Government Areas (LGAs), having had an additional four carved out of the old ones. One of these sixteen LGAs is Ado – Ekiti LGA. Ado - Ekiti is surrounded by Irepodun / Ifelodun LGA in the North, Gbonyin LGA in the East, Ekiti Southwest / Ikere LGAs in the West and Ise / Orun LGA in the South. The City itself is the Capital of Ekiti State and headquarters of Ado-Ekiti LGA ([9], [15]).

Ado – Ekiti is located between latitude $7^{\circ} 15'N$ and $8^{\circ} 51'N$; and longitude $4^{\circ} 51'E$ and $5^{\circ} 45'E$. Its landscape consists of ancient plains broken by steep sided outcropping dome rocks situated within tropical climate of Nigeria. Geologically, the study area is underlain by metamorphic rocks of the Precambrian basement complex of Southwestern part of Nigeria, the great majority of which are very ancient in age. These basement complex rocks show great variations in grain size and in mineral composition. The rocks are quartz gneisses and schists consisting essentially of quartz with small amounts of white mizageous minerals. In grain size and structure, the rocks vary from very coarse-grained pegmatite to medium-grained gneisses. The rocks are strongly foliated and occur as outcrops. The soils derived from the basement complex rock are mostly well drained, having medium to coarse in texture. The geological nature of the study area and its increased urbanization make it more vulnerable and of public health concern when it comes to water quality. The study area is mainly an upland zone, rising over 250 meters above sea level. It lies on an area underlain by metamorphic rock ([1], [2], [9], [15]). The State is within tropical climate of South-western Nigeria with two distinct seasons namely rainy season (April–October) and dry season (November–March). Its Temperature is between 21° and $28^{\circ}C$ with high humidity. The south westerly wind and the northeast trade winds blow in the rainy and dry (Harmattan) seasons respectively ([9], [15]).



Fig. 1: Location of the Study area – Ado Ekiti, Ekiti State, Nigeria ([10]).

Previous studies of authors such as [1], [2], [3], [4], [5], [6], [12], [13], [14] etc looked into stabilisation of soil through the use of locally available additives made from agricultural and environmental wastes such as Eggshell, Rice Husk, Palm Kernel Shell, Sawdust etc. According to [4], previous studies have proved that Chicken Eggshell is an aviculture by-product that has been worldly known as one of the worst environmental problems, especially in those countries where the egg production and consumption is very high. [12] expressed that efforts in the application of conversion of Eggshells to important use is an idea worth embracing in the ever increasing efforts of “Waste to Wealth Policy”.

Generally, egg shell structure is a protein lined interconnected with mineral crystals, commonly of a calcium compound like calcium carbonate. It is cheap, lightweight and has low load-bearing composite. It is a biomaterial which has 95% calcium carbonate by weight (in form of calcite) and 5% organic materials (i.e. Al_2O_3 , SiO_2 , S, Cl, P, Cr_2O_3 and MnO). It is agricultural waste materials generated from domestic sources such as chick hatcheries, poultry, bakeries, fast food restaurants etc which can litter environment and thus result in environmental pollution without proper disposition and management. Scientifically, eggshell majorly comprised of calcium compounds that is very similar to that of cement ([3], [4], [5], [12]). According to [3], the quality of lime in eggshell waste is majorly affected by its degree of exposure to sunlight, raw water and harsh weather circumstances.

Rice Husk is surrounds of paddy grains; a rice by-product generated from rice milling. Rice Husk is made up of 22% of paddy while the rest percentage is rice. It is used as fuel in the rice mills for generation of steam for the purpose of boiling process. During heating process, Rice Husk is usually converted to approximately 75% organic volatile matter and 25% Ash (of its weight). This Ash is called Rice Husk Ash (RHA). RHA usually comprises of 85% - 90% amorphous silica and poses serious environmental threat ([14]).

In this study, assessment of performance properties of lateritic soil stabilized with Cement, Egg Shell Ash (ESA) and Rice Husk Ash (RHA) would be conducted. This entails looking into changes in the Engineering properties of the Soil due to addition of these additives; thus foster availability and affordability of construction materials in developing world like Nigeria especially Ekiti State.

II. MATERIALS AND METHODS

2.1 Performance Properties

These are properties of soil that have to do with Compaction and California Bearing Ratio (CBR) tests of the soil. It is an indirect measure of strength. Compaction test comprises of Dry density and Moisture content ([8]).

2.2 Compaction Test

This is type of test(s) conducted on soil sample in other to determine its Maximum Dry Density (MDD) and Optimum Moisture Content (OMC). This test measures the dry density of the compacted soil in relationship to moisture content depending on the manner of the compactive effort. Compaction influences the shear strength and compressibility of the soil and is frequently used in earthworks and road construction. It is primarily used as a rapid test to determine the moisture suitability of earthwork materials at the construction phase. Calibration lines are usually determined through a range of moisture contents in the laboratory. The Moisture Content Value (MCV) is used to quantify the compactive effort to produce near full compaction and can be correlated with shear strength and CBR value. It is also used for the evaluation of subgrade strength in road design. The test measures the load required to cause a plunger to penetrate a specimen of soil ([8]).

2.3 California Bearing Ratio (CBR)

is a test of penetration for the purpose of acquiring relative value(s) of shearing resistance of materials of road pavement layers. It is a dimensionless exponent carried out in a standard laboratory or on the field during construction. It is always serves purpose of soil evaluation for pavement design particularly in tropical and subtropical nations ([8]).

2.4 Sample Collection and Analysis

Soil samples were collected from pits dug within the study area (Sample A – front of the Federal Polytechnic, Ado-ekiti and Sample B – Ago Aduloju as shown in Fig.

1) at depth between 1.50m and 2.5m after topsoil removal using method of disturbed sampling. The soil samples collected were stored in polythene bag to maintain its natural moisture contents. The samples were then taken to the laboratory where the deleterious materials such as roots were removed. The samples were air dried, pulverized and large particles were removed. Some Additives were then added to the soil samples (i.e. Cement, Rice Husk Ash (RHA) and Egg Shell Ash (ESA)) at varying proportions between 2% and 8%. The Cement Additive was added at 6% and 8% by soil sample weight. While the RHA and ESA additives were added at 2%, 4%, 6% and 8% by soil sample weight. Then soil samples and additives were thoroughly mixed to ensure homogeneous samples. Moulding of test specimens was started as soon as possible after completion of identification. All tests were performed to standards as in [8]. Their features were also examined. The tests carried out on the samples were Grain Size Distribution and Atterberg limits. The results were compared to the standard specified values and grouped in accordance with [7] and [11].

2.5 Egg Shell Ashes (ESA)

The collected Eggshells were oven dried at 110°C and further heated in a furnace to 450°C at Civil Engineering laboratory, the Federal Polytechnic, Ado – Ekiti, Nigeria. The product is Egg Shell Ash (ESA) that was used for this piece of study.

2.6 Rice Husk Ashes (RHA)

The collected Rice Husks were oven dried at 110°C and further heated in a furnace to 700°C at Civil Engineering laboratory, the Federal Polytechnic, Ado – Ekiti, Nigeria. The product is Rice Husk Ash (RHA) that was used for this piece of study.

III. RESULTS AND DISCUSSION

From Table 1, the results showed that all the soil samples stabilized with RHA have Maximum Dry Density (MDD) values varied from 1650Kg/m³ to 1930Kg/m³ and 1566Kg/m³ to 1896Kg/m³ for soil samples A and B respectively. While from table 2, the results showed that all the soil samples stabilized with ESA have Maximum Dry Density (MDD) values varied from 1541Kg/m³ to 1930Kg/m³ and 1637Kg/m³ to 1896Kg/m³ for soil samples A and B respectively.

Table 1: Compaction Test Results for the Stabilized Soil Samples (RHA)

ADDITIVE VE (%)	ADDITION OF 6% CEMENT				ADDITION OF 8% CEMENT			
	MDD (Kg/m ³)		OMC (%)		MDD (Kg/m ³)		OMC (%)	
	MP LE A	MP LE B	MP LE A	MP LE B	MP LE A	MP LE B	MP LE A	MP LE B
0	1930	1930	14.1	13.1	1930	1930	14.1	13.1
2	1650	1575	14.4	15.6	1905	1600	11	11.85
4	1765	1847	14.3	7.53	1847	1700	7.55	12.92
6	1575	1720	15.7	9	1675	1709	10.1	9
8	1840	1699	17.95	16.9	1900	1799	18.5	13.2
10	1650	1566	13.22	14.93	1759	1601	10.1	15.05

The results from table 1 also showed that all the soil samples stabilized with RHA have Optimum Moisture Content (OMC) values varied from 7.55% to 18.50% and 7.53% to 16.90% for soil samples A and B respectively.

While from table 2, the results showed that all the soil samples stabilized with ESA have Optimum Moisture Content (OMC) values varied from 7.60% to 14.10% and 6.70% to 13.10% for soil samples A and B respectively.

Table 2: Compaction Test Results for the Stabilized Soil Samples (ESA)

ADDITIVE (%)	ADDITION OF 6% CEMENT				ADDITION OF 8% CEMENT			
	MDD (Kg/m ³)		OMC (%)		MDD (Kg/m ³)		OMC (%)	
	SAMP LE A	SAMP LE B	SAMP LE A	SAMP LE B	SAMP LE A	SAMP LE B	SAMP LE A	SAMP LE B
0	1930	1896	14.1	13.1	1896	1896	14.1	13.1
2	1775	1785	10.95	10.1	1578	1769	8.1	6.7
4	1670	1760	7.6	6.8	1921	1705	7.85	12.2
6	1800	1637	9.75	10.7	1800	1775	11	11.4
8	1785	1719	13.15	12.7	1839	1761	13.1	12.7
10	1740	1750	12.6	10.91	1541	1910	10.95	12.8

Figure 2 and 3 graphs were plotted from tables 1 and 2 results. From figure 2, it could be observed that MDD values decrease as Additives Contents increases for all the soil samples of RHA and ESA except soil sample B (8% Cement – ESA). This is due to the replacement of soil by the additives in the mixture. It could also be due to coating of the soil by the additives which resulted in large particles with larger voids and density. And addition of the additives also decreased the quality of free silt, clay fraction and coarse materials with large surface areas formed ([1]). These soil samples did not meet the required specification for subgrade course materials (i.e. MDD > 1760kg/m³), base and subbase course materials (i.e. MDD > 2000kg/m³) after stabilization process ([7], [11]). From figure 3, it could be observed that OMC increases as Additives Contents increases for all the soil samples of RHA and ESA. Though, that of RHA increases more than that of ESA. These portrayed that the increase in Additives Contents resulted to increase in the amount of water required in the stabilization process which will adequately lubricate all the particles in the mixture. Though the moisture content in the study area remains very high compared to required values, however the

stabilization process improved the soil properties by reducing its moisture content ([1], [7], [11]).

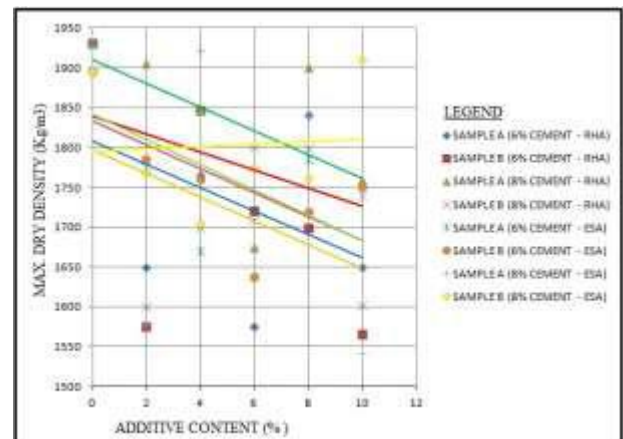


Fig.2: Graphs of Maximum Dry Density (MDD) for the Stabilized Soil Samples

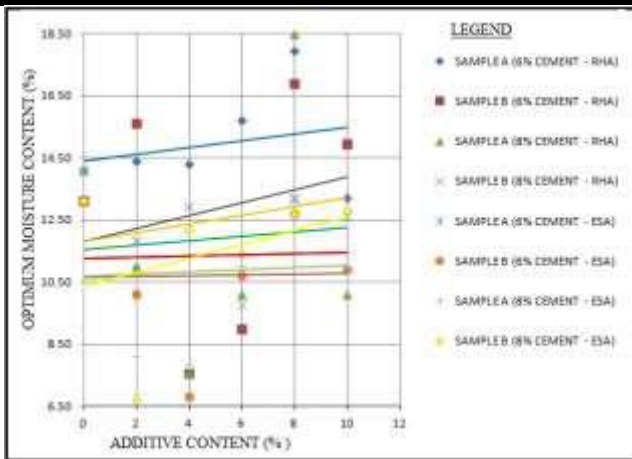


Fig.1: Graphs of Optimum Moisture Contents (OMC) for the Stabilized Soil Samples

From table 3, the results showed that all the soil samples stabilized with RHA have California Bearing Ratio (CBR) values varied from 20% to 131% and 16% to 98% for soil samples A and B respectively.

Table 3: California Bearing Ratio (CBR) Test Results for the Stabilized Soil Samples (RHA)

ADDITIVE (%)	ADDITION OF 6% CEMENT				ADDITION OF 8% CEMENT			
	CBR - 2.5mm (%)		CBR - 5.0mm (%)		CBR - 2.5mm (%)		CBR - 5.0mm (%)	
	SAMP LE A	SAMP LE B	SAMP LE A	SAMP LE B	SAMP LE A	SAMP LE B	SAMP LE A	SAMP LE B
0	89	43	91	49	89	43	91	49
2	87	77	84	86	20	16	20	24
4	43	73	64	74	26	36	33	22
6	91	83	131	80	79	65	97	20
8	107	98	90	97	63	46	78	76
10	69	75	86	80	52	18	56	53

While from table 4, the results showed that all the soil samples stabilized with ESA have CBR values varied from 24% to 98% and 16% to 97% for soil samples A and B respectively.

Table 4: California Bearing Ratio (CBR) Test Results for the Stabilized Soil Samples (ESA)

ADDITIVE (%)	ADDITION OF 6% CEMENT				ADDITION OF 8% CEMENT			
	CBR - 2.5mm (%)		CBR - 5.0mm (%)		CBR - 2.5mm (%)		CBR - 5.0mm (%)	
	SAMP PLE A	SAMP PLE B	SAMP PLE A	SAMP PLE B	SAMP PLE A	SAMP PLE B	SAMP PLE A	SAMP PLE B
0	89	43	91	49	89	43	91	49
2	26	18	34	24	24	20	26	24
4	31	17	36	27	24	24	32	26
6	26	16	79	36	39	20	26	24
8	91	97	83	70	86	90	98	87
10	59	48	63	64	57	47	54	26

Figures 4 and 5 graphs were plotted from tables 3 and 4 results. From figure 4 and 5, it could be observed that CBR values increase as Additives Contents increases for all the soil samples of RHA and ESA. This is due to gradual formation of cementitious compound between the additives and Calcium Hydroxide (Ca(OH)₂) present in

the soil, thus increase in coarse particles of the soil through cementation ([1]).

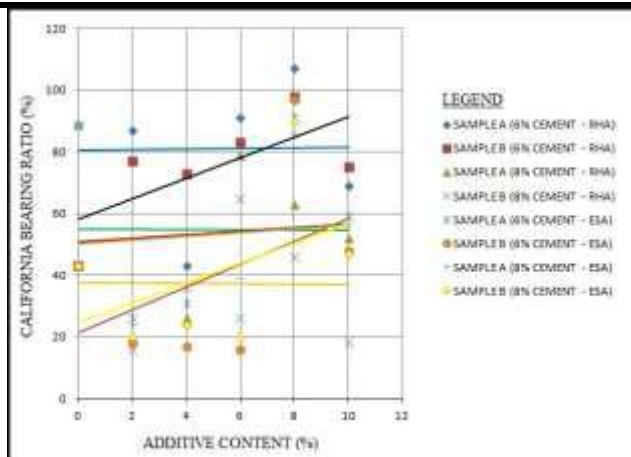


Fig.2: Graphs of California Bearing Ratio (CBR – 2.5%) for the Stabilized Soil Samples

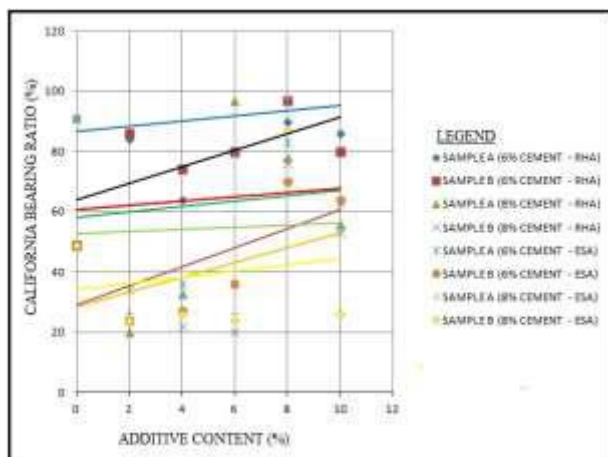


Fig.3: Graphs of California Bearing Ratio (CBR – 5%) for the Stabilized Soil Samples

IV. CONCLUSION

From the results of the above study, the following conclusions were drawn:

- The CBR and OMC values of the soil samples increase with increase in additives contents; while MDD value decrease with increase in additives contents.
- The decrease in MDD values is due to the replacement of soil by the additives in the mixture. It could also be due to coating of the soil by the additives which resulted in large particles with larger voids and density.
- Addition of the additives also decreased the quality of free silt, clay fraction and coarse materials with large surface areas formed.
- Increase in OMC values is due to increase in amount of water required in the system and to lubricate the mixture.
- Increase in CBR values is due to gradual formation of cementitious compound between the additives

and Calcium Hydroxide ($\text{Ca}(\text{OH})_2$) present in the soil, thus increase in coarse particles of the soil through cementation

- The additives (i.e. mixture of Cement and RHA/ESA) stabilized the soil.

Moreover, there is need for further research on this study.

REFERENCES

- [1] A. E. Adetoro and S. O. Faluyi (2015). Potentials of Non-Cementitious Additives for Stabilization of Oye Local Government Area Soil, Ekiti State, Nigeria. International Journal of Scientific Research in Knowledge, vol. 3(11), pg. 288 – 296.
- [2] A. E. Adetoro and J.O. Adam (2015). Comparative Analyses of Ekiti State Soil Stabilized with Different Additives. Asian Journal of Science and Technology, vol.6 (12), pg. 2054 -2058.
- [3] D. Gowsika, S. Sarankokila and K. Sargunan (2014). Experimental Investigation of Eggshell Powder as Partial Replacement with Cement in Concrete. International Journal of Engineering Trends and Technology, vol. 14(2), pg. 65 – 68.
- [4] S.B. Hassan and V.S. Aigbodion (2015). Effects of Eggshell on the Microstructures and Properties of Al–Cu–Mg/Eggshell Particulate Composites. Journal of King Saud University – Engineering Sciences, 27, pg. 49–56.
- [5] K.M. Muthu and V.S. Tamilarasan (2014). Effects of eggshell Powder in the Index and Engineering Properties of Soil. International Journal of Engineering Trends and Technology, vol. 11(7), pg. 319 – 321.
- [6] O. U. Orié and O. J. Omokhiboria (2014). Mechanical Properties of Eggshell and Palm Oil Fuel Ashes Cement Blended Concrete. Research Journal in Engineering and Applied Sciences, vol. 3(6), pg. 401- 405.
- [7] American Association of State Highway and Transportation Officials (AASHTO) (1986). Standard Specification for Transportation Materials and Methods of Sampling and Testing (14th ed.). USA: Washington DC, AASHTO.
- [8] British Standard 1377 (BS 1377) (1990). British Standard Methods of Test for Soils for Civil Engineering Purposes. UK: London, British Standards Institution.
- [9] Ekiti State Directorate of ICT (2017). The Official Website of the Government of Ekiti State, Nigeria. Available:<https://ekitistate.gov.ng/administration/local-govt/ido-osi-lga/>.
- [10] Europa Technologies (2017). Google Earth. Available: <http://earth.google.com/>, 2017.

-
- [11] Federal Ministry of Works and Housing (FMWH) (1997). General Specification (Roads and Bridges) – Revised Edition (Volume II), Nigeria. Abuja: Federal Ministry of Works.
- [12] U. N. Okonkwo, I. C. Odiong and E. E. Akpabio (2012). The Effects of Eggshell Ash on Strength Properties of Cement – Stabilized Lateritic. *International Journal of Sustainable Construction Engineering and Technology*, vol. 3(1), pg. 18-25.
- [13] M. B. Qasim, A. M. Tanvir and M. M. Anees (2015). Effects of Rice Husk on Soil Stabilization. *Bulletin of Energy Economics*, vol. 3(1), pg. 10-17.
- [14] G. Vishwanath, , K. R. Pramod and V. Ramesh (2014). Peat Soil Stabilization with Rice Husk and Lime Powder. *International Journal of Innovation and Scientific Research*, vol. 9(2), pg. 225-227.
- [15] Wikimedia Foundation Inc. (2017). Ekiti State. Available: https://en.wikipedia.org/wiki/Ekiti_State.

Some aspects of Cold Deformation studies of Al-ZrB₂ composites

C. Venkatesh¹, B. Chaitanya², K S M Yadav³

^{1,2} Asst. Professor, Dept. of Mechanical Engineering, Ace Engineering college, Ghatkesar, Hyderabad, India.

³ Research Scholar, Department of Metallurgical and Materials Engineering, NIT Warangal, India

Abstract— In the present study Al-ZrB₂ composite were made by powder metallurgy route adding different amounts of synthesized ZrB₂ powder (2, 4, 6, 8, 10 wt. %). The ZrB₂ powder was synthesized by using self-propagating high temperature synthesis (SHS). The samples of different aspect ratios (0.35, 0.5 and 0.65) were made and then sintered at 550°C under continuous argon gas atmosphere in a tubular furnace for 1 hour. The microstructure of the composites had shown that there is no chemical adhesion between Al matrix and ZrB₂ reinforcement. Hardness of the composites increased with increase in the amount of ZrB₂ reinforcement. The hardness of the composites increased with increase in amount of ZrB₂ reinforcement. It was found that the formability stress index increased with the increase of preform fractional density and decreased with the aspect ratio. Relation between various stress ratios, axial strain and relative densities were analyzed. Statistical fitting methods are used on the curve drawn between the axial strain and the stress formability index. The compacts of lower aspect ratio and high initial preform density were found to have a very high fracture strain.

Keywords— Powder metallurgy, ZrB₂, Workability, Relative density, Fracture strain.

I. INTRODUCTION

In some situations Powder metallurgy (P/M) may be the only manufacturing technique which can be used for the production of composite materials, porous materials, refractory materials and high duty special alloys. P/M gives an edge over other manufacturing techniques in cost efficiency, for higher volume production of complicated components. In most cases such components are manufactured using a conventional P/M route which involves deformation of the metal powder followed by sintering [1].

Aluminium metal matrix composites were gaining great scope for applications within aerospace, defense, automotive industries and various other fields [2]. Aluminium MMCs have a great application potential in automotive engineering components i.e, braking systems, piston rods, piston pins, pistons, structural frames, valve spring caps, brake discs, disc brake caliper, brake pads, cardan shaft, engine heads etc. Axle tubes, reinforcements, blade, gear box casing, turbine, fan and compressor blades are some other significant applications in military and civil aviation for Aluminium MMCs. MMCs and alloys are extensively used over metals as they offer higher specific properties (properties/unit weight) of strength, stiffness, higher specific modulus, thermal stability, tribological properties and various other mechanical properties which enhances the product performance [3-4].

Titanium diboride (TiB₂) and zirconium diboride (ZrB₂) are significant boride ceramics which exhibit superior properties like high melting point, extremely high hardness and wear resistance, low specific gravity, magnetic, electrical properties, with high mechanical properties and chemical inertness at elevated temperatures.

In the present study an attempt was made to investigate the deformation behavior of Al-ZrB₂ composites under triaxial stress state conditions. There were few researchers who reported on the deformation behavior of Cu-SiC, Cu-TiC, Al-Cu, Cu-ZrB₂ etc. The ZrB₂ used was synthesized by using self-propagating high temperature synthesis (SHS).

II. EXPERIMENTAL DETAILS

Aluminium:

Aluminium powder (99.99%) was procured from SRL pvt.ltd, Mumbai, India. The particle size of the Al powder is found to be 40µm (-325 mesh size). The particle morphology of aluminum powder was shown Fig. (1a).

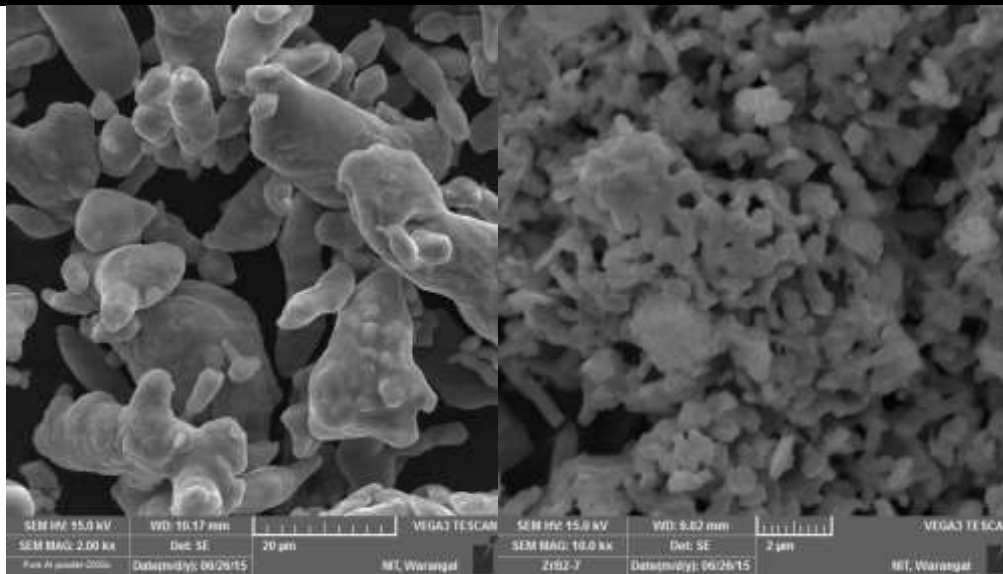
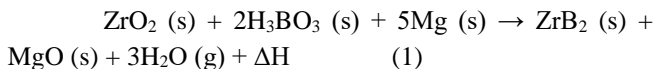


Fig. 1: a) SEM image of Al powder. b) SEM image of ZrB₂ powder

Zirconium Diboride (ZrB₂):

ZrB₂ powder was synthesized by self-propagating high temperature synthesis (SHS) technique with ZrO₂, H₃BO₃ and Mg as raw materials mixed homogeneously in quantities according to stoichiometric equation (1).



The 20gm mixture of charge was placed in a stainless steel boat and heated upto 800°C at a rate of 10⁰C/min. The reaction gets initiated at 720°C. The whole reaction process was carried out in a tubular furnace with continuous supply of argon gas to maintain controlled atmosphere. The reacted mixture was grounded and leached with HCL solution and ZrB₂ powder was tapped [5]. The particle morphology of SHS ZrB₂ powder was shown Fig. (1b).

Compaction:

Compacts of 20mm diameter of pure Al and Al- ZrB₂ (2, 4, 6, 8, 10 wt%) were made in different aspect ratios (L/D) i.e; 0.35, 0.5, 0.65 The variations were achieved by varying powder quantities and compaction loads respectively. A 25Ton manual hydraulic press was used for compaction of powder preforms.

Micro-hardness test:

The surface of the preforms was polished to mirror finish by conventional polishing techniques. Micro-hardness tests

were conducted on SCIMADZU micro-hardness tester. 200gm load and 10sec dwell time during loading are the parameters used during micro-hardness tests.

Cold deformation experiments:

The density measurements of preforms were carried out using Archimedes principle. The height and diametric measurements were recorded by digital vernier calipers. All the deformation experiments were carried out on a 50Ton hydraulic press with mirror polished flat dies (top and bottom flatens). A constant ram feed rate of 0.7mm/min was maintained during all the deformation experiments [6]. Extreme care was taken to place the cylindrical specimen within the platens, concentric with the central axis of the hydraulic press (loading direction). Cylindrical preforms were cold upset between flat platens. A set of 6 preforms of same composition were used in incremental loading conditions in order to make a plot for true axial stress and true axial strain. This was because, to determine dimensional measurements and other calculations at different points during loading upto fracture. Axial deformation was continued until a visible crack appeared on the free surfaces of the deforming compacts as shown in Fig 2.



Fig. 2: Al composite before and after deformation between the flatens.



Fig. 3: Deformed Al-ZrB₂ composites of different aspect ratios covered with Teflon tape for density measurements.

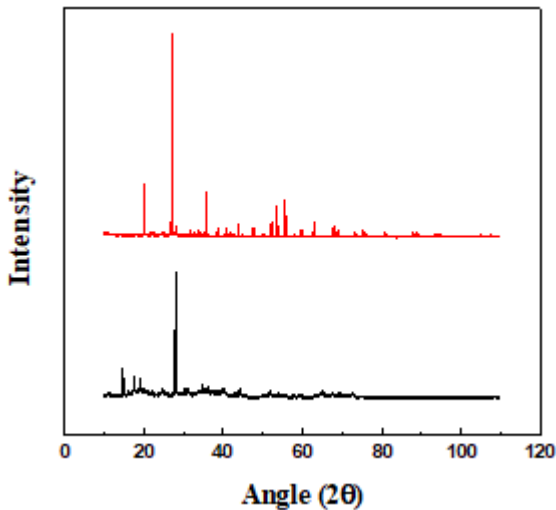


Fig. 4: XRD patterns of Al and ZrB₂ elemental powders.

2.6 Theoretical analysis:

In the upsetting of P/M parts as shown in Fig. (3), the height decreases, the average density increases, and the various stress increases. The expressions for the normal stress (σ_z), normal strain (ϵ_z), hoop stress (σ_θ), hoop strain (ϵ_θ),

hydrostatic stress (σ_m), effective stress (σ_{eff}), and effective strain (ϵ_{eff}) are taken from Selvakumar *et al.*[7] and Narayanasamy *et al.*[8].

- Initial diameter- (D_o).
- Initial height- (h_o).
- Initial preform density (ρ_o).
- Contact diameter at the top- (D_{CT}).
- Contact diameter at the bottom- (D_{CB}).
- Bulged diameter- (D_B).
- Height of the preforms- (h_f).
- Density of the preforms- (ρ_f).

Using the load, dimensional parameters and density, different true stresses (namely σ_z , σ_θ , σ_m and σ_{eff}) and different true strains, (namely ϵ_z and ϵ_θ) and workability parameters (β_σ).

Triaxial Stress State Condition

$$\alpha = \frac{A}{B} \tag{2}$$

$$A = (2 + R^2)\sigma_\theta - R^2(\sigma_z + 2\sigma_\theta) \tag{3}$$

$$A = (2 + R^2)\sigma_z - R^2(\sigma_z + 2\sigma_\theta) \tag{4}$$

$$\text{Hoop stress, } \sigma_\theta = \left[\frac{2\alpha + R^2}{(2 - R^2 + 2R^2\alpha)} \right] \sigma_z \tag{5}$$

$$\text{Hydrostatic stress, } \sigma_m = \frac{\sigma_z + 2\sigma_\theta}{3} \tag{6}$$

$$\text{Effective stress, } \sigma_{eff} = \left[\frac{\sigma_z^2 + 2\sigma_\theta^2 - R^2(\sigma_\theta^2 + 2\sigma_z\sigma_\theta)}{2R^2 - 1} \right]^{0.5} \quad (7)$$

$$\text{Relative density, } R = \left[\frac{\rho_f}{\rho_{th}} \right] \quad (8)$$

$$\text{Formability Stress Index, } \beta = \frac{3\sigma_m}{\sigma_{eff}} \quad (9)$$

III. RESULTS AND DISCUSSIONS

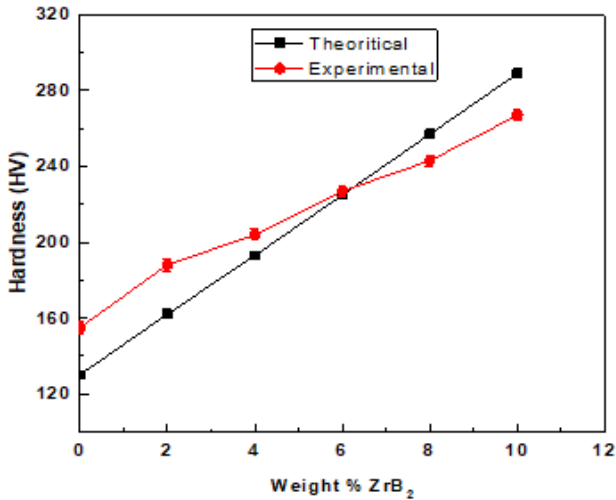


Fig. 5: Hardness of Al - ZrB₂ composites.

The Fig. (5) shows that the experimental micro hardness values of the composites are higher than the theoretical hardness values upto 6% ZrB₂ and then lower than theoretical values because of increased porosity as the ZrB₂ quantity increased in the composites.

The sintered microstructure of pure Al and Al+10% ZrB₂ were as shown in fig. (6). the scanning electron microscope micrographs show that there was no chemical bonding between aluminum and ZrB₂ particles. The porosity increased with the increase in the ZrB₂ reinforcement in the composite. This was because the hard ZrB₂ reinforcement particles inhibiting the transfer of load during compaction which resulted in low relative density. The Fig. (7) shows the microstructure of Al+10% ZrB₂ composite showing the closure of pores due to deformation there by increase in the density.

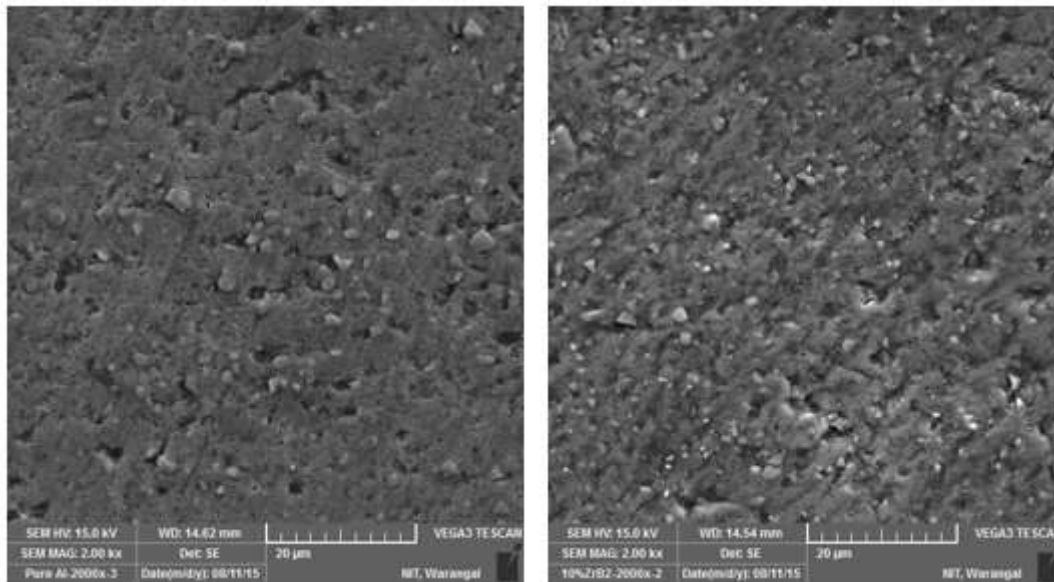


Fig. 6: a) SEM micrograph of pure Al & b) SEM micrograph of Al+10% ZrB₂.

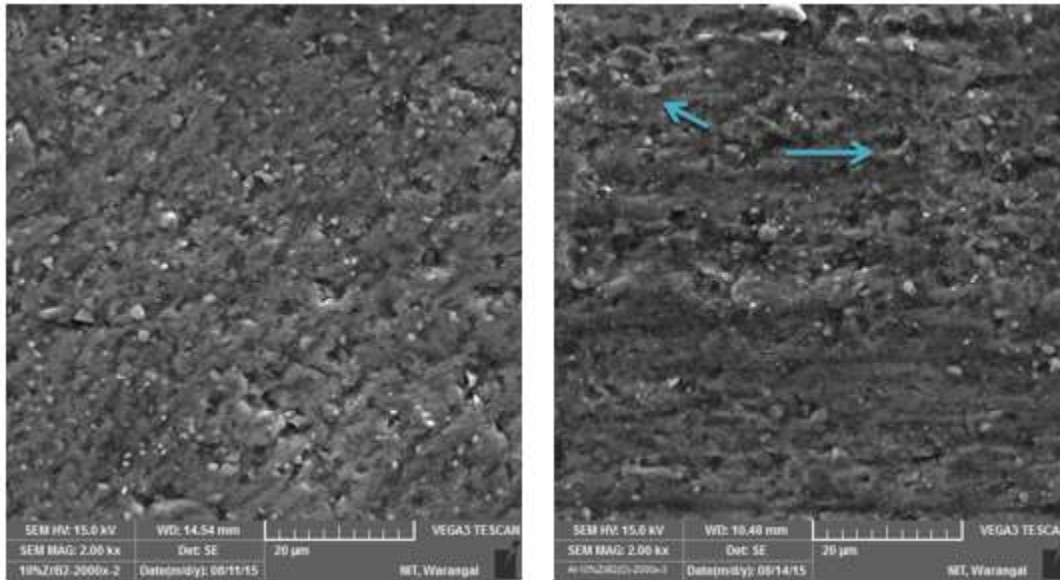


Fig. 7: a) SEM micrograph of Al+10% ZrB₂ before deformation & b) SEM micrograph of Al+10% ZrB₂ after deformation upto fracture

The Fig. (8) Shows the relation between the relative densities attained and the axial strain for the Al-ZrB₂ preforms.

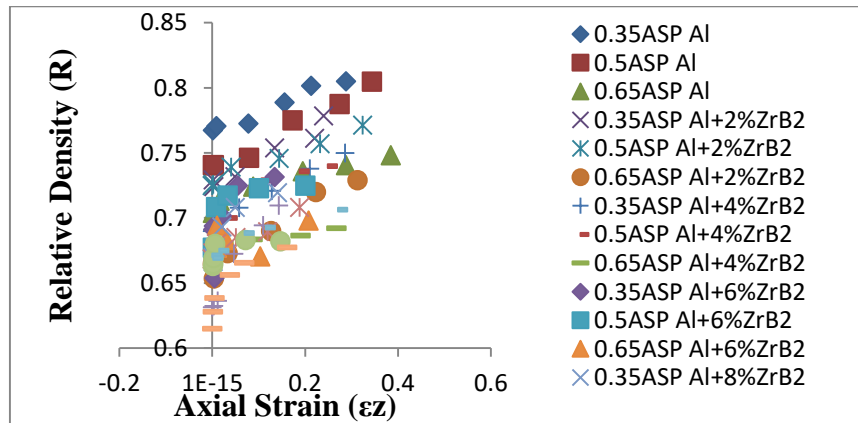


Fig. 8: Relative density(R) Vs Axial strain.

A statistical curve fitting techniques were adopted on the curves of results obtained and the prediction equation developed from the curves was checked for its applicability by comparing the correlation coefficient ‘R²’ values. These values can be used for modeling purposes and can also serve as prediction equations. In the present study, two

different curve fitting techniques namely power law and parabolic curve fitting were used.

Fig. (9-11) shows the plot drawn between relative density and formability stress index (β). A statistical fit was made using polynomial function and power law function.

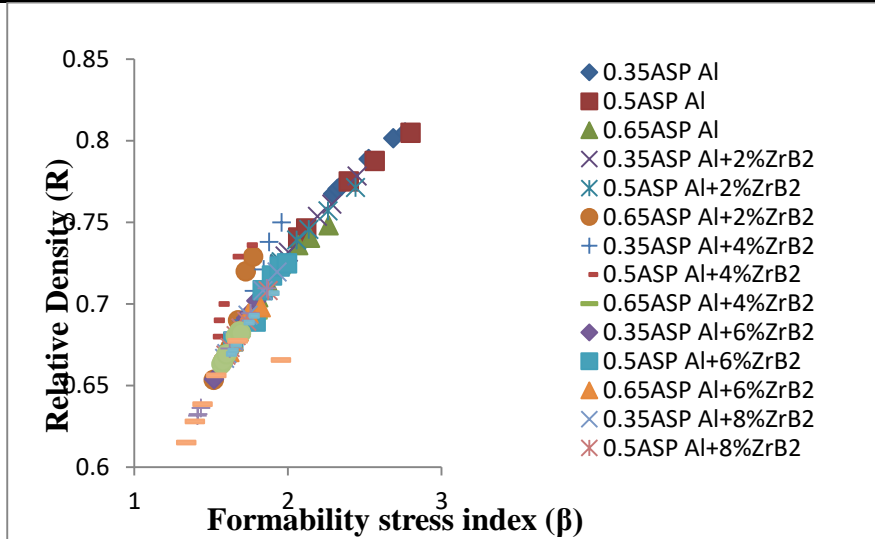


Fig. 8: Relative density (R) Vs Formability stress index (β).

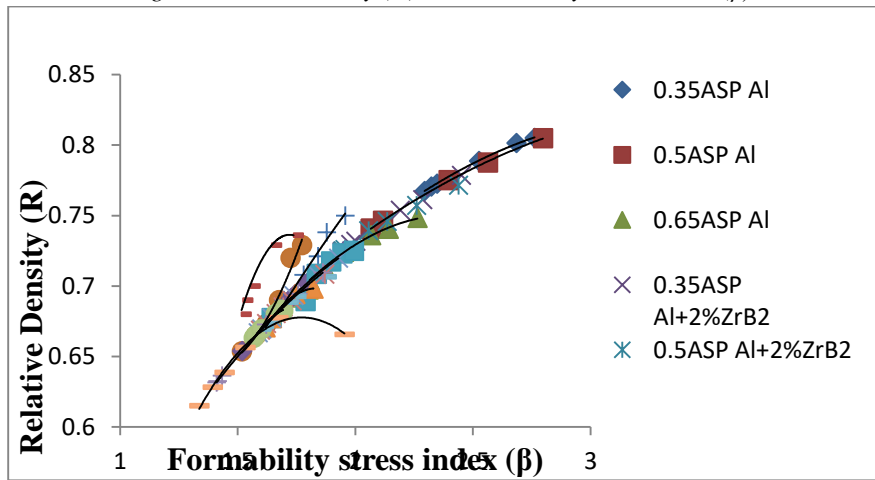


Fig. 9: Relative density (R) Vs Formability stress index (β) (parabolic curve fitting).

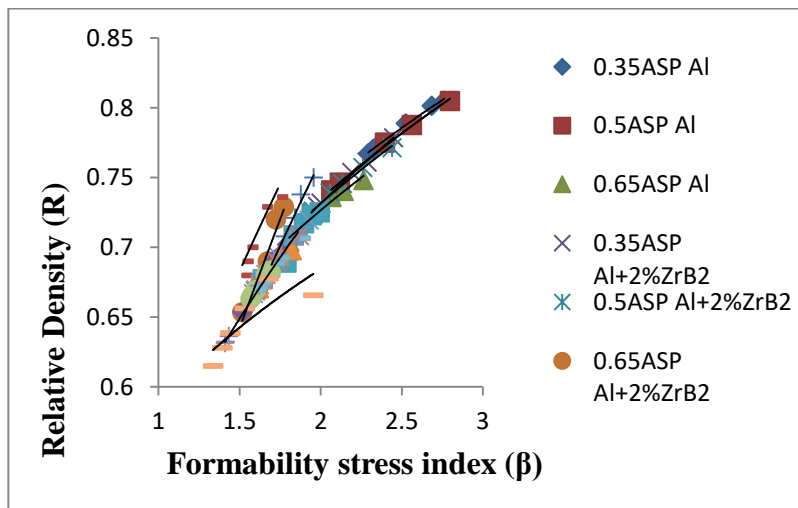


Fig. 10: Relative density (R) Vs Formability stress index (β) (power law curve fitting).

Table. 1: Parabolic curve fitting equations and R² values of Relative density (R) Vs Formability stress index (β).

Aspect ratio	Sample	Equation	R ² value
0.35	Pure Al	$y = -0.0517x^2 + 0.3429x + 0.2528$	0.9994
0.5		$y = -0.0369x^2 + 0.2669x + 0.3467$	0.9997
0.65		$y = -0.1281x^2 + 0.6164x + 0.0088$	0.999
0.35	Al+2%ZrB ₂	$y = -0.0312x^2 + 0.2423x + 0.3715$	0.9985
0.5		$y = -0.0591x^2 + 0.3528x + 0.2623$	0.9985
0.65		$y = 0.5965x^2 - 1.6489x + 1.7814$	0.9767
0.35	Al+4%ZrB ₂	$y = -0.0652x^2 + 0.485x + 0.0522$	0.9819
0.5		$y = -0.9354x^2 + 3.2948x - 2.1615$	0.9876
0.65		$y = -0.3836x^2 + 1.416x - 0.614$	0.9931
0.35	Al+6%ZrB ₂	$y = -0.0311x^2 + 0.2797x + 0.3008$	0.9937
0.5		$y = -0.001x^2 + 0.1548x + 0.4239$	0.9393
0.65		$y = -0.6005x^2 + 2.2015x - 1.3196$	0.9975
0.35	Al+8%ZrB ₂	$y = -0.1078x^2 + 0.5343x + 0.0905$	0.9999
0.5		$y = -0.1123x^2 + 0.5328x + 0.1045$	0.9987
0.65		$y = -0.5879x^2 + 2.0782x - 1.1503$	0.9946
0.35	Al+10%ZrB ₂	$y = -0.0901x^2 + 0.4676x + 0.1515$	1
0.5		$y = -0.1924x^2 + 0.8034x - 0.1235$	0.9999
0.65		$y = -0.3428x^2 + 1.2145x - 0.398$	0.9911

From the Fig. (12-13) it was found that the relative density increases as the stress ratio parameter increases.

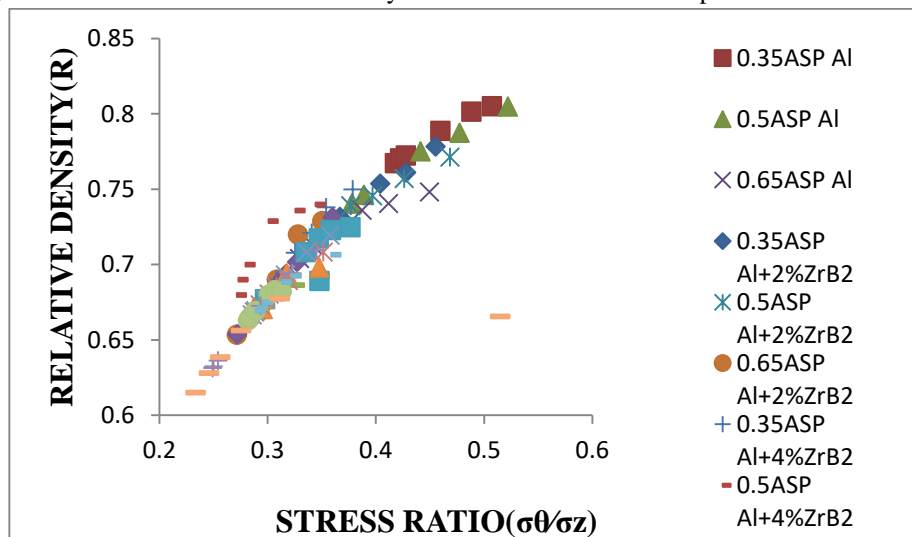


Fig. 11: Relative density Vs Stress ratio(σθ/σz).

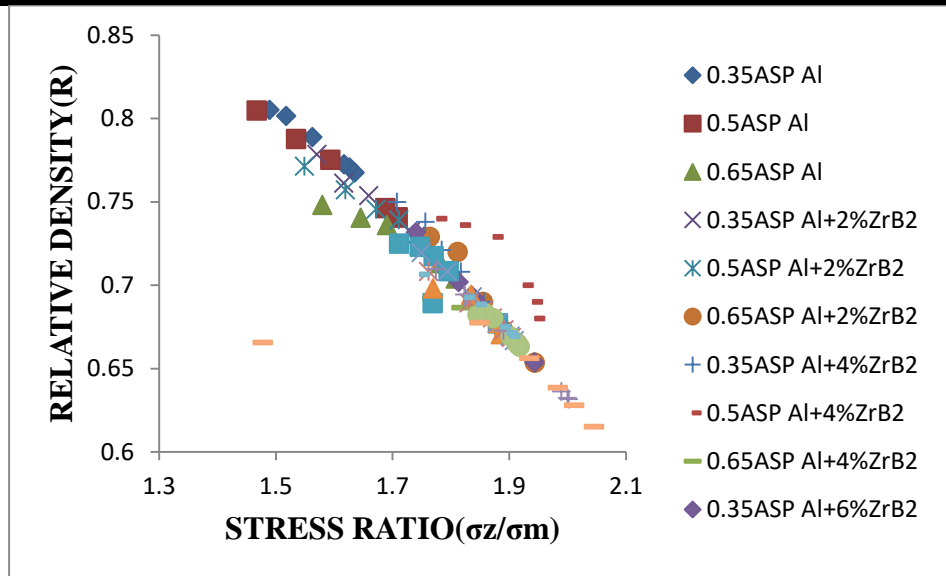
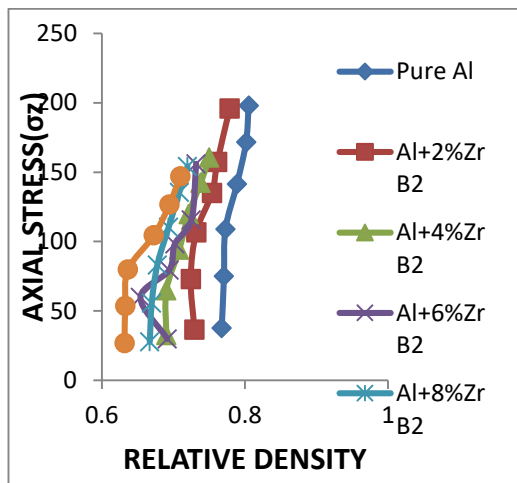
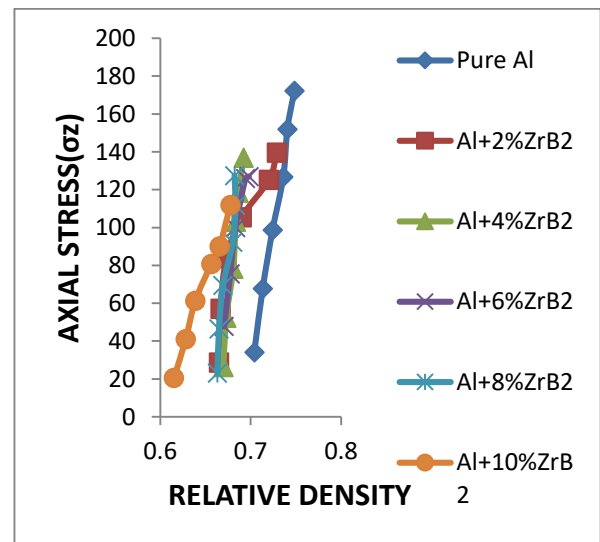


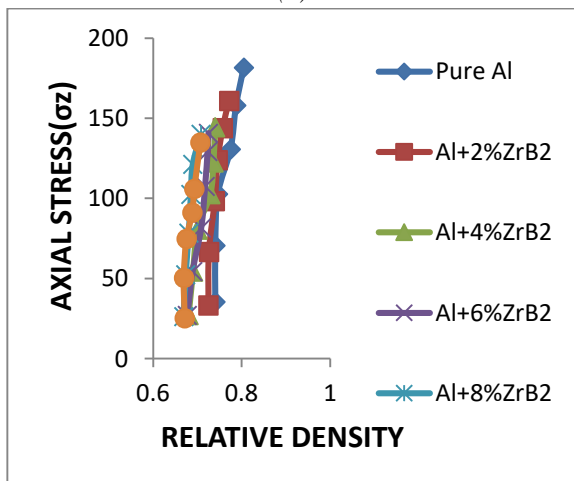
Fig. 12: Relative density Vs Stress ratio(σ_z/σ_m).



(a)



(c)



(b)

Fig. 15: Axial stress (σ_z) Vs Relative density (R) (a) 0.35 ASPR, (b) 0.5 ASPR and (c) 0.65 ASPR

The Fig. 15(a-c) shows the plot of axial stress (σ_z) against the relative density R. The experiment has been done with preforms with initial densities ranging from 0.6 to 0.75 and aspect ratios ranging from 0.35 to 0.65. Along with the densification, the load bearing capability of the preforms also increase, as is evident from the higher stress values in the plot 15(a-c)

It was found that the preform with 10 % ZrB₂ and 0.35 aspect ratio had densified more. Preforms with high initial preform density had higher load bearing capacity and longer

strain to failure. This was due to the presence of lesser number of pores.

IV. CONCLUSIONS

- The porosity increased with increased quantity of ZrB₂ reinforcement, as the ultra-hard ZrB₂ particles in the composite don't allow the load applied while compaction to close the pores.
- The hardness of the composites increased with increased amount of ZrB₂ reinforcement in the composite.
- The formability behaviors of sintered Al-ZrB₂ composite preforms had been studied in this paper. The formability stress index increased with increase in initial preform fractional density and decreases with the aspect ratios. A statistical fitting methods were to draw curves between the relative density and axial strain, axial strain and the formability stress index. The parabolic curve fitting was found to give better prediction results. The initiation of crack appeared at a very high fracture strain for the compacts with higher value of the aspect ratio and high initial preform density.

REFERENCES

- [1] J. Mascarenhas, Powder metallurgy: a major partner of the sustainable development, Materials Science Forum, 455- 456 (2004), 857–860, doi: 10.4028/ www.scientific.net/ MSF.455-456.857.
- [2] Dieter GE, Mechanical Metallurgy, New York: McGraw-Hill 3rd ed., 1981.
- [3] A. Riaz Ahamed , P. Asokan and S. Aravindan, EDM of hybrid Al–SiCp–B4Cp and Al–SiCp–Glassp MMCs, Journal Advance Manufacturing Technol (2009) 44:520–528. DOI 10.1007/s00170-008-1839-0.
- [4] M. Ramulu, G. Paul and J. Patel, EDM surface effects on the fatigue strength of a 15vol% SiCp/Al metal matrix composite material, Composite structures 54 (2001) 79-86.
- [5] Sumathi, M., Selvakumar, N., & Narayanasamy, R., Workability studies on sintered Cu-10SiC preforms during cold axial upsetting, Materials and Design, 39 (2012), 1–8, doi: 10.1016/j.matdes.2012.02.004
- [6] Narayanasamy, R., Anandkrishnan, V., & Pandey, K. S., Effect of carbon content on workability of powder metallurgy steels, Materials Science and Engineering A, 494 (2008), 337–342, doi:10.1016/j.msea.2008.04.022
- [7] Selvakumar N and Narayanasamy R., Phenomenon of strain hardening behaviour of sintered aluminium preforms during cold axial forming, Journal of Materials Processing Technology, 142 (2003), 347-354, doi:10.1016/S0924-0136(03)00605-8
- [8] Harsh Saini, Irfan Khan, Sushil Kumar, Sahil Kumar(2017).Optimization of Material Removal Rate of WEDM Process on Mild Steel Using Molybdenum Wire. International Journal of Advanced Engineering, Management and Science (ISSN: 2454-1311), 3(10), 1001-1005. <http://dx.doi.org/10.24001/ijaems.3.10.5>
- [9] Narayanasamy R, Ramesh T and Pandey KS., Some aspects on workability of aluminium–iron powder metallurgy composite during cold upsetting, Materials Science and Engineering, A391 (2005), 418–426, doi: 10.1016/j.msea.2004.09.018

Study of Irrigation Water Supply Efficiency to Support the Productivity of Farmers (Case Study at Kobisonta North Seram Central Maluku District)

Hengky Jhony Soumokil, Obednego Domingus Nara

Lecturer Polytechnic Ambon, Jl. Ir Putuhena Wailela – Ambon Indonesia

Abstract— *The need of water is a major media of irrigation in order to support the effectiveness of agricultural business which is manifested as the supporting of food provision. The purpose of this study is to analyze the amount of discharge in each channel and the efficiency in Kobisonta irrigation area, Seti North Seramsubdistrict, Central Maluku district with area of 3,150 ha. The study was conducted on secondary channels Kobisonta includes BKS7, BKS8, BKS9, Kobisonta Secondary Channel includes BKS10, BKS11, BKS12 and Seti Secondary Line includes BS1, BS2 and BS3*

The water debit requirement in the rice field and the efficiency in the irrigation area of Kobisonta was analyzed by using the incoming debit - discharge method based on flow velocity measurement. Providing irrigation water for efficiently is not simple because many factors affect the way and the process, besides that if the water supply and irrigation on the channel is inefficient, then it can reduce or decrease agricultural productivity.

From the result of actual debit analysis on channel BS3, BKS9, BKS11, and BKS12, they are able to meet therequirement of irrigation water thoroughly in irrigation area. In BS1, BS2, BKS8 and BKS10 channels, actual discharge has not been able to meet the irrigation water needs in its irrigation area. The efficiency of irrigation channels in Kobisonta Irrigation Area varies by channel. According to the efficiency standard by the Directorate General of Irrigation, the secondary Saluaran in Irrigation Area is categorized as efficient where for BKS7 is 90%, BKS8 is 97% and BS2 is 91%.

Keywords— *discharge, efficiency, irrigation.*

I. INTRODUCTION

Irrigation is an effort to supply and regulate water with the purpose of agriculture supporting that can include surface

water irrigation, underground water irrigation, pump irrigation and local irrigation. Kobisonta is located in East Seram District Seti, Central Maluku district with a population of 14,923. It is one of the rice production centers.

The construction of Kobi weir which is located in the village of Kobisonta, North Seram District Seti, Central Maluku District which in this case, has a water catchment area of 145.4 km², is expected to meet the water needs for irrigated rice fields of 3,150 ha. So here, researchers use the object of research located in one of the villages located in the Central Maluku District.

In supporting the water needs in the agricultural sector with irrigation system, indeed there will be some problems that arise. One of them is the loss of water that occurs in each channel on the way to the rice field. This study is conducted can give contribution in completing the existing irrigation network study information, by focusing more on the efficiency and effectiveness of irrigation network operating system on the level of service of primary channel, secondary and tertiary channels to water requirements in rice crops.

II. LITERATURE REVIEW

The meaning of Irrigation

Irrigation is a watering activity on an agricultural land that aims to create moist conditions in the root of the plant to meet the water needs for plant growth. According to Basri, 1987 irrigation is the provision of water in plants to meet the water needs for its growth. According to Karta Saputro, 1994 irrigation is an activity of supply and regulation of water to meet the interests of Agriculture by utilizing water from surface water and soil. According to Suharjo, 1994 irrigation is a number of water that is generally taken from

rivers or weirs that flowed through the irrigation system to maintain balance the amount of water in the soil.

2.1 Irrigation Network

The irrigation network is the unity of the canals and structures necessary for the regulation of irrigation water from the provision, collection, distribution, delivery and use. There are two kinds of irrigation networks:

1. The main irrigation network: irrigation network that is located in an irrigation system, starting from main building, main / mainline, secondary channel, and tapping building and its complementary building.
 - a. Main / primary channel
 - b. Secondary irrigation channels
2. Tertiary Irrigation Network: a network that serves as a water service infrastructure within a tertiary grid consisting of a carrier channel called a tertiary channel, a dividing channel called a Quaternary channel, and a drainage channel and auxiliary channels.

2.2 Irrigation Efficiency

Irrigation efficiency shows the use of water that is the ratio between the amount of water used and the amount of water given expressed in percent (%).

$$EfisiensiIrigasi = \frac{debitairyangkeluar (m^3 / detik)}{debitairyangmasuk (m^3 / detik)} \times 100\% \text{ (eq 1)}$$

Estimated efficiency of irrigation is set as follows (KP-01, 1986: 10):

1. tertiary network = 80%
2. secondary network = 90%; and
3. primary network = 90%.

While the overall irrigation efficiency factor is 80% x 90% x 90% = 65%.

2.3 Water Discharge

The amount of liquid that flowing through a cross-section of flow per one unit of time is called flow discharge (Q).

$$Q = A \cdot V \text{ (eq.2)}$$

2.4 Water Loss

Water loss is generally divided into 2 categories, among others:

1. Loss of physical consequences where water loss occurs due to water seepage in the channel and percolation at farm level (paddy field); and
2. Operational loss occurs due to exhaust and excess water discharges during channel operation and waste of water used by farmers.

The loss of water on each inlet measurement (Inflow - Outflow) is calculated as the difference between inlet and outflow discharge. (IPB Water Management Research Team, 1993: 1-05):

$$h_n = I_n - O_n \text{ (eq 3)}$$

Table.1: Flow Velocity Measurement Method

Depth (m)	Velocity Observation	Average Velocity
0.00 - 0.60	0.6d	= V _{0.6d}
0.60 - 3.00	0.2d	= 0.5 (V _{0.2d} + V _{0.8d})
	0.8d	
3.00 - 6.00	0.2d	= 0.25 (V _{0.2d} + V _{0.6d} + V _{0.8d})
	0.6d	
	0.8d	
> 6.00	S	= 1/10 (V _s + 3V _{0.2d} + 2V _{0.6d} + V _b)
	0.2d	
	0.6d	
	0.8d	

2.5 Water Requirement

Parameters that is used in water demand analysis are:

1. Coefficient of plant (Kc)

The magnitude of Kc varies, in this study used the numbers suggested by FAO (Irrigation Planning Standards, KP-01 p. 164).
2. Irrigation efficiency (e)

The need for water in rice fields for rice crops can be determined by the following factors (MawardiEman 2007: 103);

 - o How to prepare the land
 - o Water needs for plants / consumptive used
 - o Percolation and seepage
 - o Replacement of water layers
 - o Effective rainfall

2.6 How to prepare the land

Water requirements for land preparation were calculated using the methods of Van de Goor and Zijlstra (1968) as follows:

$$IR = M (e^k / (e^k - 1)) \text{ (eq 4)}$$

2.7 Water requirements for plants / consumptive use

The water requirement for plants is water that is used up for plant growth. This water requirement is calculated by multiplying the crop coefficient with potential evapotranspiration.

$$Etc = Kc \times Etp \text{ (eq 5)}$$

2.8 Effective rainfall

A. Water Requirement for Irrigation Irrigation water demand in paddy field is calculated for rice-rice planting pattern with the following conditions:

- o Need for clean water in paddy fields (NFR):

$$NFR = ET_c + P - Re + WLR \text{ (eq 6)}$$

- o Irrigation water needs for rice (WRD):

$$IR = NFR / e \quad (eq7)$$

- o Irrigation water needs for crops (WRP):

$$IR = (ET_c - Re) / e \quad (eq 8)$$

The determination of effective rainfall is based on monthly rainfall that is using R80, which means 20% probability is unavailable. The amount of effective rainfall for rice plants is 70% of the minimum monthly rainfall with a 5 year re-period (Irrigation Network Planning, KP-01, 1986,165), with the following equation:

$$Re = 0.7 \times 1/15 \times (R_{80}) \quad (eq 9)$$

Effective rainfall is a plumper rainfall that falls in an area and is used for growth crops.

b) Select the propeller corresponding to the channel depth, so it can be used for some vertical dots ie (0.2h, 0.6h, 0.8h) where h is the channel depth.

c) The current meter is mounted on a static mast with a depth of 0.2h, 0.6h, and 0.8h, then the measuring rod is inputted into the water until the baseband is located at the bottom of the duct with the propeller facing the flow direction (water current).

d) The number of turns per unit of time, which occurs at each water depth, is calculated.

3.3 Source of Data

Source of data used in this research are:

1. Primary Data

Primary Data is data obtained by measuring the Geometric cross section of the velocity flow channel (V), and the channel length (L).

2. Secondary Data

Secondary data obtained from other parties or from existing reports and research, and which have relevance to the issues discussed, including the number and types of irrigation networks studied, the network scheme of the P3A existing in the Kobisonta Irrigation Area, data on water demand on irrigation area kobisonta, as well as data from several government agencies related among others Office of Public Works.

3.4 Data Analysis Technique

Data analysis techniques in this writing done through the stages as follows:

1. Analyze flow velocity by measuring instruments Current meters and or buoys.
2. Analysis of inlet and outflow discharge on secondary channel kobisonta, channel kobisonta, and channel setunder secondary, (equation 3).
3. Analysis of water loss in secondary channel kobisonta, channel kobisonta, and secondary channel seti, by the difference between inlet and outflow (equation 3)
4. Efficiency analysis on the secondary channel kobisonta, channel kobisonta, and secondary channel seti (equation 1).
5. Analysis of water needs in rice plants in Kobisonta Irrigation Area.

III. METHOD

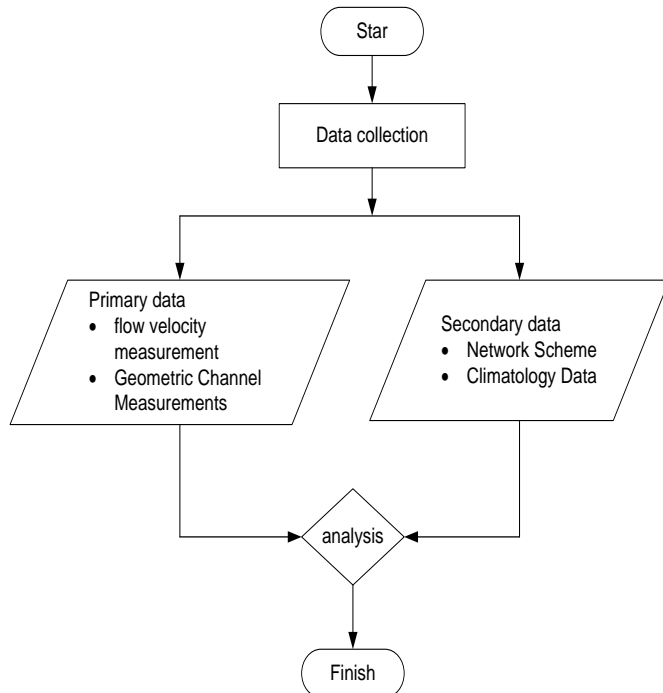


Fig.1: Flowchart Metodologi

3.1 Tools

The tools that are used in this study are: current meter, meter roll, stopwatch, measuring ruler.

3.2 The Measurement Steps are:

Measurement Steps on the Ground:

1. Current Meter

Current velocity measurements are illustrated by the following measurement procedures:

- a) Measure the depth of the channel with the measuring pole of the current meter device

IV. RESULT

Description about the location

Administratively, Kobisonta Irrigation Area is located in Kobisonta village, North Seramsubdistrict of Seti, Central Maluku regency. This sub-district is an expansion of the District of North Seram through the Regional Regulation

(Perda/region regulation) of Central Maluku Number 9 of 2010, with a population of 14,923 inhabitants. The village of Kobisonta is one of the rice production area centers where almost all the local people live as farmers. The construction of Kobi Dam is located in Kobisonta Village, North Seram District Seti, Central Maluku Regency. The Kobi River has a water catchment area of 145.4 km² on the site dam position with a river length of 12.3 km.

Kobidam is expected to meet the water requirement for irrigation 3.150 ha of rice fields equal to 31.5 km². Irrigation water management at farmer level in Kobiosonta Irrigation Area conducted by Water User Farmers (P3A), which is summarized into the Water User Farmers 'Margorejo'

The working area of this association is the Tertiary Plot with a working area of 52 Ha. The source of water used comes from WaiKobi's Bend water which is tapped through the primary channel to the secondary door and then distributed three secondary channels. The first secondary channel is the Seti secondary channel that includes the areas of BS.1, BS.2 and BS.3, the second secondary channel of Kobisonta secondary channel covers the area BKS.7, BKS.8 and BKS.9 and for the secondary secondary channel Kobisonta's face covers the area of BKS.10, BKS.11 and BKS.12.

4.1 Flow Rate Analysis In Irrigation Channels

Measurements of velocity on the irrigation can be done directly by using a buoy or indirectly which usually uses a current meter. Measurement of flow velocity in the Kobisonta Irrigation area the researchers used the Current Meter type C2 tool. Here the researcher uses propeller type current meter, this type rotates to the horizontal axis.

The number of turns per unit time can be converted to current velocity. To shorten the time and save costs, measurements can be made only at some point on the vertical, ie at 0.6 d; 0.2 d; and 0.8 d; with d is the flow depth.

The average velocity performed on the intake door is done by using two (2) points method because the depth of the intake door ranges from 0.6 to 3 meters, where the average velocity is the average of velocity at 0.2 and 0.8 depth.

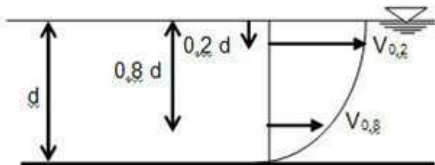


Fig.2: Measurement method of flow velocity

The research that is conducted at the intake door by using the Current Meter obtained the formula of the tool on the propeller current meter type that is:

$$v = 0.2397.n + 0,018 \dots\dots (n < 1,01)$$

$$v = 0.2556 .n + 0.002 \dots\dots (1.01 \leq n < 8.06)$$

$$v = 0.2494 .n + 0,052 \dots\dots (8.06 \leq n < 9.82)$$

To prove the measurement data available with the formula of the tool then the researchers will describe the example calculation to get the value of speed on each segment:

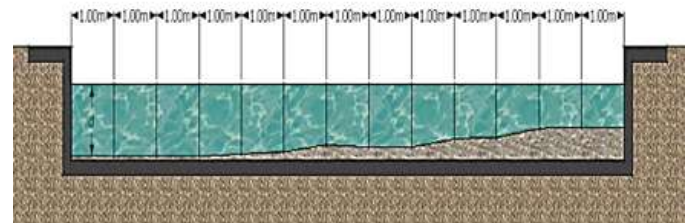


Fig.3: Division of flow rate measurement segments in the field

While the mean velocity on the secondary channel that the researchers do only use the method one (1) point because the depth is at 0.0 - 0.6 meters, which can only be used for shallow water where the method of two or more points can not be done. Speed is measured at 0.6 water depth.

Table.2: Data flow recapitulation dataon channel BS.2

Point (m)	Wide (m)	Depth (m)	Depth of mill (m)	number of rounds	Time (Sec)	Velocity (m/sec)		
						at Point	Average	
0	LW Left	0.30						
0.28	0.28	0.30	0.60	96	40	0.615	0.615	
0.56	0.28	0.30	0.60	84	40	0.539	0.577	
0.84	0.28	0.30	0.60	93	40	0.596	0.568	
1.12	LW Right	0.30						
Average								0.587

Table.3: Average velocity on each channel

Channel code	Velocity (m/sec)
Intake	0.203
BKS 7	1.0692
BKS 8	0.368
BKS 9	0.3077
BKS 10	0.5633
BKS 11	0.3517
BKS 12	0.3854
BS 1	0.4068
BS 2	0.5867
BS 3	0.5143

2 Sectional area of the flow For cross-sectional area of the intake is obtained by multiplying the width of the intake cross-sectional area by the depth of the intake channel.

Table.4: cross-sectional area of the intake door

Segmen	Wide (w) (m)	Depth (d) (m)	Area (A) (m2)
A1	1	0.95	0.95
A2	1	0.95	0.95
A3	1	0.95	0.95
A4	1	0.92	0.92
A5	1	0.89	0.89
A6	1	0.80	0.80
A7	1	0.83	0.83
A8	1	0.83	0.83
A9	1	0.72	0.72
A10	1	0.70	0.70
A11	1	0.58	0.58
A12	1	0.57	0.57
A13	1	0.57	0.57

4.3 Sectional area of the secondary channel

The recapitulation data of the cross-sectional area for the entire channel in the Kobisonta Irrigation Area is included in table 4

Table.5: Sectional area on the intake door

Channel code	Area (m2)
Intake	10.26
BKS 7	0.35
BKS 8	0.48
BKS 9	0.53
BKS 10	0.27
BKS 11	0.39
BKS 12	0.29
BS 1	0.40
BS 2	0.25
BS 3	0.24

4.4 Flow Debit Analysis

Calculation of the discharge in the channel in Kobisonta Irrigation area is intended to know how far the effectiveness of these channels in fulfilling the water requirement for paddy crop in paddy field. Based on the measurements with current meter in the field obtained the flow of water of each channel on the DI. Kobisonta as follows:

Table.6: Debit recapitulation data on each channel

Channel code	Area (m2)	Velocity (m/sec)	Discharge (m3/sec)
Intake	10.26	0.203	2.083
BKS 7	0.35	1.0692	0.374
BKS 8	0.48	0.368	0.177
BKS 9	0.53	0.3077	0.163
BKS 10	0.27	0.5633	0.152
BKS 11	0.39	0.3517	0.137
BKS 12	0.29	0.3854	0.112
BS 1	0.40	0.4068	0.163
BS 2	0.25	0.5867	0.147
BS 3	0.24	0.5143	0.123

4.5 Irrigation Efficiency

Table.7: Standard Efficiency Levels for Irrigation Channels

Channel	efficiency (%)
Primary	90
Secondary	90
Tertiary	80

From the results of research conducted then researchers get the value of efficiency on each channel, which is appropriate (equation 1):

Table.8: Percentage of Irrigation Efficiency

Channel code	Inflow (m3/sec)	Outflow (m3/sec)	efficiency (%)
BS 2	0.126	0.148	85
BS 1	0.148	0.161	92
BKS 11	0.113	0.137	83
BKS 10	0.137	0.152	90
BKS 9	0.152	0.164	93
BKS 8	0.164	0.177	93
BKS 7	0.338	0.375	90

4.6 Water Loss

To calculate the amount of water loss that occurred in secondary channel in Kobisonta Irrigation area, the following equation is used : $h_n = I_n - O_n$

Table.9: Percentage of Water Loss on DI Channels. Kobisonta

Channel code	Inflow (m3/sec)	Outflow (m3/sec)	Losses (%)	Percentage (%)
BS 2	0.126	0.148	0.022	15
BS 1	0.148	0.161	0.013	8
BKS 11	0.113	0.137	0.024	17
BKS 10	0.137	0.152	0.015	10
BKS 9	0.152	0.164	0.012	7
BKS 8	0.164	0.177	0.013	7
BKS 7	0.338	0.375	0.037	10

4.8 Effective rainfall

Calculates effective rainfall for rice by 70% of R80 of time in a period, with the following equation: $Re = 0,7 \times \frac{1}{15} \times (R_{80})$

4.9 Estimated evaporation

Evaporation is expressed as the evaporation rate given in millimeters per day. Evaporative measurements of the water surface can be done in several ways. The most used way to know the evaporative volume of the free water surface is to use an evaporating pan. The method used in kobisonta irrigation area is using class evaporation pans tool. The result of ET0 analysis using Software Cropwat 8.0

Table.10: Results of Effective Rainfall Recapitulation

Month	R 80% (mm)	comparative number	R 80% 1/2 month (mm)	multiplier factor Re %	Re-Rice (mm/15 day)	Re-Rice (mm/day)
Des 1	157.90					
Jan 1	154.70	155.50	84.54	70.00	59.18	3.95
Jan 2		129.05	70.16	70.00	49.11	3.27
Peb 1	52.10	77.75	25.51	70.00	17.86	1.19
Peb 2		81.03	26.59	70.00	18.61	1.24
Mrt 1	167.80	125.85	76.76	70.00	53.73	3.58
Mrt 2		149.25	91.04	70.00	63.73	4.25
Apr 1		70.20	42.08	70.00	29.46	1.96
Apr 2	93.60	85.95	51.52	70.00	36.06	2.40
Mei 1	63.00	47.25	30.48	70.00	21.34	1.42
Mei 2		50.40	32.52	70.00	22.76	1.52
Jun 1	12.60	9.45	2.68	70.00	1.88	0.13
Jun 2		35.00	9.92	70.00	6.94	0.46
Jul 1	102.20	76.65	43.80	70.00	30.66	2.04
Jul 2		102.20	58.40	70.00	40.88	2.73
Ags 1	102.20	76.65	42.57	70.00	29.80	1.99
Ags 2		107.35	59.63	70.00	41.74	2.78
Sep 1	122.80	92.10	55.98	70.00	39.18	2.61
Sep 2		109.95	66.82	70.00	46.78	3.12
Oct 1	71.40	53.55	30.63	70.00	21.44	1.43
Oct 2		71.28	40.77	70.00	28.54	1.90
Nov 1	70.90	53.18	25.85	70.00	18.10	1.21
Nov 2		92.65	45.05	70.00	31.53	2.10
Dec 1	157.90	118.43	67.87	70.00	47.51	3.17
Dec 2		157.10	90.03	70.00	63.02	4.20

Table.11: Calculation of ET0

Month	Min Temp °C	Max Temp °C	Humidity %	Wind km/day	Sun hours	Rad MJ/m ² /day	ET0 mm/day
January	24.0	31.7	60	64	8.0	20.6	4.35
February	22.9	30.4	45	73	7.0	19.9	4.41
March	23.7	30.4	36	62	6.0	18.8	4.19
April	25.0	32.3	53	62	8.0	21.6	4.71
May	21.0	31.7	48	47	9.0	22.1	4.39
June	21.0	31.5	41	54	7.0	18.6	3.92
July	20.0	30.3	43	63	8.0	20.3	4.16
August	20.0	30.3	61	70	10.0	24.1	4.73
September	20.0	29.5	53	78	8.0	21.7	4.47
October	22.0	31.1	53	70	9.0	23.0	4.74
November	22.0	28.8	48	65	8.0	20.7	4.21
December	23.7	28.0	41	57	7.0	18.8	3.90
Average	22.1	30.5	49	64	7.9	20.9	4.34

4.10 Water requirements for land preparation

Calculation of water requirements during land preparation, used methods developed by Van de Goor and Zijlstra (irrigation planning standard KP-01, 1986) with the formula:

$$IR = M (e \wedge k / (e \wedge k - 1))$$

Table.12: Calculation of Water Requirement Processing Period

Month	E ₀	E ₀ =1.1*E _{t0}	P	M=E ₀ +P	k=M*T/S		LP=(M*e ^k)/(e ^k -1) mm/day	
					T=45 day		T=45 day	
					S=250 mm	S=300 mm	S=250 mm	S=300 mm
Jan	3.88	4.27	2.00	6.27	1.13	0.94	9.27	10.28
Feb	4.55	5.01	2.00	7.01	1.26	1.05	9.78	10.77
Mar	5.39	5.93	2.00	7.93	1.43	1.19	10.43	11.40
Apr	4.86	5.35	2.00	7.35	1.32	1.10	10.02	11.00
May	4.68	5.15	2.00	7.15	1.29	1.07	9.88	10.87
Jun	3.96	4.36	2.00	6.36	1.14	0.95	9.33	10.34
Jul	4.15	4.57	2.00	6.57	1.18	0.98	9.47	10.48
Aug	4.63	5.09	2.00	7.09	1.28	1.06	9.84	10.83
Sep	4.56	5.02	2.00	7.02	1.26	1.05	9.78	10.78
Oct	5.20	5.72	2.00	7.72	1.39	1.16	10.28	11.26
Nov	4.30	4.73	2.00	6.73	1.21	1.01	9.58	10.59
Dec	4.21	4.63	2.00	6.63	1.19	0.99	9.52	10.52

4.11 Water requirements for each field

Water requirement for rice crops seen from the maximum requirement that is at age of rice aged two months. The results of field measurements obtained data on the water requirement of each rice field plot in the age of paddy aged 0.5 months to 4 months as follows.

Table.13: Water Requirements for each Plot

Plot Code	Water needd (Lt/s)								extensive rice fields (Ha)
	0.5	1	1.5	2	2.5	3	3.5	4	
BS3	0.21	0.71	0.40	1.04	0.66	0.33	0.21	0	179.80
BS2	0.21	0.71	0.40	1.04	0.66	0.33	0.21	0	95.80
BS1	0.21	0.71	0.40	1.04	0.66	0.33	0.21	0	50.90
BKS12	0.21	0.71	0.40	1.04	0.66	0.33	0.21	0	72.00
BKS11	0.21	0.71	0.40	1.04	0.66	0.33	0.21	0	45.00
BKS10	0.21	0.71	0.40	1.04	0.66	0.33	0.21	0	84.70
BKS9	0.21	0.71	0.40	1.04	0.66	0.33	0.21	0	39.50
BKS8	0.21	0.71	0.40	1.04	0.66	0.33	0.21	0	26.30

Plot Code	water needs of each field (m3/s)								extensive rice fields (Ha)
	0.5	1	1.5	2	2.5	3	3.5	4	
BS3	0.04	0.13	0.07	0.19	0.12	0.06	0.04	0.00	179.80
BS2	0.02	0.07	0.04	0.10	0.06	0.03	0.02	0.00	95.80
BS1	0.01	0.04	0.02	0.05	0.03	0.02	0.01	0.00	50.90
BKS12	0.02	0.05	0.03	0.07	0.05	0.02	0.02	0.00	72.00
BKS11	0.01	0.03	0.02	0.05	0.03	0.01	0.01	0.00	45.00
BKS10	0.02	0.06	0.03	0.09	0.06	0.03	0.02	0.00	84.70
BKS9	0.01	0.03	0.02	0.04	0.03	0.01	0.01	0.00	39.50
BKS8	0.01	0.02	0.01	0.03	0.02	0.01	0.01	0.00	26.30

4.12 Water Requirement (Q Actual) on Channels and Rice Fields

The water requirements in the canals and areas in the study were performed when the actual 2-month-old rice was calculated by the following scheme:

Table.14: Comparison of water requirements in the plot rice field with actual water discharge

Channel code	Area (Ha)	Needs Water debit (m ³ /sec/ha)	Actual debit (m ³ /sec)
BS 3	179.8	0.19	0.125
BS 2	95.8	0.1	0.148
BS 1	50.6	0.05	0.161
BKS 12	72	0.07	0.113
BKS 11	45	0.05	0.137
BKS 10	84.7	0.09	0.152
BKS 9	39.5	0.04	0.164
BKS 8	26.3	0.03	0.177

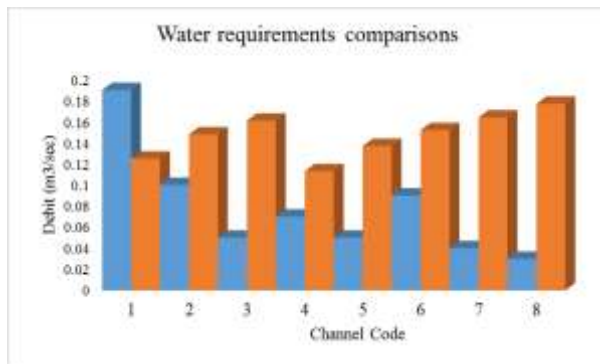


Fig.4: Graph of Water Requirement comparisons

Based on the graph above, the actual debit on BS3, BKS9, BKS11 and BKS12 channels can meet the overall requirement of irrigation water in the irrigation area. In BS1, BS2, BKS8 and BKS10 channels, actual discharge has not been able to meet the irrigation water needs in its irrigation area.

4.13 Discussion

The area of rice fields in Kobisonta irrigation area of 3,150 ha has three secondary channels namely kobisonta secondary channel (BKS7, BKS8, and BKS9), secondary channel faces kobsionta (BKS10, BKS11 and BKS12) and secondary channel seti (BS1, BS2 and BS3) which take water from Bend WaeKobi. Each of the secondary channels studied has different irrigation areas, channel lengths, and wet cross-sectional areas.

In the dry season the farmers in Kobisonta village still plant rice, this is because the water supply in BendungWaeKobi is considered still able to meet the needs of irrigation. Management of irrigation water distribution that is less

good or optimal cause some of its debit channel is not sufficient to meet the needs of irrigation of rice crops in the village kobsionta.

Lacks of the farmer’s discipline in the distribution of water were found in many fields. Distribution of irrigation water in Kobisonta Village is done by opening the water gate as high as possible without taking into account the water requirement in every irrigation area.

At each of irrigation in secondary irrigation area kobisonta has different efficiency value. According to Irrigation Secondary Irrigation Planning Standart is said to be efficient if the efficiency rate of irrigation above 90%.

Based on the results in Table 8 Channel BKS7 which has irrigation area of 185.10 ha and channel length 697.55 meters with actual discharge 0.37528 m³ / s has a watering efficiency of 90%. In BKS8 channel with 700 meters channel length with actual discharge 0.17664 m³ / s has a watering efficiency of 93%. In BKS10 channel which has irrigation area of 39.5 ha with actual discharge 0.1639 m³ / s has water efficiency of 93%. In BKS11 channel which has an irrigation area of 84.7 ha with actual discharge of 0.1521 m³ / s has irrigation efficiency of 90% and In channel BS1 with irrigation area 50.9 ha and a length of 800 meter channel with actual discharge 0.1611 m³ / watering by 92%. In BKS7, BKS8, BKS9, BKS10 and BS1 value efficiency above 90% then the channel can be said to be efficient.

In BS2 channel which has irrigation area 95,8 ha and channel length 1000 meter with actual discharge 0,1478 m³ / s has watering efficiency equal to 85%. And Channel BKS11 with irrigation area 45 ha and channel length 700 meters with actual discharge 0.1372 m³ / s has 83% efficiency value. Secondary channel BS1, and BKS11 value of efficiency below 90%. Then the channels have an efficiency value below the standard. This is due to the amount of mud deposits along the channel and leaks along the channel.

For the percentage of losses in each channel in the Kobisonta Irrigation Area has a different percentage values per channel. According to DPU Republik Indonesia KP-03 (1986: 7), generally water loss in the irrigation network on the secondary channel 5 - 10%.

Based on the results of the data in table 9 On the secondary channel BKS7 the percentage value of water loss of 10%, channel BKS8 percentage value of water loss of 7%, channel BKS9 water loss percentage value of 7%, channel BKS10 percentage value of water loss by 10% and secondary channel BS1 percentage value of water loss of

8%. For BKS7, BKS8, BKS9, BKS10 and BS1 meet the standard according to the Public Works Department.

In BKS11 channel the percentage value of water loss is 17% and BS2 channel value of water loss percentage is 15%, so for BKS11 and BS2 channels do not meet DPU standard because water loss percentage value is below 5-10%. This is due to the seepage on a part of the bottom of the drained channel, the amount of soil deposits, sand, loads of loads in the form of wood, foliage, the amount of garbage and the theft of water made by farmers that slows the flow of water in the secondary channel in the irrigation area Kobisonta.

Based on 15 comparisons of debit requirements with the actual water debit, the actual debit on channel BS3, BKS9, BKS11, and BKS12 able to meet the requirement of irrigation water as a whole in irrigation area. In BS1, BS2, BKS8 and BKS10 channels, actual discharge has not been able to meet the irrigation water needs in its irrigation area. In water supply for irrigation, there needs to be efficiency and effectiveness of water supply. Efforts that need to be made to improve the efficiency and effectiveness of irrigation are:

1. To reduce the impact of vegetation damage and channel cracking in Kobisonta Irrigation Area it is necessary to maintain by Margorejo P3A either regularly or periodically on each channel.
2. Need to be socialized about the process of water distribution by P3A to farmers so that farmers are expected to be more disciplined in implementing irrigation water taking schedule.

V. CONCLUSION AND SUGGESTIONS

5.1 Conclusions

Based on the results and discussion, then we obtained the following conclusions:

1. The efficiency of discharge in every secondary channel in Kobisonta Irrigation area has different value. On the secondary channel BKS.7 efficiency value 90%, BKS.8 93% efficiency value, BKS.9 efficiency value 93%, BKS.10 value of efficiency 90% and BS. 1 efficiency value of 92% on average has met the efficiency standard according to Planning Standards of Secondary Irrigation Planning for the efficiency of irrigation above 90%. While for secondary channel BKS.11 83% efficiency value, and BS.2 85% efficiency value does not meet the standard of efficiency because the average value of efficiency on the channel is below 90%.
2. Total water loss in Kobisonta Irrigation area for secondary channel BKS.7 10%, BKS.8 7%, BKS.9 7%,

BKS.10 10% and BS.1 8% have met the planning criteria which is the standard of Public Works Service. In general, water loss in irrigation networks in the 5-10% secondary channel while in the 17% BKS.11 channel, and BS.2 15% has exceeded the water loss planning criteria. This is due to the seepage of some of the bottom of the eroded channel, the amount of soil sediment (sedimentation), waste and also because of the theft of water conducted by farmers resulted in the slow speed of water flow in the secondary channel DI. Kobisonta

5.2 Suggestions

1. The need for socialization to the water users farmers (P3A) Margorejo to understand and adhere to the way of distribution of irrigation water so as not to harm other farmers.
2. To improve the efficiency and effectiveness of water distribution there needs to be cooperation between the Public Works Department and the P3A.
3. Margorejo P3A is expected to always review the conditions of existing channels in the Kobisonta Irrigation System and repair the damaged channels, clean up the sludge, waste along the canal.

REFERENCES

- [1] Anonymous, Irrigation Planning Standards (KP - 01). Jakarta, 1986.
- [2] Directorate General of Water Resources. 1986. Irrigation Planning Standards. Jakarta.
- [3] DPU Irrigation. 2004. Law No.7 on Water Resources. Jakarta.
- [4] DPU Indonesian Republic KP-03 (1986: 7) Kartasapoetra, A.G., 1994. Post-Harvest Handling Technology. RinekaCipta, Jakarta.
- [5] Saptana, Sumaryanto, Hendiarto, R.S. Rivai, Sunarsih, A. Murtiningsih and V. Siagian. 2001. Engineering Optimization of Irrigais Water Allocation in Order to Increase Food Products and Farmers Income. AgroEconomy Bulletin, Vol 1 No. 3. Center for Agricultural Socio Economic Research and Development.
- [6] Enock Dashu, P.(2017).Microbial Effect of Refuse Dump on the Composition of Leafy Vegetables Grown in the Vicinity of Dump Site Along River Benue, Mubi Road, Yola. International Journal of Environment Agriculture and Biotechnology(ISSN: 2456-1878).2(4), 1895-1899.10.22161/ijeab/2.4.54

- [7] Sumaryanto and T. Sudaryanto, 2001. Paradigm Change of Water Resources Utilization and Its Implication on Food Production Development Strategy. FAE. Volume 19, No. 2. Center for Agricultural Socio Economic Research and Development.
- [8] Standart Irrigation planning, planning criteria of irrigation network part KP-01 1998.
- [9] Sudjarwadi, 1990. Theory and Practice of Irrigation. Inter-University Center of ScienceTechnique, UGM, Yogyakarta
- [10] Triatmodjo, B. 2015. Applied Hydrology, Faculty of Engineering, GadjahMada University, Yogyakarta
- [11] Wusunahardja, P.J., Efficiency and Irrigation Water Loss. Journal of Information Engineering, 1991.

The Air Flow Analysis of Coffee Plantation Based on Crops Planting Pattern of the Triangular Grid and Shackle of Wheel graphs by using a Finite Volume Method

Dafik, Muhammad Nurrohim, Arif Fatahillah, Moch. Avel Romanza P, Susanto

Mathematics Education Department, FKIP University of Jember, Jember, Indonesia

Abstract— Coffee bean is one of the Indonesia major export commodity. Based on the data from the 2012, Indonesia was ranked at third biggest coffee beans exporter in the world, after Vietnam and Brazil. A coffee land expansion have been done to increase the productivity of coffee beans, however it is not so effective. One of the factors that affect the productivity is a crops planting pattern. A good crops planting pattern will make a good air circulation and it will finally affect to the productivity of coffee beans. We will use a finite volume method to analyze the air flow of coffee plantation based on the soil roughness level, crops planting pattern of the triangular grid and shackle of wheel graphs. The simulation process is carried out by using MATLAB and FLUENT softwares. The result shows that the crops planting pattern of triangular grid and shackle of wheel graphs gives a better air circulation process in the coffee bean plantation.

Keywords— Coffee Plants, Air Flow, Soil Roughness Level, Triangular grid graph, Finite Volume Method.

I. INTRODUCTION

Coffee is one of the second largest export product of Indonesia Country (Institute of Education, Training and Agricultural Extension; 1984). During 20 years the total area and production of coffee plantations in Indonesia have risen a significant improved. However, as an exporter country, Indonesia is still left behind the other countries such as Vietnam and Brazil (FAO, 2012), it is due to the decrease of the coffee production. One of the factors that affect the productivity is a crops planting pattern. A good crops planting pattern will make a good air circulation and it will finally affect to the productivity of coffee beans.

In this research will be constructed a mathematical model of differential equations of the air circulation on the coffee plantation based on the soil of roughness level and

cropping pattern of the triangular grid and shackle of wheel graphs of two dimensions shapes. The governing equation for this model are the momentum equation and the energy equation.

$$\frac{\partial \rho \phi_0}{\partial t} + \nabla \rho u_i u_j = \rho \nabla g - \nabla p + 2\mu \left(\frac{\partial^2 v_i}{\partial x_i^2} + \frac{\partial^2 v_j}{\partial x_j^2} \right) + \mu \left(\frac{\partial^2 v_i}{\partial x_j^2} + \frac{\partial^2 v_j}{\partial x_i^2} \right) \quad (1)$$

$$\frac{\partial j}{\partial t} + \nabla u_i u_j = \nabla \left(-p u_i' + 2m u_i' - \frac{1}{2} r u_i' u_j' \right) - 2m \left(\frac{\partial u_i'}{\partial x_i} + \frac{1}{2} \left(\frac{\partial u_i'}{\partial x_j} + \frac{\partial u_j'}{\partial x_i} \right) + \frac{\partial u_j'}{\partial x_j} \right) - r u_i' u_j' \left(\frac{\partial u_i}{\partial x_i} + \frac{1}{2} \left(\frac{\partial u_i}{\partial x_j} + \frac{\partial u_j}{\partial x_i} \right) + \frac{\partial u_j}{\partial x_j} \right) \quad (2)$$

where: ρ is the density of air fluid, g is the acceleration of gravity, p is the air pressure, μ is the viscosity of air fluid, τ_{ij} is displacement force, u and v are respectively the average velocity direction of X axis and Y axis, u' and v' are respectively turbulent flow direction of X axis and Y axis.

Mathematics model for air circulation of coffee plantation is affected by profile of vertical's air velocity (Kindangen, 2005):

$$\frac{v_y}{v_r} = \left(\frac{x}{x_r} \right)^\alpha \quad (3)$$

where: v_y is the average air velocity at a height y , v_r is the average air velocity at the height benchmark, x is the distance between plants, x_r is the benchmark distance,

and α is the characteristic value of roughness. The model formed will be simulated and analyzed by using MATLAB and FLUENT software.

II. RESEARCH METHODS

The study is started by collecting some relevant literatures and references to the coffee plant, fluid, turbulent flow and finite volume method. It will be designed a model of air circulation on the coffee plantation based on the level of the soil of roughness and cropping pattern of the triangular grid and shackle of wheel graphs. Furthermore, the researcher will discretize the model by using finite volume method of Quick technique.

The simulation of air circulation will be carried out by MATLAB and FLUENT softwares to analyze the relation between the level of the soil of roughness and air circulation on coffee plantation. Finally we test and evaluate the programme simulation to know weather the programming is doing well or not in obtaining the air circulation of coffee plantation based on the level of the soil roughness.

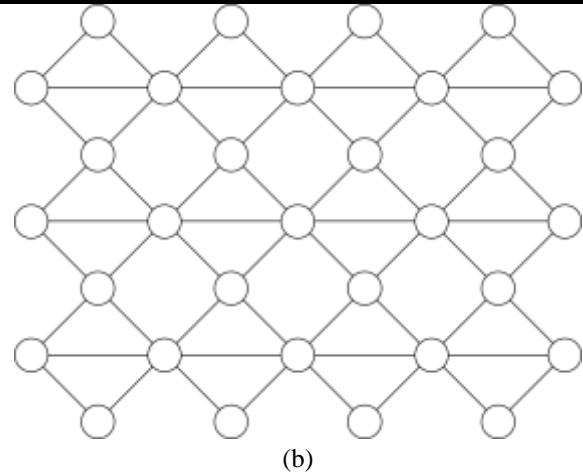
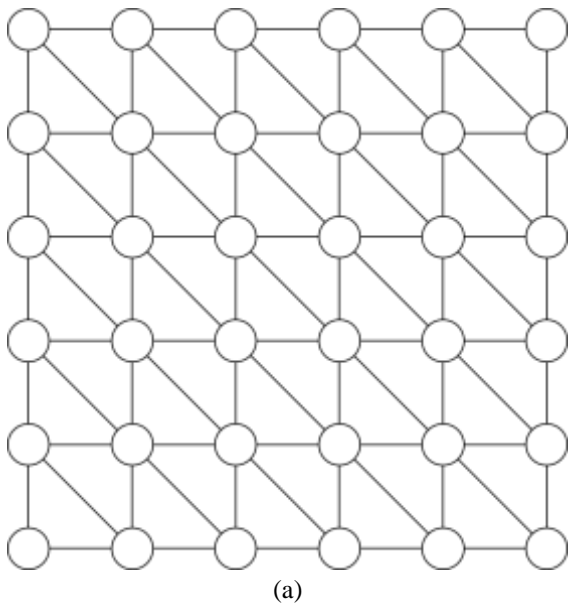


Fig.1: (a) Triangular Grid Graph Cropping Pattern, (b) Shackle of Wheel Graph Cropping Pattern

III. RESULTS AND DISCUSSION

The simulation is done by comparing the soil roughness level and the air circulation of the coffee plantation. The soil of roughness level are 0,1; 0,5; and 0,9. The initial velocity of air circulation is 1,2m/s. The number of trees at cropping pattern of a triangular grid and shackle of wheel graphs of the direction of X axis (p_x) and the direction of Y axis (p_y) is 10. By substituting the level in the soil of roughness we get Figure 2.

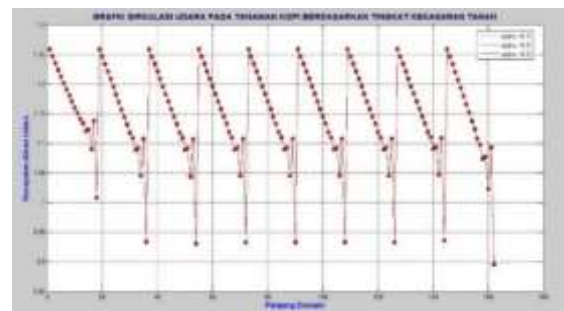


Fig.2: The air circulation on coffee plantation with different level of soil roughness by MATLAB

It is shown in Figure2(a) that the initial velocity of 1,2m/s gives the value of air circulation 1,26m/s at the first point. The air velocity has almost the same value at the point of the 19th, 37th, 55th, 73th, 91th, 109th, 127th, and145th,because the points are located on the front rows of coffee plantation and cropping pattern. In the point 1st to point 18ththe figure decrease and increase at the point 19th.In discretization, point 1st lies in the front row of coffee plantation so the air velocity is almost equal to the initial velocity of the air source. Then point 18th lies in the back rows of the coffee plantation, so the air velocity is smaller than the point 1st.There exist a difference between air velocity in front rows and back rows, it is due to the existence of coffee plants in between. However, the air velocity is quite stable, so the pollination can process properly. The same situation also occurs at the point of 19thto 36th, point 37th to 54th, and so on.

Figure2(a) shows three different simulation figure showing the air circulation with three level of soil roughness values, namely 0,1; 0,5; and 0,9. By enlarging the figure we get Figure 2(b).At the point 85th, the air velocity of the soil roughness level of (respectively0,1; 0,5; 0,9) is respectively1,1096 m/s; 1,10983 m/s; 1,10986 m/s. Figure 2 show sthat the higher the soil roughness, the faster velocity of air circulation of coffee plantation.

The FLUENT simulations shows the air circulation of coffee plantation on each level of soil roughness. The simulations is done twice yielding two different figures. The first simulation was conducted to determine air circulation coffee plantation based on cropping pattern namely triangular grid and shackle of wheel graphs.

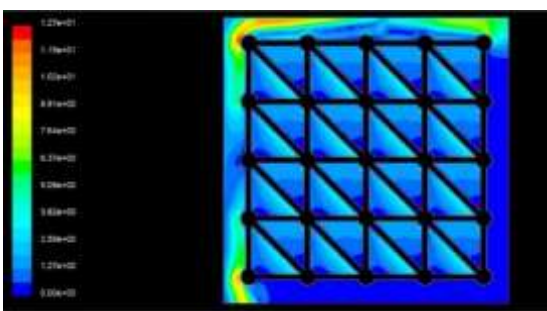


Fig.3: The air circulation on coffee plantationbased on cropping patterns of triangular grid graph

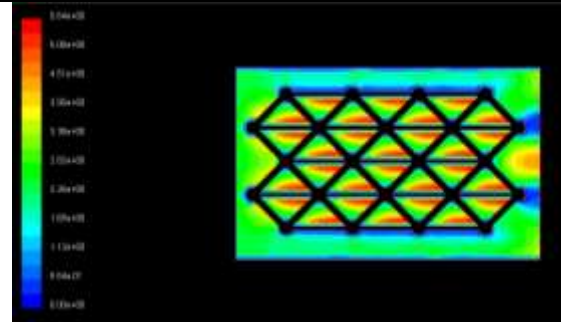


Fig.4: The air circulation on coffee plantationbased on cropping patterns of shackle of wheel graph

The first simulation usesan initial air velocity of 1 m/s. The simulation results isshown in Figure 3. It tell us that the air circulation in the front row of coffee plantation give a high air velocity of between 3 m/s - 5 m/s. But getting into the middleof plantation the air circulation tends to be reduced and stable. The velocity of air circulation has a velocity range between 0,6 m/s until 2 m/s. This indicates that the air velocity in front side of the plantation areas is higher thanthe other side. So we need protection plants.



(a)



(b)

Fig.5: The air circulation on coffee plantationwith the level of soil roughness

The second simulation was conducted to determine the effect of soil roughness on the air circulation in the coffee plantation. The initial velocity of air used is 1 m/s. The simulation results isshown in Figure 5. Figure 5(a) shows the velocity of air circulation coffee plantation

with a large level of soil roughness of 0,9 is 2 m/s to 10 m/s, even reaches 20 m/s. It endangers the coffee plantation as the higher the air circulation cause a bad pollination of coffee plantation. It also cause many coffee plants flowers are falling down. So the productivity of coffee bean will be low. Figure 5(b) shows the velocity of air circulation coffee plantation with a low level of soil roughness of 0,1 is 0,5 m/s to 10 m/s. The lower the air circulation give a good pollination of coffee plantation, then it will gain a good productivity of coffee beans.

The velocity a average of air circulation of coffee plantation taken from coffee field is 1,27m/s. while the a average of air velocity of simulation results on the first rows is 1,25927m/s. It shown that the simulation is relatively accurate. The error and relative error values is respectively 0,01073 and 0,85%.

IV. CONCLUSIONS

It can be concluded that the level of soil roughness affect to the air circulation of coffee plantation. The higher the level of soil roughness the higher air circulation of coffee plantation. The crops planting pattern of triangular grid and shackle of wheel graphs give a better air circulation process in the coffee bean plantation. A cropping pattern in a plantation area of low air circulation velocity, the soil roughness level should be high to have good air circulation. In this research we do not involve a protection tree. It will be more challenging if it is also considered a protection tree with a different cropping patterns for further research. Apart from this, the other researcher can study the effect of the humidity and soil of slope to the air circulation of coffee plantation.

REFERENCES

- [1] Anonymous. 1984. *Coffee*. A center of Education, Training, Counseling, Jakarta, Indonesia.
- [2] Kindangen. 2005. *The Investigation of Air Flow Pattern of skyscraper Building of the constrain of Front and Back Burrier of the building*. Science Journal, Vol. 11 Issue 4, p20-31.
- [3] Muhidong, J., Mursalim, & Rahman, A. 2013. *The effect of air flow rate on single-layer drying characteristics of Arabica coffee*, International Food Research Journal, October 2013, Vol. 20 Issue 4, p1633.
- [4] Najiyati, S. dan Danarti. 2001. *Coffee, Plant Copping, Post Harvest Management*. XI Edition. Penebar Swadaya, Jakarta, Indonesia
- [5] Nilnont, W. dkk. 2012. *Finite element simulation for coffee (Coffea arabica) drying 269,* Food & Bioproducts Processing: Transactions of the Institution o, April 2012, Vol. 90 Issue 2, p341.
- [6] Streeter, V. L. & Wylie, E. B. 1986. *Fluid Mechanic*. (Eight Edition). Jakarta: Erlangga, Indonesia.
- [7] Versteeg, H. K. & Malalasekera, W. 1995. *An Introduction to Computational Fluid Dynamics : The Finite Volume Method*. Loughborough: Longman Scientific & Technical.
- [8] White, F. M. 1994, *Fluid Mechanic*. (Eight Edition). Jakarta: Erlangga, Indonesia.

Seismic Study at Subba Oil Field Applying Seismic Velocity Analysis

Nawal Abed Al-Ridha¹, Zahraa Shakir Jassim²

Department of Geology, College of Science, University of Baghdad, Baghdad. Iraq

Abstract— This research is seismic interpretation of two-dimensional seismic data from oil exploration company in Subba oil field. The field data process for the purpose of interpretation, synthetic seismogram was done for the well (Su-7) by using the sonic log and seismic velocity, where the seismic reflectors were picked up (Nhr Umr, Shuaiba, Zubair and Ratawi). Time and depth maps were prepared, showing convex structure with a north-south axis in the center of the study area, with two main dome at northern and southern of the study area. Velocity model from which velocity maps (Average velocity, and interval velocity) were drawn. Seismic inversion technique is used to shows the units within Formations and delineate the increase or decrease of porosity in the Nhr Umr and Zubair Formations.

Keywords— Velocity analysis, Seismic attribute, Subba oil field.

I. INTRODUCTION

The geophysical techniques that most widely employed for exploration are the seismic, gravity, magnetic, electric, and electromagnetic methods. Less common method involves the measurement of radioactivity and temperature at or near the Earth's surface and in the air [1]. The reflection method is depending on the study of the elastic waves reflected from the interface between two geological layers. The reflection method is used exclusively for petroleum prospecting; it is more suitable in areas where the oil is in structural traps, but also it is useful for locating and detailing certain types of stratigraphic features [2], reflection technique measures the arrival time of seismic wave to travel from a source at the Earth's surface down into the ground where it's reflected back to a receiver which is located near the surface. The seismic wave can be generated on the ground by a near-surface explosion of dynamite, weight dropping and vibrate [3]. The studied area is located south Iraq between provinces of Basra, Dhi Qar and AlMuthanna, as shown in Figure (1). The aim of this research is using velocity model and maps (vertical and horizontal average velocity slices) to show variation of seismic velocities, acoustic impedance and total porosity for Nahr Umr and Zubair Formations.



Fig.1: Location map of study Area (Subba field)

II. DATA PROCESSING

Geophysical data processing is the use of computers for the analysis of geophysical data. a major task in geophysics is to determine as much as possible about the constitution of the interior of the earth, [4]. we will explain how to obtain the field data used and how to process this data.

Processing steps:

1. Reformat applications: Field data are recorded in a multiplexed mode using a certain type of format [5].
2. Geometry update: is an update of the field records received from seismic teams in the field by sps file containing the information recorded in the field such as the values of (x , y , elevation and location ...).
3. Static up date: is a correction of the delayed waves. and eliminates the effect of differences in earth's surface- level elevations.
4. Gain applications: is a time-variant scaling in which the scaling function is based on a desired criterion
5. Noise attenuation: is classified into two categories, random noise and coherent noise [6], as shown in Figure (2).

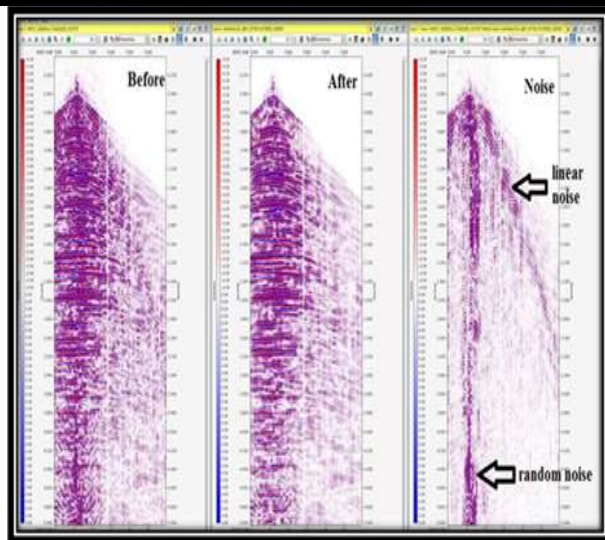


Fig.2: types of noise

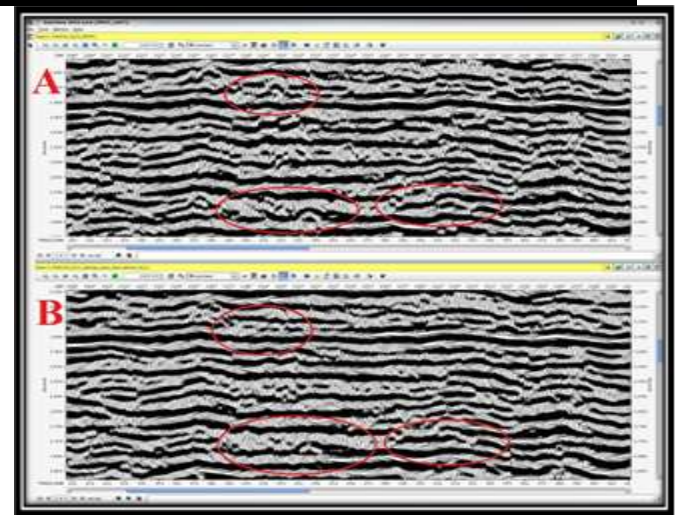


Fig.3: seismic section stack, A) old pick, B) new pick, showing the changes in many places

6. Deconvolution: is aimed at improving temporal resolution by compressing the effective source wavelet contained in the seismic trace to a spike (spiking deconvolution).
7. Common - midpoint (CMP) Sorting: is the most important data-processing application in improving data quality. The principles involved have already been discussed along with the field procedures used to acquire the data, [7].
8. Normal-moveout correction: the velocity field is used in normal moveout (NMO) correction of CMP gathers, based on the assumption that, in a CMP gather reflection travel times as a function of offset follow hyperbolic trajectories, the process of NMO correction removes the moveout effect on travel times, [8].
9. Residual statics corrections: is one additional step in conventional processing of land and shallow-water seismic data before stacking [9].
10. Stacking: is one of the most advanced stages in the treatment of seismic data, It aims primarily at improving the quality of these data, Stacking depends heavily on velocity derived from velocity analyzes, It is applied after the procedures of the NMO corrections, for best seismic sections, as shown in Figures (3)
11. Velocity analysis: normal moveout is the basis for determining velocities from seismic data. Computed velocities can in turn be used to correct for NMO so that reflections are aligned in the traces of a CMP gather before stacking, as shown in Figure (5)

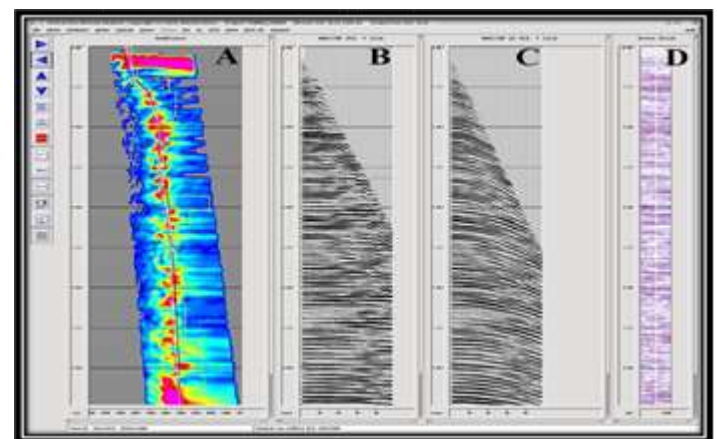


Fig.4: A) Semblance panel, B) NMO-Corrected gather, the wave field is flat, C) Un-corrected gather, D) The area of stack to define the velocity.

III. SYNTHETIC SEISMOGRAM

The subsurface mapping and enhanced by the correlation of seismic data with borehole data using the synthetic seismogram, explain synthetic seismogram for well Su-7 where the density log, sonic log and check shot, as shown in Figure (5)

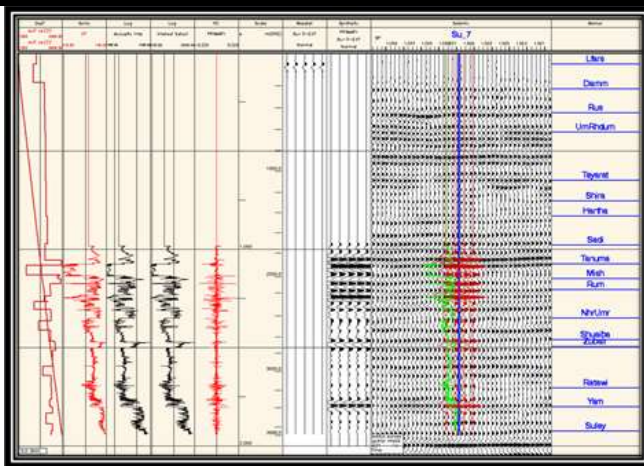


Fig.5: Synthetic seismogram

IV. TWO WAY TIME (TWT) MAP

(TWT) map have been constructed from the picked horizons Nahr Umr and Zubair Formations with contour interval (20 msec).

The TWT values of Nahr Umr Formation are increasing in the direction of the north-east and decreasing in the south-west. at the south of subba field have small structure at Su-8 well, and Zubair Formation shown structure in the north part of study area, as shown in Figures (6),(7)

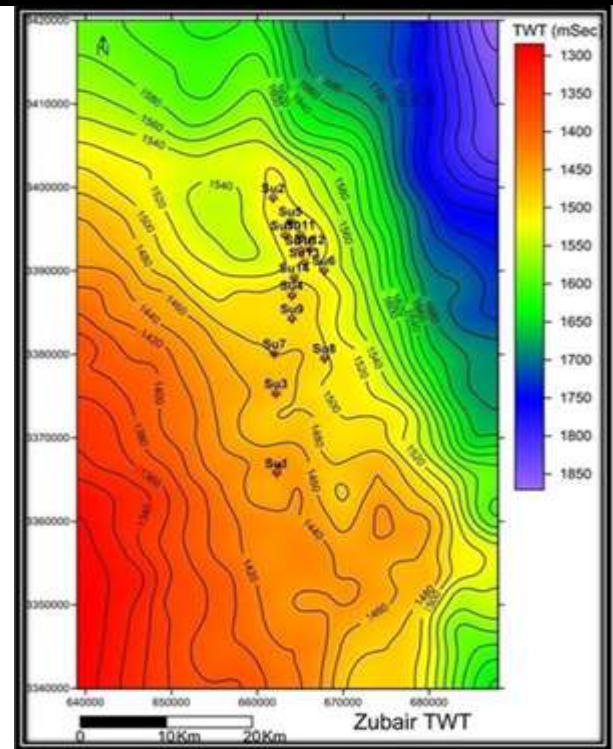


Fig.7: Two way time maps of Zubair Formation

V. VELOCITY MODEL

Velocity models are key components of seismic imaging, and consequently, to reservoir description and geo mechanical analysis.

Velocity model has been created by inserting surfaces which were picked in time domain and well tops of Nahr Umr, and Zubair horizons, the average velocity model explain the change toward the basin, the velocity decrease to north-east and increase to the south-west of the field, as shown in Figure (8).

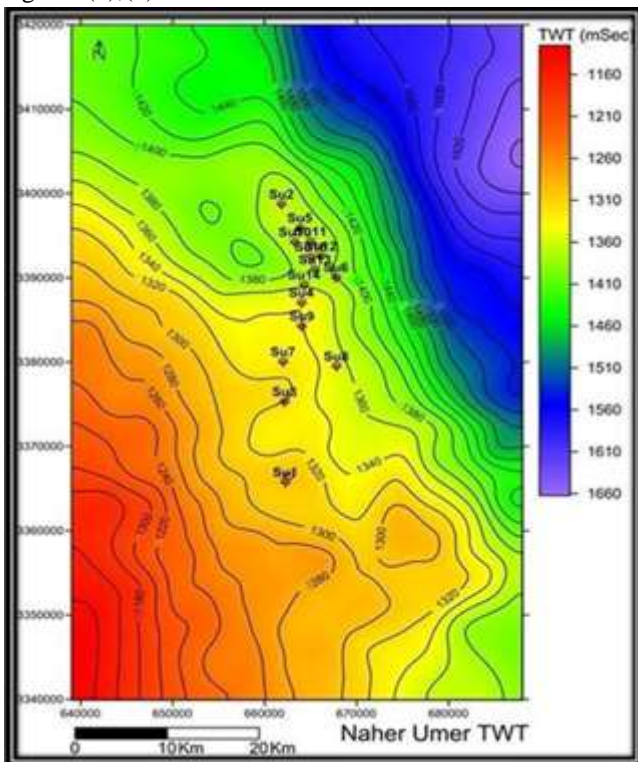


Fig.6: Two way time maps of Nahr Umr formation

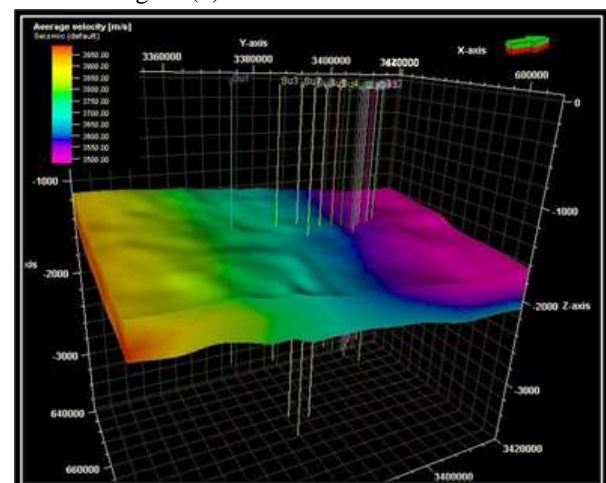


Fig.8: Velocity model of NahrUmr and Zubair Formation

VI. VERTICAL AVERAGE VELOCITY SLICES

-In line slice:

The average velocity values decrease at the top of the Nahr Umr Formation to the east at well Su-8, and low of the average velocity values in Zubair Formation to the same direction, the increase of values at the bottom of the Ratawi Formation, as shown in Figure (9).

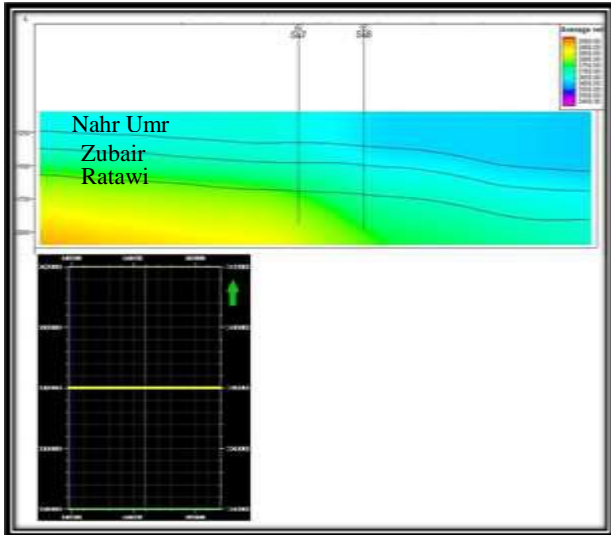


Fig.9: Vertical average velocity slices (In line slice)

-Cross line slice:

The cross line slice explain the lateral changes along of the field shown the average velocity values decrease at the top of the Nahr Umr to the north-east part especially at wells Su-5 and Su-10 and continue low velocity zone in Top Zubair and Ratawi Formation in same direction, as shown in Figure (10).

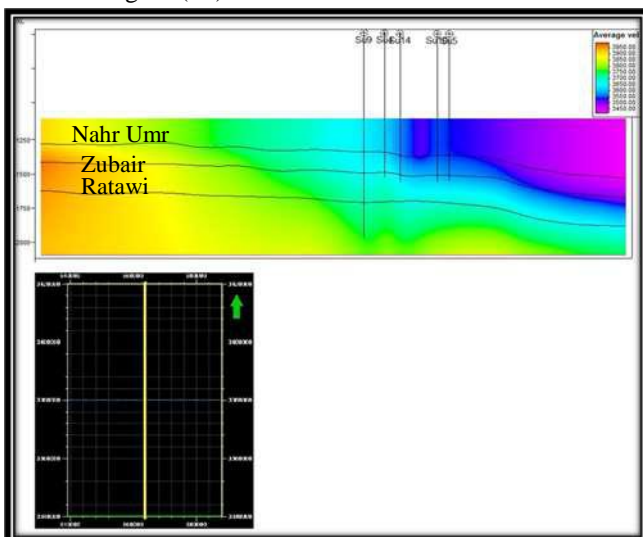


Fig.10: Vertical average velocity slices (Cross line slice)

VII. Horizontal average velocity slice

Horizontal average velocity slice decrease toward the north-east part of the field, and low average velocity

appears at boreholes area, and the velocity values increase toward south-west, as shown in Figure (11).

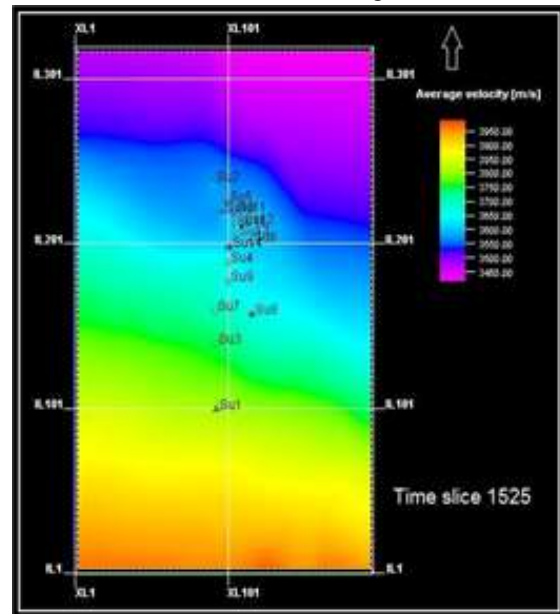


Fig.11: Horizontal average velocity slice

VIII. VELOCITY MAPS

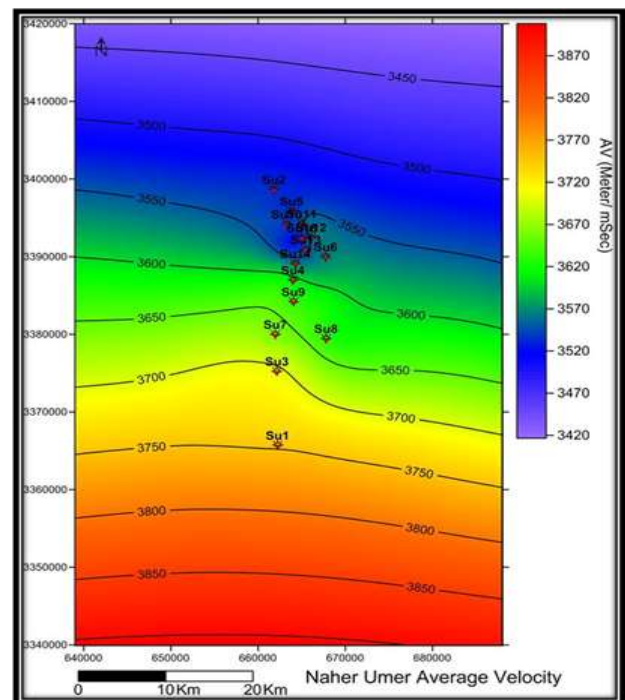


Fig. 12: Average velocity map of Nahr Umr Formation

1. Average velocity map:

It's obtained from dividing the total distance travelled by the wave by the time spent in [10]. The average velocity maps of Nahr Umr and Zubair Formations explain the increase and decrease in velocity, of Nahr Umr Formation map the values are ranged from 3420 to 3870 m/s, having closure average velocity in contour value 3550 m/s to the north of field, where most of the oil wells were drilled.

The average velocity increase in velocity values in the southern part and a decrease in the northern part, and Zubair Formation the average velocity values are ranged from 3500 to 3950 m/s, having closure average velocity in contour value 3580 m/s to the north of field, as shown in Figures (12),(13)

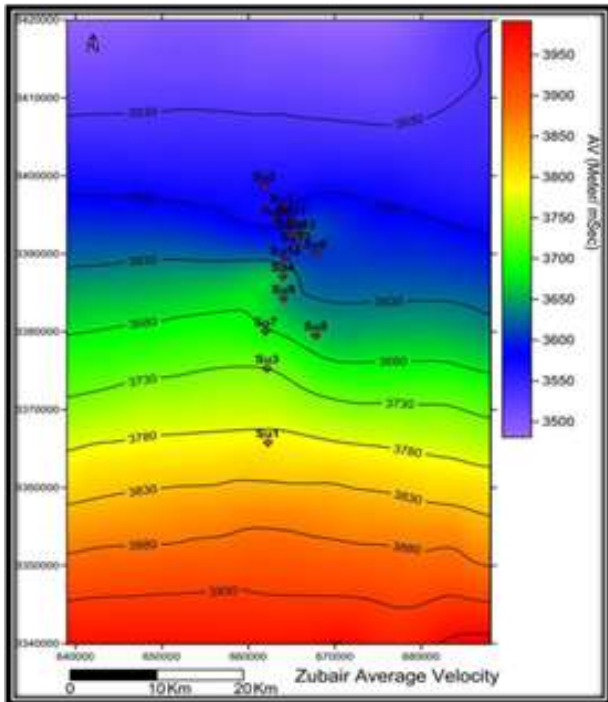


Fig. 13: Average velocity map of Zubair Formation

2. RMS velocity map:

Is defined as the square root of the average, can be calculated from the interval velocity data [10].

The RMS velocity maps extracted from processing data, Nahr Umr Formation map, the values are ranged from 3450 to 4350 m/s, having many closures to the north of the field, between contour values (3400-4000 m/s), when the oil wells were drilled, the velocity values decrease to the north-east part and increase to the south-west part, and Zubair Formation map explain the values range from 3550 to 4350 m/s, shown many closure of cantor interval in center field, between contour values (3500-4100 m/s), and having many smaller closure distributed to the south of field, as shown in Figures (14),(15).

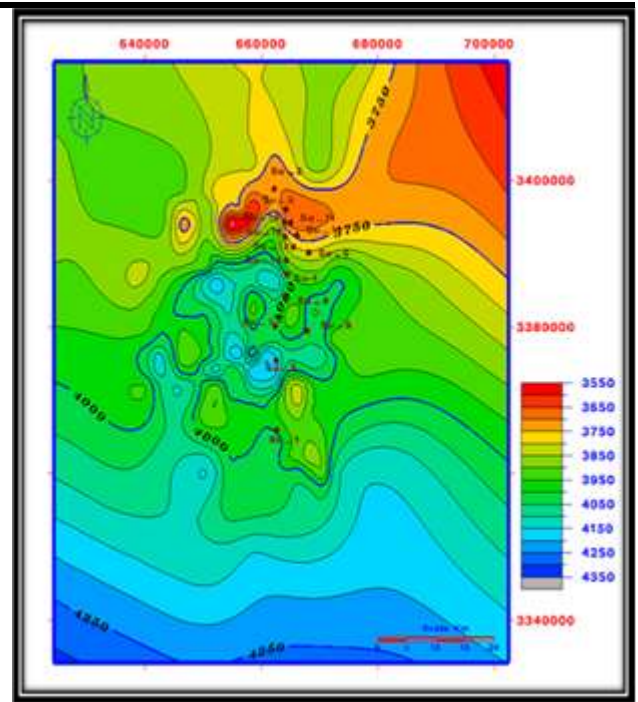


Fig. 14: RMS velocity map of Nahr Umr Formation

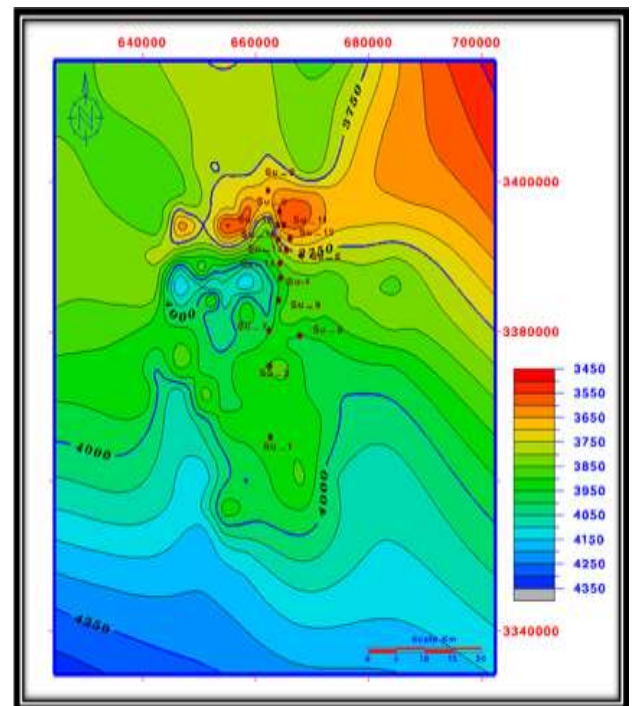


Fig. 15: RMS velocity map of Zubair Formation

IX. DEPTH MAPS

Depth estimation can be done via a wide range of existing methods, but which can be separated into two broad categories (direct time-depth conversion and velocity modeling for time-depth conversion), [11].

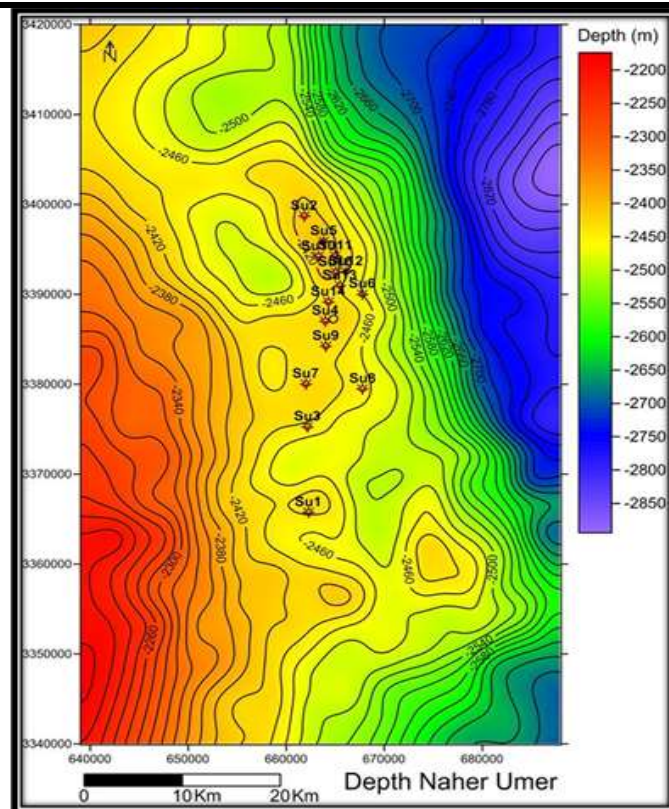


Fig. 16: Depth map of Nahr Umr Formation

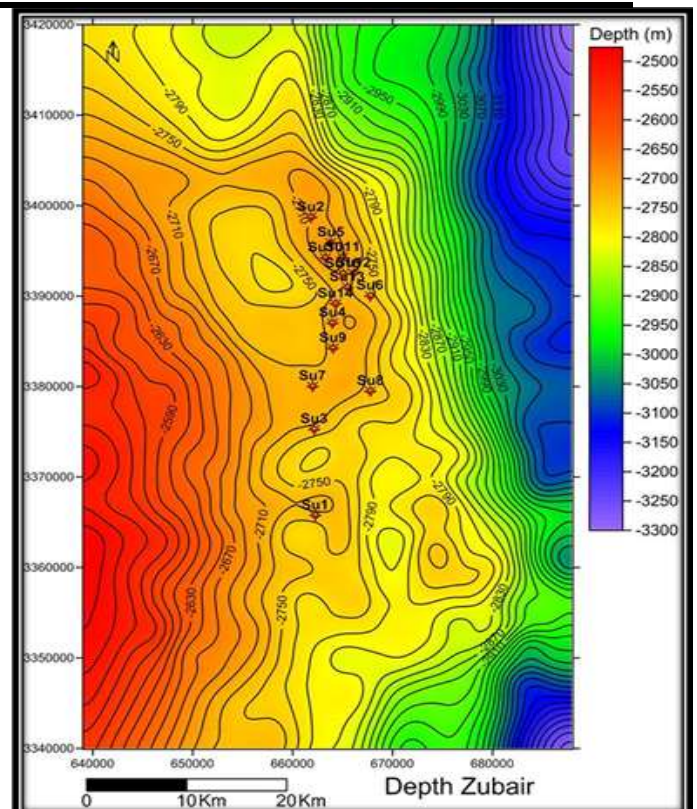


Fig. 17: Depth map of Zubair Formation

Nahr Umr Formation map explain the depth increasing to the north-east part a depth of 2850 m, and the depth is reduced toward the crest of the structure reaching a value of 2450m near wells drilling, and depth map of Zubair Formation is Match description to Nahr Umr depth map, where the depth increasing to the north-east part a depth of 3300 m, and the depth decrease toward the south-west reaching to 2500 m, as shown in Figures (16),(17)

X. ISPACH MAP

Isopach maps constructed by subtracting the depth value of two different horizons at each shot point, [12]. Thickness map of Nahr Umr Formation represent the interval limited between top of Nahr Umr and the top of Zubair using a contour interval of 5m. This map shows the increasing in thickness to the south-west, and south part of the area where a maximum thickness of 263m, and the thickness decreases towards the north-east of the area reaching a value of 203m, Thickness map of Zubair Formation is the interval limited between top of Zubair and the top of Ratawi using a contour interval of 10 m. and the thickness decreases to the south of the area reaching a value of 438 m, and the increasing in thickness to the north, where a maximum thickness of 478m to the north, as shown in Figures (18),(19).

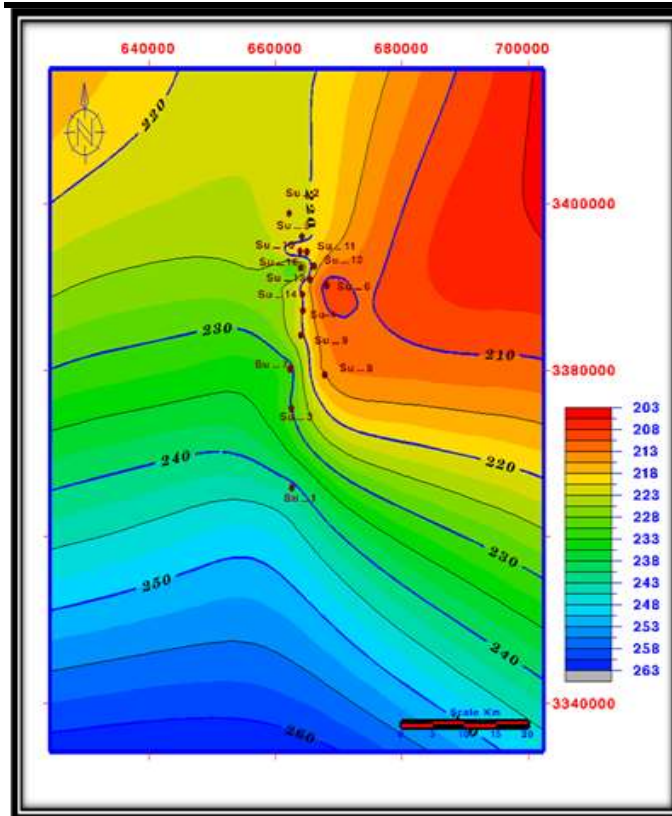


Fig. 18: Thickness map of Nahr Umr Formation

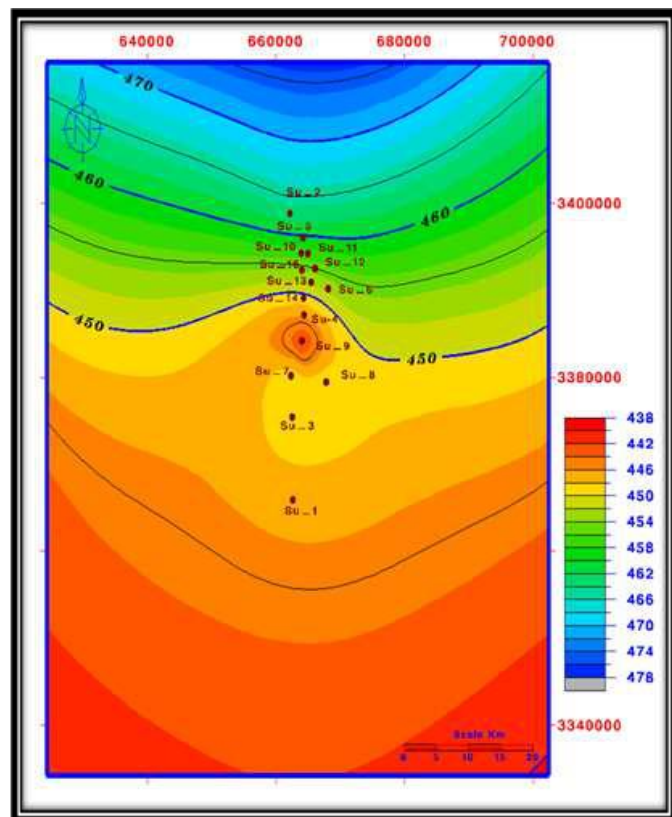


Fig. 19: Thickness map of Zubair Formation

XI. SEISMIC INVERSION

The seismic inversion is applied on the line SI-21 and well Su-7, the result shows the low acoustic impedance in green color show high porosity, and the violet color is high acoustic impedance show low porosity. The inversion section show the Nahr Umr reservoir divided into three units and separate by one cap rock, and Zubair reservoir divided into nine units and separate by four cap rocks, as shown in Figure (20).

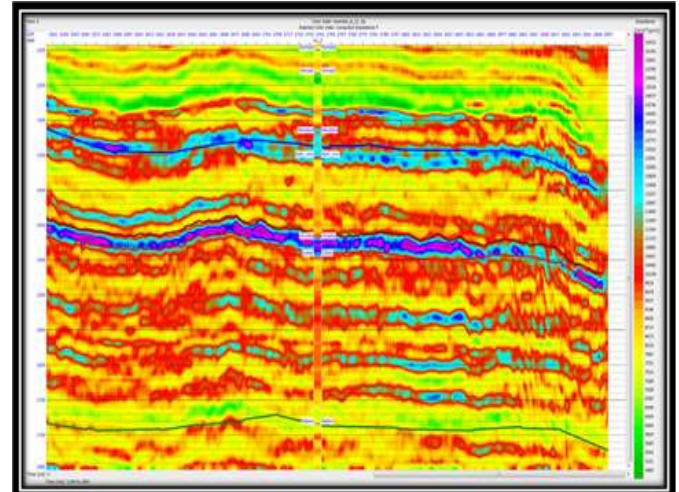


Fig.20: Seismic inversion section

The relationship between acoustic impedance and porosity, as shown in Figure (21), where the increased porosity to the Nahr Umr and Zubair Formations with decreased in acoustic impedance, and the porosity decreased when there is cap rock.

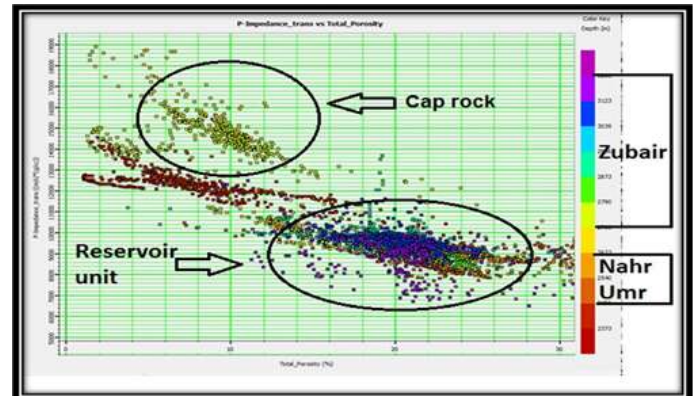


Fig.21: Cross plot show the relationship between acoustic impedance and total porosity

XII. CONCLUSIONS

1. Seismic information indicates of that the area is not affected by the fault system.
2. Time and depth maps explain the dipping of the horizons to the south of field, and have high structure to the north of field in drilling wells .
3. The average velocity maps of the Nahr Umr and Zubair Formations are provided by using velocity

- models. These maps show a decrease of average velocity in the north part which due to the high porosity and increases in the south part direction for Nahr Umr and Formations, The average velocity values affected by thickness and porosity .
4. RMS velocity of Nahr Umr and Zubair Formations contain many closures in the central field.
 5. Isopach maps explain Nahr Umr reflector was increase in thickness in the south and decrease in the north, Zubair reflector: Increase in thickness in the north and decrease in the south.
 6. Seismic inversion process was used to deduce the reservoir units and total porosity, Nahr Umr reservoir as shown divided to three units, and Zubair reservoir divided into nine units and increasing of the total porosity when the acoustic impedance decreasing.

ACKNOWLEDGEMENTS

Praise is to Allah who guided us and prayer and peace be upon the messenger of Allah Muhammad bin Abdu Aullah.

I would like to express my appreciation and deep gratitude to my supervisor, Prof. Dr. Nawal Abed Al-Ridha , for her unwavering support ,collegiality and encouragement at all stages of this work.

The researcher is grateful to the Department of Geology at the University of Baghdad for providing opportunities and facilities for the completion of this research.

I am so grateful to the Oil Exploration Company and its managers for providing me all the facilities and information that helped me in performing this research., especially to Mr. Jameel R. Kamoona , Mr. Muthana Dawood, Miss. Ryhab Fadl Mahde, Mr. Suhail Ubaid Muhsin, Mr. Salar Hasan, Mr. Amar Ahmed Jabir, Mr. Mohammed Hashim Jiter, and Mr. Muhnd Ahsan .

Also, I present my greatest thanks and gratitude to everyone in my family for their encouragement and support .

REFERENCES

- [1] Dobrin, M. B. and Savit, C. H., 1988: Introduction to geophysical prospecting, 4th ed, McGraw-Hill public., New York ,730 p.
- [2] Al-Sinawi, 1981: Introduction to Applied Geophysics, first ed., 142p.
- [3] Dobrin, M. B., 1960: Introduction to geophysical prospecting, 2nd ed McGraw– Hill. Int. co., International Student Edition, 446p.
- [4] Claerbout, J. F., 1985: Fundamentals of Geophysical Data Processing with applications to petroleum prospecting, Department of Geophysics, Stanford University, 266 p.

- [5] Yilmaz, O., 1987: Seismic data processing, SEG series: Investigation Geophysics, V.2, 526 p.
- [6] Sengbush, R.L., 1983: Seismic exploration methods: Internat. Human Res. Dev. Corp., Boston.
- [7] Sheriff, R.E. and Geldart, L.P. 1995: Exploration Seismology, 2nd edition. New York: Cambridge University Press. 592 P .
- [8] Mayne, W. H., 1962: Common-reflection-point horizontal data stacking techniques: Geophysics, 27, 927-938.
- [9] Taner, M. T., Koehler, F., and Alhilali, K. A., 1974: Estimation and correction of near- surfaceTime anomalies: Geophysics, 41, 441-463.
- [10] Alsadi H. N., 2017: Seismic Hydrocarbon Exploration 2D and 3D Techniques, Advances in Oil and Gas Exploration & Production. Baghdad: Data Processing Section Ministry of Oil. 331 P.
- [11] Etris, E. L., Crabtree, N. J., and Dewar, J., 2001: True Depth Conversion, Canada Society of Exploration Geophysicists, pp. 11-22.
- [12] McQuillin, R., Bacon, M, and Barclay, W., 1984: An Introduction to Seismic Interpretation, Graham and Trotman, 287p.

Peculiarities of a Colloidal Polysaccharide of Newly Isolated Iron Oxidizing Bacteria in Armenia

Levon Markosyan^{1,*}, Hamlet Badalyan², Arevik Vardanyan¹, Narine Vardanyan¹

¹Institute of Microbiology of SPC "Armbiotechnology" of the NAS of Armenia, Yerevan, 0056, Armenia

²Physical Ecology Laboratory of the Yerevan State University, Yerevan, 0025, Armenia

Abstract—Microorganisms belonging to different systematic and physiological groups produce various intra- and extracellular polysaccharides, which both play an important role in the life of microorganisms and have great practical application. Iron and sulfur oxidizing bacteria produce capsular (EPS) and colloidal polysaccharides. At present the properties and functional role of EPS are well studied. However, the properties of the colloidal polysaccharides produced by iron oxidizing bacteria have not been sufficiently explored. A new iron oxidizing bacteria *Leptospirillum ferriphilum* CC was isolated from sulfide ores of Armenia. Its morphological and physiological features have been studied. A colloidal polysaccharide has been isolated with the use of an original method developed by the authors, and its physical and chemical properties have been studied. It has been shown that the colloidal polysaccharide consists of three different monomers- glucose, fructose, mannose.. Investigations with a complex method of optical polarization microscopy and analytical programs allowed determining the size, shape change, perimeter, degree of hydration and crystallization at 0.07% and 0.04% of polysaccharide concentration. It was shown that the size of a polysaccharide colloidal particle does not much depend on polysaccharide concentration, however, the number of identical colloidal formations is dependent on the concentration of polysaccharide.

Keywords— cell morphology; colloidal polysaccharide; iron oxidizing bacteria.

I. INTRODUCTION

Microorganisms, like eukaryotes and prokaryotes produce polysaccharides, with different biological, chemical, physical properties and functional activity. Iron and sulfur oxidizing chemolithotrophic bacteria produce intra- and exopolysaccharides. The properties of the intracellular polysaccharides - lipopolysaccharides (LPS) of iron and sulfur oxidizing bacteria have been studied. It was revealed that the inter-specific diversity as well as the conditions of cultivation and sources of energy define various properties

of LPS [1-7]. Generally the exopolysaccharides produced by the above-mentioned bacteria are subdivided into capsular and soluble/colloidal forms. Extensive research undertaken in the past decades has been focused on understanding the properties of the exopolysaccharides contained in the extracellular substances (EPS) including *Acidithiobacillus ferrooxidans*, *Leptospirillum ferriphilum*, *Leptospirillum ferrooxidans* and formig a capsule around the bacterial cell. EPS play an essential role for the formation of a biofilm, which mediates adhesion of cells to the minerals surface and form a cohesive three-dimensional polymer interconnecting and immobilizing cells in the process of bioleaching by iron and sulfur-oxidizing bacteria. An important role of capsular polysaccharides as a fundamental structural element of the EPS, determining the mechanical stability of biofilm was disclosed [8-12].

However, the properties of colloidal polysaccharides produced by iron and sulfur oxidizing chemolithotrophic bacteria remains understudied. The objective of the present study is to investigate the properties of a colloidal polysaccharide of the iron oxidizing chemolithotrophic bacteria *Leptospirillum ferriphilum* CC newly isolated in Armenia.

II. MATERIALS AND METHODS

Bacterial culture and media. The *Leptospirillum ferriphilum* CC was isolated from natural biotopes of sulfide ores in Armenia. Cultivation was carried out in 9K liquid medium with ferrous iron as a sources of energy at 37°C for 5-7 days.

Identification of strain. The isolated strain was identified both by morphological, physiological properties [14] and by the sequencing of 16S rRNA. The primary analysis of the data was carried out using the BLAST program. The phylogenetic tree was constructed with the help of MEGA 6.06 and neighbor-joining, and boot star programs.

Isolation of colloidal polysaccharide. The colloidal polysaccharide produced by *L. ferriphilum* has been

isolated according to the method developed by the authors. The isolation protocol is summarized in Fig 3.

Determination of the chemical composition of the colloidal polysaccharide. Chemical composition of the colloidal polysaccharide was analyzed after hydrolysis by 2 N HCl at 100°C for 2 hours by high performance liquid chromatography (HPLC) on the Shimidzu 2010 C analyzer, column ULTKON , P5-80-H 2 x 250 mm, the mobile phase – 0.1 mM acetat buffer/acetonitril-1:5, pH 5.8, flow rate 1ml/min. Measurements were made by RI.

Properties of colloidal formation. Properties of colloidal formation of polysaccharide were studied by a complex method combining optical polarization microscopy and analytical programs LobViEW15 and WOVA [15, 16].

III. RESULTS AND DISCUSSION

Investigations of morphological properties of the isolated iron oxidizing bacteria by light and optical polarization microscopy and analytical programs disclosed that the cells of the their area is 7033 μm , the length is 125 μm , perimeter is 462 μm and the shape of the cells is 0.0392. The observed scatter of the morphological parameters of *L. ferriphilum* is due to the non-synchronous growth of culture in the population (Fig.1,Tabl. 2).

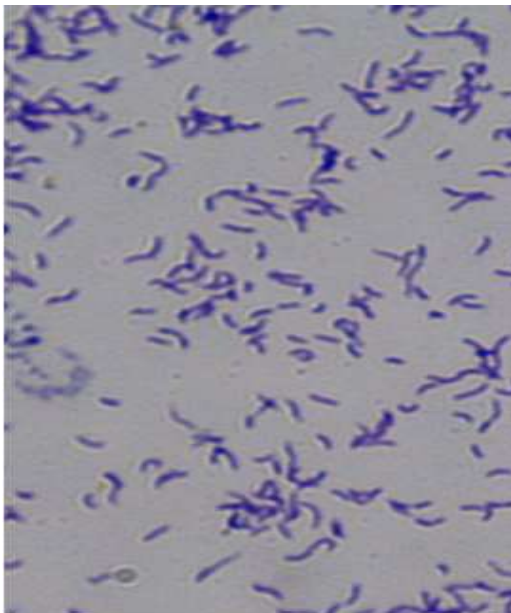


Fig.1: Microphotography of *L. ferriphilum* the investigated bacteria have a curve rod- shape,

Based on the morphological and physiological characteristics, as well as on the sequence of nucleotides in 16SrRNA, the isolated strain was identified as *L. ferriphilum* CC (Fig. 2). The strain was deposited at the Republican Center for the Deposition of Microorganisms, Armenia, MDC 7047. The results of sequencing are included in the data base of Geen Bank.

Table.1: Phenotypic characteristics of *L. ferriphilum* CC

Unit	Area	Average Size	Length	Perimeter	
	μm^2	μm	μm	μm	α
Average	7033.052	82.356	125.743	462.21	0.03292
SD	2469.569	15.824	17.899	93.828	
1	9438	97.149	137.693	521	0.03477
2	6860	82.825	119.406	500	0.02744
3	8182	90.454	125.342	445	0.041318
4	5977	77.311	125.907	443	0.030456
5	8952	94.615	149.862	602	0.024702
6	7044	83.928	114.885	420	0.039932
7	9320	96.54	132.468	467	0.042735
8	5361	73.218	125.02	395	0.03436
9	1946	44.113	86.44	280	0.024821
10	10984	104.804	149.862	647	0.026239
11	4095	63.992	98.943	333	0.036929
12	10017	100.084	140.789	531	0.035526
13	6534	80.833	115.542	470	0.029579
14	7953	89.179	135.714	604	0.0218
15	7183	84.752	130.189	448	0.035789
16	4414	66.437	115.982	392	0.028725
17	3450	58.736	94.509	321	0.033482
18	5279	72.656	141.431	458	0.025166
19	10639	103.145	149.141	505	0.041717

α - shows the shape of the bacterial cells, as determined by the formula

$\alpha = S/P^2$, where S is the area, P is the perimeter of cells. The value of α less than 0.06 means that the investigated object is rod-shaped.



Fig. 2: Dendrogram of *Leptospirillum ferriphilum* CC

Previously, we have studied the peculiarities of bioleaching of sulfide minerals by the above-mentioned bacteria, the adhesion on the surface of the mineral, the capsular EPS and the properties of immobilized cells on natural carriers [11, 18-21]. In continuation of these studies, we set out to study the characteristics of the colloidal polysaccharide produced by *L. ferriphilum*.

Isolation and chemical composition of the colloidal polysaccharide. *L. ferriphilum* was cultivated in a reactor in a Macintosh medium [22], under aeration and stirring for 120 hours. Then, after harvesting the biomass by centrifugation ferrous sulfate was precipitated from the

solution by addition of NaOH up to pH 7.5-8.0. After removal of pellets by centrifugation, the centrifugate was concentrated to 15-20% of the initial volume at 40°C in a rotary evaporator. The polysaccharide was precipitated with ethanol (1:3v/v). The precipitate of polysaccharide was dissolved in 50 ml of distilled water and then the traces of proteins were removed and the solution was desalted by adsorption and gel chromatography using columns with ToyoPerl 650 M and Sephadex G25, respectively. The polysaccharide was then re-precipitated with ethanol and dried at 25-30°C in vacuum (Fig. 3).

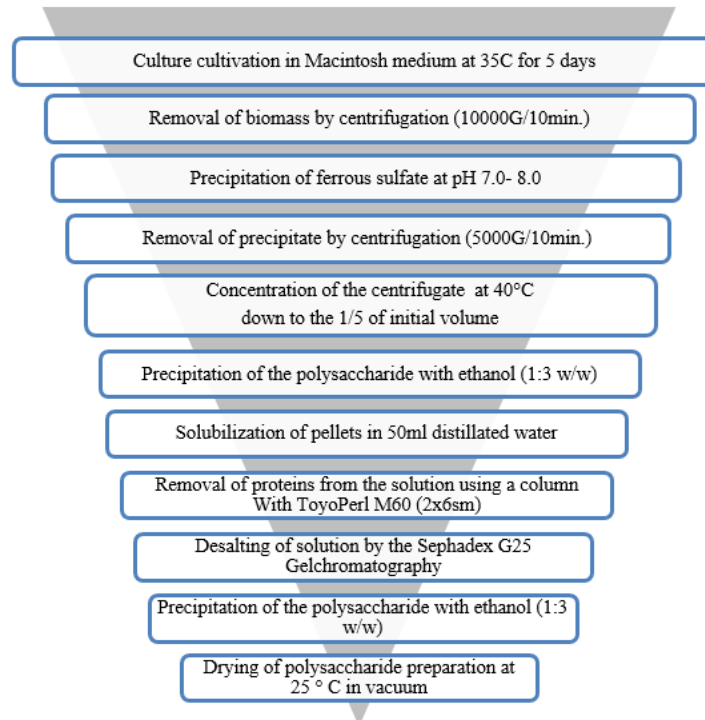


Fig.3: General procedure for isolation of colloidal polysaccharide

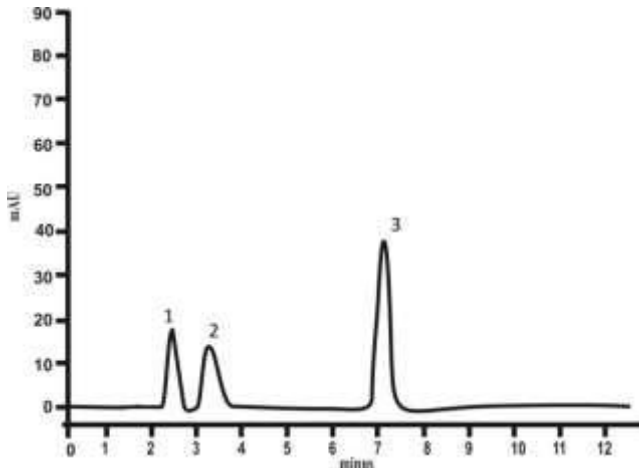


Fig.4: Chromatogram (HPLC) of chemical composition of colloidal polysaccharide of *L. ferriphilum* CC (1 - glucose, 2 - fructose, 3 - mannose)

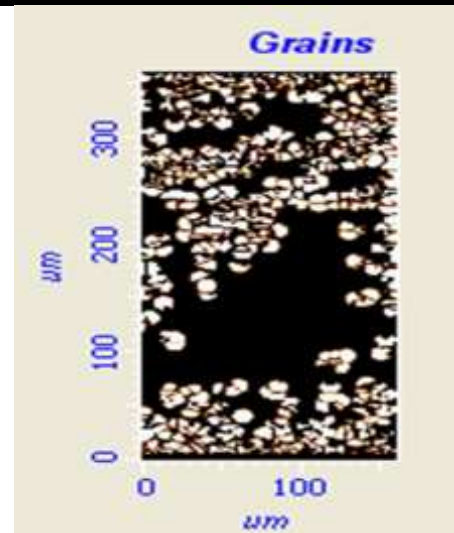


Fig. 5: Microphotography of colloidal formations at the concentration of the polysaccharide in solution of 0.07%.

Studies of the chemical composition of isolated colloidal polysaccharides show the presence of various monomers (Fig. 4).

The physico-chemical properties of the isolated exopolysaccharide were also studied with a complex method developed by the authors and based on optical polarization microscopy (MEIJI) as well as the analytical programs LabVIEW-15 and WISION [15,16]. The obtained results of microscopy studies were transformed in accordance with the NOVA program, which allows identifying the size, shape changes, the degree of hydration, and the crystallization of colloidal formations of the exopolysaccharide in solution.

It was shown that at 0.07% concentration of the polysaccharide the dimensions, average area, shape and perimeters of the colloidal particles are 19773, 0.079 and 14, 077 μ m respectively (Fig. 5, 6, Tab.2). It has also been explained that the degree of crystallization of colloidal formations is 82.79 (Fig. 7).

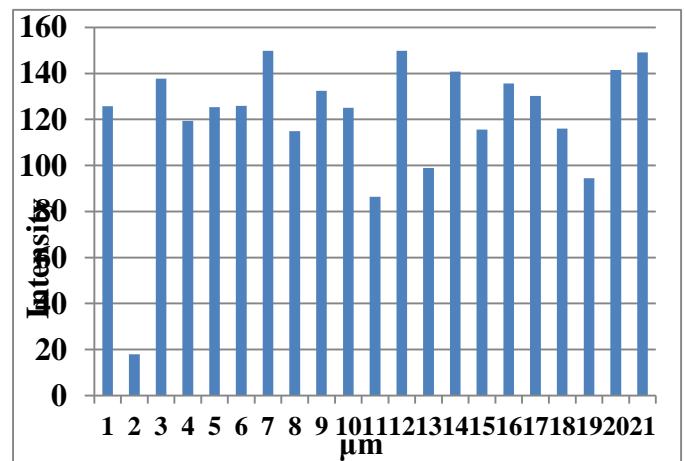


Fig. 6: Histogram of the sizes of colloidal formations obtained as a result of processing of microscopy at the sugar concentration of 0.07%

Table 2. The average of the size, area, perimeter and forms of colloidal formations at the polysaccharide concentration 0.07%

	Area	Average S	Peremeter	α
Unit	um*um	um	um	
Average	19.893	4.028	14.9777	0.088685
SD	17.586	1.913	9.867	0.180736

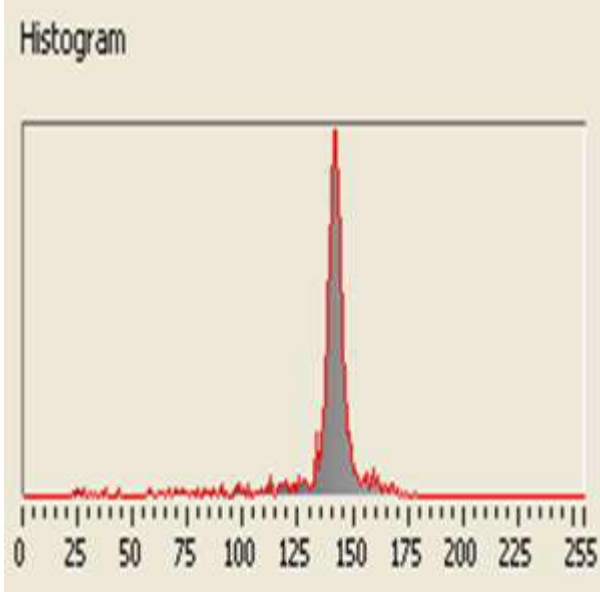


Fig. 7: Histogram of the micrometry of colloidal formations at the concentration of the polysaccharide at 0.07%.

It has been shown that reducing polysaccharide concentration by half (0.04%), the sizes of colloidal particles increase on average by 5.079, and their average area is 29.61. The shape and perimeters of the colloidal formations significantly increase, to 0.073 and 20.175 μm , respectively (Fig 8,9, Tab. 3). At a low concentration of the polysaccharide, the degree of crystallization of the colloidal particles is also significantly lower (Fig. 10).

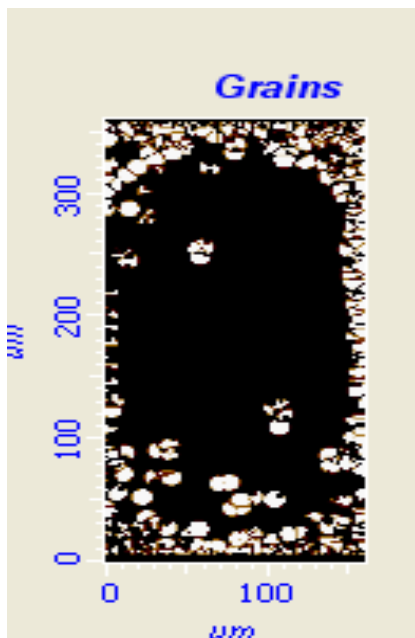


Fig.8: Microphotography of colloidal formations at the concentration of the polysaccharide at 0.04%.

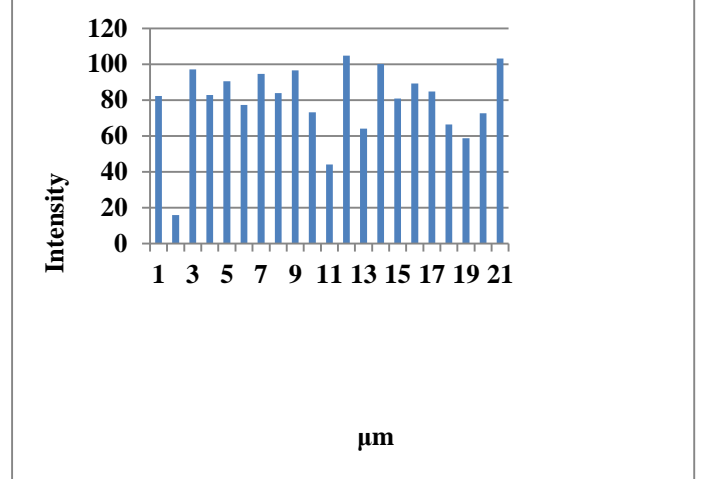


Fig.9: Histogram of the sizes of colloidal formations obtained as a result of processing of microscopy at the sugar concentration of 0.04%.

Table.3: The average of the size, area, perimeter and forms of colloidal formations at the polysaccharide concentration of 0.04%.

Area	Average S	Peremeter	α
um*um	um	um	
29.671	5.079	20.175	0.072896
20.448	1.967	9.93	0.207373

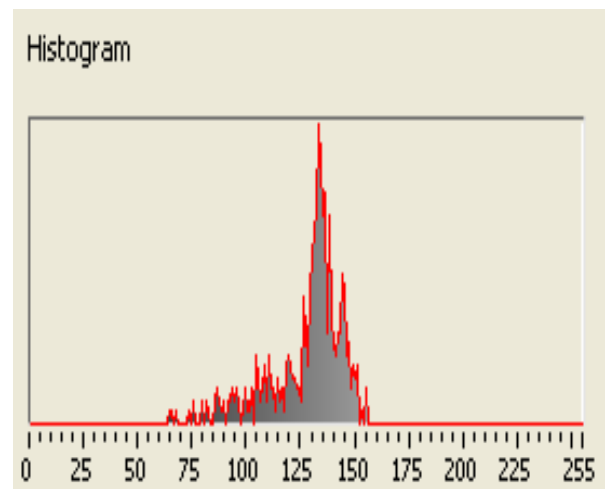


Fig. 10: Histogram of the sizes of colloidal formations (μm), obtained as a result of processing of microscopy at the sugar concentration of 0.04%.

IV. CONCLUSION

Iron oxidizing chemolithotrophic bacteria have been isolated from the sulfide ores and identified as *L. ferriphilum* CC on the bases of their morphological and physiological characteristics, as well as on the sequences of nucleotides in 16SrRNA. It has been shown that in addition to the EPS *L. ferriphilum* produces a colloidal polysaccharide. Isolation of the above-mentioned

polysaccharide was carried out according to a method developed by the authors, and its chemical and physical properties were studied. Studies of the chemical composition showed that the colloidal polysaccharide synthesized by *L. ferriphilum* CC consists of three monomers- glucose, fructose, mannose. The crystallization degree of colloidal particles and the shape parameters basically depended on polysaccharide concentration, which were conditioned by the hydration degree of a particle. A comparison of histograms (Fig.5 and Fig. 8) indicates that an increase in polysaccharide concentration does not lead to bigger colloidal particle formation, but contributes to increasing the quantity of shaped particles. This means that the dispersion of colloidal particles (size) does not much depend on polysaccharide concentration. However, the number of identical colloidal formations basically depend on the concentration of polysaccharide.

REFERENCES

- [1] Y.A Yokota, Y. Yamada, K.O. Imai, "Lipopolysaccharides of Iron Oxidizing *Leptospirillum ferrooxidans*," *J. Gen. Appl. Microbiol*, vol. 34, pp. 27-37, 1988.
- [2] M. Rodriguez, M. Campos, S. Gomez-Silvia, "Studies on Native Strains of *Thiobacillus ferrooxidans*. III: Studies on the Outer Membrane of *Thiobacillus ferrooxidans*. Characterization of the lipopolysaccharide and some Proteins," *Biotechnology*, vol. 8, issue 4, pp. 292-299, 1986.
- [3] A. P. Harrison JR, "Genomic and Physiological Comparisons Between Heterotrophic Thiobacilli and *Acidiphilium cryptum*, *Thiobacillus versutus* sp. nov. and *Thiobacillus acidophilus* nom. rev.," *International Journal of Systematic and Evolutionary Microbiology*, vol. 33, pp. 211-217, 1983.
- [4] E.H.William, R. Vestal, "Physical and Chemical Studies of *Thiobacillus ferrooxidans* Lipopolysaccharides," *Journal of Bacteriology*, vol. 123, issue 2, pp. 642-650, 1975.
- [5] A. P. Harrison "Genomic and Physiological Diversity Amongst Strains of *Thiobacillus ferrooxidans*, and Genomic Comparison with *Thiobacillus thiooxidans*," *Arch. Microbiol*, vol. 131, pp. 68, 1982.
- [6] W.S. Wang, M.S Korczynski, D.G. Lundgren, "Cell Envelope of an Iron-Oxidizing Bacterium: Studies of Lipopolysaccharide and Peptidoglycan," *J. Bacteriology*, vol. 104, issue 1, pp. 556-565, 1970.
- [7] J.R. Vestal, D.G. Lundgren, K.C. Milner, "Toxic and Immunological Differences Among lipopolysaccharides from *Thiobacillus ferrooxidans* Grown Autotrophically and Heterotrophically," *Canadian Journal of Microbiology*, vol. 19, issue 11, pp. 1335-1339, 1973.
- [8] J. Wingender, T.R. Neu, H.C. Elemming, "Microbial Extracellular Polymeric Substances," Characterization, Structure and Function, (Eds) J. Wingender et al. pp. 1-15, 1999.
- [9] W. Sand, T. Gehrke, "Analysis and Function of the EPS From Strong Acidophile *Thiobacillus ferrooxidans*, Microbial Extracellular polymeric Substances (Eds) J. Wingender et al. pp. 127-140, 1999.
- [10] H. Nielsen, A. Jahn, "Extraction of EPS" In: Microbial Extracellular polymeric Substances, Characterization, Structure and Function (Eds) J. Wingender et al. pp. 50-69, 1999.
- [11] A. Vardanyan, N. Vardanyan, L. Markosyan, W. Sand, M. Vera, R. Zhang, "Biofilm Formation and Extracellular Polymeric Substances (EPS) analysis by new Isolates of *Leptospirillum*, *Acidithiobacillus* and *Sulfobacillus* from Armenia," *Advanced Materials Research*, vol. 1130, pp.153 – 156, 2015.
- [12] G.P. Sheng, H.Q Yu, X.Y. Li, "Extracellular Polymeric Substances (EPS) of Microbial Aggregates in Biological Waste Water Treatment Systems: a review," *Biotechnology*, vol. 28, pp. 882-894, 2010.
- [13] M.P. Silverman, D.G. Lundgren, "Studies on the Chemoautotrophic Iron Bacterium *Ferrobacillus*: 1An Improved Medium and a Harvesting Procedure for Securing High Cell Yields," *J. Bacteriol*, vol. 77, issue 5, pp. 642, 1959.
- [14] Bergey's Manual of Systematic Bacteriology, (Eds) P. Vos, G. Garrity, D. Jones, N.R. Krieg, W. Ludwig, F.A. Rainey, K.H. Schleifer, W. Whitman, 2009.
- [15] H. Badalyan, N. Baghdasaryan, K. Ohanyan, M. Stepanyan, A. Kishmiryan, "Dependence of Erythrocyte Shape Parameter on the Low Dose γ -Irradiation," *Journal of Physics*, vol. 9, issue 1, pp.95-99, 2016.
- [16] M. Margaryan, H. Badalyan, A. Trchounian, "Comparative Analysis of UV Irradiation Effects on *Escherichia coli* and *Pseudomonas aeruginosa* Bacterial Cells Utilizing Biological and Computational Approaches," *Cell Biochemistry and Biophysics*, vol. 74 issue 3, pp. 381-389, 2016.
- [17] A.K. Vardanyan, L.S. Markosyan, N.S. Vardanyan, "Extraction of Non-ferrous and Other Valuable Metals from Complex Concentrate," *Forum of Young Scientists of Armenia "Achievements and Perspectives of Young scientists*, Tsakhkadzor, Armenia, pp.51-53, 2012.
- [18] A.K Vardanyan, L.S. Markosyan, N.S. Vardanyan, "Immobilization of New Isolated Iron Oxidizing Bacteria on Natural Carriers," *Advanced Materials Research*, vol. 825, pp.388-391, 2013

- [19] A.K.Vardanyan, N.S. Vardanyan, L.M. Markosyan, "Peculiarities of Adhesion and Bioleaching of Pyrite by New Isolated *Leptospirillum* spp. Bacteria," *Universal Journal of Microbiology Research*, vol. 1, issue 2, pp.22 – 25, 2013.
- [20] N. Vardanyan, S. Stepanyan, A. Khachatryan, Z. Melqonyan, A. Vardanyan, "Biooxidation of Chalcopyrite by Iron and/or Sulfur Oxidizing Bacteria Isolated in Armenia," *International Journal of Innovative Research in Science, Engineering and Technology*, vol. 5, issue 9, pp.15901 – 15907, 2016.
- [21] A. Vardanyan, S. Stepanyan, N. Vardanyan, L. Markosyan, W. Sand, V. Vera, R. Zhang, "Study and Assessment of Microbial Communities in Natural and Commercial Bioleaching Systems," *Minerals Engineering*, vol. 81, pp. 167 – 172, 2015.
- [22] M. E. Makintosh, "Nitrogen Fixation by *Thiobacillus ferrooxidans*," *J. Gen. Microbiol.*, vol. 105, pp.215-218, 1978.

Daylight Performance of Middle-rise Wide Span Building in Surabaya (Case Study: G-building ITATS)

Dian P.E. Laksmiyanti¹, Poppy F Nilasari²

¹Department of Architecture, Institute Technology Adhi Tama Surabaya, Indonesia

²Department of Interior, Petra Christian University, Indonesia

Abstract— Global warming and increase of energy consumption issues has encourages architect to design energy efficient building. The most crucial aspect in designing building in warm humid climate is solar irradiance and wind flow. High level of irradiance increase heat gain of the building and it also cause a higher cooling load and cooling energy. More compact the building form, the cooling energy consumption will be less. Compact or bulky building usually consumes less cooling energy than the slim one because it has lower s/v ratio. Thus the bulky form, middle rise wide span building usually uses atrium to help distribute daylight in to every room of the building. Unfortunately the daylight from the atrium brings considerable heat because the solar radiation that hit the horizontal plane is very high and it's very difficult to minimize solar gain in the roof. This research aims to evaluate the daylight performance of middle rise wide span building in Surabaya. Case study of this research is G-Building of Institute Technology Adhi Tama Surabaya.

To evaluate the daylight performance daylight factor of the building was measured by lux-meter and then compared to daylight factor standard for any rooms. Daylight performance of the buildings was found to bear some relations to cooling energy performance and composition of fenestration-opaque roof in atrium.

Keywords— Atrium, Daylight, Energy Efficient, Middle-rise, Tropics.

I. INTRODUCTION

According to Green Building Index 2010, most of consumption of operational energy in a building used for cooling and lighting energy. Architect can save the operational energy of the building with a good design that concern the environment and climatically responsive. Indonesia is a warm humid country which has a high level of solar exposure whole year. High solar irradiance in tropics being a challenge for architect to build a comfortable building with low energy consumption. Building façade and roof should be designed to minimize

the heat gain in to the building, and maximize the daylight and air circulation in the building^[1].

Operational energy in a building can be reduced if the building has a good design. Right choice of building materials, proper form, appropriate location and site planning will reduce the heat gain of the building moreover the cooling load and cooling energy^[1,2]. Envelope design of tropics building should be careful because architect better design room with daylight and good air circulation, on another hand daylight and air circulation in to the building may also cause heat flow in to the building. Gaining heat in the building means increasing cooling load and cooling energy.

One of factor overheating external façade caused by domination of fenestration surface on building envelope^[3]. Most of fenestration surface such as clear glass, fiber glass, polycarbonate, usually have a great U-value and the decrement factor of that materials almost 0, it means that materials receive a lot of heat from environment and transmit almost all that heat in to the building.

By previous research octagonal building consume less cooling energy consumption than other shape such as rectangle, square, L shape, H shape, etc in the same volume^[4]. Other research says more compact the building, energy consumption will be less^[5]. Compact form has less surface to volume ratio which is mean less heat transfer from building envelope and heat gain. Trouble in bulky building is distribution of the daylight. Natural lighting can't achieve the middle of the building even though there's a huge window in the perimeter area. Put an atrium in to a bulky building can be one of easiest solution to solve this problem^[1]. Skylight on the atrium let the sun light came into the middle area of the bulky building so the daylight can be evenly distributed^[6]. In warm humid area envelope design has a big contribution in thermal comfort, visual comfort, and energy consumption^[7], so it will be necessary too think about façade and roof design.

II. LITERATURE STUDY

2.1 Advantages of Warm Humid Climate in Daylighting

Warm humid climate has the following characteristics:

- a. Cloudy sky throughout the year with cloud cover 40% -80% which can cause glare.
- b. The sun shines all year long which results in high radiation
- c. Very high humidity (40% -90%)
- d. The difference in temperature is relatively the same day and night, and small amplitude of daily and a year temperature (23°C – 34°C)
- e. Low wind speed 1,1m / s - 4,3m / s.
- f. High rainfall (1200mm / year)

Table 1 describe the advantage and disadvantages of tropics characteristic on a building.

Table.1: influence of climate^[7,8]

No	Element	Influence	
		Positif	Negatif
1	Sun Irradiance	<ul style="list-style-type: none"> • Day Lighting • Solar Energy 	<ul style="list-style-type: none"> • External heating load
2	Temperatur	<ul style="list-style-type: none"> • Cooling and heating need • Mixture Temperatur e 	<ul style="list-style-type: none"> • Heat load of structure and organism • Potentially cause air pollution
3	Angin	<ul style="list-style-type: none"> • Ventilation design of building • Reduce heating load 	<ul style="list-style-type: none"> • Wind load on buildings • Spread of air pollution • Dust carrier • Causes of rainwater enter the building
4	Curah Hujan	<ul style="list-style-type: none"> • Urban Hydrology 	<ul style="list-style-type: none"> • Causes of flood • Structural load because of water
5	Kelembaban	<ul style="list-style-type: none"> • Help thermal comfort 	<ul style="list-style-type: none"> • The cause of fog • Pollution modifiers • The cause of rust • Can raise the temperature

The light produced by the sun and which affects the earth directly, indirectly, or both are natural light (daylight). The daylight includes:

- Sunlight (directly from the sun)

- Sky light (either clear, cloudy or partly cloudy)
- Sunlight and / or sky light reflecting off other surfaces (e.g. land, surrounding buildings, water)

Factors that affect natural lighting include:

1. The amount of sunlight in an area
2. The required level of lighting (lux)
3. Building elements that affect, such as: The size and position of the light hole, The reflection factor of light from the surfaces inside and outside the building, The width of the eaves and the size of the space and color and elements of space

2.2 Daylight Strategies

This following strategies of making huge daylight in to the building:

1. Building Orientation
The best building energy performance usually has North-South Orietation
2. Daylight from roof (skylight)
The horizontal opening has two advantages:
 - a. Let the illumination not be equally fair on the vast interior area, while the natural light from the openings is limited (fig.1).
 - b. The horizontal opening jg receives more light than the vertical aperture (fig.2).

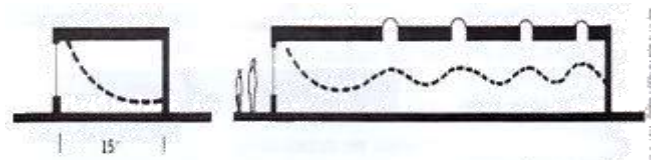


Fig.1: When the natural lighting of the openings is confined to the outer wall, the openings on the roof will be able to flatten the illumination along the limited space area (Lechner, 2001)

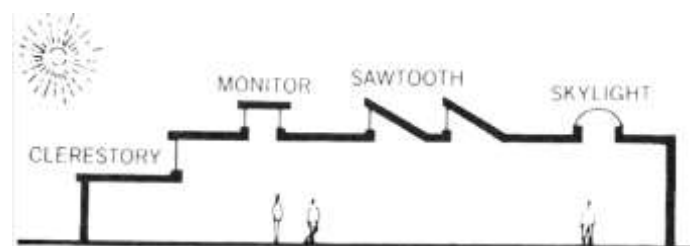


Fig.2: Option of Skylight design of atrium (Lechner, 2001)

3. Building Form
the square plan, 16% did not get natural light and 33% got, but only partially. On a rectangular plan can remove a central area that does not receive light, but still has a large area that gets partial light.^[9]
4. Spatial plan
Open space planning is very beneficial for bringing light into the interior. The glass partition can be made of glass at an elevation above the eye level. A higher mounted surface on a wall provides a more

uniform distribution of natural lighting for every corner of the room than lowered openings. The higher openings will give less light contour lines with more coverage than the same-sized openings placed in the lower positions.^[6]

2.3 Daylight factor

The magnitude of the ever-changing sky light makes the level of illumination from the sky into the building requires a ratio. Daylight Factor (DF) is the ratio between the bright forces at a given point in a room with the bright force of the open area in the same horizontal plane ^[10]. DF is influenced by:

1. Direct light from the sun on the work plane (SC = Sky Component)
2. Light reflection from the surrounding surface (ERC = Externally Sky Component)
3. Light reflections from indoor surfaces (IRC = Internally Sky Component)

$$DF = \frac{E_i \times 100}{E_o} \dots\dots\dots (1)$$

Where DF is Daylight Factor, E_i = indoor luminance, and E_o = Outdoor luminance.

III. METHODOLOGY

To get data of Daylight Factor measure the luminance level outdoor and indoor in a same time with lux-meter and then count the DF with formula 1 in subheading 2.3. Usually DF was measured as high as work area, for Indonesia is about 0,75-1m high from floor. So in this case lux meter put in 0.8m high from floor. Node of measurement in outdoor located in free obstruction open space so the real luminance level can be recorded. Measurement in indoor area taken in every window.

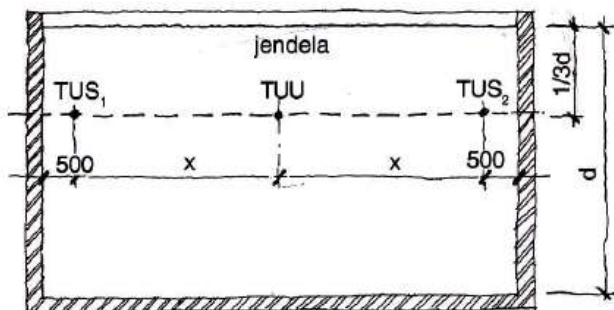


Fig.3.: Determination of measuring point (Frick, 2008)

In the calculation indoor luminance level used two types of measuring point:

- Main Measure Point (TUU), taken in the middle between the two side walls located at a distance of 1/3 from the effective plane of the opening.

- Side Side Assessment (TUS), taken at a distance of 0.50m from the side wall which is also located at 1/3 distance from the effective hole field of light. (fig.3)

IV. RESULT AND DISCUSSION

G-Building in ITATS is a building for Civil engineering and planning faculty. There are classrooms, studios, workshop, café, office department and library in this building. This building is so bulky with about 50m long and 31m wide. It is 4 storeys building. It has rigid frame structure from concrete and steel. Roof of this building is made from concrete deck (for perimeter room), galvalum, and polycarbonate as a skylight in the atrium. Fig 4 and fig 5 may give a description of this building. There 4 department in this faculty: Civil engineering, Architecture, Product Design and Environmental Engineering.

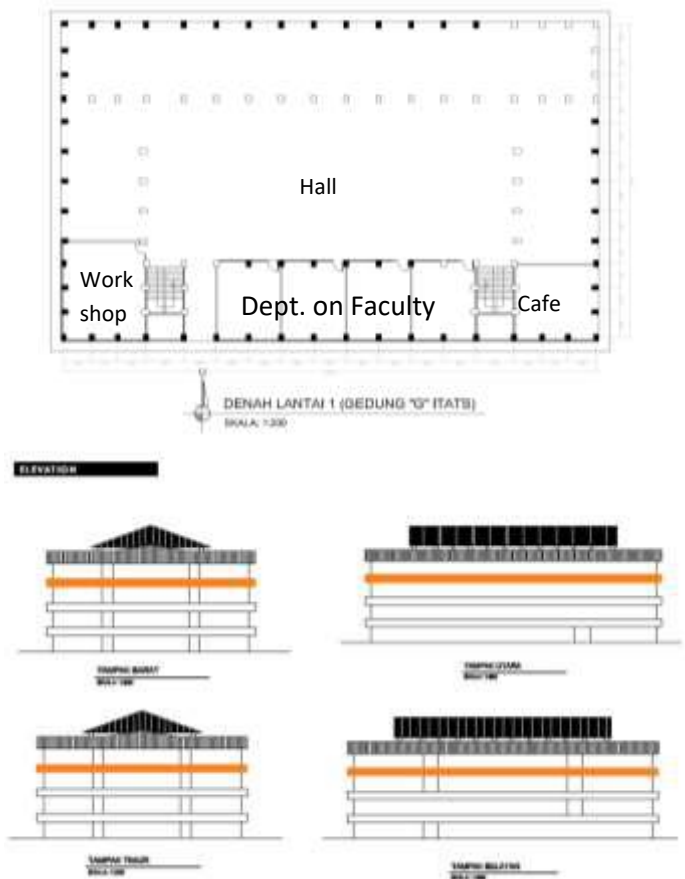


Fig.4: 1st floor Plan and Elevation of G-Building ITATS

Most of room in this building surrounded by fenestration wall made of a clear glass. To make a privacy in classrooms and studio, sandblast sticker put on it up to about 1,8m high (fig.5). There is no vertical, horizontal or roller blind in every room. It may give full access of the daylight from atrium and outside separated equally in every room. The atrium used for hall. Usually collegians use this hall for indoor sport, tournament, music event, etc.



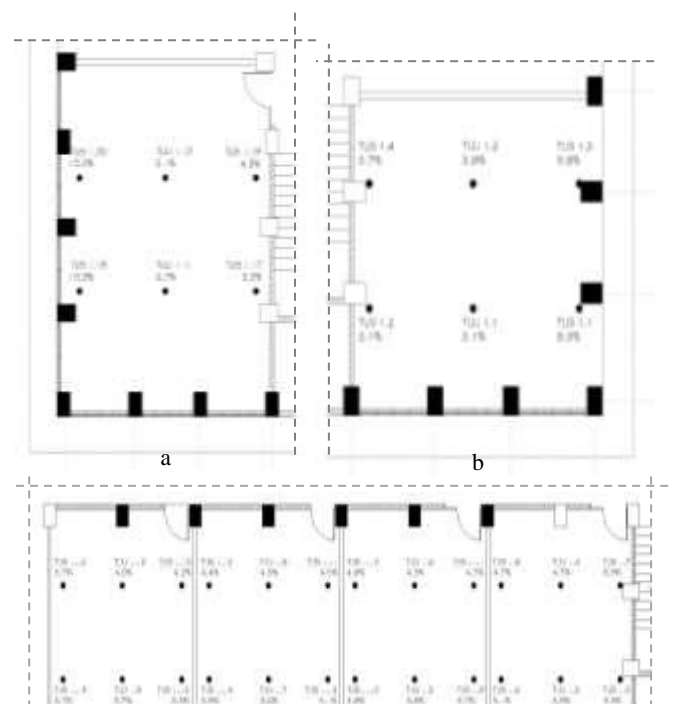
Fig.5: Interior of atrium and windows in the envelope of G-Building ITATS

When viewed from the results of daylight factor measurement in the this case study, the overall quality of natural lighting in this building can be said to be not eally good. Indeed a lot of light that enter into the room, but because amount of light entering too much, so it can cause glare, especially on the perimeter area.

Floor 1 used for administrative functions (Fig.4). There is a cafeteria on the lower left side. There 4 rooms for office of any departments in that faculty: Department of Civil Engineering, Department of Architecture, Department of Product design, Department of Environmental Engineering, and workshop for Product Design in the left side (fig.4). In front of the room functioned for the hall. This hall is usually used for events that invite many people such as exhibition, Introduction of Campus Life for new students, etc.

Table.2: Average Daylight Factor in every room

Floor	Functin of Room	TUU/ TUS	DF	Standard of DF
1	Café	TUU	3.5	4%
		TUS	6.2	
	Office of department	TUU	4.4	4%
		TUS	4.9	
Workshop	TUU	5.9	9%	
	TUS	7.5		
	Hall	-	10.7	4%
2	Classroom	TUU	8.3	4%
		TUS	8.7	
3	Classroom	TUU	8.0	4%
		TUS	9.3	
	LAB	TUU	7.3	9%
		TUS	7.7	
	Studio	TUU	8.7	6%
		TUS	9.4	
4	Kelas	TUU	8.3	4%
		TUS	9.8	
	Library	TUU	7.2	4%
		TUS	7.7	
	Workshop	TUU	8.4	9%
		TUS	9.0	



Different functions has different standard of illumination. Table 2 shows the amount of lighting needs and it result for some room functions. In general, the amount of lighting in the cafe, office, and workshop is sufficient to meet the standards. The number of natural lighting in the hall seems excessive (figure 6) because in the hall there is an atrium with a skylight composition of 50%. Quite a lot of natural light that passes through the skylights, in addition to the color of the white floor da use glossy ceramics that can add reflectance on the surface so that the Daylight Factor (DF) in this area is very high (Figure 7). Due to excessive lighting in this hall area, will cause inconvenience if the event held in the hall requires LCD display. Of the large DF in this area, can be sure LCD screen will be difficult to see because of glare.

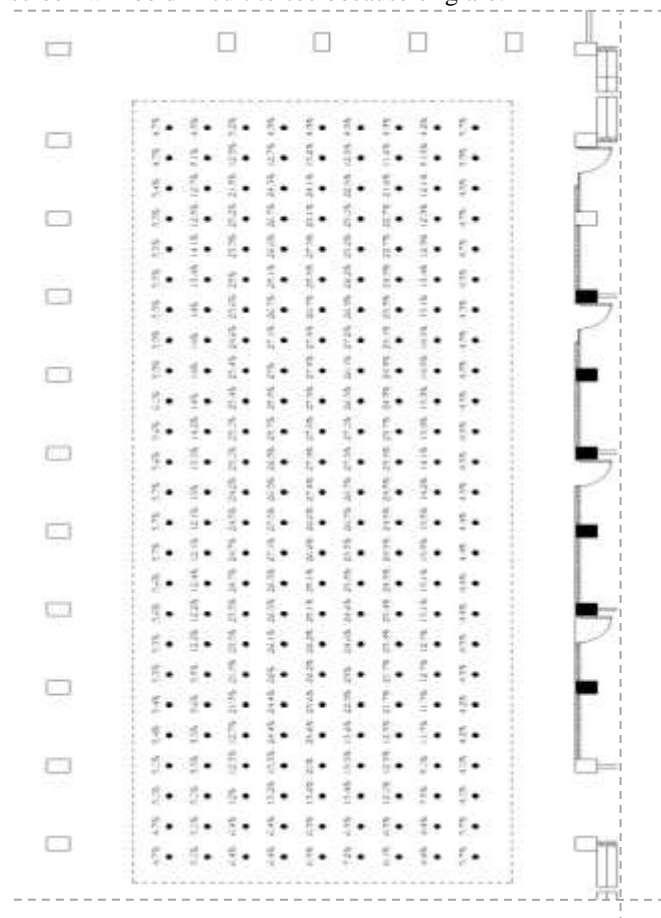


Fig.6: DF in Hall of G-Building ITATS

2nd floor is functioned for classroom of theoretical course and lecture room of civil engineering. Natural lighting needs in each room about 400 lux. With the atrium in the G building and the wall adjacent to the corridor in the form of a transparent wall, the amount of natural light entering into the classroom little bit more, up to doubled from the existing standard. Indeed, with the atrium and transparent walls along the space adjacent to the corridor cause the spreading of sunlight into the room becomes more evenly distributed, but if the amount of incoming light is too much it will have the potential to cause discomfort. In terms of architecture, the use of transparent walls in the classroom is considered not effective and can disrupt the teaching-learning process in it.

The amount of natural light in the class on the north side more than the classrooms on the other side because on the north side of this building there is no obstruction. Seen in Figure 7, with the Daylight Factor data in the building, it is certain that the building is capable of not using artificial lighting at all during the day in fine weather. On the second floor of this building students are less able to see the clear LCD screen because too many light sources into the classroom.

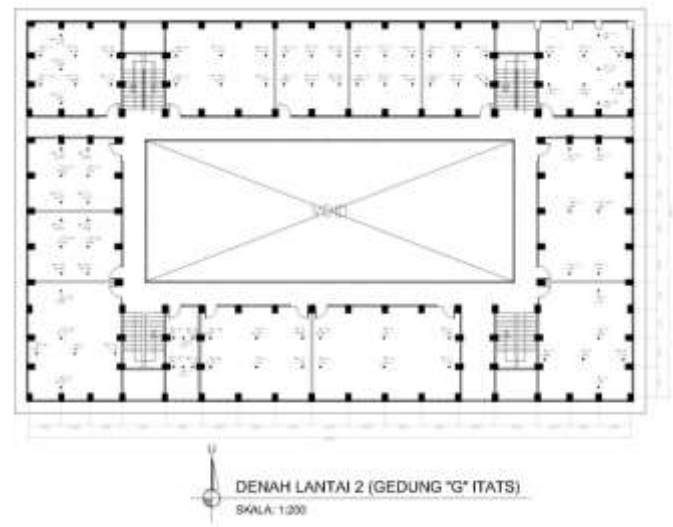


Fig.7: DF in 2nd of G-Building ITATS

3rd floor of this building function as classes, studio and laboratory of architecture majors. The architecture department needs a class for drawing and modeling design. Lighting requirements for the studio is larger than the any classroom because in the studio there are several other activities besides reading and writing, among others, create a drawing, making a model, assemble lego and so on. Likewise for the architecture lab. There are 4 labs on the 3rd floor, including the Science lab and the structure, the Design lab, the urban and residential labs, as well as the History Lab and the Architecture theories. Activities covered in this lab include literature studies, design experiments and form ideas, simulations, experiments

using wind tunnel and helliodon. Lighting requirements for a 900lux or DF 9% lab.

In general, the performance of lighting on the 3rd floor is quite good and the spread is also evenly distributed (figure 8). In DF classes and incoming studios is greater than the standard, but the natural incoming LAB inbox is still less than required. This is because the layout of the room is less laid out optimally.

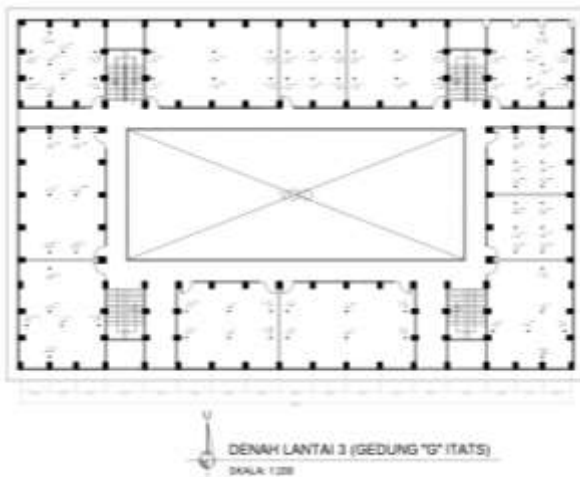


Fig.8: DF in 3rd of G-Building ITATS

The 4th floor has an identical floor plan with 3rd floor. This 4th floor room is used for classrooms, reading rooms and studios in department of product design. Studio product design more likely a workshop so that the need for lighting is also greater than the studio in architecture department. The 4th floor in overall has an average bigger lighting than 1st-3rd floor. This is because the 4th floor does not have any obstruction outside the room and is the top floor so that the natural daylight distribution in the atrium can be directly distributed in the classroom. (Figure 9)

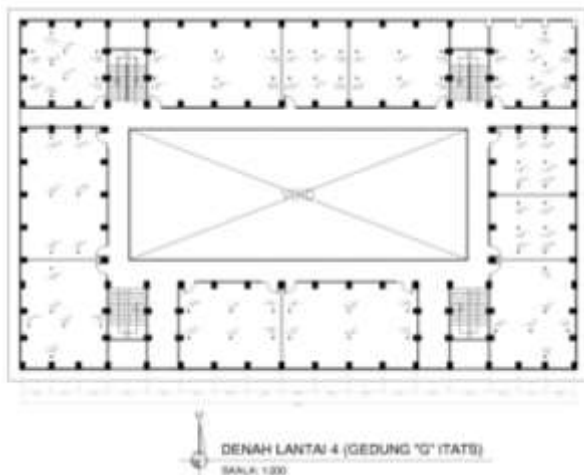


Fig.9: DF in 4th of G-Building ITATS

The natural light on the 4th floor in the workshop room is enough to fulfill the standard and the spreading of the light is quite evenly, for the reading room and classroom too much natural light coming into the room so this allows inconvenience for the users in it. Solutions for the classroom can be overcome with curtains or blinds on the room so that when teaching and learning process lecturers and students can adjust the amount of natural light that enters the room.

V. CONCLUSION

Building with 50% fenestration roof in the atrium was able to provide a lot of natural lighting into the building and quite effective in helping the distribution of lighting in the perimeter space. Indeed, in some rooms amount of natural light level is too big, but there is a solution by installing the curtain on the window. Subsequent research can evaluate the amount of percentage of skylight on the atrium to make the distribution of natural lighting more evenly and the amount of heat entering the building is not too large.

ACKNOWLEDGEMENTS

Thanks to ristekdikti has been a sponsor of this research.

REFERENCES

- [1] Yeang Ken (1996), *Bioclimatic Skyscraper*. London: Artemis London Limited
- [2] Baker Nick dan Koen Steemers, (2005), *Energy and Environmental in Architecture*, Taylor & Francis Group, New York
- [3] Knowles, R.L. (2003), "The Solar Envelope: Its Meaning for Energy and Buildings", *Journal of Energy and Buildings*
- [4] Dian P.E. Laksmiyanti (2016), *Kinerja Bentuk Bangunan Perkantoran Bertingkat Menengah Di Surabaya Terhadap Efisiensi Energi Pendinginan*, *Jurnal IPTEK ITATS* vol:20 no 1.
- [5] Crawford Robert H, Czerniakowski Isabella, Fuller Robert J (2010), A comprehensive framework for assessing the life cycle energy of building construction assemblies, *Journal Science Direct, Architectural Science Review* 53 (2010) 288–296.
- [6] Heerwagen Dean (2004), *Passive and Active Environmental Controls Informing The Schematic Design of Building*, Mc Graw Hill, New York
- [7] Markus T.A, Morris E.N (1980), *Buildings, Climate and Energy*, Pitman Publishing Limited, London
- [8] Olgyay, V (1972). *Design with Climate- Bioclimatic approach to architectural regionalism*, Princeton University Press, New Jersey

- [9] Lenchner Norbert (2007), Heating, Cooling and Lighting, PT. Raja Grafindo Persda, Jakarta
- [10] Szokolay, S.V. (1987), Thermal Design of Buildings. RAAIA Education Division, Canberra, Australia.

Application of Cubic Spline Interpolation to Fit the Stress-Strain Curve to SAE 1020 Steel

Otávio Cardoso Duarte, Pedro Américo Almeida Magalhães Junior

Department of Mechanical Engineering, Pontifícia Universidade Católica de Minas Gerais, Brazil

Abstract —This article presents the methodology to use cubic splines interpolation method to fit the stress-strain curve, in the field of permanent deformation, based on experimental data obtained on performed tests on a standardized specimen of SAE 1020 steel hot rolled flat. The third-order polynomial for each interval between knots was used to fit the stress-strain curve.

Keywords— Cubic Spline, Permanent Deformation, Curve, Interpolation, Steel.

I. INTRODUCTION

According to Vicente Chiaverini (1986), the materials tend to deform when subjected to mechanical stresses, and, depending on the nature of each material, their behavior during deformation may vary. Metals can undergo considerable permanent deformation before to rupture. The application of cubic splines for the construction of the strain-strain curve, in the field of permanent deformation, through the mathematical manipulation of data obtained in experimental tests, allows the identification of third-order interpolator polynomials to obtain the value of the acting axial tension for a certain measured deformation.

The benefits are the possibility of obtaining values of the axial tension for a given deformation, point of constraint and better approximation of the stress-strain curve.

II. MATERIAL AND METHODOLOGY OF THE TEST

The experimental data were obtained by tensile tests performed on samples of specimens made of SAE 1020 hot rolled material. The tests were performed on a vertical traction machine.

2.1 SPECIMEN USED ON EXPERIMENTAL TESTS

The specimens used in the tensile tests were prepared according to the recommendations of ASTM E8 / E8M. The material used was SAE 1020 hot rolled steel.

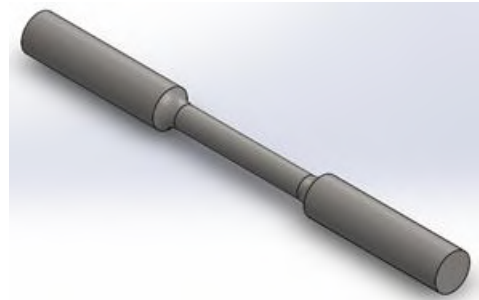


Fig. 1: Specimen Used on Experimental Tests

2.2 METHODOLOGY OF THE EXPERIMENTAL TESTS

The tests were carried out on four identical samples of the test specimen, in order to compare the values obtained in the tests and to guarantee the responses of the equipment used.

The specimens were fixed to the vertical traction machine by means of wedge-shaped jaws, suitable to reduce slippage during load application, which reduces errors in data collection.

The axial tensile load was applied to the test pieces gradually, causing the deformation of the same. The axial tensile load was raised until fracture of each of the test specimens used in the tests.

2.3 RESULTS OBTAINED IN THE EXPERIMENTAL TESTS

The results obtained in the tensile tests of each of the four test specimens are described in the table below. Seven measuring points were taken, all within the permanent deformation field, where the values of the axial tensile load and its respective value of permanent deformation of the specimen were collected.

The value of the deformation collected in the first measurement covers the field of elastic deformation, which was linear for all the specimens tested. As this work aims to work only with the data of the curve of permanent deformation, which is not linear, the data referring to the field of elastic deformation were suppressed.

Table. 1: Results of Experimental Tests

Sample	Measurement	Valor	Valor	Valor	Valor	Valor	Valor	
		1 ^a	2 ^a	3 ^a	4 ^a	5 ^a	6 ^a	7 ^a
#01	Load (kgf)	2501	2989	3294	3447	3443	3447	3386
	Stress (kgf/mm ²)	38,20	45,66	50,31	52,65	52,59	52,65	51,72
	Strain (mm)	7,44	9,30	11,16	13,02	14,88	16,74	18,60
#02	Load (kgf)	2562	2987	3233	3386	3507	3509	3385
	Stress (kgf/mm ²)	39,13	45,63	49,38	51,72	53,57	53,60	51,70
	Strain (mm)	7,44	9,30	11,16	13,02	14,88	16,74	18,60
#03	Load (kgf)	2555	2980	3244	3380	3450	3452	3383
	Stress (kgf/mm ²)	39,03	45,52	49,55	51,63	52,70	52,73	51,67
	Strain (mm)	7,44	9,30	11,16	13,02	14,88	16,74	18,60
#04	Load (kgf)	2531	2981	3270	3375	3448	3451	3380
	Stress (kgf/mm ²)	38,66	45,53	49,95	51,55	52,67	52,71	51,63
	Strain (mm)	7,44	9,30	11,16	13,02	14,88	16,74	18,60

III. MATHEMATICAL ANALYSIS OF RESULTS OF EXPERIMENTAL TESTS

3.1 MATHEMATICAL TREATMENT OF TEST RESULTS

Based on the results obtained in the experimental tests, a new the table was elaborated with the results that will be taken as basis for the application of the interpolating polynomials of the cubic splines. "Table 2" was constructed by taking as reference the mean values obtained in the experimental tests of the four specimens of the specimen.

Table. 2: Mean values obtained in the experimental tests.

Measurement	Value	Value	Value	Value	Value	Value	Value
	1 ^a	2 ^a	3 ^a	4 ^a	5 ^a	6 ^a	7 ^a
Load (kgf)	2537,25	2984,25	3260,25	3397,00	3462,00	3464,75	3383,50
Stress (kgf/mm ²)	38,76	45,56	49,80	51,89	52,88	52,92	51,68
Strain (mm)	7,44	9,30	11,16	13,02	14,88	16,74	18,60

The data in Table 2 will be used to develop the mathematical equations that will be demonstrated in the next topic.

3.2 MATHEMATICAL TREATMENT OF TEST RESULTS

According to Steven C. Charpa and Raymond P. Canale (2011), the spline concept originated from a drawing technique in which a thin, flexible strip (called a spline) was used to draw a smooth curve through a set of points . A smooth cubic curve results from interspersing the strip between the pins. Thus, the name "cubic splines" was adopted for such polynomials.

Cubic splines will be applied to determine a third-order polynomial, for each of the intervals, of the seven experimental measurements, in order to approximate the strain x strain curve of the experimental results.

First, we will write the third-order polynomials for each of the experimental data ranges.

$$S(x) = a_1x^3 + b_1x^2 + c_1x + d_1 . x \in [7,44;9,30] \quad (1)$$

$$S(x) = a_2x^3 + b_2x^2 + c_2x + d_2 . x \in [9,30;11,16] \quad (2)$$

$$S(x) = a_3x^3 + b_3x^2 + c_3x + d_3 . x \in [11,16;13,02] \quad (3)$$

$$S(x) = a_4x^3 + b_4x^2 + c_4x + d_4 . x \in [13,02;14,88] \quad (4)$$

$$S(x) = a_5x^3 + b_5x^2 + c_5x + d_5 . x \in [14,88;16,74] \quad (5)$$

$$S(x) = a_6x^3 + b_6x^2 + c_6x + d_6 . x \in [16,74;18,60] \quad (6)$$

Applying the condition that the function values must be equal at the interior knots, and the first and last functions must pass through the end points, we have the following equations:

$$S(7,44)=411,83.a_1+55,35.b_1+7,44.c_1+d_1=38,76 \quad (7)$$

$$S(9,30)=804,36.a_1+86,49.b_1+9,30.c_1+d_1=45,56 \quad (8)$$

$$S(9,30)=804,36.a_2+86,49.b_2+9,30.c_2+d_2=45,56 \quad (9)$$

$$S(11,16)=1389,93.a_2+124,55.b_2+11,16.c_2+d_2=49,80 \quad (10)$$

$$S(11,16)=1389,93.a_3+124,55.b_3+11,16.c_3+d_3=49,80 \quad (11)$$

$$S(13,02)=2207,16.a_3+169,52.b_3+13,02.c_3+d_3=51,89 \quad (12)$$

$$S(13,02)=2207,16.a_4+169,52.b_4+13,02.c_4+d_4=51,89 \quad (13)$$

$$S(14,88)=3294,65.a_4+221,41.b_4+14,88.c_4+d_4=52,88 \quad (14)$$

$$S(14,88)=3294,65.a_5+221,41.b_5+14,88.c_5+d_5=52,88 \quad (15)$$

$$S(16,74)=4691,01.a_5+280,23.b_5+16,74.c_5+d_5=52,92 \quad (16)$$

$$S(16,74)=4691,01.a_6+280,23.b_6+16,74.c_6+d_6=52,92 \quad (17)$$

$$S(18,60)=6434,86.a_6+345,96.b_6+18,60.c_6+d_6=51,68 \quad (18)$$

Applying the condition that the first derivatives at the interior knots must be equal, we have the following equations:

$$259,47.a_1+18,60.b_1+c_1=259,47.a_2+18,60.b_2+c_2 \quad (19)$$

$$373,64.a_2+22,32.b_2+c_2=373,64.a_3+22,32.b_3+c_3 \quad (20)$$

$$508,56.a_3+26,04.b_3+c_3=508,56.a_4+26,04.b_4+c_4 \quad (21)$$

$$664,24.a_4+29,76.b_4+c_4=664,24.a_5+29,76.b_5+c_5 \quad (22)$$

$$840,68.a_5+33,48.b_5+c_5=840,68.a_6+33,48.b_6+c_6 \quad (23)$$

Applying the condition that the second derivatives at the interior knots must be equal, we have the following equations:

$$55,80.a_1+2.b_1=55,80.a_2+2.b_2 \quad (24)$$

$$66,96.a_2+2.b_2=66,96.a_3+2.b_3 \quad (25)$$

$$78,12.a_3+2.b_3=78,12.a_4+2.b_4 \quad (26)$$

$$89,28.a_4+2.b_4=89,28.a_5+2.b_5 \quad (27)$$

$$100,44.a_5+2.b_5=100,44.a_6+2.b_6 \quad (28)$$

Applying the condition that the second derivatives at the end knots are zero, we have the following equations:

$$44,64.a_1+2.b_1=0 \quad (29)$$

$$111,60.a_6+2.b_6=0 \quad (30)$$

Solving the linear system, from equation 7 to equation 30, with their respective twenty-four unknowns, the following values were obtained.

$$\begin{aligned} a_1 &= -0,05497, b_1 = 1,22701, c_1 = -5,28285 \text{ e } d_1 = 32,78479; \\ a_2 &= -0,03342, b_2 = 0,62565, c_2 = 0,30979 \text{ e } d_2 = 15,44759; \\ a_3 &= 0,07327, b_3 = -2,94646, c_3 = 40,17451 \text{ e } d_3 = -133,42537; \\ a_4 &= -0,00696, b_4 = 0,18739, c_4 = -0,62827 \text{ e } d_4 = 43,65871; \\ a_5 &= -0,02213, b_5 = 0,86487, c_5 = -10,70909 \text{ e } d_5 = 93,65957; \\ a_6 &= 0,04421, b_6 = -2,46692, c_6 = 45,06517 \text{ e } d_6 = -217,5607. \end{aligned}$$

In this way, we can write the polynomials that approximate the value of the acting axial stress as a function of the deformation measured in the experimental tests, for each of the intervals between the measurements.

$$S(x) = -0,05497.x^3 + 1,22701.x^2 - 5,28285.x + 32,78479; \text{ if } x \in [7,44;9,30]$$

$$S(x) = -0,03342.x^3 + 0,62565.x^2 + 0,30979.x + 15,44759; \text{ if } x \in [9,30;11,16]$$

$$S(x) = 0,07327.x^3 - 2,94646.x^2 + 40,17451.x - 133,42537; \text{ if } x \in [11,16;13,02]$$

$$S(x) = -0,00696.x^3 + 0,18739.x^2 - 0,62827.x + 43,65871; \text{ if } x \in [13,02;14,88]$$

$$S(x) = -0,02213.x^3 + 0,86487.x^2 - 10,70909.x + 93,65957; \text{ if } x \in [14,88;16,74]$$

$$S(x) = 0,04421.x^3 - 2,46692.x^2 + 45,06517.x - 217,56079; \text{ if } x \in [16,74;18,60]$$

3.3 APPROXIMATION OF THE STRESS-STRAIN CURVE WITH THE USE OF THE CUBIC SPLINES

The cubic splines that approximate the stress values for the deformations evidenced in the experimental tests, obtained through the mathematical methods demonstrated in topic 2.2, were used to construct the strain-strain curve, as can be seen in Fig. 2.

The curve was constructed with the application of the cubic splines in the numerical calculation software VCN.

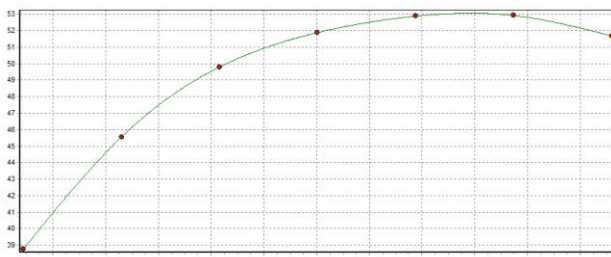


Fig. 2: Stress x strain curve obtained through the cubic spline polynomials

ACKNOWLEDGEMENTS

I thank the staff of the mechanical testing laboratory of the Pontifícia Universidade Católica de Minas Gerais, for the help they gave me in the execution of the traction tests, and to Professor Dr. Pedro Américo Almeida Magalhães Junior, for the technical support in the elaboration of this article.

REFERENCES

- [1] Chapra, Steven C., Canale, Raymond P., 2011. Métodos Numéricos para Engenharia. McGraw-Hill.
- [2] Chiaverini, Vicente., 1986. Tecnologia Mecânica: Estruturas e Propriedades das Ligas Metálicas. McGraw-Hill.

Tensile Test: Comparison Experimental, Analytical and Numerical Methods

Tatiana Lima Andrade, Pedro Américo Almeida Magalhães Júnior, Wagner Andrade de Paula

Department of Mechanical, Pontifical Catholic University of Minas Gerais, BRAZIL

Abstract—The objective of this work is to study and analyze the stress-strain curves obtained through the experimental tensile test and the comparison of the data obtained with the analytical and numerical methods. For the development of the analytical method, we proposed equations for the stress-strain curve of the material, using MS-EXCEL 2016. For the numerical method, a modeling of the test specimen was elaborated using the ANSYS Workbench® version 16 software. The steel selected for the studies was ABNT 1020.

Keywords—Hooke’s Law, Plastic-strain, Tensile test.

I. INTRODUCTION

Tensile test was used for evaluating the mechanical properties of material and the plastic strain modify this properties.

Use tensile test for determinate the final of plastic phase. ([2])

The state of tension in which plastic deformation occurs dependent on the degree of current plastic deformation and this phenomenon is called hardening. ([1])

II. METHODOLOGY

2.1 Experimental Methodology

The methodology based on experimental analysis using ABNT 1020 material specimen.

After the test will be collected the data obtained and generated the stress-strain curves of the engineering and actual deformation of the test.

The data obtained of the test will shown in Table 1.

Table 1: Tensile Test Data

Data	Value
Maximum Stress [MPa]	546.60
Area [mm ²]	63.62
Initial length [mm]	55.50
Final length [mm]	73.00
Initial diameter [mm]	9.00
Final diameter [mm]	5.10

With the achievement tensile stress, the stress-strain curve constructed, as shown in Figures 1 below.

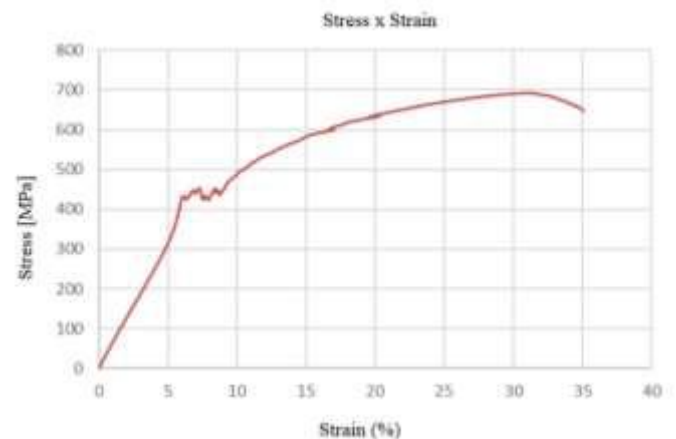


Fig. 1: Experimental curve

2.2 Analytical Methodology

In the analytical method, it proposed the determination of a curve that approached the stress strain curve obtained from the tensile test.

To determination the curves describing the behavior of the material, divided the curve experimental curve through pre-established intervals.

Four different equations has developed to divide into the following phases of the behavior of the material: elastic phase, beginning of the flow stage, ending of elastoplastic transition and plastic phase.

The selected interval of the curves has approximated by log, exponential or polynomial tendency curves. Thus, equations has developed that approached the maximum of the real curve of the tensile test.

2.3 Elastic Phase

The proposed curve for the elastic phase of the material uses Hooke’s law, (1) and shown in Fig. 2.

$$\sigma = E \cdot \varepsilon < \sigma_{esc} \quad (1)$$

σ = tensile stress [MPa]

ε = strain [MPa]

E = elastic modulus

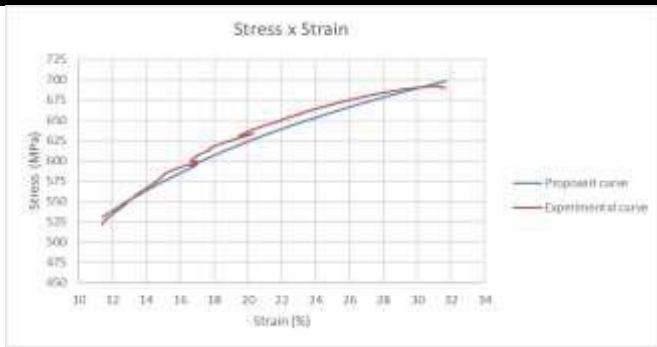


Fig. 2: Elastic phase curve

2.4 Beginning of the flow stage

The curve proposed for the beginning of the flow stage uses, (2) with the constants values of A and b shown below. The curves shown in Fig. 3.

$$\sigma = A \cdot e^{b \cdot \varepsilon} \quad \varepsilon > \varepsilon_{esc} \quad (2)$$

σ = tensile stress [MPa] ε = strain [MPa]
 A = 432.248 b = 0.001

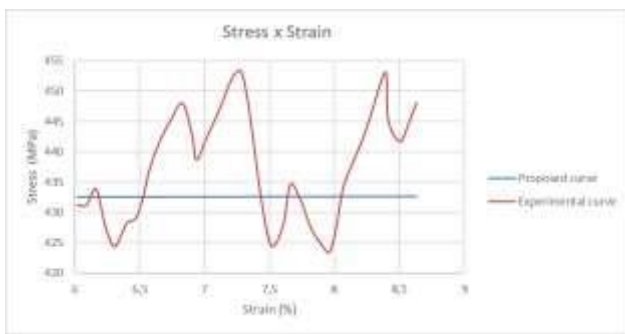


Fig. 3: Beginning of the flow stage

2.5 Ending of elastoplastic transition

The curve proposed for the ending of elastoplastic transition considers, (3) with the constants values of C and d shown below. The curves shown in Fig. 4.

$$\sigma = C \cdot \varepsilon^d + F \cdot \varepsilon + G \quad \varepsilon < \varepsilon_{ep} \quad (3)$$

σ = tensile stress [MPa] ε = strain [MPa]
 c = -6.5945 d = 2
 F = 163.39 G = -485.62

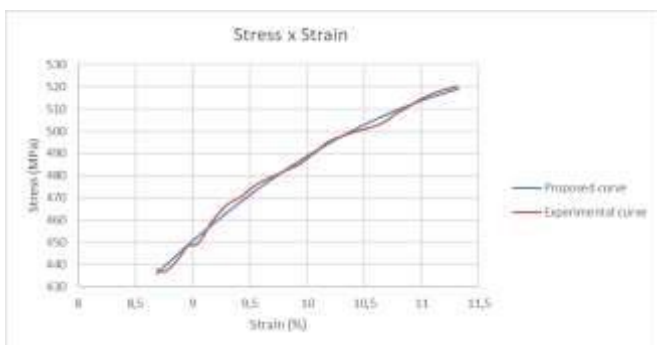


Fig. 4: Ending of elastoplastic transition

2.6 Plastic Phase

The curve proposed for the plastic phase uses, (4) with the constants values of H and K shown below. The curves shown in Fig. 5.

$$\sigma = H \cdot \ln \varepsilon + K \quad \varepsilon > \varepsilon_{ep} \quad (4)$$

σ = tensile stress [MPa] ε = strain [MPa]
 H = 160.674 K = 140.04



Fig. 5: Plastic phase

2.7 Developed curve using the proposed equations

For development of proposed curve has been used the equations 3 to 6. The Fig. 6 shown the proposed curve of performed tensile test.

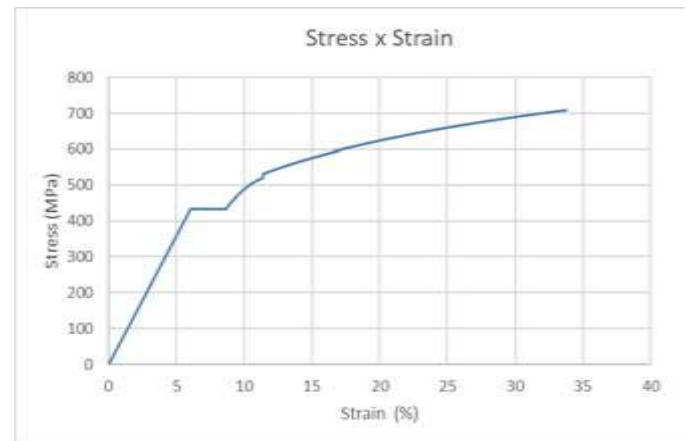


Fig. 6: Proposed curve

III. COMPARISON OF EXPERIMENTAL AND ANALYTICAL METHODS CURVES

The Fig. 7 shown the comparison of experimental and analytical methods curves of the ABNT 1020 material.



Fig. 7: Comparison curves

IV. NUMERICAL METHODOLOGY

The test specimen of ABNT 1020 material modeled in the AutoCad 16 and imported to ANSYS 16, in the Mechanical module a mesh has defined for it and its restrictions and loads were created. A fixed support has created at the base of the specimen and load has applied to the top of the specimen, as seen in Figs. 8 and 9.

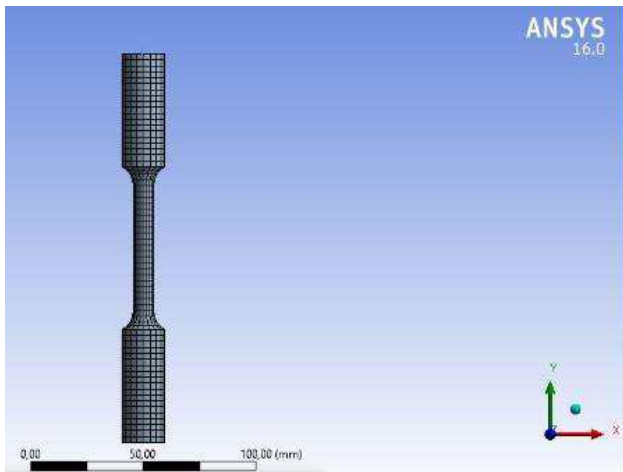


Fig. 8: Test specimen mesh



Fig. 9: Test specimen constrain

The displacement are show in Fig. 10 and tensions obtained are shows in Fig.11.

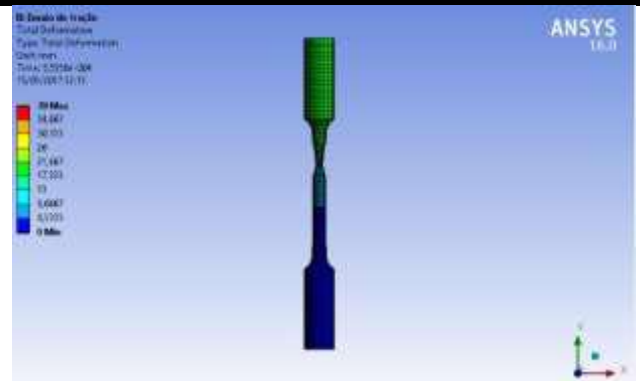


Fig. 10: Test specimen displacement

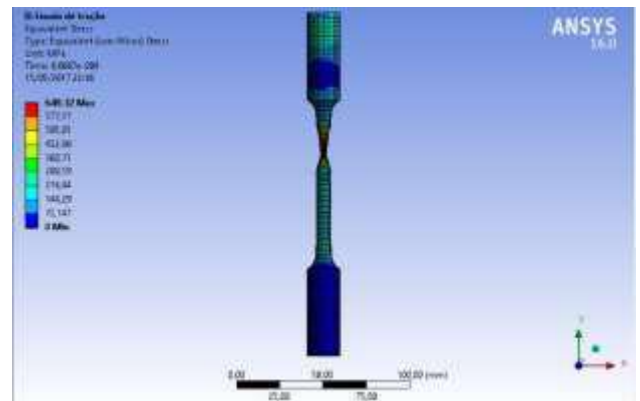


Fig. 11: Test specimen stress

The obtained curve through the numerical simulation shown in Fig. 12.

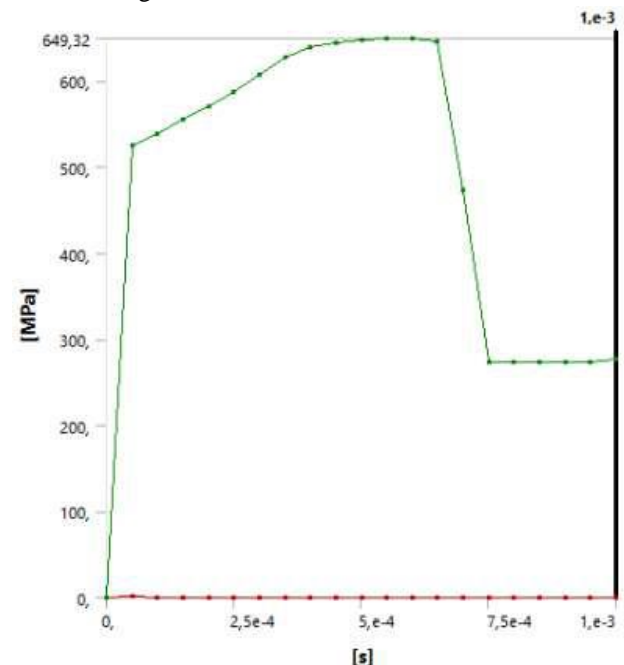


Fig. 12: Numerical curve

A curve of Fig. 13was designed in MS-Excel. The curve were created stress as a function of time, but it can be observed that the behavior of the curve is similar to those

found in the experimental and analytical analyzes, because it presents an elastic phase, an elastoplastic transition and the plastic phase.

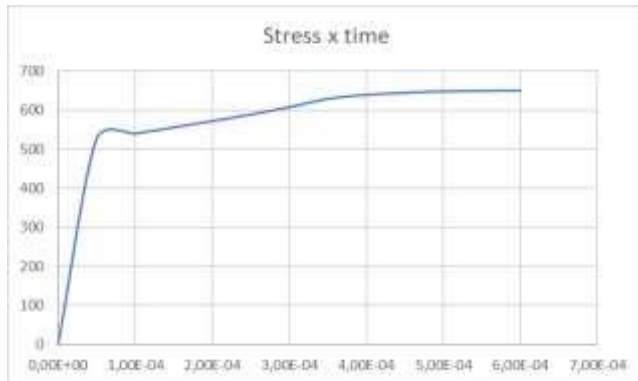


Fig. 13: Numerical curve – MS-Excel

V. CONCLUSION

The results were as expected. The specimen rupture occurs approximately 35 mm, as shown in Fig. 11.

The tensile test was of great importance to have a practical knowledge of the engineering data used in mechanical designs.

By comparing the experimental, analytical and numerical methods, one can note the importance of each one of them and how important it is to have an idea of the behavior of the material for the use of a numerical method in a safe and reliable way.

The results were as expected. The specimen rupture occurs approximately 35 mm, as shown in Fig. 11.

The advantage of this study is the confidence obtained in the execution of the proposed methodology, since the results obtained are very close to the experimental test.

ACKNOWLEDGEMENTS

The authors thank the support of the Pontifícia Universidade Católica de Minas Gerais – PUCMINAS-“Pontifical Catholic University of Minas Gerais”, the Conselho Nacional de Desenvolvimento Científico e Tecnológico-CNPq-“National Counsel of technological and scientific Development”, the Fundação de Amparo a Pesquisa de Minas Gerais-FAPEMIG-“Foundation for Research Support of Minas Gerais”.

REFERENCES

[1] EVANGELISTA, Sérgio Henrique, 2000. Diagrama de limite de conformação aplicados a análise por elementos finitos de um processo de estampagem de chapas metálicas. 135f. Dissertação (Mestrado) – Universidade de São Paulo Escola de Engenharia de São Carlos, São Carlos, 2000.

[2] RISITANO, A. et al, 2017. Fatigue assessment by energy approach during tensile tests on AISI 304 steel. *Fracture and Structural Integrity*, [S.l.], n. 39, p. Pages 201-215, dec. 2016. ISSN 19718993. Available at: <<http://www.fracturae.com/index.php/fis/article/view/IGF-ESIS.39.20/1858>>. Date accessed: 30 set 2017. doi:<http://dx.doi.org/10.3221/IGF-ESIS.39.20>.

[3] K. Polaiah, Hemalatha. Naidu, P. Satheesh Kumar (2017). Friction Stir Welding of Similar Metals by Taguchi Optimization Technique -A Review. *International Journal of Advanced Engineering, Management and Science*(ISSN: 2454-1311),3(10), 0991-0994. <http://dx.doi.org/10.24001/ijaems.3.10.3>

[4] B.S. Krishnamurthy, R. Balamuralikrishnan, Mohammed Shakil (2017). An Experimental Work on Alkaline Resistance Glass Fiber Reinforced concrete. *International Journal of Advanced Engineering, Management and Science*(ISSN: 2454-1311),3(7), 730-737. <http://dx.doi.org/10.24001/ijaems.3.7.4>

Review on Exhaust Heat Recovery Systems in Diesel Engine

Mohamed Shedid, Moses Sashi Kumar

Mechanical Engineering Department, SUR University College, Sur 411, Oman

Abstract— Exhaust heat recovery system converts the thermal losses in the exhaust zone in engines into energy for work. This technology also reduces exhaust emission from engines. This review paper extends the classification of various methodologies on EHR in diesel engine. In spite of their indigenous benefit for various technologies, it has some limitation over applications to different context. From the current researches the variation in usage of exhaust heat from the diesel engine is evaluated and compared to find which methodology is suitable to attain high efficiency in thermal recovery for power generation. Finally a novel method of an EHR system is proposed to increase high percentage of heat recovery from the exhaust gas in diesel engines.

Keywords— Exhaust heat recovery system, diesel engine.

I. INTRODUCTION

Diesel engines are used in varied applications and it is also a part of a widely networked global system defined by the concepts of “resources” and “environmental pollution”. It is based purely on energy and economics aimed at minimizing the heat losses that fails to satisfy present day demands specified by the ecological imperative according to which energy and material must always be converted with maximum efficiency while minimally polluting the environment [1]. Just like gasoline engines, diesel engines are, in principle, energy converters that convert chemically bound fuel energy into mechanical energy (effective work) by supplying the heat released by combustion in an engine to a thermodynamic cycle. The heat released from the engine can be recovered to appropriate work. Researchers confirm that more than 30–40% of fuel energy gets wasted from the exhaust and just 12–25% of the fuel energy converts to useful work [2,3]. On the other aspect the toxic emissions from the exhaust gases leads to public awareness of the finiteness of fossil fuel. It has receded into the background somewhat after being raised in the 1970s; the impact of pollutant and CO₂ input into the earth’s atmosphere is again making the need for a longer-range environmentally compatible energy policy with concrete goals evident to suppress the greenhouse effect. For a better future, both

challenges conserving resources and protecting the environment would require an approach that endeavors to take full advantage of the ample potentials to save energy and additionally intensify the utilization of inexhaustible energy sources. These challenges will necessitate the research on various waste heat recovery schemes that accumulate on diesel engine through various forms for conserving the primary energy of the fuel and protecting the environment.

Exhaust heat recovery system

Exhaust heat recovery system is an energy recovery heat exchanging process that recovers heat with high potential energy in sources like diesel engine for improving its efficiency. In the present scenario there is a substantial demand of energy for global applications, so the usage of conventional fuels and its toxic exhaust gases will increase the effect of global warming. With the aspect to dwindle the usage of fossil fuels many researchers attempt to recover the waste heat from diesel engines. Various forms of heat can be categorized from engines on their origin

- Heat losses from the exhaust gas through exhaust pipeline, [1]
- Waste heat produced as cooling energy to protect engine seize, [1]
- Waste heat from intercooling to boost engine power and net efficiency,
- Waste heat convected through the engine surface.

During combustion cycle in engines the exhaust gases are dissipated through gas exchange process at a range of 300-500°C. Other sources of waste heat from engine will be transferred to the surroundings with the aid of coolant. Heat transfer occurs through the coolant medium (air, water or oil) at various points of engine to recover its complex issues. The cooling energy is transferred through heat exchangers. In case of the exhaust gas loaded with particulate matter and soot particulates is more critical in heat transfer through HXs. Aerated heat from the under hood parts usually transfer heat through radiation and convection or heat pump which works on thermal absorption cycle. To implement the heat recovery for different temperature operating conditions in engines,

various technologies has been proposed by many researchers. In this paper, a short review of the technologies for heat recovery from engines is presented.

Review on EHR systems

Thermo electric generators

Thermoelectric generators (TEG) or Seebeck generators are devices, which directly convert waste heat energy into electrical energy. These devices work on Seebeck effect, which was discovered by Thomas Johann Seebeck in 1821 [4]. Recently, for increasing the efficiency of these devices, semiconductor p-n junctions were added (Fig. 1) that are made up of new materials such as Bi-Te (bismuth telluride), CeFeSb (skutterudite), Zn-Be (zinc-beryllium), Si-Ge (silicon-germanium), Sn-Te (tin telluride) and new nano-crystalline or nanowire thermoelectric which increase their efficiency to around 5–8%. Although TEG devices have many advantages such as clean energy, without sound, without movable component and lesser maintenance costs, they are however only economical when used at high temperatures (4200 K) and when only small amounts of the power (a few milliwatts) are needed. TEG's advantages motivated many of the researchers to use it in automobile waste heat recoveries which can be seen in [5]. For instance, Karri et al. [6] studied two cases of exhaust waste heat recovery using TEGs. Also, Zhang and Chau [7] reported that using TEG has low effect on engine performance and it can improve the engine power up to 17.9% due to their smaller size of energy absorbing ratio.

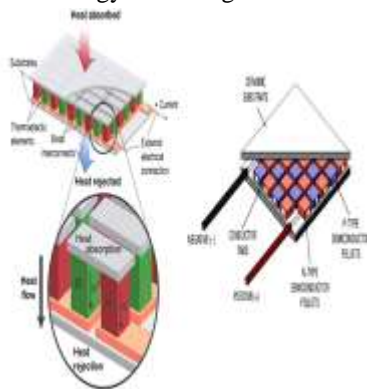


Fig.1. Detailed view of p-n junction semiconductor device

In this work, the heat exchanger connected with TEGs for recovering waste heat from an automotive channel is analyzed. As per the assertion between the infrared experimental results and the CFD simulation, a brass heat exchanger with accordion shape and surface territory (660 mm 305 mm) is chosen to form the hot side. It can reduce the thermal resistance between the exchanger and the TEMs and obtain a relatively high surface temperature and uniform temperature distribution to improve the efficiency of the TEG as shown in fig.2. The current study

focuses on the structural optimization of the heat exchanger and the coolant system to improve the efficiency of the vehicular exhaust gas heat. In the later study, the way of the simulation modeling and the infrared experimental verification that has been introduced in this article needs to be combined with the heat transfer theory, to make further structural design and optimization to improve the overall exhaust heat utilization [8].

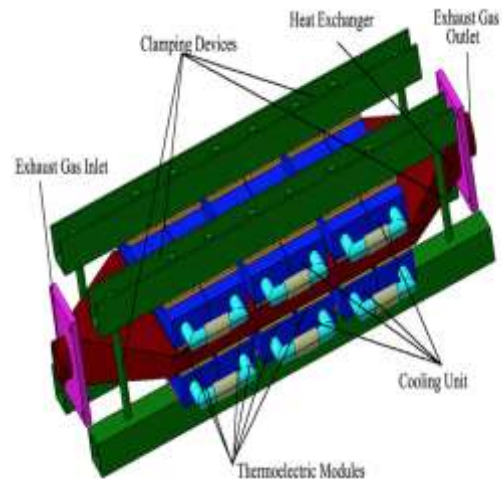


Fig.2: Schematic of automotive exhaust based TEG

Organic Rankine Cycle

Among these cycles, Organic Rankine Cycle (ORC) can be introduced as the most efficient cycle for low temperature sources such as engine exhaust. Simple ORC contains boiler, expander, condenser, pump and working fluid [9]. Many works are performed in this field and complete reviews of them are presented by Sprouse et al. [10] and Wang et al. [11]. Most of these works are based on the effect of working fluid type on the ORC performance. The different types of working fluids are wet, dry and isentropic fluids with their T-S diagram slopes being positive, negative and infinite. Chen et al. [12] by comparing 35 kinds of working fluids reached to the fact that suitable working fluid depends on the operating condition and a working fluid does not have maximum efficiency at all conditions. Dai et al. [13] mentioned that organic working fluids are more suitable for low temperature sources such as engine exhaust from the knowledge that wet fluids are never recommended for ORC due to the interaction between fluid particles and turbine blades. With a complicated system, Teng and Regner [14] exploited waste heat from the EGR system of a class-8 truck diesel engine to operate a supercritical RC with R245fa as working fluid, as demonstrated in Fig. 9. The fluid was superheated upstream of the expander, which was coaxially assembled with the alternator. The system achieved a 15.8% Rankine efficiency, which could

reach to 25.5% with ethanol as a substitute fluid. The composite fuel savings over the ESC 13-mode test cycle was up to 5%.

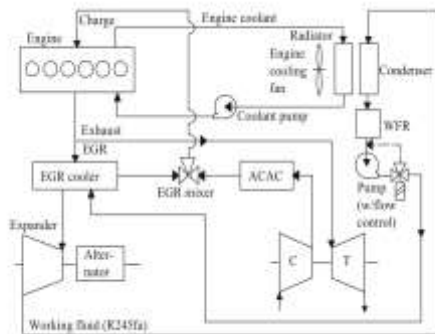


Fig.3: ARC system for waste heat recovery from diesel engine

Five stroke cycle

The concept of five-stroke engine, invented by Schmitz [15], does not reduce compression but increases expansion. The 5-stroke engine is a three-cylinder in which two cylinders perform a four-stroke cycle and alternatively a second expansion of the burnt gases is performed in the third cylinder. Turbocharger is adopted to deliver the boost pressure and the system is controlled by an innovative system called smart waste gate. It consist of variable valve timing of the two valves of the low pressure cylinder. [16].

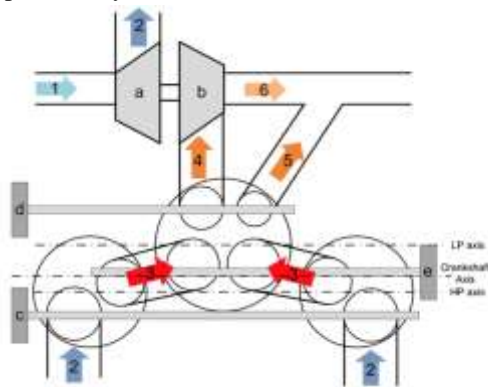


Fig.4: Architecture of the 5-stroke engine showing the valves location and the smart waste gate

Six stroke cycle

The six-stroke engine is a type of internal combustion engine based on the four-stroke engine but with additional complexity intended to make it more efficient and reduce emissions. Three types of six-stroke engines have been developed since the 1890s [17], but in one of them proposed by Conklin and Szybist [18], the engine captures the heat lost from the four-stroke diesel engine and uses it to generate an additional power without more fuel consumption. A schematic of the operation of this engine is shown in Fig. 3. As seen, there are two power strokes: one with fuel, the other with water injection by

using the waste heat of burned gases in the previous stroke. Water injection is occurred after compressing the burned gases from first stroke when the crank shaft angle is 720° . Mean effective pressure (MEP) of these engines will be increased by increasing the injected water amount. The main advantages of this engine is reducing the emissions and using from two main waste heat sources because injected water can be preheated by using an exhaust heat exchanger.

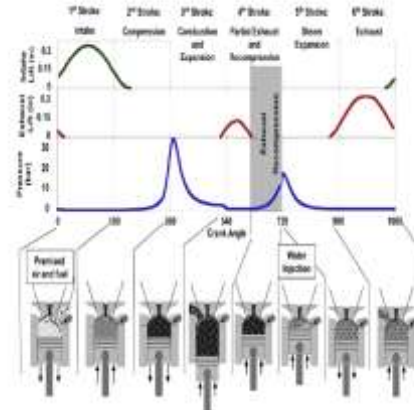


Fig.5: Six stroke engine cycle

Turbo charging

Dr. Alfred J. Buchi proposed the first idea of turbochargers in 1915, which he developed it on a diesel engine. Actually, a turbocharger is a supercharger driven with exhaust gases energy and increases the engine power by compressing the inlet air to engine. Fig. 4 shows a turbocharger with its appurtenances. A turbocharged engine is more powerful and efficient than a naturally aspirated engine because the turbine forces more air and proportionately more fuel into the combustion chamber than atmospheric pressure alone, but it has some shortcomings. Turbo- lag i.e., (hesitation or transient response) during low speed acceleration and major concerns with heated bearings are two main shortcomings in turbochargers which are approximately solved by using two stages turbochargers and variable geometry turbines (VGT) [19]. Another concern in turbochargers is increasing the intake air temperature due to its pressure increase. The warmer intake air has the less density and the less oxygen is available for the combustion event which reduces volumetric efficiency, it also leads to engine knock or detonation known as a destructive factor in engines. So, turbocharger units often use an intercooler (also known as a charge air cooler) to cool down the intake air as shown in Fig. 4. Recently, a novel exhaust steam recovery system (steam turbocharging) is presented by Fu et al [20]. They set a Rankine steam cycle system coupled on engine exhaust pipe, which utilizes the exhaust energy of engine in order to generate steam and

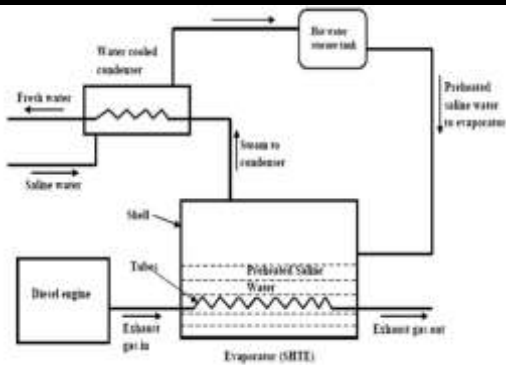


Fig.7: Circuit view of thermal distillation from EHR system

Internal combustion (IC) engine supercharging. The setup consists of IC engine working cycle and bottom cycle of waste heat recovery (WHR). IC engine exhaust gas is used to run the bottom cycle and its power used to drive the gas compressor. Numerical calculation were performed for both the heat transfer and thermodynamic processes of combined air cycle for different cycle parameters and IC engine operating conditions. Results show that the cycle efficiency and exhaust gas energy recovery efficiency depend largely on the working pressure and their maximum values appear at the working pressure of 0.35 MPa and 0.2 MPa respectively. This approach can make the fuel utilization efficiency of IC engine increase by 8.9% points and 4.1% points at most respectively compared with the naturally aspirated (NA) engine and turbocharging engine due to the reduction of exhaust gas pressure. [31]. Gao et al. [32] have proposed a WHR system where a high speed turbocharged diesel engine acts as the topper of a combined cycle with exhaust gases used for a bottoming Rankine cycle. And the result shows that heat recovery system can increase the engine power output by 12%, when diesel engine operates at 80 kW/2590 rpm.

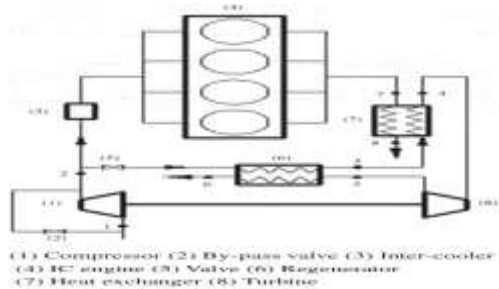


Fig.8: Schematic view of combined air cycle EHR system

Thermal storage system

Schatz [33] introduced the concept of a heat battery to store the engine waste heat using a PCM. They reported that the possible way of recovering the waste heat from the IC engine coolant and storing the heat in a PCM heat battery through experiments. This stored heat is used

during engine cold start condition by transferring heat from PCM to the engine coolant, which ensures the engine to attain operating temperature substantially faster. The energy available in the exit stream of many energy conversion devices goes as waste, if not utilized properly. The exhaust gas from an internal combustion engine carries away about 30% of the heat energy of combustion. The major technical constraint that prevents successful implementation of waste heat recovery is due to its intermittent and time mismatched demand and availability of energy. In the present work a shell and finned tube heat exchanger combined with an IC engine setup to is used to recover the heat from the exhaust gas and a thermal energy storage tank used to store the excess energy available is investigated in detail. A combined sensible and latent heat storage system is designed, fabricated and tested for thermal energy storage using cylindrical phase change material (PCM) capsules. The performance of the engine with and without heat exchanger is evaluated. Results shows that nearly 10–15% of fuel power is stored as heat in the combined thermal storage system. The performance parameters pertaining to the heat exchanger and the storage tank such as amount of heat recovered, heat lost, charging rate, charging efficiency and percentage energy saved are evaluated and reported in this paper [34].

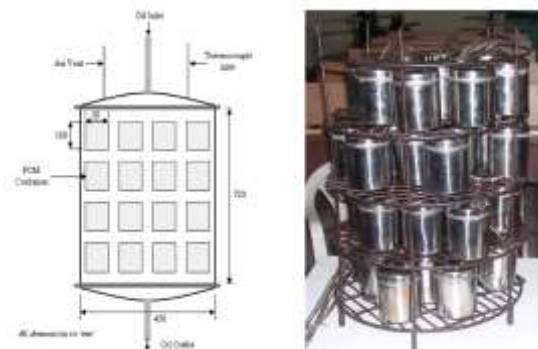


Fig.9: Layout setup of thermal storage PCM tank

Proposed methodology

The proposed methodology is an integration of thermoelectric generator with shell and tube heat exchangers for exhaust heat recovery system. The model consists of a shell and tube heat exchanger with a modified slot for TEG device i.e. (current conducting medium) placed on the middle of heat exchanger. The surface of the p-n junction device will be in contact with the thermo-electric fluid (ionic fluid) acts as a carrier medium. This absorbs the heat losses from the exhaust gas produced in the diesel engine and the cold fluid from the radiator outcome. With this integration effect, we can achieve a greater efficiency in HER system. The typical circuit of the proposed heat exchanger is shown in Fig.10.

- control of a small gasoline engine with a variable nozzle turbine turbocharger. SAE paper no. 2009-32-0169. 2009.
- [19] Sauersteina R, Dabrowski R, Becker M, Bullmer W. Regulated two-stage turbocharging for gasoline engines. BorgWarner Turbo Systems 2010.
- [20] Fu J, Liu J, Yang Y, Ren C, Zhu G. A new approach for exhaust energy recovery of internal combustion engine: Steam turbocharging. Appl Thermal Eng 2013;52:150–9.
- [21] Wei H, Zhu T, Shu G, Tan L, Wang Y. Gasoline engine exhaust gas recirculation—a review. Appl Energy 2012;99:534–44.
- [22] Zheng M, Reader G T, Hawley JG. Diesel engine exhaust gas recirculation—a review on advanced and novel concepts. Energy Convers Manage 2004;45: 883–900.
- [23] Abd-Alla GH. Using exhaust gas recirculation in internal combustion engines: a review. Energy Convers Manage 2002;43:1027–42.
- [24] Higelin P, Charle A, Chamaillard Y. Thermodynamic simulation of a hybrid pneumatic-combustion engine concept. International Journal of applied Thermody- namics 2002; 5:1–11.
- [25] Schechter M. New cycles for automobile engines. SAE Technical Paper 1999; 1999-01-0623. Chen P, Xu J. Analysis on hybrid effects of parallel pneumatic hybrid vehicle. Applied Mechanics and Materials 2013; 264-267:103–107.
- [26] Huang KD, Tzeng S, Chang W. Energy-saving hybrid vehicle using a pneumatic-power system. Applied Energy 2005; 81(1):1–18. Dönitz C, Vasile I, Onde C, Guzzella L. Dynamic Programming for Hybrid Pneumatic Vehicles. American Control Conference: St. Louis, MO, 2009; 3956–3963.
- [27] Huang KD, Quang KV, Tseng K. Study of recycling exhaust gas energy of hybrid pneumatic power system with CFD. Energy Conversion and Management 2009; 50(5):1271–1278.
- [28] Brejaud P, Charlet A, Chamaillard Y, Ivanco A, Higelin P. Pneumatic-combustion hybrid engine: a study of the effect of the valvetrain sophistication on pneumatic modes, study of a pneumatic hybrid aided by a FPGA controlled free valve technology system. Oil & Gas Science and Technology 2010; 65(1):27–37.
- [29] Trajkovic S. Study of a Pneumatic Hybrid aided by a FPGA Controlled Free Valve Technology System. Lund University: Lund, 2008.
- [30] K.S. Maheswari, K. KalidasaMurugavel, G. Esakkimuthu. Thermal desalination using diesel engine exhaust waste heat—An experimental analysis. Desalination. 2015; 358: 94–100.
- [31] Jianqin Fu, Qijun Tang, Jingping Liu, Banglin Deng, Jing Yang, RenhuaFeng. A combined air cycle used for IC engine supercharging based on waste heat recovery. Energy Conversion and Management. 2014; 87: 86–95.
- [32] Gao WZ, Zhai JM, Li GH, Bian Q, Feng LM. Performance evaluation and experiment system for waste heat recovery of diesel engine. Energy 2013;55:226–35.
- [33] Schatz Oskar. Cold start improvement by use of latent heat stores. Automotive Eng J 1992:1458–70.
- [34] V. Pandiyarajan, M. Chinna Pandian, E. Malan, R. Velraj, R.V. Seeniraj. Experimental investigation on heat recovery from diesel engine exhaust using finned shell and tube heat exchanger and thermal storage system. Applied Energy. 2011; 88: 77–87.

Estimation of Reservoir Storage Capacity and Maximum Potential Head for Hydro-Power Generation of Propose Gizab Reservoir, Afghanistan, Using Mass Curve Method

Khan Mohammad Takal¹, Abdul Rahman Sorgul², Abdul Tawab Balakarzai³

^{1,2}Assitant Professor in Civil Engineering Department, Helmand University, Afghanistan

³Professor in Water and Environmental Department, Kandahar University, Afghanistan

Abstract— The present study objective is to estimate reservoir storage capacity and maximum potential head for hydro-power generation of the proposed Gizab multipurpose dam site in the Upper-Helmand river basin, Afghanistan. The mass curve is used to estimate the reservoir capacity and maximum potential head for power generation with the utilization of various years mean monthly flow data of the Upper-Helmand River Basin at the proposed Gizab dam site. The reservoir volume is 4709.12 Mm³ at 1435m elevation from mean sea level with reservoir capacity of 1114.3 Mm³ with annual average inflow of 100.9m³/s and annual demand of 100m³/s. The net potential head of the proposed Gizab site is 117m with power generation of 91.822 MW with using of Francis turbine efficiency of 80%.

Keywords— Gizab, Upper-Helmand, Mass Curve, Maximum Potential Head, Francis Turbin.

I. INTRODUCTION

In order to professionally operate reservoirs for hydropower generation, irrigation, and flood control, the management of water quantity within the reservoir is required (Salami et al., 2012). Beside volume of water in the reservoir the water surface elevation within the reservoir can be an indication of available storage. These relationships between elevation and storage volume, similar to area-volume and elevation-area relationships makes it possible that engineers can find fairly accurate value of one parameter from the other (Magome et al., 2003).

From surface water resources the adequacy and reliability of the water supplies for deferent propose are dependent upon the ability of reservoirs to make available sufficient water storage during the critical dry periods (Bharali, 2015). But these surface storage reservoirs also face many

problems for their decrease of safe yields such as increases in water demand due to increases in population and gradual loss of reservoir capacity yield because of sedimentation in the reservoirs.

For water resources management the remote sensing and GIS is a supplementary solution, therefore, this techniques provide cost and time-effective estimation of storage capacity, require little human supervision, free of secretarial barriers or political interference, and must be demonstrably reliable over long periods and in all kinds of weather (Salami et al., 2012). Remote sensing data is used to provide elevation contours and water spread area of each contour and volume of reservoir at different water levels of a reservoir.

II. STUDY AREA

The proposed Gizab reservoir (Fig. 1) is a multi-propose project across the Helmnad river basin, Afghanistan. The proposed reservoir is located between 33° 22' 10"N and 33° 33' 25" N and 66° 10' 00" E and 66° 27' 40" E. The length of the reservoir is measure about 43 km in length and 15.10 km in width at its longest and widest point of reservoir. The reservoir surface area is 74.82 km² in 1435m elevation from mean sea level with volume of 4709.12 Mm³.

Hight of the proposed Gizab reservoir catchment area is varying from 1299m to 5036m w.r.t mean sea level (Fig. 2) with area of 22070 sq km. The catchment area is embodied by large hills, buried pediments, vallies and alluvial plains. The soil textures are silty clay, sandy, loamy and alluvium. The upper-Helmand river basin originated in a westerly extension of the Hindu Kush mountain range near Paghman about 40 kilometers west of Kabul and runs southwesterly to the proposed Gizab reservoir. The river water runoff comes mostly from rainfall at the average elevations of the

basin in winter and spring season and from snow melting of the glaciers at the high altitude of mountains which escalate to elevations of 5036 meters. Range of Annual precipitations varies between 100mm to 670mm and precipitate mostly at higher altitudes during winter and spring. The Mountains cause many local variations, though

the upper-Helmand river basin is categorized by a dry continental climate. The temperature of this region is varying from minus (-)10 °C in winter to plus (+) 34 °C in summer. The fluctuations in temperature are not uniform in character all over the whole basin.

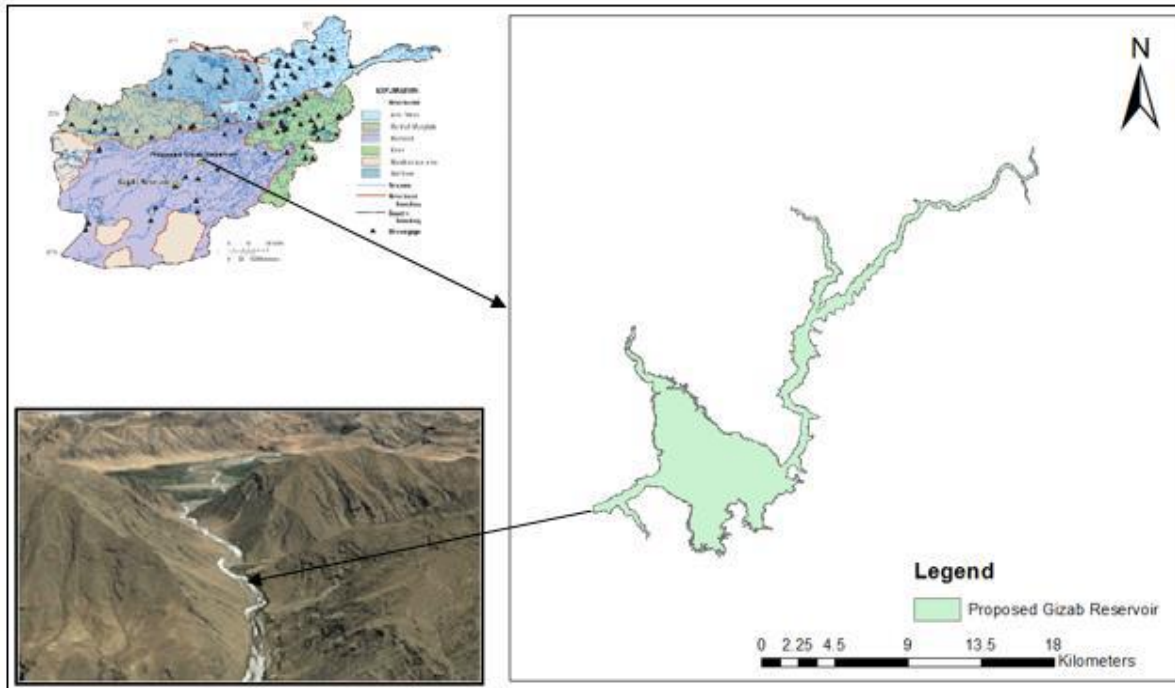


Fig.1: Study Area of proposed Gizab reservoir

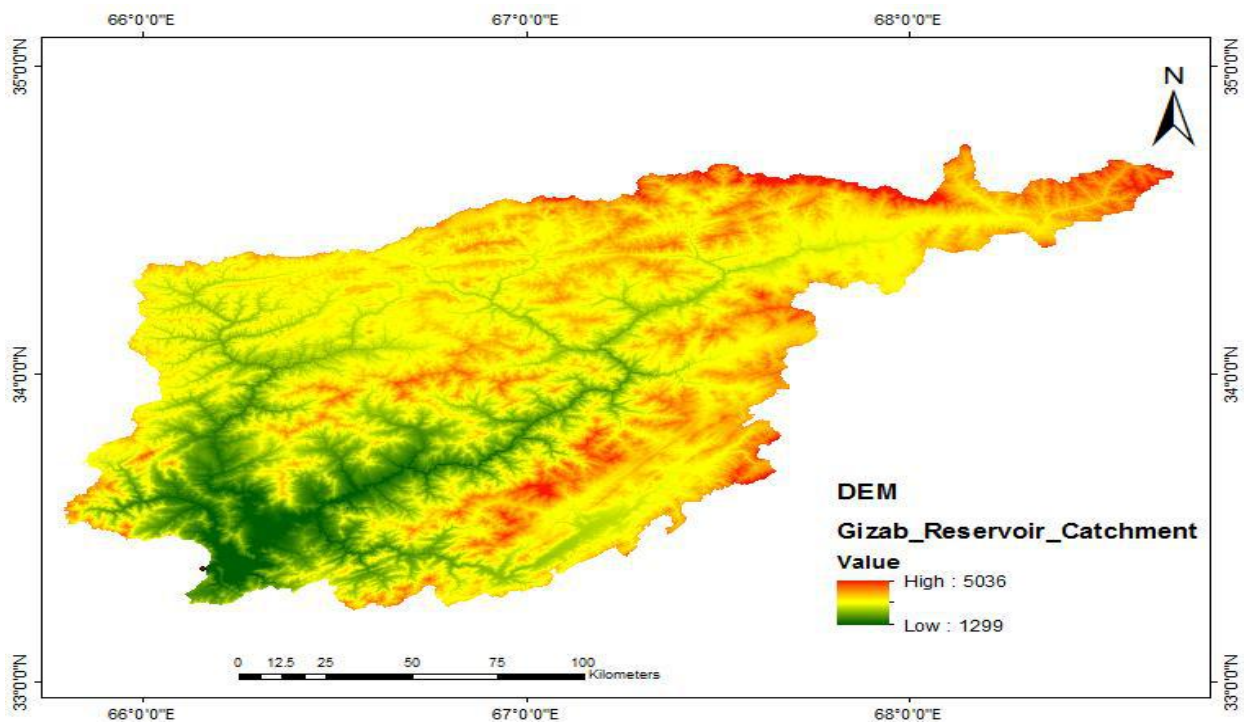


Fig.2: Digital Elevation Model of Gizab Reservoir Catchment Area

III. METHODOLOGY

3.1 Data Accusation

DEM (Digital Elevation Model) is derived from ASTER (Advanced Space borne Thermal Emission and Reflection Radiometer) and downloaded from <http://earthexplorer.usgs.gov/>. The contour map is generated from ASTER DEM in Global Mapper 18. Stream flow of the Gizab reservoir is downloaded from Water Atlas of Afghanistan.

3.2 Mass Curve

A cumulative plotting of net reservoir inflow versus time duration is a mass curve (or Ripple diagram, 1882) and is expressed as:

$$V(t) = \int_0^t Q(t) dt \tag{1}$$

Where V (t) = Volume of runoff and Q (t) = Reservoir inflow, both as function of time.

At any point on the mass curve the slope of the tangent of that point shows the rate of flow at that point on the mass curve and expressed as

$$Q(t) = dV(t) / dt \tag{2}$$

In the design of a reservoir storage capacity, operations procedure and flood routing the mass curve hasvaluable applications.

Mass curve preparation procedure is given below:

Plot mass inflow curve from the flow hydrography of the site for a number of consecutive years

Plot the mass demand curve corresponding to the given rate of demand.

Draw the tangential line parallel to the mass demand curve at peak point of mass inflow curve

Determine the vertical intercepts between the tangential lines and the mass inflow curve.

Determine the largest of the vertical intercept determined in step (4).

The largest vertical intercept represents the storage capacity required.

3.3 Hydro-Power Potential Head

ASTER DEM 30 x 30m is used in Arc-GIS 10.3 platform with Arc-Hydro Tools to delineate catchment area under the study. The delineated watershed and ASTER DEM 30 x 30m of proposed Gizab reservoir is used in Global Mapper 18 to generate contours line map for the reservoir and dam site. The area of each contours are created in Global Mapper 18. Both shape files of contours line map and area of each contour are exported to Arc-GIS 10. Further, from contours line map the Triangular Irregular Network (TIN) is created from Data Management in 3D Analyst Tools. The volume and surface area of each contour is derived from Triangular Surface in 3D Analyst Tools. MS-Excel is used to find the

net head of reservoir all the methodology framework is described in Fig.4.

Power generation is always depending on two important parameters discharge and head of water from upstream to downstream. Penstock is conveying water from storage reservoir to powerhouse with turbines. The power potential of flowing water is function of discharge, specific weight of water and head between turbine and reservoir active storage capacity level. Hydro-Power potential of water is express mathematically as below:

$$P = \eta \gamma Q H \tag{3}$$

Where P = Power (W)

$\gamma = \rho g$ = Specific weight of water (N/m³)

ρ = Mass density (kg/m³) = 1000 kg/m³ for water

g = Acceleration due to gravity (m/s²)

Q = Discharge (m³/s)

H = Head (m)

η = hydraulic turbine efficiency and its typically value is taken from Table. 1

Table.1: Typical efficiency value of different type of turbine

Turbine Type	Efficiency value range
Impulse Turbine	
Pelton	80-90%
Turgo	80-95%
Cross flow	65-85%
Reaction Turbine	
Francis	80-90%
Pump as turbine	60-90%
Propeller	80-90%
Kalpan	80%

Based on the below chart Fig. 3 the turbine was selected for the propose Gizab reservoir

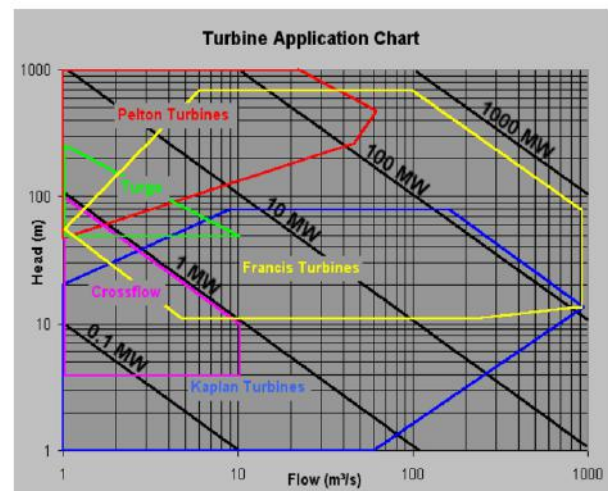


Fig.3: Turbine selection chart

<http://rivers.bee.oregonstate.edu/book/export/html/35>

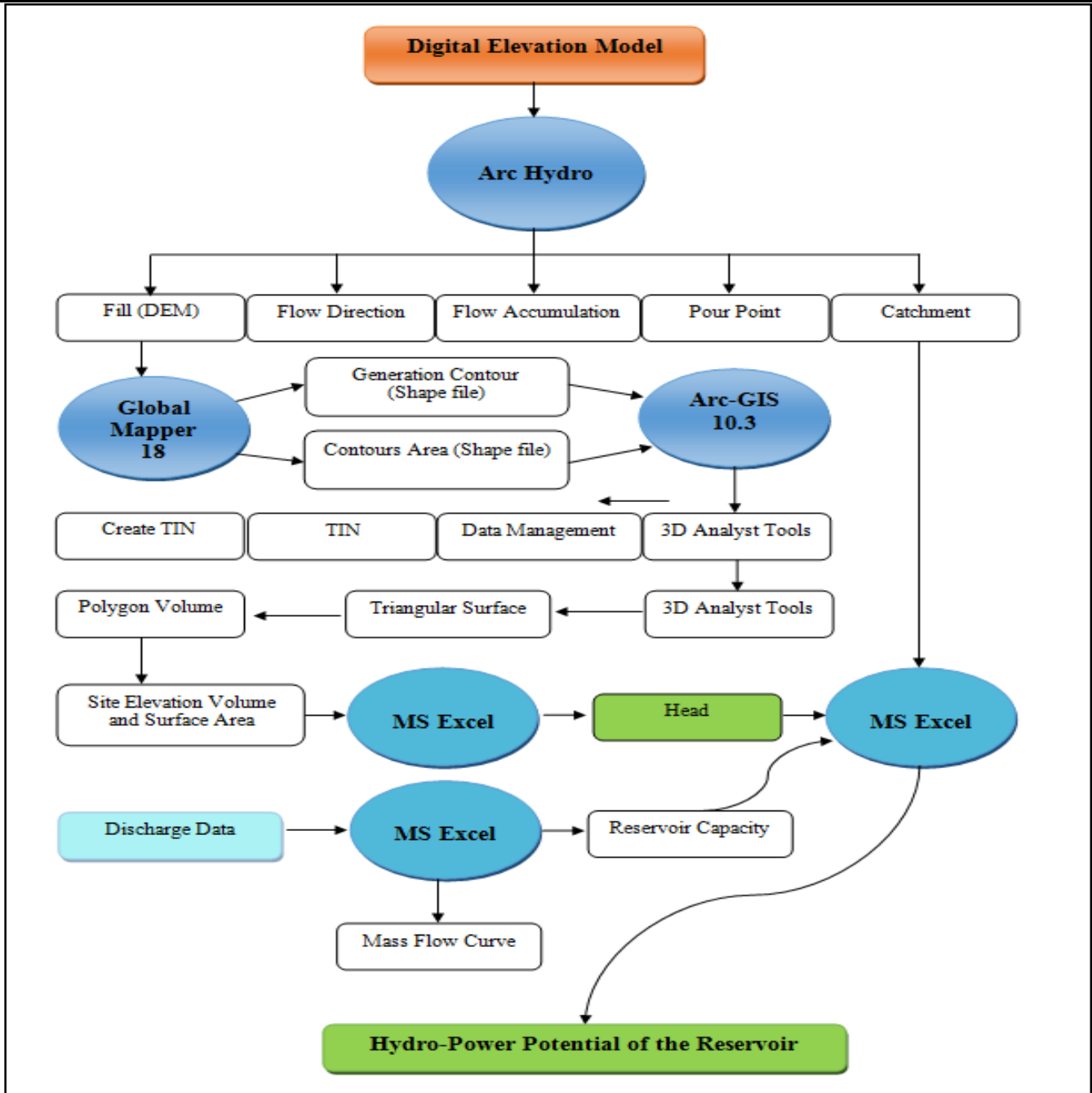


Fig.4: Methodology Framework of Reservoir Capacity and Hydro-Power Potential Head

IV. RESULTS AND DISCUSSION

The relief of the proposed Gizab reservoir catchment area is 3737m. The contours elevation of the proposed reservoirin proposed site is started from 1310m to 1530mfrom mean sea level and carried out by Global Mapper 18. Therefore, reservoir area and volume of each contour is carried out form ASTER DEM using Global Mapper 18and Arc-GIS 10.3 which is given in Table 2.The relationship between elevation -volume and relationship between elevation-area

is shown in Fig. 5. Finally the gross potential head of the reservoir full supply level to powerhouse is 130m and the net potential head is 117m with 10% head loss in the conveying. Ten percent of total reservoir storage capacity is used for dead storage capacity of sediment trapping for the design period. The volume of dead storage capacity is 470.912 Mm³ which is coming under the contour of 1349m height from mean sea level.

Table.2: Contours Elevation, perimeter, volume and surface area of proposed Gizab reservoir

Contour Name	Contour Elevation (m)	Perimeter (sq km)	Volume (Mm ³)	Surface Area (sq km)
1310	1310	0	0	0
1315	1315	13.67	3.633	0.866
1320	1320	42.914	20.354	4.608
1325	1325	32.796	67.914	10.849
1330	1330	37.824	129.316	13.043
1335	1335	41.243	200.831	15.099
1340	1340	45.301	284.119	17.477
1345	1345	50.918	379.391	20.308
1350	1350	52.088	490.504	22.861
1355	1355	68.907	640.255	27.266
1360	1360	82.246	790.932	30.948
1365	1365	92.505	956.390	34.211
1370	1370	103.76	1141.456	37.831
1375	1375	103.58	1335.163	40.461
1380	1380	108.42	1543.405	43.199
1385	1385	111.87	1758.255	45.502
1390	1390	129.6	2000.683	49.065
1395	1395	133.49	2248.741	51.769
1400	1400	137.12	2508.345	54.407
1405	1405	143.84	2781.632	57.305
1410	1410	153.51	3071.348	60.459
1415	1415	153.2	3372.173	63.308
1420	1420	159.39	3686.185	66.030
1425	1425	162.8	4013.118	68.960
1430	1430	166.98	4353.152	71.769
1435	1435	175.06	4709.118	74.822

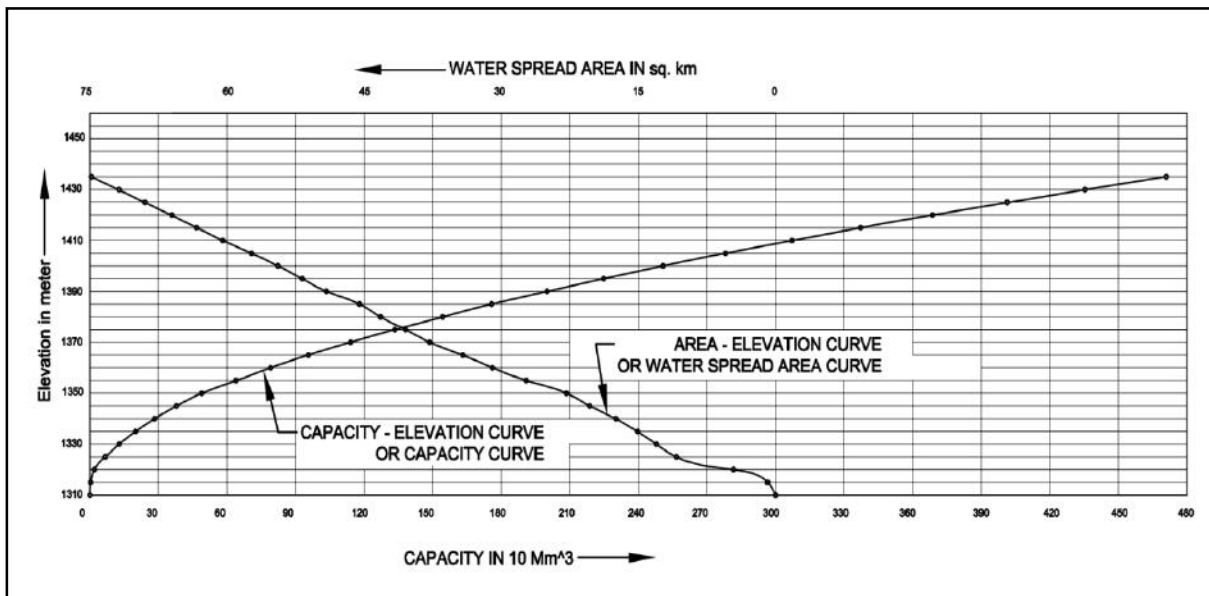


Fig.5: Capacity-Elevation and Area-Elevation curve of proposed Gizab Reservoir

The mean monthly discharges are given in Table.3 the maximum discharge is 310.347 m³/s in the month of June and the minimum discharge is 30.119 m³/s in the month of December. The average discharge of 12 month is 100.899

m³/s. The reservoir storage capacity from the mean monthly inflow is driven from mass curve is 1114.356 Mm³ Fig.6. Also the reservoir storage capacity is driven analytically from monthly mean inflow Table.3.

Table.3: Mean monthly inflow and propose Gizab reservoir capacity

Date	Inflow in m ³ /s	Inflow in Mm ³	Demand in m ³ /s	Demand in Mm ³	Deficit In Mm ³	Surplus in Mm ³
Jan.	32.465	86.955	100	262.660	175.705	
Feb.	36.081	93.523	100	262.660	169.137	
Mar.	38.577	103.326	100	262.660	159.334	
Apr.	55.657	149.073	100	262.660	113.587	
May.	55.227	133.606	100	262.660	129.054	
Jun.	178.966	479.344	100	262.660		216.684
Jul.	310.347	804.419	100	262.660		541.759
Aug.	240.462	644.053	100	262.660		381.393
Sep.	105.050	272.290	100	262.660		9.630
Oct.	97.372	260.801	100	262.660	1.859	
Nov.	30.119	80.670	100	262.660	181.990	
Dec.	30.467	78.971	100	262.660	183.689	
Total					1114.356	1149.465

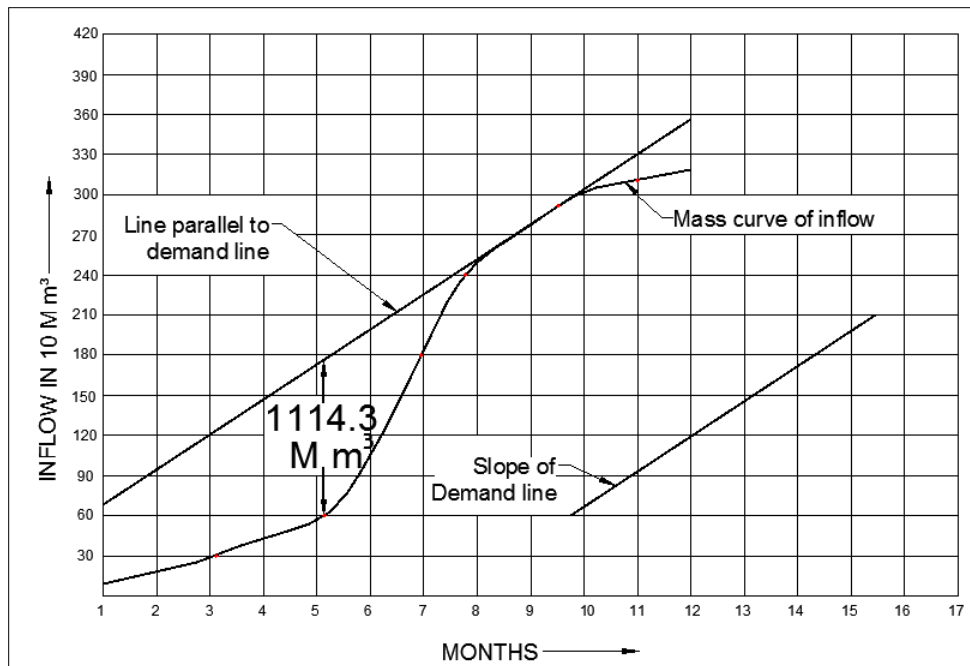


Fig.6: Mass inflow curve diagram of Gizab reservoir

Based on the flow rate and estimated net available water potential head 117 m the assessed hydropower potential is calculated using Eq. (3) as 91.822 MW. Francis turbine has selected for this study from turbine selection chart and the hydraulic efficiency of the turbine is 80%. The analysis

shows that the Gizab reservoir has a good storage capacity with a good water potential head for the generation of hydropower establishment.

V. CONCLUSION

- The reservoir capacity is the most important aspect for hydrologic design.
- The reservoir capacity is design for mean monthly inflow data of several years using Mass Curve method and the storage capacity is 1114.3 Mm³.
- The gross storage volume of the proposed Gizab reservoir is 4709.118 Mm³ and carried out from ASTER DEM using Global Mapper 18 and Arc-GIS 10.3.
- The gross potential head of the reservoir full supply level to powerhouse is 130m and the net head for the generation power is 117m with 10% head loss of gross potential head at system operation.
- The Francis turbine with 80% efficiency has used for the study.
- At available head with use of Francis turbine and its efficiency of 80%, the hydropower potential is 91.822 MW.

REFERENCES

- [1] Magome J, Ishidari H, Takeuchi K (2003). "Method of Satellite Monitoring of Water Storage in Reservoirs for Efficient Regional Water Management" Water Res. Systems-Hydrological Risk, Manag.
- [2] Salami Y, Nnadi F (2012). "Seasonal and Inter-annual Validation of Satellite-Measured Reservoir Levels at the Kainji Dam". Int. J. Water Res. Environ. Eng., 4(4): 105-113.
- [3] Bharali Biswadeep (2015). "Estimation of Reservoir Storage Capacity by using Residual Mass Curve" Journal of Civil Engineering and Environmental Technology., 2(10): 15-18.
- [4] Sharma K.R., Sharma .K.T (2008). "Irrigation Engineering Including Hydrology" S. Chand & Company PVT.LTD, Rama Nagar, New Delhi-110055.
- [5] Garg. K.S (2016). "Irrigation Engineering and Hydraulic Structures" Khanna Publishers Daryangani, New Dehli-110002.
- [6] Purnia.B.C, (2009)." irrigation and water power engineering"; Laxmi publication (P) ltd, New Delhi,.

Pronunciation Remedy of Scientific Plants Names with Pair Exercise Using Flash card Media at Students Plant Taxonomy Course

Pujiastuti, Imam mudakir, Iis Nur Asyiah, Siti Murdiah, Ika Lia Novenda, Vendi Eko Susilo

Lecturer in Biology Education, Faculty of Teacher Training and Education, University of Jember, Indonesia

Abstract— *The botanical nomenclature is a part of plant taxonomy. International communications of the name of plants in the oral and written forms are arranged in the botanical nomenclature system, using the scientific names of plants in Latin or Latinized language. From the point of view of Indonesian language the oral form or the pronunciation of the scientific names of plants are not always similar to Reviews their written form. The written form and the oral forms of scientific names of plants are arranged in the chapter of Pronunciation of the Scientific Names of Plants. In fact it was found that the pronunciations of the scientific names of plants are often pronounced wrongly by about 57.2% of the students. The improvement steps in terms of students' abilities in pronouncing the scientific names of plants are needed to be done using flash card media containing pictures and the scientific names of plants. The research result shows that after four training periods, the couple training using flash cards media can decrease the range of errors in pronouncing the scientific names of plants made by the students. The number of the students who Pronounce the scientific name of plants wrongly Decrease from the number of 57.2% into the number of 9.7%. As many as 17 scientific names of plants that are pronounced wrongly by the students now Decreased into 14 scientific names, from a total of 30 names.*

Keywords— *pronunciation, the scientific names of plants, flash card.*

I. INTRODUCTION

The nomenclature of plants is a part of Plant Taxonomy. The scientific names of the plants that are written in Latin or Latinized language have a different character with the Indonesian name or region. The scientific names in Latin, often differ between the written form and the oral form (or the pronunciation), so it can be something difficult for the students. The fact shows that college students do mistakes

in pronouncing certain names of plants which have been stipulated in the scientific nomenclature. For example, the name *Rhoeodiscolor*, where the letter *oe* on word *Rhoeo* should be spoken *e*, but it is pronounced *oe*. by 85% of the students, while only 15% of students who pronounce it correctly. Likewise for the other names, error rate of pronunciation is also high. Education Workforce Institutions like FKIP has the duty to prepare educators to be. Errors that occur in the *pronunciation* of scientific names of plants among college students, must be minimized, even should be eliminated. Errors that occur among prospective teachers, can cause errors among the students at the school, later in life.

Based on the description above, this paper discusses about the efforts made and implemented in Biology Education Study Program (P.BIO) FKIP University of Jember, particularly in Plant Taxonomy Course, in terms of pronunciation of the scientific names of the plants. This work is done in order to minimize pronunciations errors of scientific names of plants among students that are going to be teachers.

Pronunciation of the scientific names of plants

Scientific names of Plants are the names that are known by the whole world. The scientific naming of plants are based on the rules that have been defined in the *International Code of Botanical Nomenclature* (ICBN). The scientific names of plants use Latin words or Latinized words from some other languages (Tjitrosoepomo, 2009). New information about the type of plant, or a scientific name change must be authorized by ICBN (Llomas, 2003). One of the methods of Latin pronunciation method agreement used today is the *English method*. The use of English method of pronunciation has the consequence of following the English words pronunciation. Some general rules for the pronunciation of the scientific names of plants are;

1. If a single consonant exists between two vowels, consonant is read with vowels that follow it. Example: acer, is read a-cer
2. If two consonants exist between two vowels, then the first consonant is read with the first vowel, and the second consonant is read with the second vowel. Example: albidus, is read albidus.
3. The final vowel, is pronounced in a long way. Example: Alsine, is read al-si-nee, except the letter *a*, is sounded with *ah*.
4. Letter *ae* and *oe* are pronounced with a long *e*. Example: laevis is read lee-vis; rhoeas, is read ree-as.
5. The letter *C* is read with the sound *s*, letter *g* is read with the sound *j* if they meet the letters *e*, *i*, *y*, *ae* or *oe*. Example: Cedrus, see-drus; cyaneus, si-ne-us; -a g, eneralis je-ne-ra-lis. But the letter *C* will be read with the sound of *k*, if it is followed by the letters *a*, *o*, or *u*. Example: Candidus, is read kan-in-dus
6. If a word begins with one of these consonant pairs, the first letter is not pronounced: *cn*, *ct*, *gn*, *mn*, *pn*, *ps*, *pt*, *tm*. Example: *cnicus*, is read *nicus*; *ctenium* is read *te-ni-um*; *psyllium*, is read sil Li-um.
7. If a couple of letters *ti*, followed by the vowels: *a*, *u*, *e*, *o*. then *t* is sounded *s* example: *Opuntia* is read *Opunisia* (Radford, 1986) as well as some other rules, which generally are used to be spoken correctly.

Exercise In Couples

Pair pronunciation exercise of the scientific names of plants is intended to stimulate mutual peer correction. In essence, this activity gives students opportunities to practice activities pronouncing the scientific names of plants, more often. Mispronounce done by students, are expected to be corrected by the partner of training. Practicing in pairs with friends, give a better chance of success, rather than if it is performed alone. Learning in this manner substantially is similar to the discussion. Discussion train students to get used to listen to the others' opinions, even though it may be different from their own opinions; it also trains students to tolerate (Asmani 2010). Cooperation learning oriented between friends is essentially the Cooperative Learning model. Cooperative learning model, not only helps the students understand difficult concepts, but also improves the cooperative ability, social skills, and thinking ability (Susilo, 2007). Such conditioning effort is one of the classroom management elements. Classroom Management conducted by educators, aims at creating a good social atmosphere in the classroom, so that it can provide the satisfying conditions, discipline atmosphere, intellectual, emotional, positive attitude and appreciation for the learners (rusydie, 2011). Intellectual, emotional, positive

attitude and appreciation of the learners, enabling the better achievement of learning goals. Errors that are occurred, are expected to be minimized, in this case primarily scientific errors in pronouncing the names of the plants .

Media flashcard

Media comes from the Latin word *medius* which mean is central, introduction or intermediary. Learning media is a means of intermediaries in the learning process. Benefits of the media, are: it can clarify the message, overcome the limitations of space, time and senses, it also gives rise to common perception, stimulates learning, creates a positive attitude toward the subject matter and provides the condition of direct interaction between learners and learning resources (Daryanto, 2011). *Flashcard* media is a small card containing images, texts, or symbols that reminding or guiding students to something related to the pictures. The card size is usually 8 x 12 cm, or can be adjusted to the size of the class face (Arsyad, 2009). The images that are used in the cards can be selected in the form of photographs. A representative photograph gives an overview that can represent the real thing, gives the same perception to the learner. Photos that are selected and used in accordance with the specified learning objectives, can fulfill their functions to raise the motivation and interest of the students (Arsyad, 2009). Motivation determines the learning persistence, someone who has been motivated to learn something, will give his effort to obtain good results (Uno, 2011). Photos of a wide variety of plants are equipped with regional and scientific names. Some of the plants that are shown in the photos can be found in the students surrounding environments, and some of them are still unfamiliar for the students or they just seen them for the first time. Photos of the new plants that are first seen by the students, attract the students' attention, they give a real picture of what is imagined by the students from the names that they have ever heard or read. Watching photos of plants helps the students to remember the characteristics or the names of plants better than hearing or reading. Dale put the visual symbols experience more concrete than verbal symbols (Daryanto, 2011). Photographs of plants which accompanied the plant names both local and scientific names, give more impression for students. This impression is an extrinsic factors that can encourage students to learn more hard and diligent (Uno, 2011).

Plant Taxonomy Courses

Plant Taxonomy Course is one of the subjects in the Biology Education Studies Program at FKIP University of Jember. This course has 4 SKS (Semester Credit Units) , with details of 2 credits of practicum (1 time meeting), 2

credits lecture consists of two meetings a week. Total meetings are 3 times in a week. Plant Taxonomy Class syllabus contains competencies that must be achieved by the student after taking this course, those competencies are as follows: After taking this course, students can analyze the diversity of plants based on the classification system of plants and can apply it in daily life. Furthermore, to achieve these outcomes, the student must have the ability to describe, identify, apply the nomenclature of plants, including mention the scientific names of plants properly.

Plant taxonomy is the main part of the Plant Systematic consists of four components: *Description, Identification, Nomenclature, Classification* (Simpson, 2006). Formal naming plants and all the rules have been set in the ICBN. The scientific name of the plant is set on the term of writing and pronunciation.

The fact that encountered in the implementation of Plant Taxonomy courses, mainly on the part of the nomenclature, students often make a serious mistake when they pronounce the scientific names. The main cause is due to a lack of knowledge, lack of exercise on students, because between words and sounds are not always similar according to the Indonesian character. Mistakes made by students even have been done they were at the previous education level. Errors that have been occurred for a long time then become a habit for the students and it is very difficult to be repaired. That is why it needs special trick to fix it. The way in pronouncing the scientific names, as well as the language, needed to be practiced repeatedly. Exercises are performed with friends in pairs, where each other give correction and motivation. Practice with friends is more comfortable for the students because it reduces inhibitions and embarrassment when they are making mistakes, rather than if it is corrected by the teacher. How learning takes place, will determine the learning quality of the learners. Beside affected by external factors learning quality of the learners is also affected by individual factors of the learners, such as difficult to concentrate, less passionate, selfish, shy or less socialize with friends (Rusydie, 2011). Practicing in pairs, is expected to minimize those factors. Creating a pleasant situation in the learning process, is an attempt to attract learners attention to what they learn. Utilization of *flashcard* media that contains the scientific name of plants that are concerned with image (an image from the photo), beside increase the students' interest, also help the students to remember the names and characters of the plants. The learning activity is a complex process that involves several aspects and components that mutually affect each other, so it requires good management skill (Sobri et al, 2009). Integrating pair exercise and the use of *flashcard* media is an

effort in managing instructional activity to achieve the learning objectives.

II. METHODOLOGY

Application of cooperative learning with pair exercises using flash card media containing photographs and scientific names and characters of plants in the subject of Plant Taxonomy, aims at repairing the pronunciation errors of the scientific name of plants that are often done by the students. Furthermore, to achieve competence in Plant Taxonomy courses generally. Cooperative learning with pair exercises using *flashcard* media, in the subject of Plant Taxonomy consider the aspects that are contained in the National Education Act No. 20 of 2003 (Iskandar, 2011). Those aspects are included in the lesson plans of learning and applied in the learning process and evaluated at the time or at the end of the lesson. Steps taken in this study were as follows:

As many as 40 students of Plant Taxonomy course are required to read the scientific names of plants at the beginning of the course, as the initial data. They do this by saying / reading 30 scientific names of plants in rotation and marked on a list of names that are spoken wrongly by the students. After all students read and marked on the names that are spoken wrongly by the students, then counted how many students who do the mistakes in reading the scientific names of plants. Errors that are already on the list, then discussed based on the theory of plant nomenclature set out in the ICBN. After the rules of nomenclature and *pronunciation* / pronunciation have been known and mastered by the students, then the students are trained to pronounce the name.

Flash card plants names are made by the students. Each student make a card with the prefix letters in the order, each letter on 5 different plants names, so the number of *flash card* that are made are as many as $5 \times 26 = 130$ pieces for one series. As many as 200 pieces cards are made by 40 students by repeating the series, each student makes 5 pieces with different name for every letter. Plants cards that have been made by students, then verified and compliance with the provisions, including the names which are often pronounced wrongly.

The implementation is set as follows: 40 students divided into five major groups, each group consists of 8 students. Each group set themselves sitting opposite in pairs. A pair of students hold 10 sheets of *flash card* / card. One person practice reading scientific name, while his partner to listen and observe. if something goes wrong, the partner tries to correct. This be repeated in 5 minutes duration, then change the turn with their partner. After completion of the partner turn, exchange the cards with another couple in the same

group, and it is repeated in the same way for each pair. Once completed in one group, exchange the cards with another group, until all groups have read all the cards available. The exercise is repeated until 4 meetings.

Evaluation was conducted in the same manner by obtaining initial data. The results then compared with the initial data, the analysis is done for each of the representatives of the plants names, to count how many students pronounce wrongly. After it is viewed as a whole, see how many pronunciation errors made by the students after being trained in learning. Interviews are done to the students, at the end of the study. Interviews provide an opportunity for students to express what they feel after what happened in

the learning with in pairs training methods using *flashcard* media. For students who do not have the opportunity to speak, are excused to write their opinion to be submitted to the lecturer.

III. RESULTS AND DISCUSSION

After the evaluation to the pronunciation of scientific names of plants, it was obtained 17 scientific names of plants that were pronounced incorrectly by some students of 30 scientific names of plants selected. The result can be seen in the following table;

Table.1: Scientific names of plants spelled wrongly and the number of student who pronounce wrongly

	scientific name of plants	beginning	the end of the course
1	<i>Caesalpinia pulcherima</i>	32	4
2	<i>Eugenia aromatica</i>	28	2
3	<i>Flacourtia rukam</i>	34	8
4	<i>Gnetum gnemon</i>	26	4
5	<i>Hedychium coronarium</i>	12	8
6	<i>Ipomoea aquatica</i>	37	4
7	<i>Justica brook</i>	21	7
8	<i>Kaempferia rotunda</i>	19	5
9	<i>Leucaena glauca</i>	21	4
10	<i>Morinda citrifolia</i>	8	0
11	<i>Nephelium litchi</i>	7	4
12	<i>Opunthe vulgaris</i>	32	4
13	<i>Psidium guajava</i>	29	0
14	<i>Pteris ensiofrmis</i>	29	0
15	<i>Psilotum nudum</i>	29	2
16	<i>Rhoeo discolor</i>	34	7
17	<i>Triticum aestivum</i>	12	4
	Total	389	66
	average	22.88	3.88

Data on tabel.1 showed that at the beginning of the lecture, of 30 scientific names of plants chosen, there are 17 names of plants were pronounced incorrectly by the general students, while the rest, which were 13 plants names (not diagramed), generally pronounced correctly by students, or pronounced incorrectly by no more than 3 students. The error occurred on the pronunciation of the underlined letter in tabel.1 above. At the beginning of the term, from 30 scientific names of plants that should be read by all the 40 students, there were 17 scientific name spelled wrongly by more than 3 students. Data show that 17 scientific names

plants pronounced incorrectly by an average of 22.88 students, which means 57.2% of the 40 students.

After the students getting an explanation about the correct pronunciation, and after practicing in pairs using *flashcard* media during the four periods, the error were greatly reduced. From 17 scientific names of plants that were spelled wrongly by an average of 22.88 students, which means 57.2% of the 40 students, after the learning process the number decreased into 3.88 students, which means that 9.7% of 40 students. From the information obtained from the students, it was known that they pronounce the namely wrongly way since before entering

the college level. Although they pronounce the name correctly, they claimed that they did not to know grammatical rules. Their mistakes sometimes were corrected by a friend or an assistant on the course before the taxonomy of the plants, then they changed the pronunciation. But then they forgot again afterwards. After learning grammar pronunciation rules, the student tried to change the wrong habits with practicing in pairs with friends. Practicing in pairs is a more effective way rather than discussing with the crowd. The discussion becomes ineffective if the group is too large, the group could be dominated by certain people who like to talk (Asmani, 2010). Practicing in pairs is also approved by the students, it gives them the opportunity to develop their potential. Atmosphere of learning and the learning process that allow students to actively develop their potential, is one of the things implied in the Act Sis Dik Nas 20 yrs, 2003 (Iskandar, 2011). Learning is doing and it is a process that makes the learners more active, means that learners should dominate the activity (Sardiman, 2007).

Flashcard media give a more concrete pictures of the plants studied, and also help the students to remember how to pronounce the names correctly. In general, the students stated that the Flash card containing photos of plants are very helpful to remind how to pronounce the scientific name, especially if they can see the plant everyday in their surrounding environments. Data showed that as many as 3 of 17 plants, even pronounced correctly by all of the students. Those plant are *Morindacitrifolia*, *Psidium guajava* and *Pterisensiformis*. the first 2 plants mentioned are well-known by all students, because there are many of them that can be found in the daily life. The picture of Dale cone experience put the visual symbol more concrete than verbal experience (Daryanto, 2011). Visual symbols contribute larger memory than the verbal symbol. Pictures from the photo illustrate the plant are easily remembered by the students, and it also make them easier in considering how to pronounce it. Visualizing images in the mind is also called *visualimagery*, it is one way to improve memory (Waid, 2011). Practicing pronounce the scientific names correctly and repeatedly, is the way of habituation. The more frequent the practice, the more accustomed students to pronounce correctly. It is proved that after practicing repeatedly, during the four periods, errors which were performed by as many as 22.88 or 23 students in the beginning, were reduced to an average of 3.88 or 4 people. Information obtained from the students both orally and in written, providing information that practicing with friends provides emotional flexibility, eliminates awkward feeling and provides free-error-correcting by friends. Media containing

photos of plants studied were also very helpful in remembering the object and pronouncing the scientific names correctly. Considering the object of the photograph is the mental activity of each individual learner. Practice saying in pairs is a group activity. In Teaching and Learning Activities (KBM), the approach taken by the lecturer will produce various learners activities, whether individually or in groups, and the combination of both will produce better learning outcomes (Djamarah, 2002). It was proven that after the end of the lesson students pronounce the scientific names of plants wrongly, which had an average of 22.88 students from 40 students or 57.2% down to an average stay of 3.88 students from 40 students, or 9.7%. Plant Scientific names that were spelled wrongly were also decreased from 17 names into 14 names.

IV. CONCLUSIONS

1. Learning Application with pair exercise using flashcard media can fix the faulty pronunciation of scientific names of plants on students who took Plant Taxonomy course. Error which was previously performed by an average of 22.88 from 40 students or 57.2% of students, decreased to an average of 3.88 out of 40 students, or 9.7%.
2. The number of the scientific names of plants which were spelled wrongly by most of the students, decreased from the number of 17 names into 14 names. Those 14 scientific names of plants were still pronounced incorrectly by a few students.

REFERENCES

- [1] Arsyad, A. 2009. *Media Learning*, 119-120. Jakarta: King Grafindo Persada.
- [2] Asmani, JM 2011. *Tips to Master Inspiring, Creative and Innovative*, 138-142. Jogjakarta: Diva Press.
- [3] Daryanto. 2011. *Learning Media*, 11-13. Bandung: PT Sarana Tutorial Conscience prosperous.
- [4] Djamarah, SB, Zain, A. 2002. *Teaching and Learning Strategies*, 129-130. Jakarta: Rineka Reserved.
- [5] Llamas, KA 2003. *Tropical Flowering Plants: a guide to identification and cultivation*, 19-20. Cambridge: Timber Press, Inc.
- [6] Muhaimin, Akhmad, A. 2011. *Education Frees*, 15-18. Jogjakarta: Ar-Ruzz Media.
- [7] Radford, AE 1986. *Fundamentals of Plant Systematics*, 98-103. New York: Harper & Row Publishers Inc.

- [8] Rusydie, S. 2011. *Principles of Classroom Management*,77-100. Jogjakarta: Diva Press.
- [9] Sardiman, AM 2007. *Interaction and Motivation and Learning*,97-98. Jakarta: King Grafindo Persada.
- [10] Simpson, Michael G. 2006. *Plant Systematic*,9-10. Canada: Elsevier Academic Press.
- [11] Sobri, Jihad, A., Rochman, CH 2009. *Education Management*,23-34.Jogjakarta: Multi Pressindo.
- [12] Susilo, H.2007. *Thinking Ability Development dan Assesmen preformance Cooperative Strategy* Papers submitted in Authentic Assessment Training and Capability Development of Thinking and Implementation in Cooperative Learning. 2007 at the University of Muhammadiyah Malang, Malang, January 29.
- [13] Tjitrosoepomo, G. 2009. *General Taxonomy: Fundamentals of Plant Taxonomy*,81-82. Yogyakarta: Gadjah Mada University Press.
- [14] Uno, HB 2011. *Motivation Theory and Measurement*,23-32. Jakarta: PT Earth Literacy
- [15] Waid, A. 2011. *Reveals the Secrets of Learning Jews*,165-166. Jogjakarta: DIVA Press.

The Effect Analysis of Traffic Volume, Velocity and Density in Dr.Siwabessy Salobar Road

Selviana Walsen, La Mohamat Saleh

Civil Engineering of Politeknik Negeri Ambon

Abstract—Traffic density has been considered to be affected by the traffic volume and the traffic velocity. This study focuses on investigating the roles of both aspects on the traffic density along the street of Dr. Siwabessy, from Ambon City to Air Salobar or vice versa. This street has been considered to be one busy street in Ambon City with various vehicles passing by along with the crowded pedestrian activities and with new business centrals (e.g. school) along the road describing the complexity of the street traffics. From the study, it was found that the traffic velocity was statistically the more significant factor in determining the traffic density compared to the traffic volume following the use of the coefficient regression model. The other finding is that the traffic along the street can be classified to be under-saturated

Keywords— Traffic volume, traffic velocity, traffic density, regression model.

I. INTRODUCTION

According to Mashuri (2012) more and more community activity affect the characteristics of traffic flow like speed, volume and traffic density. According to Ekawati et al (2014), one of the main causes of traffic jam is unbalanced road capacity with an increasing number of vehicles. Dr. Siwabessy street in Air Salobar is one of the important streets in Ambon City, which serves the traffic flow from Ambon to Air Salobar. This road is used as a connecting lane from Ambon to Nusaniwe Sub-district. In recent years population growth in Nusaniwe sub-district has been caused the significant increase of vehicles through Dr. Siwabessy street. On the other hand, traffic jam caused by the activity from several new office and school building at this area. So Dr. Siwabessy highway segment will be more crowded because of the volume of vehicles and will affect to the capacity of existing highway. By looking at these conditions it is necessary to do a study to determine the speed, volume and density of roads Dr. Siwabessy-Air Salobar which is a highway that always passes many types of vehicles, as well as daily

activities of society. So we will know the road capacity feasibility.

II. LITERATURE

2.1 Highway Definition

Highway are transport infrastructures covering all parts of the road, including auxiliary buildings and equipment intended for traffic. The other hand it means a place passed by vehicle that through a road so that the highway is a very important in all aspects of life. The highway is also affect of an economy and the progress of a country.

2.2. Capacity

The capacity of the highway is the maximum number of vehicles that can pass through the road within a period of one hour without causing traffic jam (Warpani, 1985). According to MKJI (1997) capacity is the maximum current vehicle through a path that can be maintained per unit of hours under certain conditions. The basic equation for calculating road capacity in Indonesian Road Capacity Manual (1997) is:

$$C : Co \times FCw \times FCSP \times FCSF \times FCCS$$

with :

C : road capacity (smp/hour)

Co : basic capacity (smp/hour)

FCw : preparation of wide traffic lane factor (smp / hour)

FCSP: direction separation adjustment factor

FCSF :adjustment factor due to abstacles

FCCS :adjustment factor of city capacity

For urban road capacity, basic capacity can be seen in table 2.1

Table.2.1 The Basic Capacity of Urban Roads

Type	Basic capacity (smp/hour)
four-divided lane	1650/ lane
Four-undivided lane	1500/lane
Two undivided lane	2900/two lane

Table.2.2: Preparation of Wide Traffic Lane Factor (fcw)

Type	effective traffic width, (Wc) (m)	FCw
four-divided lane	3.00	0.92
	3.25	0.96
	3.50	1.00
	3.75	1.04
	4.00	1.08
Four-undivided lane	3.00	0.91
	3.25	0.95
	3.50	1.00
	3.75	1.05
	4.00	1.09
Two undivided lane	5	0.56
	6	0.87
	7	1.00
	8	1.14
	9	1.25
	10	1.29
	11	1.34

Table.2.3: Direction Separation Adjustment Factor (FCsp)

direction separation (SP) % - %	50-50	55-45	60-40	65-35	70-30
(2/2)	1.00	0.97	0.94	0.91	0.88
(4/2)	1.00	0.985	0.97	0.955	0.94

Table.2.4: Adjustment Factor Due to Abstacles

Type	Side barriers Class	FCSF			
		Effective width (Ws) (m)			
		≤ 0.5 m	1.0 m	1.5 m	≥ 2 m
4/2 D	VL	0.96	0.98	1.01	1.03
	L	0.94	0.97	1.00	1.02
	M	0.92	0.95	0.98	1.00
	H	0.88	0.92	0.95	0.98
	VH	0.84	0.88	0.92	0.96
4/2UD	VL	0.96	0.99	1.01	1.03
	L	0.94	0.97	1.00	1.02
	M	0.92	0.95	0.98	1.00
	H	0.87	0.91	0.94	0.98
	VH	0.80	0.86	0.90	0.95
(2/2 UD) atau jalan satu arah	VL	0.94	0.96	0.99	1.01
	L	0.92	0.94	0.97	1.00
	M	0.89	0.93	0.95	0.98
	H	0.82	0.86	0.90	0.95
	VH	0.73	0.79	0.85	0.91

Table.2.5: Adjustment Factor of City Capacity (FCcs)

City size	FCcs
< 0.1	0.86

0.1-0.5	0.90
0.5-1.0	0.94
1.0-3.0	1.00

> 3.0	1.04
-------	------

V : velocity (km/hour)
 S : distance (km)
 T : time(hour)

2.3. Traffic Volume

The parameter used to determine daily traffic patterns is an average traffic (LHR), LHR obtained by traffic monitoring for 24 hours, in a few days and the result is averaged, expressed in vehicle / day or day / day can be calculated by the formula:

$$Q = \frac{N}{T}$$

with :

Q : volume
 N : number of vehicle
 T : observation time

2.4. Velocity

Speed is the ratio between distance and time. The formula for calculating speed that is:

$$V = \frac{S}{T};$$

with:

The relationship between volume, speed, and density is as follows:

$$D = \frac{Q}{U_s}$$

with :

D : Traffic density (vehicle/hour)
 Q : Traffic volume (vehicle/km)
 Us : mean traffic velocity of space (km/hour)

2.6. Saturation ratio

Saturation ratio defined as the ratio of traffic flow Q (smp / hour) to capacity C (smp / hour) is used as the main factor in determining the level of road segment performance. aturation is defined as the following formula;

$$DS = Q/C$$

with :

Q : traffic flow
 C : capacity

2.7. Relation between Volume, Speed, and Traffic Density

The mathematical relationship between speed, volume, and density can be expressed by the following equation:

$$Q = D \times S$$

with:

2.5. Density

Traffic density is the number of vehicles that exceed the capacity of the highway. Density can be calculated based on speed and volume.

Table.2.6: Q/C Ratio

Q/C	Condition
< 0,8	road segment can still serve the volume requirements of vehicles passing through the road
0,8 - 1,0	unstabled condition ,ecause the condition of the road segment can not accommodate the number of vehicles passing through the road
> 1,0	a condition in which the road segment can accommodate the movement of vehicle volume.

Q : volume (SMP/hour)
 D : density(vehicle/km)
 S : speed (km/hour)

2.8. Passenger Car Unit

The passenger car unit abbreviated as SMP (indonesian factor) is the unit of vehicle in the traffic flow which is equivalent to the light vehicle / passenger car, using the passenger car's equivalence or multiplier factor of the vehicle type into one unit of SMP, where the SMP is influenced by the type / type vehicles, vehicle dimensions, and motion capabilities. The quantities of passenger car units vary according to the Indonesia Road Capacity Manual 1997 shown as follows:

Table.2.2: SMP Factor

Vehicle	(smp)
HV	1,20
LV	1,00
MC	0,25

Table.2.3: Classification of Vehicles

Classification of vehicles	Vehicle
HV	Trucks and Buses
LV	Passenger Car, Mini Bus, Truck pick up
MC	Motorcycle

III. METHOD

3.1 Location

This research is located on Jln Dr Siwabessy - Air salobar of Ambon Street

3.2 Research Time

This research was conducted on 30 August 2017 until September 2017

3.3 Data Type

1. types of data used are as follows:

- a. Traffic Volume
- b. Speed
- c. Road geometric

3.4. Data Analysis Techniques

a. Data Processing Technique

This writing uses the data obtained, with the aim of obtaining an effective approach based on the existing theoretical studies with the following survey steps:

Preliminary studies

-Preliminary study is the process of collecting data to support this writing

- Library Studies

Conducted by collecting references related to the support of writing, which is a theoretical study.

- Data Compilation

Data compilation, is basically a process of collecting, processing and reporting data to get the final result of data half-baked ready to be processed at the stage of data analysis.

- Data Processing and Analysis.

Data processing is an activity for converting raw data that has been obtained into a standard format approached by theoretical studies.

IV. RESULTS AND DISCUSSION

4.1. Traffic Volume Analysis

The number of motor vehicles operating on Dr.Siwabessy road is obtained based on survey during peak hours, in the morning, afternoon and evening, are presented in Table 4.1.

Based on survey results of traffic volume on road Dr. Siwabessy can be seen that the maximum vehicle volume is at 08.00-09.00 with the direction of Ambon - Air Salobar of 1909 vehicles / hour and at 07.00-08.00 with the direction of Air Salobar - Ambon of 1283 vehicles / hour. Subsequently converted into units of passenger cars (smp) using the Highway Manual Capacity Indonesia 1997 for each road segment.

Based on the table 4.5. can be seen for Dr.Siwabessy road segment ratio has less than 1, this indicates that the condition of traffic flow is still below saturated From the above table it is known that in the direction of Ambon to Air Salobar vehicle speed is slower than the direction of Air Salobar to Ambon, this is because vehicles entering Air Salobar area are more dense than vehicles from Ambon to Air Salobar.

Table.4.1: Traffic Volume of Dr.Siwabessy Road

Time	Traffic Volume (Vehicle/hour)	
	Ambon - Air Salobar	Air Salobar - Ambon
06:00 - 07:00	1062	622
07:00 - 08:00	1659	1283
08:00 - 09:00	1909	1003
09:00 - 10:00	839	506
10:00 - 11:00	923	819
11:00 - 12:00	1293	1222
12:00 - 13:00	1625	1001
13:00 - 14:00	1383	1160
14:00 - 15:00	1081	1129
15:00 - 16:00	481	1042
16:00 - 17:00	1085	999
17:00 - 18:00	1148	1102
18:00 - 19:00	1021	1262

Table.4.2: Dr.Siwabessy Road Traffic direction Ambon to Air Salobar (smp / jam)

Time	Vehicle Classification			Total
	HV	LV	MC	
06:00 - 07:00	10	594.1	238	842.1
07:00 - 08:00	12	1173.9	297.6	1483.5
08:00 - 09:00	13	957	375.6	1345.6
09:00 - 10:00	5	456.3	193.2	654.5
10:00 - 11:00	12	562.9	191.2	766.1
11:00 - 12:00	20	830.7	253.6	1104.3
12:00 - 13:00	22	1136.2	291.6	1449.8
13:00 - 14:00	14	890.5	273.6	1178.1
14:00 - 15:00	15	586.3	246	847.3
15:00 - 16:00	18	601.9	246	865.9
16:00 - 17:00	19	586.3	246	851.3
17:00 - 18:00	14	690.3	241.2	945.5
18:00 - 19:00	13	625.3	210.8	849.1

Table.4.3: Dr.Siwabessy Road Traffic Direction Air Salobar to Ambon (smp / jam)

Time	Vehicle Classification			Total
	HV	LV	MC	
06:00 - 07:00	12	404.3	119.6	535.9
07:00 - 08:00	20	703.3	288.8	1012.1
08:00 - 09:00	8	616.2	208.4	832.6
09:00 - 10:00	5	308.1	105.6	418.7
10:00 - 11:00	8	591.5	142.4	741.9
11:00 - 12:00	12	742.3	255.6	1009.9
12:00 - 13:00	13	551.2	225.6	789.8
13:00 - 14:00	16	718.9	236.4	971.3
14:00 - 15:00	18	694.2	230.8	943
15:00 - 16:00	20	648.7	209.2	877.9
16:00 - 17:00	21	582.4	212	815.4
17:00 - 18:00	13	634.4	240.4	887.8
18:00 - 19:00	16	802.1	251.6	1069.7

4.2. Capacity Calculation

Table.4.4: Result of Road Capacity Calculation

Location		Basic Capacity (smp/hour)	Adjustment Factor				Road Capacity (smp / hour)
			Line width	Separation of direction	Side Barriers	City ratio	
Dr. Siwabessy Street	Ambon to Air Salobar	2900	0.96	1	0.94	0.93	2433.77
	Arah Air Salobar to Ambon	2900	0.96	1	0.94	0.93	2433.77

Table.4.5: V / C Ratio Each Lane

Location		Period	Volume	Capacity	VCR	Max VCR
Dr. Siwabessy Street	Ambon to Belakang Soya	Morning	691	3200.79	0.22	0.34
		Noon	963.5	3200.79	0.30	
		Afternoon	1073.8	3200.79	0.34	
		Evening	776.5	3200.79	0.24	
	Belakang Soya to Ambon	Morning	1238.9	3200.79	0.39	0.45
		Noon	1165.4	3200.79	0.36	
		Afternoon	1432.1	3200.79	0.45	
		Evening	1297	3200.79	0.41	

4.3. Velocity analysis

Table.4.6: Velocity analysis at Dr.Siwabessy Street (Ambon-Air Salobar)

Period	Time Mean Speed	Space Mean Speed
Morning	42	42
Noon	42	42
Afternoon	48	48
Evening	44	44

Table.4.7: Velocity Analysis at Dr.Siwabessy Street (Air Salobar –Ambon)

Period	Time Mean Speed	Space Mean Speed
Morning	47	47
Noon	49	49
Afternoon	49	49
Evening	46	46

Table.4.8: Traffic Velocity Recapitulation

Period	Velocity (Km/Hour)			
	Time	Ambon - Air Salobar	Time	Air Salobar - Ambon
Morning	0.00123	41.98	0.00109	47.11
Noon	0.00116	42.24	0.00117	48.89
Afternoon	0.00139	48.00	0.00120	48.89
Evening	0.00146	44.38	0.00117	46.17
Average	0.00131	44.15	0.00	47.76

4.4. Density Analysis

4.4.1. Calculating Traffic Density

Table.4.9: Calculation of Traffic Density of Road Sections Dr.Siwabessy Directions Ambon to Air Salobar.

Time	Ambon - Air Salobar		
	Volume	Velocity	Density
06:00 - 07:00	842.1	41.98	20.06
07:00 - 08:00	1483.5	41.98	35.34
08:00 - 09:00	1345.6	41.98	32.05
09:00 - 10:00	654.5	41.98	15.59

10:00 - 11:00	766.1	41.98	18.25
11:00 - 12:00	1104.3	41.98	26.31
12:00 - 13:00	1449.8	42.24	34.32
13:00 - 14:00	1178.1	42.24	27.89
14:00 - 15:00	847.3	48	17.65
15:00 - 16:00	865.9	48	18.04
16:00 - 17:00	851.3	48	17.74
17:00 - 18:00	945.5	48	19.70
18:00 - 19:00	849.1	44.38	19.13

Table.4.10: Calculation of Traffic Density of Road directions Air Salobar to Ambon

Time	Air Salobar - Ambon		
	Volume	Velocity	Density
06:00 - 07:00	535.9	47.11	11.38
07:00 - 08:00	1012.1	47.11	21.48
08:00 - 09:00	832.6	47.11	17.67
09:00 - 10:00	418.7	47.11	8.89
10:00 - 11:00	741.9	47.11	15.75
11:00 - 12:00	1009.9	47.11	21.44
12:00 - 13:00	789.8	48.89	16.15
13:00 - 14:00	971.3	48.89	19.87
14:00 - 15:00	943	48.89	19.29
15:00 - 16:00	877.9	48.89	17.96
16:00 - 17:00	815.4	48.89	16.68
17:00 - 18:00	887.8	48.89	18.16
18:00 - 19:00	1069.7	46.17	23.17

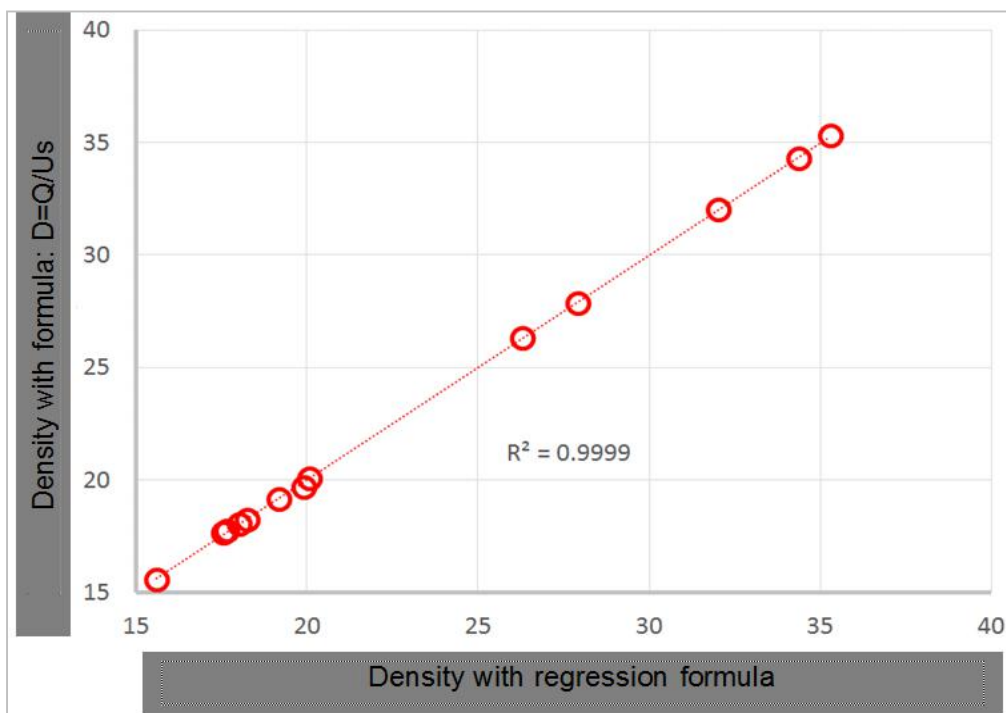


Fig.4.1: The Relationship between Predictions of Vehicle Density Using Regression Formula with the Calculation of Vehicle Density

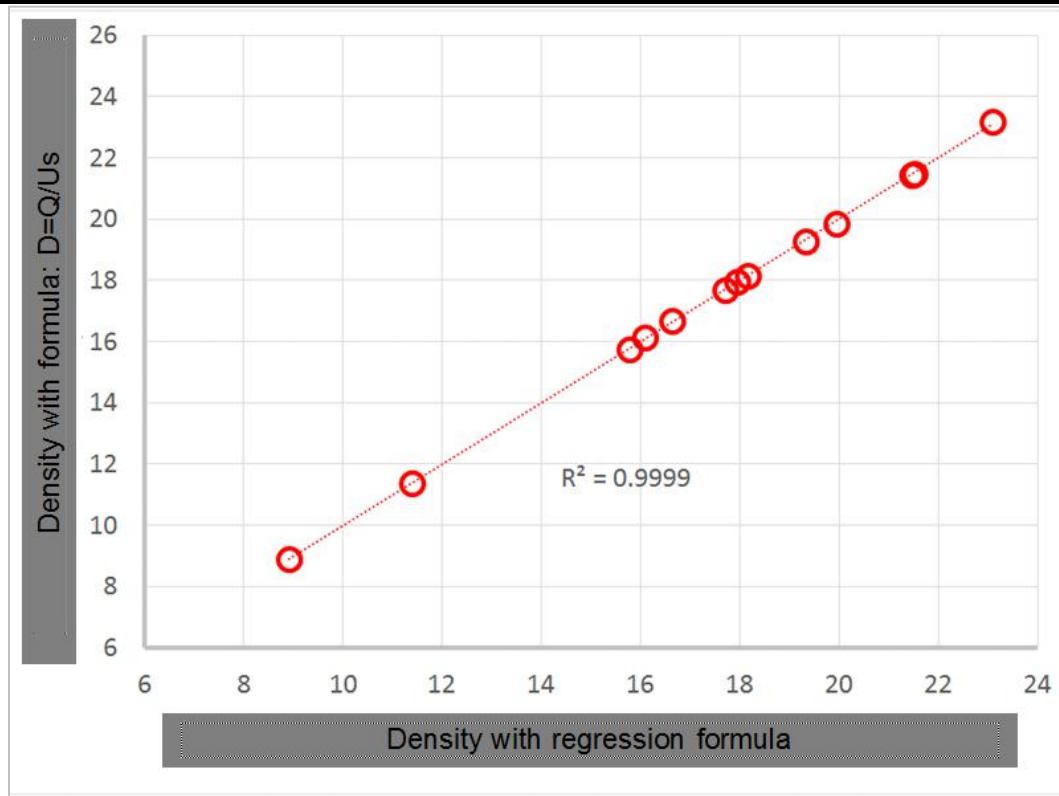


Fig.4.2: The Plot of the Relationship between the Predictions of Vehicle Density Using the Regression Formula with the Calculation of Vehicle Density.

4.5. Relationship Speed, Volume And Density by Regression Analysis

4.5.1. (Ambon to Air Salobar)

The following relationship between volume (Q), speed (Us) and vehicle density (D) by using regression analysis on Dr.Siwabessy road direction Ambon to Air Salobar. By using regression data processing using Excel function, it is known that the regression equation, $D = 18,32 - 0,435 [Us] + 0,024 [Q]$ gives prediction of vehicle density with very high correlation value ($R^2 = 0.999$) to calculation of vehicle density by using formula 2.8 (see Figure 4.1). Furthermore, based on the value of regression model equations, the effect of vehicle speed on the road direction from Ambon to Air Salobar is more dominant.

4.5.2. Air Salobar- Ambon

Relation between volume (Q), speed (Us) and vehicle density (D) by using regression analysis on Dr. Siwabessy road from Air Salobar to Ambon. By using regression data processing using Excel function, it is known that the regression equation, $D = 18,67 - 0,396 [Us] + 0,021 [Q]$ gives prediction of vehicle density with very high correlation value ($R^2 = 0.999$) to calculation of vehicle density by using formula 2.8 (see Figure 4.2). Furthermore, based on the value of regression model equations, the effect of vehicle speed on the road direction from Ambon to Air Salobar is more dominant

than the road volume where the regression coefficient of vehicle speed is 0.396 is greater than the regression coefficient of the volume which is 0,021.

V. CONCLUSION

1. Based on the results of the analysis, the flow of Dr.Siwabessy road traffic is said to have not experienced saturation because the ratio of volume to capacity has a value less than 1.
2. Based on linear regression analysis found some important things
 - a. Both traffic flow from Ambon to Air Salobar or vice versa shows the dominant influence of vehicle speed (Us) on traffic density (D) compared to traffic volume factor (V)
 - b. The regression formula of the relationship between traffic density, vehicle speed and traffic volume for traffic flow from Ambon to Air Salobar or vice versa respectively is $D = 18.32 - 0.435 [Us] + 0.024 [Q]$ and $D = 18.67 - 0.396 [Us] + 0.021 [Q]$

REFERENCES

- [1] Anonimous, 1997, Manual Kapasitas jalan Indonesia, Direktorat Jenderal Binamarga.
- [2] Anonimous,1998, Tata Cara survei Lalulintas, Ditjen Binamarga Jakarta

- [3] Ostle, B. dan R. W. Mensing. 1975. *Statistic in Research: Basic Concepts and Techniques for Research Workers*. Iowa State University Press. Iowa. 596p
- [4] Ofyar Z. Tamin, *Perencanaan dan pemodelan Transportasi*, penerbit ITB Bandung 2000
- [5] Warpani, Suwardjono. 1988. *Rekayasa lalulintas* Jakarta penerbit Bhatara
- [6] Ir. Hamirhan Saodang MSCE. 2005. *Konstruksi Jalan Raya*. Bandung Nova.
- [7] Julianto, Eko, 2010, Hubungan antara kecepatan, volume dan kepadatan ruas jalan Siliwangi Semarang, *Jurnal Teknik Sipil dan Perencanaan* No 2 Vol 2

Flexure and Shear Study of Deep Beams using Metakaolin Added Polypropylene Fibre Reinforced Concrete

S. Vijayabaskaran, M. Rajiv, A. Anandraj

Assistant Professor, Saranathan College of Engineering, Trichy, India

Abstract— Structural elements like walls of bunkers, load bearing walls in buildings, pile caps, plate elements in folded plates behave as deep beams. Beams whose span (L) to depth (D) ratio is reasonably small can be said as a deep beam. Beams with large depth, supported by individual columns, often used as transfer girders in tall buildings, long span structures etc are commonly referred to as deep beams. Deep beams are used for architectural buildings where the span is very large without any intermediate columns such as marriage halls, assembly halls, auditoriums, theatres etc. According to IS456-2000, a beam is said to be as a deep beam when the ratio of effective span to overall depth (L/D) is less than 2.0 for simply supported members and 2.5 for continuous members. The design of such structural elements requires innovative procedures to serve the functionality coupled with durability. In deep beams, the bending stress distribution across any transverse section deviates appreciably from the straight line distribution assumed as in the simple beam theory. So, assumption of “Plane section before bending remains plane after bending” does not become valid and the neutral axis does not lie at the mid depth. In deep beams, the ultimate failure due to shear is generally brittle in nature, in disparity to the ductile behavior and progressive failure with large number of cracks as observed in normal beams.

In this paper, flexural strength of M20 and M30 graded concrete deep beams with the addition of a combination of 0%,10%,20% metakaolin as a partial replacement for cement and 0%,2.5%,5% polypropylene fibre is found out and mode of failure is observed for each case. Mix designs for M20 and M30 graded concrete are carried out in worksheets and the proportions of cement, sand, coarse aggregate are calculated based on the tests conducted on cement and aggregates. Cubes are casted and 7 days compressive strengths for those cubes are tested using compressive testing machine and the mix proportions are used.

Keywords— Metakaolin, Polypropylene Fibre, Deep beam.

I. INTRODUCTION

1.1 DIFFERENCES BETWEEN SIMPLE BEAM AND DEEP BEAM

- Deep beams behave as two dimensional action whereas the simple beam behaves as one dimensional action.
- Plane section remains plane which is applicable in simple beams is not applicable for deep beams where the strain distribution is not linear.
- Shear deformation cannot be neglected in deep beams as in the case of ordinary beams. In deep beams, even at the elastic stage, stress distribution is not linear and in the ultimate limit state, the shape of the concrete compressive stress block is no longer parabolic.

1.2 IMAGES FOR SOME EXAMPLES OF DEEP BEAMS

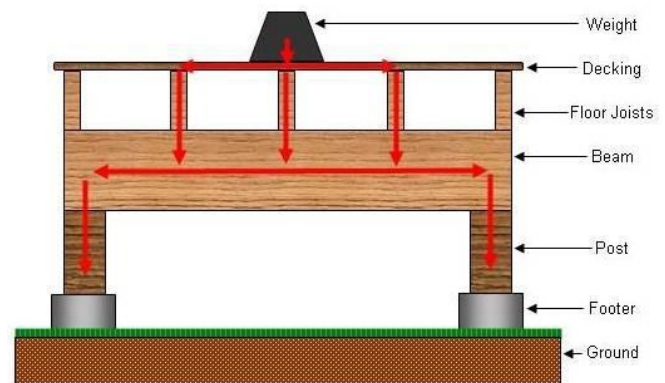


Fig.1.1: Transfer girder

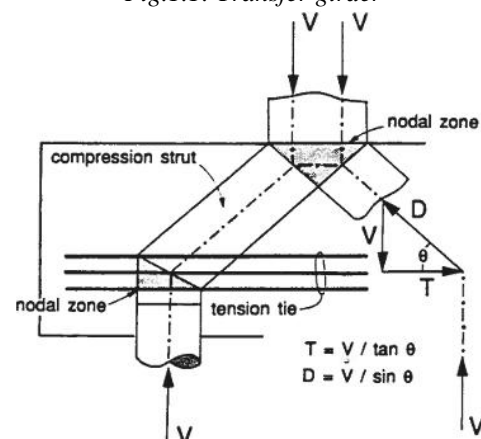


Fig.1.2: Pile cap as a Deep beam- Strut and Tie Model

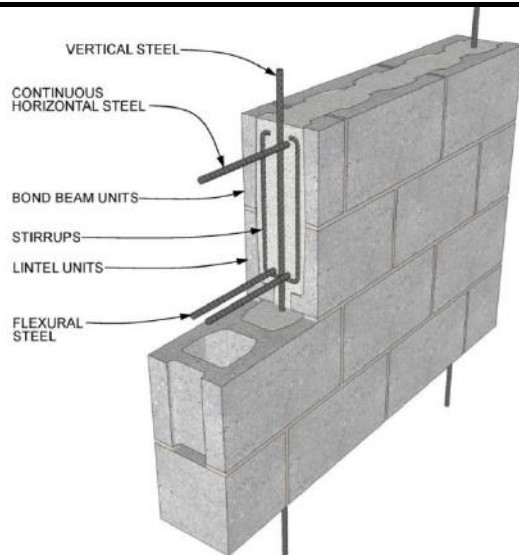
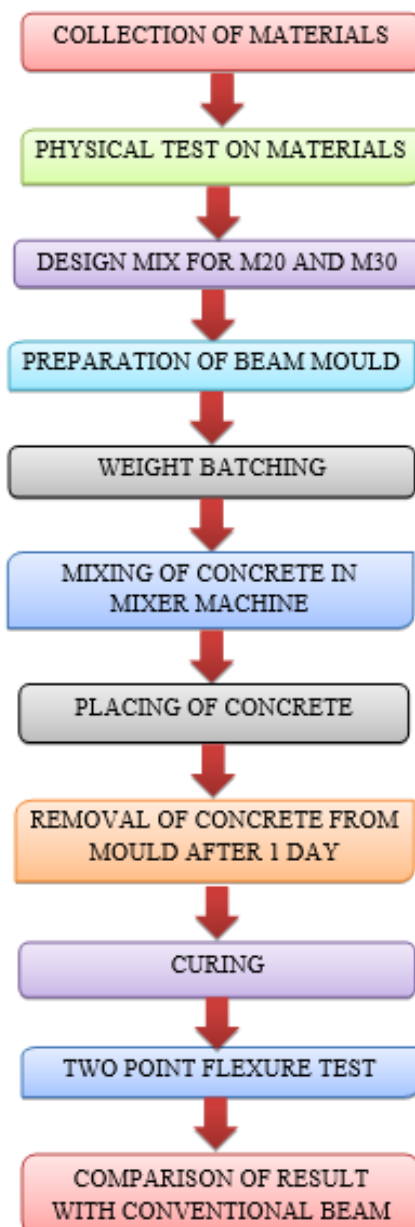


Fig.1.3: Walls of a Bunker as a deep beam

II. METHODOLOGY



III. EXPERIMENTAL WORK

3.1 MIX DESIGN FOR DEEP BEAMS

Mix design ratio for M20 grade concrete = 1:2.64:3.78

Mix design ratio for M30 grade concrete = 1:2.24:3.33

3.2 PROPERTIES OF POLYPROPYLENE FIBER

Appearance	: polypropylene fiber
Specific gravity	: 0.91 g/cm ²
Alkali content	: Nil
Sulphate content	: Nil
Air entrainment	: air content of concrete will not be significantly increased
Chlorine content	: Nil
Constituents	: Nil
Fiber thickness	: 6 denier
Young's modulus	: 5500-7000MPA
Tensile strength	: 360MPA
Fibre length	: 6mm
Aggregate max size	: 32mm



Fig.3.1: Polypropylene fibre



Fig.3.2: Metakaolin



Fig.3.3: Placing the cube in CTM machine to check for design mix.

3.3 TEST RESULTS-GENERAL

Specific gravity of fine aggregate	: 2.72
Water absorption of fine aggregate	: 1.0%
Specific gravity of coarse aggregate	: 2.68
Water absorption of coarse aggregate	: 0.50
Specific gravity of cement	: 3.15

3.4 TEST RESULTS FOR COMPRESSION TEST OF CUBES TO CHECK FOR THE DESIGN MIX FOR DEEP BEAMS

COMPRESSION TEST OF CUBE	LOAD	STRENGTH ACHIEVED	TARGETED STRENGTH
Compression test for M20 for 7 day	432kN	19.2	13
Compression test for M30 for 7 day	610kN	27.11	19.5

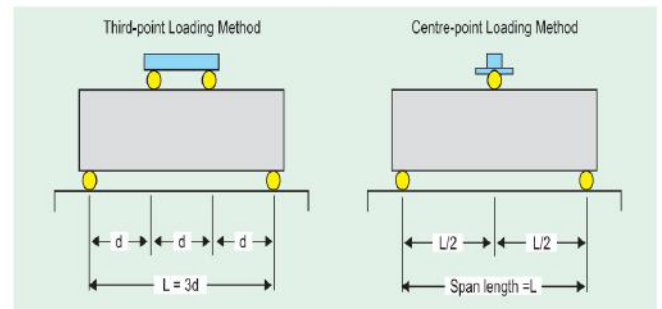


Fig.3.5: Flexural Test for Beams- Third Point Loading and Centre Point Loading



Fig.3.4: During Compression test of a cube in CTM



Fig.3.6: Deep Beam Mould



Fig.3.7: Mixer Machine



Fig.3.10: Flexure Test of a deep beam under third point loading in UTM of 400 kN capacity.



Fig.3.8: Concrete Poured in Deep Beam Mould and leveled



Fig.3.9: Marking on Deep Beams for third Point Loading with a chalk

3.5 CALCULATION OF FLEXURAL STRENGTH

The mould for deep beam used in this project is 50cm length, 15cm breadth and 28cm depth. The cured beam is removed from the mould by screwing out the bolts and the beam is marked on the surrounding by four lines, two lines for resting on the support rollers and two in-between lines for the application of point loads in two points. Here the edge distance is 5 cm on both the edges and the remaining 40 cm is divided into three equal lengths such as 13.33 cm. The flexural strength of the specimen is expressed as the modulus of rupture f_b which if 'a' equals the distance between the line of fracture and the nearer support, measured on the centre line of the tensile side of the specimen, in cm, is calculated to the nearest 0.05 MPa as follows:

$$f_b = PxL/bxd^2$$

When 'a' is greater than 20.0 cm for 15.0 cm specimen.

$$f_b = 3Pxa/ bxd^2$$

When 'a' is less than 20.0 cm but greater than 17.0 cm for 15.0 specimen,

where b = measured width in cm of the specimen.

d = measured depth in cm of the specimen.

P = Ultimate Load in kN.

L= Centre to Centre distance between supports.

3.6 FLEXURE TEST RESULTS FOR DEEP BEAM OF M20 GRADE PLAIN CONCRET

S.NO	PPF %	METAKAOLIN %	TEST AT DAYS	FLEXURAL LOAD P(kN)	MIN LENGTH B/W CRACK AND EDGE AT NEUTRAL AXIS IN TENSION SIDE 'a' (cm)	FLEXURAL STRESS f_b (N/mm ²)	TYPE OF FAILURE
1	0	0	7	91	21	3.24	SB
2	0	10	7	85	17	3.82	CRACK
3	0	20	7	142	23	5	SB
4	2.5	10	7	73	23.4	2.57	CRACK
5	2.5	20	7	77	14	2.85	CRACK
6	5	10	7	60	15.5	2.46	CRACK
7	5	20	7	71	23	2.50	CRACK
8	0	0	21	115	22.5	4.05	SB
9	0	10	21	105	22.7	3.70	CRACK
10	0	20	21	110	21.8	3.87	SB
11	2.5	10	21	112	21.6	3.94	CRACK
12	2.5	20	21	96	22.5	3.38	CRACK
13	5	10	21	91	23	3.21	CRACK
14	5	20	21	84	18	3.99	CRACK

Note:- Where 'SB' denotes Sudden Breakage of deep beam into two parts

3.7 FLEXURE TEST RESULTS FOR DEEP BEAM OF M30 GRADE PLAIN CONCRETE

S.NO	PPF %	METAKAOLIN %	TEST AT DAYS	FLEXURAL LOAD P(kN)	MIN LEN B/W CRACK AND EDGE AT NEUTRAL AXIS IN TENSION SIDE 'a' (cm)	FLEXURAL STRESS f_b (N/mm ²)	TYPE OF FAILURE
1	0	0	7	94	21	3.31	SB
2	0	10	7	70	19.5	3.60	SB
3	0	20	7	76	23.7	2.67	CRACK
4	2.5	10	7	94	20.1	3.31	SB
5	2.5	20	7	75	24.7	2.64	CRACK
6	5	10	7	79	21.5	2.78	CRACK
7	5	20	7	67	20.2	2.36	CRACK
8	0	0	21	122	21	4.30	SB
9	0	10	21	102	22.5	3.62	SB
10	0	20	21	107	24.4	3.17	SB
11	2.5	10	21	106	24	3.73	CRACK
12	2.5	20	21	112	23.5	3.94	CRACK
13	5	10	21	57	19.9	3.68	CRACK
14	5	20	21	131	21.3	4.62	CRACK

Note:- Where 'SB' denotes Sudden Breakage of deep beam into two parts

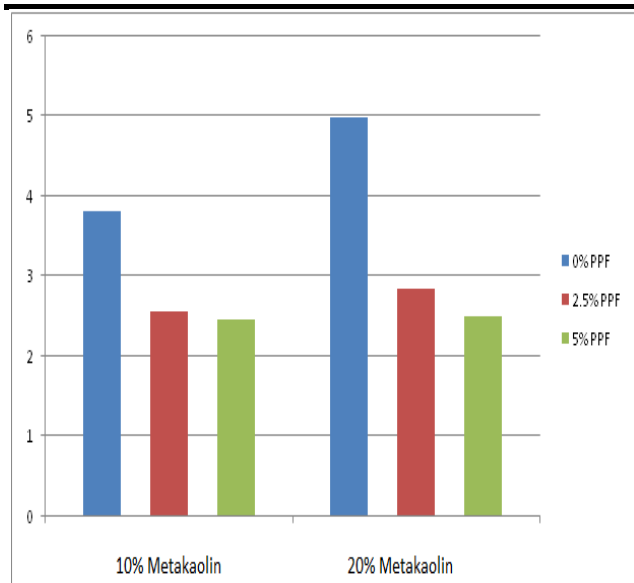


Fig.3.11: 7 Days Flexural Strength for M20

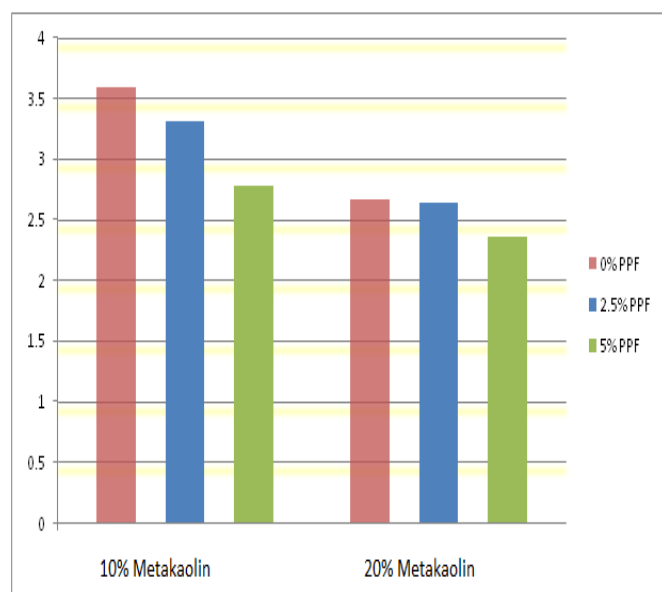


Fig.3.12: 7 Days Flexural Strength for M30

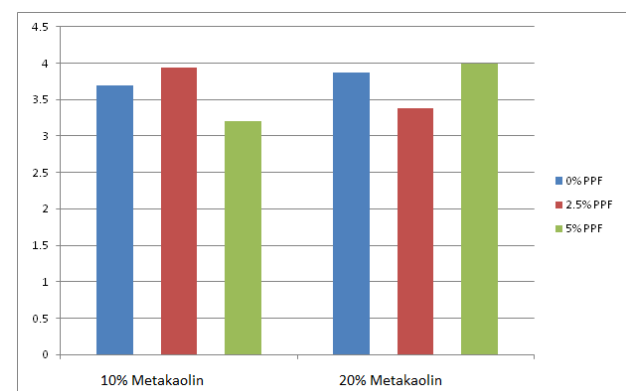


Fig.3.13: 21 Days Flexural Strength for M20

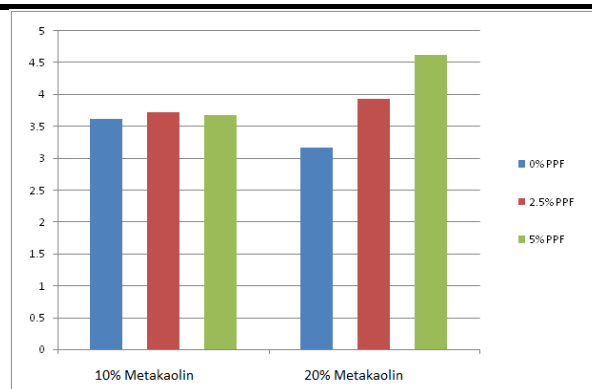


Fig.3.14: 21 Days Flexural Strength for M30

IV. SUMMARY AND CONCLUSION

On adding PPF, brittle failure is eliminated and only shear cracks are formed, thus ductile failure (failure with warning) takes place. Whereas on addition of PPF fiber, though flexural strength is less, the beam does not break and only cracks are formed and hence giving a full warning before failure.

By replacing cement with metakaolin, 7days strength of deep beams may be slightly below the targeted strength but 28 days predicted strength of deep beams might be more than the targeted strength as per 21 days flexural strength since metakaolin has to be cured for more days to achieve required strength.

REFERENCES

- [1] Indian Standard code of practice for plain and Reinforced Concrete, IS456:2000, Bureau of Indian Standards, New Delhi.
- [2] Recommended guidelines of concrete mix design, IS 10262:1982, Bureau of Indian Standards, New Delhi.
- [3] Shetty, M.S.(2006) "Concrete Technology Theory and Practice" (S.Chand and Company Ltd.New Delhi.
- [4] Gambhir. M.L,(2006) "Concrete Technology", (Tata McGraw-Hill Publishing Company Limited, New Delhi)
- [5] M.V. Krishna Rao*a , N.R. Dakhshina Murthyb and V. Santhosh Kumara "Behaviour of Polypropylene Fibre Reinforced Fly ash Concrete Deep Beams in Flexure and Shear", Asian Journal of Civil Engineering (building and housing) VOL. 12, NO. 2 (2011) PAGES 143-154

Design and Analysis of RCA and CLA using CMOS, GDI, TG and ECRL Technology

Kuldeep Singh Shekhawat¹, Gajendra Sujediya²

¹Research Scholar, Department of ECE, Rajasthan Institute of Engineering and Technology, Jaipur, India

²Assistant Professor, Department of ECE, Rajasthan Institute of Engineering and Technology, Jaipur, India

Abstract—VLSI technology has developed over the years thereby enhancing the performance of chips in terms of three basic constraints viz. delay, power and area. In today's scenario compact and small digital devices are critical concern in the field of VLSI design, which should perform fast as well as low power consumption. Optimizing the delay, area and power of an adder is a major design issues, as area and speed are usually conflicting constraints. Adders can be designed with conventional CMOS technology but for compact and low power consumption we can design circuit using adiabatic logic and with other technology GDI, ECRL, transmission Gate.

Keywords—Adders, CMOS, GDI, TG, ECRL.

I. INTRODUCTION

Full adders can be designed using multiple techniques out of which Ripple Carry Adder (RCA) and Carry Look-ahead Adder (CLA) are considered for comparison based on their power and speed. In the designing of the digital circuits speed and power is conflict to each other. A Ripple Carry Adder consumes the least power but is the slowest (propagation delay is the most) while Carry Look-ahead Adder is the fastest but requires more power.

II. BASIC ADDER BLOCKS

2.1 HALF ADDER

The circuit is created using the combination of an XOR and an AND Gate. Each gate handles a component of the output. The AND Gate takes the input and give the carry bit and the XOR gate outputs the sum bit. A and B are the inputs and SUM and CARRY are the output signals Boolean equations for a half adder is given below:

$$\text{SUM} = A \oplus B$$

$$\text{Carry} = A \cdot B$$



Fig.2.1. Half Adder Circuit

2.2 Full Adder

A Full adder is an extension of the half adder. This

works by taking the carry bit from previous addition and using this along with the two input operand bits. This means that this adder can be used to add binary numbers with more than 1 bit. It functions by taking into account the two input bits as well as the carry bit, passing them through a set of gates and giving a sum and carry bit as the output [2]. Boolean equations for a full adder are given below:

$$S = A \oplus B \oplus C$$

$$C_{out} = A \cdot B + B \cdot C_{in} + A \cdot C_{in}$$

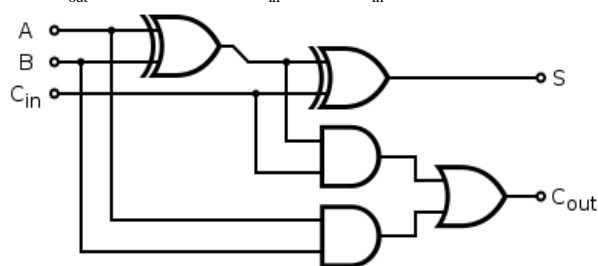


Fig.2.2. Full Adder Circuit

2.3 Multiple Bit Adders

- **Ripple-Carry Adder:** A Ripple carry adder is designed using cascading connections of multiple full adders. What this means is that the carry out signal of the preceding full adder is the carry in signal for the succeeding full adder and so on. Ripple-Carry adder is the most compact adder (O (n) Area) among all the adders. This adder can be used to design compact devices on the cost of speed as this adder is very slow (O (n) time) for computation. In case of fast addition, carry increment and carry skip architecture can be used, particularly for 8 to 16 bit lengths.
- **Carry-Look ahead Adder:** Carry-Look ahead adders (CLA) are the fastest adders, but they consume maximum area and little bit complex. This adder is preferred for addition up to 4 bit length.

III. IMPLEMENTATION

- 8-bit Ripple Carry Adders are implemented using 3 techniques – Conventional CMOS, Transmission Gate and ECRL Adiabatic.
- 8-bit Carry Look-ahead Adders are implemented

using 4 techniques – Conventional CMOS, Transmission Gate, GDI [5] and ECRL Adiabatic.[1]

3.1 Full Adder Using CMOS technology

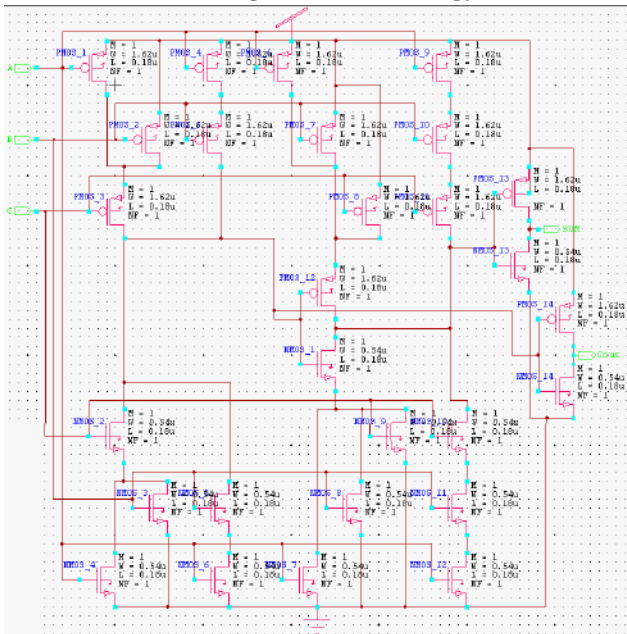


Fig.3.1. Full Adder Design Using CMOS Logic

3.2 Full Adder Using Transmission Gate Logic

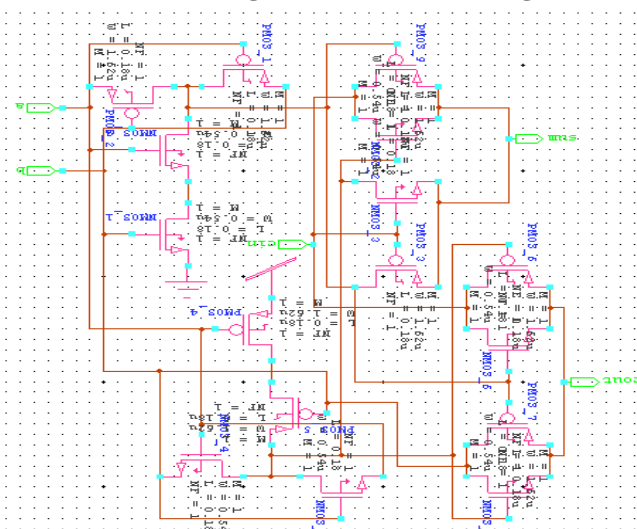


Fig.3.2. Full Adder Design Using TG Logic

3.3 Full Adder Using ECRL (Energy Charge Recovery Logic)

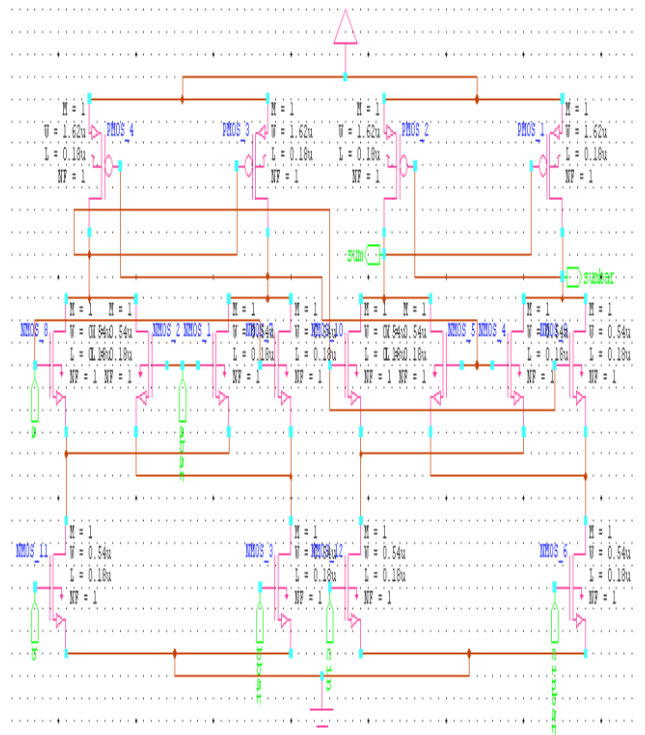


Fig.3.3.1 Sum circuit using ECRL logic

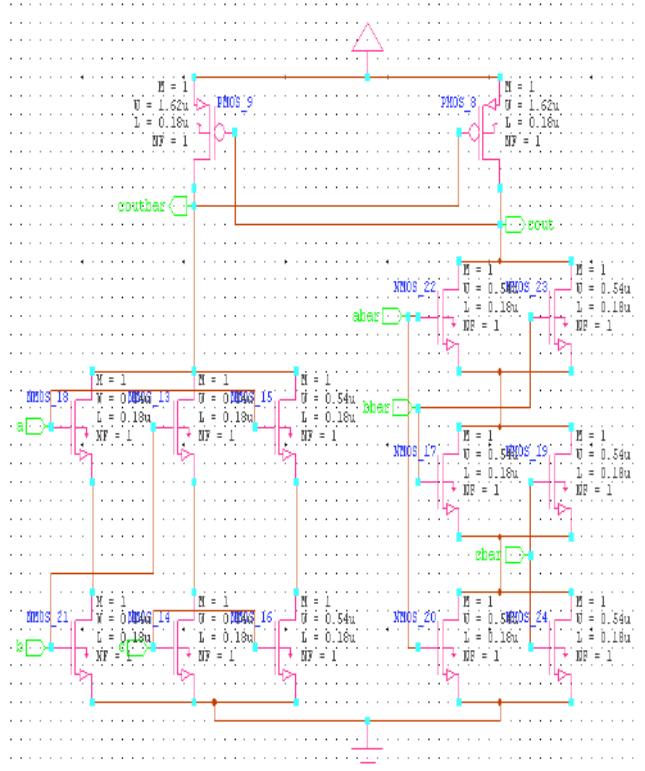


Fig.3.3.2 Carry circuit using ECRL logic

3.4 Implementation of 8-BIT RCA

For designing 8-bit adders, the corresponding 1-bit full adders described in the previous sections are used. These are cascaded together so that each carry bit from one

adder “ripples” to the next. An RCA uses lesser number of transistors thus reducing the power dissipation. The input signals to an 8-bit adder are: a_0 - a_7 , b_0 - b_7 and c_{in} and sum_0 - sum_7 & c_{out} are the output signals.

3.4.1 Implementation of a Carry Look-Ahead Adder

CLAs utilize the concept of the generate (g), kill (k) and the propagate (p) signals.

These generate and propagate signals are represented as:

$$P_i = A_i \oplus B_i$$

$$G_i = A_i \cdot B_i$$

where, a_i and b_i are the input signals. The carry signal, C_{in} , and the sum signal, S_i , are given by:

$$C_{i+1} = G_i + P_i \cdot C_i$$

$$S_i = P_i \oplus C_i$$

These sum and carry signals are generated using these main components – an XOR gate, an AND gate and a $g_i + p_i \cdot c_i$ Boolean expression logic circuit. In the following sections, working of the above mentioned components are explained for 4 different techniques – Conventional CMOS, Transmission Gate, Gate Diffusion Input and ECRL[3].

- **8-Bit CLA Using Conventional CMOS**

To design N-bit adder, N 1-bit adders are required. In the case of Carry Look-ahead adders, these 1-bit adders are designed using 2 XOR gates, 1 AND gate and a $g_i + p_i \cdot c_i$ boolean expression logic circuit. Here, for a 1-bit adder, 19-PMOS and 19-NMOS transistors are required.

- **8-Bit CLA Using Transmission Gate (TG)**

For designing a 1-bit adder based on TG logic, the circuit components used are - 2 XOR gates and a boolean expression logic, $g_i + p_i \cdot c_i$, circuit. The design of these circuit components is different from the way it is done in Conventional CMOS design. 1 TG based full adder has 11 PMOS and 11 NMOS transistors.

- **8-Bit CLA Using Gate Diffusion Input (GDI) Logic**

To reduce the power consumption as well as the transistor count further, another technique for creating a full adder is used, called Gate Diffusion Input (GDI). For designing a 1-bit full adder using GDI logic, only 5 PMOS and 5 NMOS transistors are required.

- **8-Bit CLA Using ECRL Adiabatic Logic**

To design a 1-bit adder using ECRL, 2 XOR gates, 1 AND gate and a $(g_i + p_i \cdot c_i)$ boolean expression logic circuit are used. It comprises of 11 NMOS and 25 PMOS transistors which is greater than that required in an RCA [4].

IV. RESULT, ANALYSIS AND COMPARISON

The design and simulations have been done using Tanner Tools 15.23. Comparison of the propagation delay and the power dissipation for different full adders is shown at varying supply voltages and operating frequencies. An

RCA is designed using Conventional CMOS, TG logic and ECRL techniques and a CLA using Conventional CMOS, TG logic, GDI logic and ECRL. All the simulations are carried out at 180nm technology, NMOS transistor W/L ratio – 540/180 and PMOS transistor W/L ratio 1620/180.

4.1 Ripple Carry Adder

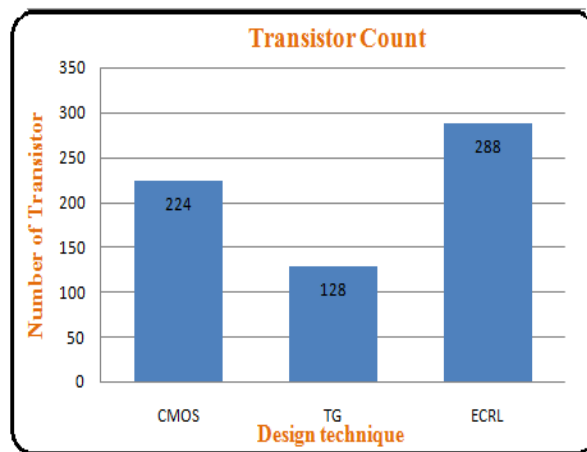


Fig.4.1.1 Transistor Count for RCA using Different Logic Design

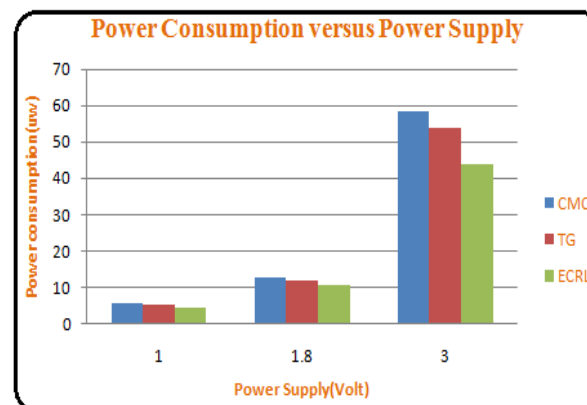


Fig.4.1.2 8-bit RCA power consumption comparison for different logic

4.2 Carry Look-ahead Adder

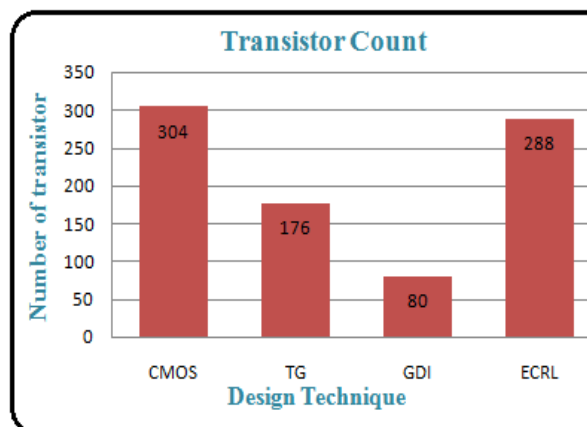


Fig.4.2.1 Transistor count for CLA using Different design technique

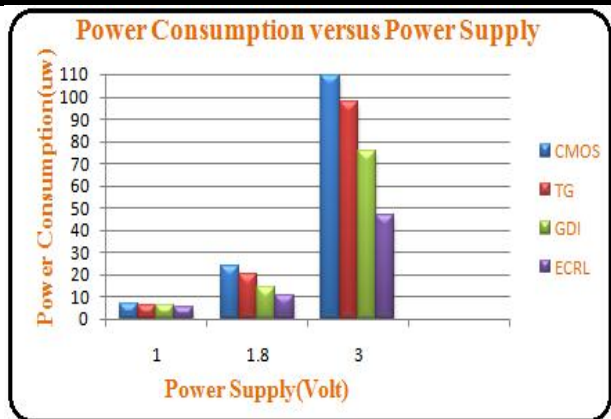


Fig.4.2.2 8 bit CLA power consumption versus power supply

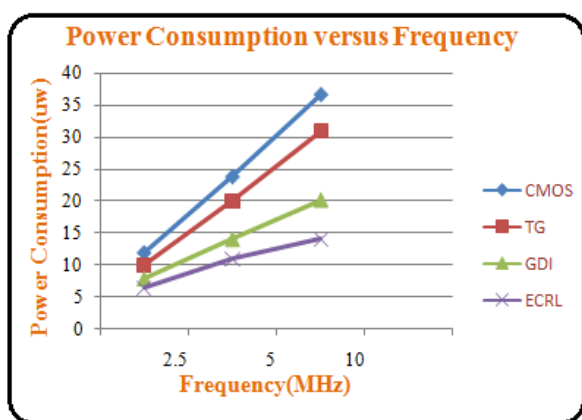


Fig.4.2.3. 8 bit CLA power consumption versus frequency

4.3 Comparative Analysis of 8-Bit RCA and CLA

By analysing 8bit RCA and CLA for different logic design for different input voltages and frequency we can see that RCA is better in terms of power consumption but delay is very high. Due to this reason, a CLA is used. To reduce the drawback of CLA power consumption we have used adiabatic logic in this work so power level decreases as in RCA circuit

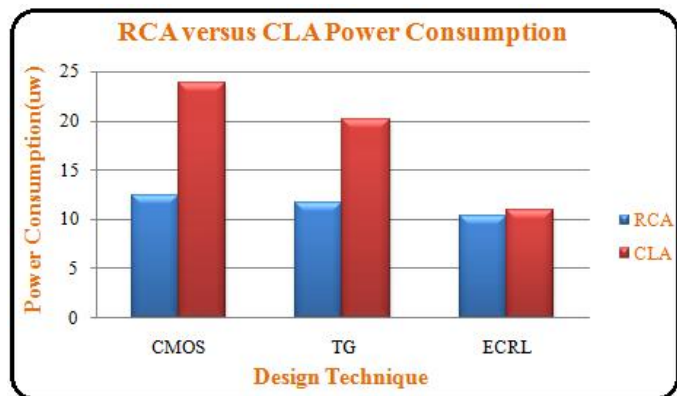


Fig.4.3.1 Power consumption for CLA and RCA

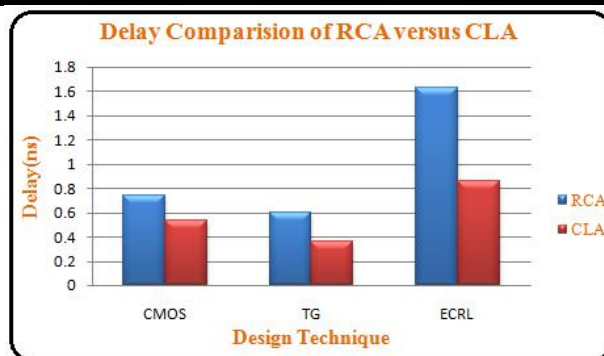


Fig.4.3.2. Delay comparison of RCA and CLA

V. CONCLUSION

When we compare Ripple Carry Adder and Carry look ahead Adder, CLA is better compare to RCA. CLA is better from RCA using ECRL adiabatic logic in which delay is reduced. And transistor count is also equal for both the logic circuits.

REFERENCES

- [1] Baljinder Kaur and Narinder Sharma, "Design of Full Adder in 180nm Technology using TG and Adiabatic Logic", International Journal of Computer Techniques, vol. 3, Issue 2, pp. 164-170, Mar-Apr 2016.
- [2] Kunjan D. Shinde, Jayashree C. Nidagundi, "Design of fast and efficient 1-bit full adder and its performance analysis", 2014 International Conference on Control, Instrumentation, Communication and Computational Technologies (ICCICCT), pp. 1275-1279, 2014.
- [3] S.Soundarya, Ms.S.Anusooya, "Design and analysis of Low power Carry Look-ahead adder using subthreshold Adiabatic logic", International Journal of Emerging Trends in Science and Technology, vol. 3, Issue 6, pp. 891-895, June 2016.
- [4] Y. Sunil Gavaskar Reddy, V.V.G.S.Rajendra Prasad, "Comparison of CMOS and Adiabatic Full Adder Circuits", International Journal of Scientific & Engineering Research, vol. 2, Issue 9, September 2011.
- [5] A. Morgenshtein, A. Fish, I.A. Wagner, "Gate-diffusion input (GDI) - a technique for low power design of digital circuits: analysis and characterization", IEEE International Symposium on Circuits and Systems, vol. 1, pp. I-477 – I-480, May 2016.

Autoregressive Integrated Moving Average (ARIMA) Model for Forecasting Cryptocurrency Exchange Rate in High Volatility Environment: A New Insight of Bitcoin Transaction

Nashirah Abu Bakar¹, Sofian Rosbi²

¹Islamic Business School, College of Business, Universiti Utara Malaysia, Malaysia

²School of Mechatronic Engineering, Unversiti Malaysia Perlis, Malaysia

Abstract— *The cryptocurrency is a decentralized digital money. Bitcoin is a digital asset designed to work as a medium of exchange using cryptography to secure the transactions, to control the creation of additional units, and to verify the transfer of assets. The objective of this study is to forecast Bitcoin exchange rate in high volatility environment. Methodology implemented in this study is forecasting using autoregressive integrated moving average (ARIMA). This study performed autocorrelation function (ACF) and partial autocorrelation function (PACF) analysis in determining the parameter of ARIMA model. Result shows the first difference of Bitcoin exchange rate is a stationary data series. The forecast model implemented in this study is ARIMA (2, 1, 2). This model shows the value of R-squared is 0.444432. This value indicates the model explains 44.44% from all the variability of the response data around its mean. The Akaike information criterion is 13.7805. This model is considered a model with good fitness. The error analysis between forecasting value and actual data was performed and mean absolute percentage error for ex-post forecasting is 5.36%. The findings of this study are important to predict the Bitcoin exchange rate in high volatility environment. This information will help investors to predict the future exchange rate of Bitcoin and in the same time volatility need to be monitor closely. This action will help investors to gain better profit and reduce loss in investment decision.*

Keywords— *Cryptocurrency, Bitcoin, ARIMA model, Volatility, Error diagnostics.*

I. INTRODUCTION

Technology is being presented as something new as it drives change at an ever-increasing rate (Chaharbaghi and Willis, 2000). The accelerating of

technology give an impact on pervades aspect of human life. Technology is convergence of computing, telecommunications and imaging technologies has had radical impacts on IT users, their work, and their working environments. In its various manifestations, IT processes data, gathers information, stores collected materials, accumulates knowledge, and expedites communication (Chan, 2000), plays an important role in many aspects of the everyday operations of today's business world.

In response to a new technological shift, criminals and consumers alike are increasingly finding new ways to evolve (Reynolds and Irwin, 2017). Therefore, accelerating technology was introduced many financial mechanisms such as bitcoin cryptocurrency.

A bitcoin cryptocurrency transaction is a new mechanism in digital currency. A bitcoin transaction was introduced based on cryptographic, allowing two parties to transact directly with each other without the need for a trusted third party. This transaction are computationally impractical to reverse would protect sellers from fraud, and routine escrow mechanisms could easily be implemented to protect buyers (Nakamoto, 2009). Blockchains are a software protocol that underlie bitcoin cryptocurrency in one sense, are nothing more than a modernizing information technology, but in another sense, are novel and disruptive (Yeoh, 2017). Cryptocurrencies, such as Bitcoin, rely on a de-centralised system based on peer-to-peer public key addresses, rather than having a central regulating body, such as a financial institution or bank, which reviews and monitors transactions. This allows potential criminal transactions to be processed through cryptocurrencies, as the process of moving money is quicker and more efficient due to the bypassing of the regulatory controls that third-party institutions, such as banks, are legally bound to perform.

This situation makes a bitcoin transaction faced with high volatility due to uncontrolled by professional body.

Volatility is a statistical measure of the dispersion of returns for a stock market. Volatility of stock markets has created much attention among investors because high volatility can bring high returns or losses to investors (Abu Bakar and Rosbi, 2017). This situation creates a risk to investors, because a rational investor always makes an investment decision based on risk and return (Lee, et al., 2016). Even there are many study focus on the volatility but no previous study are examine the volatility of bitcoin cyptocurrency using ARIMA model. Therefore this study try to fulfil this gap by investigates the volatility of bitcoin cryptocurrency using ARIMA model. According to Brailsford and Faff (1996) identify the best volatility forecasting technique is a critical job because a best predict volatility forecasting techniques not only depends on data availability and predefined assumption but also depends on the quality of data (Lee, et al., 2016; Abraham et al, 2007).

II. LITERATURE REVIEW

A number of studies have been undertaken on how the volatility is reflecting on the real returns that investors earn. Most of the previous study are investigates the performance of stock market. Study from Faff and McKenziet (2007) concluded that low or even negative return autocorrelations are more likely in situations where: return volatility is high; price falls by a large amount; traded stock volumes are high; and the economy is in a recessionary phase.

While, Abu Bakar and Rosbi (2017) investigate the reliability of Box–Jenkins statistical method to forecast the share price performance for Oil and Gas sector in Malaysia Stock found that the performance of Gas Malaysia Berhad can be forecast accurately using Autoregressive integrated moving average (ARIMA) model of (5,1,5). Similar to Malaysia, Balli and Elsamadisy, (2012) compare the linear methods, the seasonal ARIMA model provides better estimates for short-term forecasts in the State of Qatar. The range of forecast errors for the seasonal ARIMA model forecasts are less than 100 million Qatar Riyadh for the short-term currency in circulation (CIC) forecasts.

The significance of forecasting method in the stock market is also presented by Stevenson (2007), examines issues relating to the application of forecasting method. The results highlight the limitations in using the conventional approach in order to identify the best-specified ARIMA model in sample, when the purpose of the analysis is to provide forecasts. The results show that the ARIMA models can be useful in anticipating broad

market trends; there are substantial differences in the forecasts obtained using alternative specifications.

Although study from Jadevicius and Huston (2015) suggests that ARIMA is a useful technique to assess broad market price changes. Government and central bank can use ARIMA modelling approach to forecast national house price inflation. Developers can employ this methodology to drive successful house-building programme. Investor can incorporate forecasts from ARIMA models into investment strategy for timing purposes. If this player can predict the future changes in investment, they can modify future investment and reorganize strategic planning (Abu Bakar and Rosbi, 2017)

A more recent study, Coskun and Ertugrul, (2016) suggest several points. First, city/country-level house price return volatility series display volatility clustering pattern and therefore volatilities in house price returns are time varying. Second, it seems that there were high (excess) and stable volatility periods during observation term. Third, a significant economic event may change country/city-level volatilities. In this context, the biggest and relatively persistent shock was the lagged negative shocks of global financial crisis. More importantly, short-lived political/economic shocks have not significant impacts on house price return volatilities. Fourth, however, house price return volatilities differ across geographic areas, volatility series may show some co-movement pattern.

El-Masry and Abdel-Salam (2007) examine the effect of firm size and foreign operations on the exchange rate exposure of UK non-financial companies. They found that a higher percentage of UK firms are exposed to contemporaneous exchange rate changes than those reported in previous studies. In summary, while there has been a multitude of literature in the stock market literature concerned with the performance of stock market determinants, little attention has been placed on the forecasting of bitcoin cryptocurrency volatility.

III. RESEARCH METHODOLOGY

This section describes the forecasting procedure involving Bitcoin exchange rate. The process starting with data selection process then followed by forecasting process using autoregressive integrated moving average (ARIMA) method.

3.1 Data selection process

This study selects monthly data for Bitcoin exchange rate starting from January 2013 until October 2017. The data are collected from <https://www.coindesk.com>.

3.2 Forecasting procedure

This study forecast the performance of Bitcoin exchange rate using the statistical procedure as shown in Fig. 1. The

forecasting process is start with the identification of the data model using autoregressive integrated moving average (ARIMA). In developing ARIMA model, analysis of autocorrelation function (ACF) and partial autocorrelation function (PACF) need to be performed. Then, this research need to develop estimation of the parameter for chosen ARIMA model. In validating the model, diagnostics checking need to be developed. The residual is the difference between the observed value and the estimated value of the quantity of interest (sample mean). The residual should be uncorrelated, zero mean and zero variance. Then, forecasting and error checking stage can be performed.

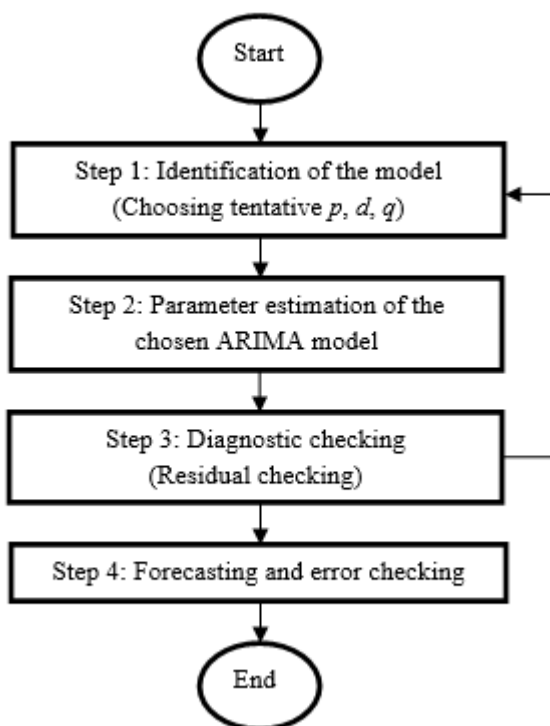


Fig. 1: Statistical forecasting procedure

3.3 Mathematical derivation of ARIMA model

This section describes mathematical derivation of autoregressive integrated moving average (ARIMA). This method is combining autoregressive (AR) with moving average (MA) method. Then, this hybrid method is integrated with data of difference process. The difference process is important to make sure data involved in this analysis can be represented as data with stationary characteristics. Therefore, the combination of this method is called as autoregressive integrated moving average. Firstly, this study describes the derivation of autoregressive (AR) method. An autoregressive (AR) model is a representation of a type of random process. It is used to describe certain time-varying processes in time series data. The autoregressive model specifies that the output variable depends linearly on its own previous values and on a stochastic term (an imperfectly

predictable term). Thus, the model is in the form of a stochastic difference equation.

The notation AR (p) indicates an autoregressive model of order p . The AR (p) model is defined as:

$$X_t = c + \varphi_1 X_{t-1} + \dots + \varphi_p X_{t-p} + \varepsilon_t$$

$$X_t = c + \sum_{i=1}^p \varphi_i X_{t-i} + \varepsilon_t \dots \dots \dots (1)$$

where $\varphi_1, \dots, \varphi_p$ the parameters of the model, c is constant, and ε_t is white noise.

Then, this study derived the equation for moving average (MA). The moving-average model specifies that the output variable depends linearly on the current and various past values of a stochastic (imperfectly predictable) term. MA of current deviation from mean depends on previous deviations.

The notation MA (q) refers to the moving average model of order q :

$$X_t = \mu + \varepsilon_t + \theta_1 \varepsilon_{t-1} + \dots + \theta_q \varepsilon_{t-q}$$

$$X_t = \mu + \varepsilon_t + \sum_{i=1}^q \theta_i \varepsilon_{t-i} \dots \dots \dots (2)$$

where μ is the mean of the series, $\theta_1, \dots, \theta_q$ are the parameters of the model, and $\varepsilon_t, \varepsilon_{t-1}, \dots, \varepsilon_{t-q}$ are white noise error terms. The value of q is called the order of the MA model.

Then, this study developed the mathematical derivation for autoregressive–moving-average (ARMA) models. In the statistical analysis of time series, autoregressive–moving-average (ARMA) models provide a parsimonious description of a (weakly) stationary stochastic process in terms of two polynomials, one for the autoregression and the second for the moving average.

Given a time series of data X_t the ARMA model is a tool for understanding and predicting future values in this series. The model consists of two parts, an autoregressive (AR) part and a moving average (MA) part. The AR part involves regress the variable on its own lagged values. The MA part involves modeling the error term as a linear combination of error terms occurring contemporaneously and at various times in the past.

The notation ARMA (p, q) refers to the model with p autoregressive terms and q moving-average terms. This model contains the AR (p) and MA (q) models. Equation (3) is an equation from adding the left term of Equation (1) and Equation (2).

$$X_t = c + \sum_{i=1}^p \varphi_i X_{t-i} + \varepsilon_t + \mu + \varepsilon_t + \sum_{i=1}^q \theta_i \varepsilon_{t-i} \dots \dots \dots (3)$$

where μ is the mean of the series is expected as zero. Then, this study re-arranged the equation (3) to become Equation (4).

$$X_t = c + \varepsilon_t + \sum_{i=1}^p \phi_i X_{t-i} + \sum_{i=1}^q \theta_i \varepsilon_{t-i} \dots \dots \dots (4)$$

where ϕ_1, \dots, ϕ_p the parameters of the AR model, $\theta_1, \dots, \theta_q$ are the parameters of the MA model, c is constant, and ε_t is white noise. The white noise ε_t is independent and has identical probability normal distribution. The model is usually referred to as the ARMA (p, q) model where p is the order of the autoregressive (AR) part and q is the order of the moving average (MA) part.

The error terms ε_t are generally assumed to be independent identically distributed random variables (i.i.d.) sampled from a normal distribution with zero mean: $\varepsilon_t \approx N(0, \sigma^2)$ where σ^2 is the variance.

Then, this study performed the derivation of autoregressive integrated moving average (ARIMA). Given a time series of data X_t where t is an integer index and the X_t are real numbers. An ARMA (p', q) model is given by Equation (4). Then, this study re-arranged to become Equation (5).

$$X_t - \alpha_1 X_{t-1} - \dots - \alpha_{p'} X_{t-p'} = \varepsilon_t + \theta_1 \varepsilon_{t-1} + \dots + \theta_q \varepsilon_{t-q}$$

$$\left(1 - \sum_{i=1}^{p'} \alpha_i L^i\right) X_t = \left(1 + \sum_{i=1}^q \theta_i L^i\right) \varepsilon_t \dots \dots \dots (5)$$

where L is the lag operator, α_i are the parameters of the autoregressive part of the model, θ_i are the parameters of the moving average part and ε_t are error terms. The error terms ε_t are generally assumed to be independent, identically distributed variables sampled from a normal distribution with zero mean.

In time series analysis, the lag operator, L or backshift operator operates on an element of a time series to produce the previous element. For example, given some time series:

$$X = \{X_1, X_2, \dots\}$$

Then, $LX_t = X_{t-1}$ for all $t > 1$.

where L is the lag operator.

Note that the lag operator can be raised to arbitrary integer powers so that:

$$L^k X_t = X_{t-k}$$

Referring to Equation (5), assume now that the

polynomial $\left(1 - \sum_{i=1}^{p'} \alpha_i L^i\right)$ has a unit root (a factor

$(1 - L)$) of multiplicity d . Then it can be rewritten as:

$$\left(1 - \sum_{i=1}^{p'} \alpha_i L^i\right) = \left(1 - \sum_{i=1}^{p'-d} \alpha_i L^i\right) (1 - L)^d \dots \dots \dots (6)$$

An ARIMA (p, d, q) process expresses this polynomial factorization property with $p = p' - d$, and is given by:

$$\left(1 - \sum_{i=1}^p \phi_i L^i\right) (1 - L)^d X_t = \left(1 + \sum_{i=1}^q \theta_i L^i\right) \varepsilon_t \dots \dots \dots (7)$$

The Equation (7) can be generalized as follows,

$$\left(1 - \sum_{i=1}^p \phi_i L^i\right) (1 - L)^d X_t = \delta + \left(1 + \sum_{i=1}^q \theta_i L^i\right) \varepsilon_t \dots \dots \dots (8)$$

This defines equation for an ARIMA (p, d, q) process with drift $\delta / (1 - \sum \phi_i)$.

IV. RESULT AND DISCUSSIONS

This section describes the result for autoregressive integrated moving average (ARIMA) model for forecasting the Bitcoin exchange rate.

4.1 Dynamic behavior of Bitcoin exchange rate

This section describes characteristics of the data that involved in this study. Figure 1 shows the dynamic behavior of Bitcoin exchange rate. The observation data are selected from January 2013 until October 2017. The total number of observations is 58. In January 2013, the value of 1 Bitcoin is 15.6 USD. Meanwhile, the value of exchange rate increased to 5350.5 USD in October 2017. The increment is 5334.9 USD.

Then, this study performed the autocorrelation function (ACF) and partial autocorrelation function (PACF) analysis. There is slow decay in autocorrelation analysis. Therefore, exchange rate data is a non-stationary data.

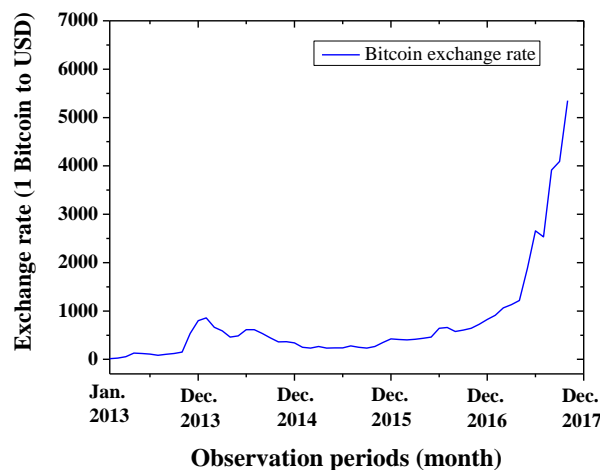


Fig. 1: Bitcoin exchange rate

Table 1: Correlogram for Bitcoin exchange rate

Autocorrelation		Partial Correlation		AC	PAC	Q-Stat	Prob
1	0.775	0.775	36.707	0.000			
2	0.632	0.076	61.494	0.000			
3	0.454	-0.144	74.550	0.000			
4	0.368	0.094	83.295	0.000			
5	0.251	-0.090	87.419	0.000			
6	0.175	-0.020	89.459	0.000			
7	0.141	0.096	90.810	0.000			
8	0.107	-0.038	91.602	0.000			
9	0.071	-0.037	91.956	0.000			
10	0.043	0.017	92.092	0.000			
11	0.026	-0.013	92.143	0.000			
12	0.015	0.003	92.161	0.000			
13	0.010	0.020	92.169	0.000			
14	0.005	-0.014	92.172	0.000			
15	-0.001	-0.013	92.172	0.000			

Table 2: Correlogram for first difference of Bitcoin exchange rate

Autocorrelation		Partial Correlation		AC	PAC	Q-Stat	Prob
1	0.133	0.133	1.0581	0.304			
2	0.539	0.531	18.844	0.000			
3	0.156	0.074	20.362	0.000			
4	0.231	-0.094	23.755	0.000			
5	0.187	0.088	26.007	0.000			
6	0.085	-0.025	26.480	0.000			
7	0.059	-0.127	26.716	0.000			
8	0.062	0.042	26.979	0.001			
9	0.009	0.029	26.985	0.001			
10	-0.006	-0.088	26.987	0.003			
11	0.040	0.072	27.105	0.004			
12	0.000	0.070	27.105	0.007			
13	-0.020	-0.120	27.135	0.012			
14	0.004	-0.006	27.137	0.018			
15	-0.011	0.085	27.147	0.028			

4.2 Stationary transformation using first difference

Figure 2 shows the first difference of Bitcoin exchange rate. The first difference results are calculated from February 2013 until October 2017. Figure 2 shows high volatility of exchange rate stating from May 2017 until October 2017.

Then, this study evaluated the stationarity characteristics for first difference of Bitcoin exchange rate. Table 2 shows the autocorrelation function (ACF) and partial autocorrelation function (PACF) analysis for first difference of Bitcoin exchange rate. Autocorrelation function (ACF) shows a significant spike on order of two with value of 0.539. This indicates the moving average is represented by order of two. In the same time, partial autocorrelation function (PACF) shows a significant spike on second order with value of 0.531. This indicates the autoregressive part can be represented by order of two. Therefore, the first difference of Bitcoin exchange rate can be represented by ARIMA (2, 1, 2).

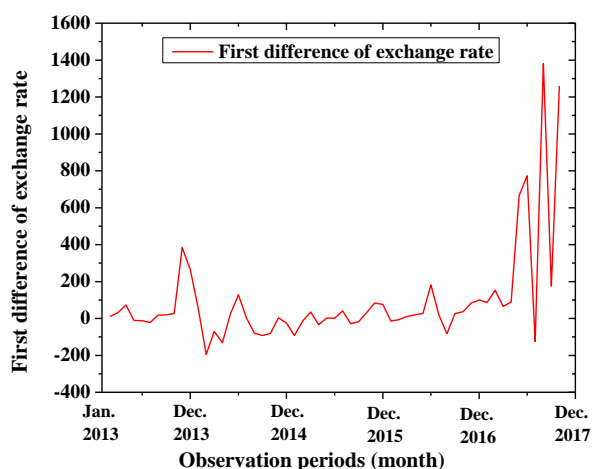


Fig. 2: First difference of Bitcoin exchange rate

4.3 Parameters estimation for ARIMA (2, 1, 2)

This section describes the estimation of parameters for ARIMA (2, 1, 2) model. This section starts with the derivation of ARIMA (p, d, q). In this study the value of p is set as 2; d is set as 1 and q is set as 2. Therefore, this study derived equation for ARIMA (2, 1, 2).

ARIMA (p, d, q) is represented by:

$$\left(1 - \sum_{i=1}^p \phi_i L^i\right) (1-L)^d X_t = c + \left(1 + \sum_{i=1}^q \theta_i L^i\right) \varepsilon_t$$

Then, this study derived equation for ARIMA (2, 1, 2).

$$\left(1 - \sum_{i=1}^2 \phi_i L^i\right) (1-L)^1 X_t = c + \left(1 + \sum_{i=1}^2 \theta_i L^i\right) \varepsilon_t$$

Then, this study expended the equation as below procedure.

$$(1 - \phi_1 L - \phi_2 L^2) (1-L)^1 x_t = c + (1 + \theta_1 L + \theta_2 L^2) \varepsilon_t$$

$$(1 - \phi_1 L - \phi_2 L^2) (x_t - x_{t-1}) = c + (1 + \theta_1 L + \theta_2 L^2) \varepsilon_t$$

$$(1 - \phi_1 L - \phi_2 L^2) \Delta x_t = c + (1 + \theta_1 L + \theta_2 L^2) \varepsilon_t$$

$$\Delta x_t - \phi_1 L \Delta x_t - \phi_2 L^2 \Delta x_t = c + \varepsilon_t + \theta_1 L \varepsilon_t + \theta_2 L^2 \varepsilon_t$$

$$\Delta x_t - \phi_1 \Delta x_{t-1} - \phi_2 \Delta x_{t-2} = c + \varepsilon_t + \theta_1 \varepsilon_{t-1} + \theta_2 \varepsilon_{t-2}$$

Therefore, ARIMA (2, 1, 2) can be represented as below

equation:

$$\Delta x_t = c + \phi_1 \Delta x_{t-1} + \phi_2 \Delta x_{t-2} + \theta_1 \varepsilon_{t-1} + \theta_2 \varepsilon_{t-2} + \varepsilon_t \dots (9)$$

Table 3 shows parameter estimation for ARIMA (2, 1, 2). Therefore, historical data of Bitcoin exchange rate can be represented by below equation of ARIMA (2, 1, 2).

$$\Delta x_t = 218 + 0.237084 \Delta x_{t-1} + 0.687976 \Delta x_{t-2} - 0.281149 \varepsilon_{t-1} - 0.024093 \varepsilon_{t-2} + \varepsilon_t \dots (10)$$

R-squared is a statistical measure of how close the data are to the fitted regression line. R-squared is represented by the percentage of the response variable variation that is explained by a linear model. This model shows the value of R-squared is 0.444432. This value indicates the model explains 44.44% from all the variability of the response data around its mean. The Akaike information criterion is 13.7805. This model is considered a model with good fitness.

Table 3: Parameter estimation for ARIMA (2,1,2)

Sample: 2013M02 2017M10 Included observations: 57 Convergence achieved after 92 iterations Coefficient covariance computed using outer product of gradients				
Variable	Coefficient	Std. Error	t-Statistic	Prob.
C	218.8310	381.8171	0.573130	0.5691
AR(1)	0.237084	0.277129	0.855501	0.3963
AR(2)	0.687976	0.208808	3.294773	0.0018
MA(1)	-0.281149	0.230441	-1.220046	0.2281
MA(2)	-0.024093	0.185385	-0.129961	0.8971
SIGMASQ	44301.25	5707.468	7.761980	0.0000
R-squared	0.444432	Mean dependent var	93.59530	
Adjusted R-squared	0.389964	S.D. dependent var	284.8936	
S.E. of regression	222.5155	Akaike info criterion	13.78035	
Sum squared resid	252517.1	Schwarz criterion	13.99541	
Log likelihood	-386.7400	Hannan-Quinn criter.	13.86393	
F-statistic	8.159581	Durbin-Watson stat	1.968995	
Prob(F-statistic)	0.000010			
Inverted AR Roots	.96	-.72		
Inverted MA Roots	.35	-.07		

4.4 Diagnostics checking for ARIMA (2, 1, 2)

Diagnostics checking process is to prove this model adequately describes the time series under consideration by subjecting the calibrated model to a range of statistical tests. For the diagnostic checks in this paper, it is assumed that a maximum likelihood estimator is used to estimate the model parameters. A random pattern of residuals supports a linear model. In discrete time, white noise is a discrete signal whose samples are regarded as a sequence of serially uncorrelated random variables with zero mean and finite variance. Table 4 shows the residual for the first difference of Bitcoin exchange rate is not significant. Therefore, the residual is considered as white noise.

Table 4: Residual diagnostics of ARIMA (2,1,2)

Sample: 2013M01 2017M10 Included observations: 57 Q-statistic probabilities adjusted for 4 ARMA terms						
Autocorrelation	Partial Correlation	AC	PAC	Q-Stat	Prob	
		1	-0.008	-0.008	0.0039	
		2	0.009	0.009	0.0093	
		3	0.004	0.004	0.0103	
		4	0.024	0.024	0.0483	
		5	0.047	0.048	0.1937	0.660
		6	0.107	0.108	0.9468	0.623
		7	0.116	0.120	1.8571	0.603
		8	0.049	0.053	2.0215	0.732
		9	-0.110	-0.115	2.8749	0.719
		10	-0.078	-0.097	3.3128	0.769
		11	0.109	0.093	4.1812	0.759
		12	0.038	0.024	4.2877	0.830
		13	-0.051	-0.079	4.4857	0.877
		14	-0.002	-0.020	4.4859	0.923
		15	-0.014	0.005	4.5012	0.953

4.5 Ex-post forecasting using ARIMA (2, 1, 2) model

In validating the prediction model of ARIMA (2, 1, 2), an ex-post analysis is needed. Firstly, this study started with calculated the parameters for ARIMA (2, 1, 2). The selected data for developing parameters are started from January 2013 until August 2017. Table 5 shows the parameters for ARIMA (2, 1, 2). Therefore, the equation for ex-post forecasting validation is represented by:

$$\Delta x_t = 148.984 + 0.593 \Delta x_{t-1} + 0.302 \Delta x_{t-2} - 0.603 \varepsilon_{t-1} - 0.166 \varepsilon_{t-2} + \varepsilon_t \dots (11)$$

Next, this study plotted the forecasted value using Equation (11). Figure 3 shows the ex-post forecasting validation. Figure 3 shows the actual value for September and October 2017 are in the range of 2 standard errors from the forecasted value. Therefore, ARIMA (2, 1, 2) is a reliable forecasting model.

Table 5: Correlogram for first difference of Bitcoin exchange rate

Included observations: 55 Convergence achieved after 130 iterations Coefficient covariance computed using outer product of gradients				
Variable	Coefficient	Std. Error	t-Statistic	Prob.
C	148.9841	289.6027	0.514443	0.6093
AR(1)	0.592845	0.767750	0.772185	0.4437
AR(2)	0.301765	0.764740	0.394598	0.6949
MA(1)	-0.603318	0.679653	-0.887684	0.3790
MA(2)	0.166194	0.615973	0.269808	0.7884
SIGMASQ	43375.50	6130.310	7.075579	0.0000
R-squared	0.242640	Mean dependent var	70.89276	
Adjusted R-squared	0.165359	S.D. dependent var	241.5214	
S.E. of regression	220.6508	Akaike info criterion	13.75470	
Sum squared resid	238565.2	Schwarz criterion	13.97368	
Log likelihood	-372.2542	Hannan-Quinn criter.	13.83938	
F-statistic	3.139687	Durbin-Watson stat	1.741713	
Prob(F-statistic)	0.015481			
Inverted AR Roots	.92	-.33		
Inverted MA Roots	.30-.271	.30+.271		

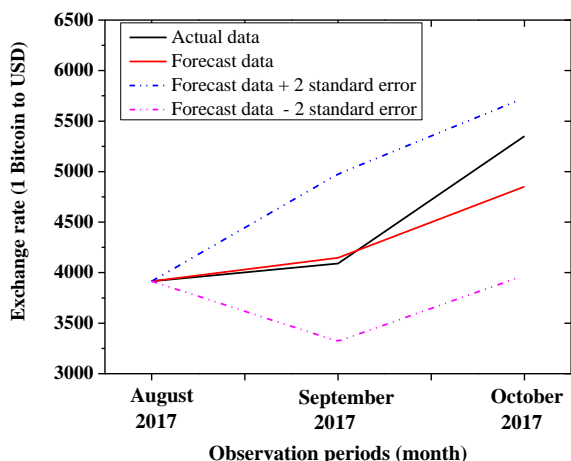


Fig. 3: Ex-post forecasting validation

Then, this study also checked the mean absolute percentage error (MAPE) between forecast value and actual value. Equation (12) shows the equation for calculating mean absolute percentage error (MAPE).

$$MAPE = \frac{100}{n} \sum_{t=1}^n \left| \frac{A_t - F_t}{A_t} \right| \dots\dots\dots (12)$$

where A_t is the actual value, F_t is the forecast value and n is number of fitted.

Table 6 shows the error analysis between forecasting value and actual data. The mean absolute percentage error for ex-post forecasting is 5.36%.

Table 6: Error analysis between forecasting value and actual data

Observation periods (Month)	Forecast data	Actual data	Absolute percentage error
September 2017	4147.7	4090.7	1.4%
October 2017	4851.8	5350.5	9.3%
Mean absolute percentage error (MAPE)			5.36%

4.6 Ex-ante forecasting using ARIMA (2, 1, 2) model

This study performed ex-ante forecasting using ARIMA (2,1,2) model for November and December 2017. Figure 4 shows ex-ante forecasting of Bitcoin exchange rate. Forecast value in November 2017 is 5700, and December 2017 is 6659. Forecast value is represented by red line. Upper limit of forecast value is forecast value add with 2 standard errors. Meanwhile, lower limit is forecast value minus with 2 standard errors.

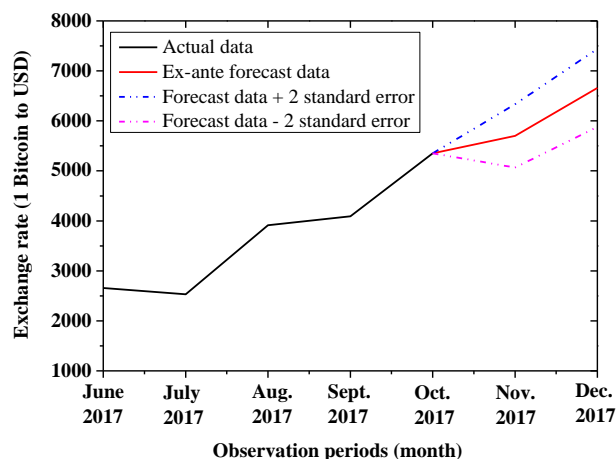


Fig. 4: Ex-ante forecasting of Bitcoin exchange rate

V. CONCLUSION

The objective of this paper is to forecast cryptocurrency exchange rate. In this study, we focus on value of 1 Bitcoin to United States Dollar (USD). The data selected for this study are started from January 2013 until October 2017. We performed the forecasting approach using autoregressive integrated moving average (ARIMA) method. The main findings from this study are:

- (a) In January 2013, the value of 1 Bitcoin is 15.6 USD. Meanwhile, the value of exchange rate increased to 5350.5 USD in October 2017. The increment is 5334.9 USD.
- (b) This study performed the autocorrelation function (ACF) and partial autocorrelation function (PACF) analysis for Bitcoin exchange rate. There is slow decay in autocorrelation analysis. Therefore, exchange rate data is a non-stationary data
- (c) Then, this study performed stationary transformation method with finding the correlogram analysis for first difference of Bitcoin exchange rate. Autocorrelation function (ACF) shows a significant spike on order of two with value of 0.539. This indicates the moving average is represented by order of two. In the same time, partial autocorrelation function (PACF) shows a significant spike on second order with value of 0.531. This indicates the autoregressive part can be represented by order of two. Therefore, the first difference of Bitcoin exchange rate can be represented by ARIMA (2, 1, 2).
- (d) Therefore, historical data of Bitcoin exchange rate can be represented by below equation of ARIMA (2, 1, 2).

$$\Delta x_t = 218 + 0.237084\Delta x_{t-1} + 0.687976\Delta x_{t-2} - 0.281149\varepsilon_{t-1} - 0.024093\varepsilon_{t-2} + \varepsilon_t$$

- (e) The error analysis is calculated between forecasting value and actual data. The mean absolute percentage error for ex-post forecasting is 5.36%.
- (f) This study performed ex-ante forecasting using ARIMA (2,1,2) model for November and December 2017. Forecast value in November 2017 is 5700, and December 2017 is 6659

As a conclusion, forecasting approach using autoregressive integrated moving average (ARIMA) method produce a reliable forecasting model. However, high volatility environment creates larger error. Therefore, Forecasting in high volatility environment need special consideration of error diagnostics.

The findings of this study are important to predict the Bitcoin exchange rate in high volatility environment. This information will help investors to predict the future exchange rate of Bitcoin and in the same time volatility need to be monitor closely. This action will help investors to gain better profit and reduce loss in investment decision.

VI. FURTHER RESEARCH

This research can be extending to discover the factors that contribute to the volatility of Bitcoin exchange rate. In the same time, the correlation of Bitcoin with other currency also is another area that can be analyze

REFERENCES

- [1] Chaharbaghi, K. and Willis, R. (2000) The technology, mythology and economy of technology, *Management Decision*, 38 (6), pp. 394-402
- [2] Chan, S.L. (2000) Information technology in business processes, *Business Process Management Journal*, 6 (3), pp. 224-237
- [3] Reynolds, P. and Irwin, A.S.M. (2017) Tracking digital footprints: anonymity within the bitcoin system, *Journal of Money Laundering Control*, 20 (2), pp. 172-189
- [4] Nakamoto, S. (2009) Bitcoin: A Peer-to-Peer Electronic Cash System, available at <http://bitcoin.org/bitcoin.pdf> (accessed 20 October 2017)
- [5] Yeoh, P. (2017) Regulatory issues in blockchain technology, *Journal of Financial Regulation and Compliance*, 25 (2), pp. 196-208
- [6] Abu Bakar, N. and Rosbi, S.(2017) Robust Pearson Correlation Analysis of Volatility for the Islamic Bank in Malaysia: An Arithmetic Approach in Islamic Financial Engineering, *International Journal of Economics, Commerce and Management*, V (3), pp. 1-15
- [7] Lee, H.S., Ng, D.C.Y., Lau, T.C. and Ng, C.H. (2016) Forecasting Stock Market Volatility on Bursa Malaysia Plantation Index, *International Journal of Finance and Accounting*, 5 (1), pp. 54-61
- [8] Brailsford, T. J. & Faff, R.W. (1996). An Evaluation of Volatility Forecasting Techniques, *Journal of Banking and Finance*, 20, 419-438
- [9] Abraham, A., Roselina, S., Siti, M. & Siti, Z. (2007). Forecasting time series data using hybrid grey relational artificial neural network and autoregressive integrated moving average model. *Neural Network World*, 573-605.
- [10] Faff, R.W. and McKenzie, M.D., (2007), The relationship between implied volatility and autocorrelation, *International Journal of Managerial Finance*, 3 (2) pp. 191 – 196
- [11] Abu Bakar, N. and Rosbi, S.(2017) Robust Diagnostics of Box-Jenkins statistical method in forecasting share price performance for Sharia-Compliant Oil and Gas sector in Malaysia Stock Exchange, *International Journal of Scientific Research and Management*, 5 (7) pp. 6364-6376
- [12] Balli, F. and Elsamadisy, E.M. (2012) Modelling the currency in circulation for the State of Qatar, *International Journal of Islamic and Middle Eastern Finance and Management*, 5 (4), pp.321-339
- [13] Simon Stevenson, (2007), A comparison of the forecasting ability of ARIMA models, *Journal of Property Investment & Finance*, 25 (3), pp.223-240
- [14] Jadevicius, A. and Huston, S. (2015) ARIMA modelling of Lithuanian house price index, *International Journal of Housing Markets and Analysis*, 8 (1), pp.135-147
- [15] Coskun, Y. and Ertugrul, H.M. (2016) House price return volatility patterns in Turkey, Istanbul, Ankara and Izmir, *Journal of European Real Estate Research*, 9 (1), pp.26-51
- [16] El-Masry, A. and Abdel-Salam, O. (2007), Exchange rate exposure: do size and foreign operations matter? *Managerial Finance*, 33 (9), pp.741-765.
- [17] Abu Bakar, N. and Rosbi, S. (2017) Data Clustering using Autoregressive Integrated Moving Average (ARIMA) model for Islamic Country Currency: An Econometrics method for Islamic Financial Engineering, *The International Journal of Engineering and Science*, 6 (6), 22-31

Design of Tuning Mechanism of PID Controller for Application in three Phase Induction Motor Speed Control

Alfred A. Idoko¹, Iliya. T. Thuku², S. Y. Musa³, Chinda Amos⁴

^{1,2,3} Department of Electrical and Electronics Engineering, Modibbo Adama University of Technology Yola, Adamawa State, Nigeria.

⁴ Nigeria National Centre for Technology Management, Modibbo Adama University of Technology Yola, Adamawa State, Nigeria.

Abstract— This paper presents a design of tuning mechanism of Proportional Integral Derivative Controller for application in three phase induction motor speed controls. It demonstrates, in detail, how to employ the MatLab tool so as to search efficiently for the optimal PID controller parameters within a mechanism system. The proposed approach has superior features, including: easy implementation; stable convergence characteristics; and less computational effort. Three phase induction motors has complex mathematical modelling which makes it difficult to design the speed controller. Software PID Tuning Mechanism was developed herein and used to obtain both the initial PID parameters under normal operating conditions and the optimal parameters of PID control under fully-loaded conditions. The proposed PID controller Tuning Mechanism will automatically tune its parameters within these ranges. In order to prove the performance of the proposed tuning mechanism for the PID controller, a three phase asynchronous motor was modelled in MATLAB, the transfer function was obtained using the software and a controller was designed using PID. The modelling and simulations results show the potential of the proposed controller to be very efficient.

Keywords— PID Controller, Modelling of Induction Motor, Design of PID Tuning Software.

I. INTRODUCTION

Speed control of an induction motor has been a major challenge since its discovery by a French physicist François Arago in 1824. The induction motor is made up of two distinct parts, stator which is a stationary part and rotor (also called armature core windings) which is the rotary part. Induction motor is an alternating current electric machine which by excitation, produces a torque[1]. The torque result from an electromagnetic induction from the magnetic flux due to the stator core windings as a result of

rotation about a fixed position in the stator core windings [2].

Induction motor is the most common electrical machine used in modern industries. It has gained such popularity due to its various advantages. The various advantages are high efficiency, low cost, good self-starting, simplicity in design, the absence of the collector brooms system, and a small inertia. Even though it has a wide range of advantages it also has quite few disadvantages. Induction motor has disadvantages, such as complex, multivariable and nonlinear mathematical model and is not inherently capable of providing variable speed operation [3].

During the past decades, process control techniques in industries have made great advances. Numerous control methods such as: adaptive control; neural control; and Fuzzy control have been studied [4]. Among these the best known is the Proportional Integral Derivative (PID) controller, which is being widely used because of its simple structure and robust performance within a wide range of operating conditions. Unfortunately, it has been quite difficult to properly tune the gains of PID controllers because many industrial plants are often burdened with problems such as: high orders; time delays; and nonlinearities [5].

Over the years, several heuristic methods have been proposed for the tuning of PID controllers. The first method used the classical tuning rules proposed by Ziegler and Nichols [6]. In general, it is often hard to determine optimal or near optimal PID parameters with the Ziegler–Nichols formula for many industrial plants [7]. For this reason it is highly desirable to increase the capabilities of PID controllers by adding new features. Many Artificial Intelligence (AI) techniques have been employed to improve the controller performances for a wide range of plants whilst retaining their basic characteristics. AI techniques such as: neural networks; fuzzy systems; and

neural-fuzzy logic have been widely applied to the proper tuning of PID controller parameters [8].

Software tool, is one of the modern tuning mechanisms. The software tool can generate a high-quality solution for shorter calculation time and stable convergence characteristics than other stochastic methods [4]. Much research is still in progress for proving the potential of the software tool for solving complex induction motor system operation problems. Because the software tool method is an excellent tuning mechanism and a promising approach to solving the PID controller parameters tuning problem. This controller is called the software-tuning PID controller. However, the PID controller is not robust to wide parameter variation and large external disturbance [11]. This serves especially for highly coupling nonlinear system where the PID controller lacks adaptive capability. The difficulty in obtaining transfer function of three phase induction motor poses a serious challenge to this mechanism.

However, if the PID controller parameters are chosen incorrectly, the controlled process input can be unstable, i.e., its output diverges, with or without oscillation, and is limited only by saturation or mechanical breakage. Instability is caused by excess gain, particularly in the presence of significant lag [1].

Generally, stabilization of response is required and the process must not oscillate for any combination of process conditions and setpoints, though sometimes marginal stability (bounded oscillation) is acceptable or desired [1].

Mathematically, the origins of instability can be seen in the Laplace domain. The total loop or close loop transfer function is:

$$H(s) = K_d + \frac{K(s)G(s)}{1+K(s)G(s)} \quad \dots (1)$$

Where,

K(s): PID transfer function

G(s): Plant transfer function

The system is called unstable where the closed loop transfer function diverges for some s. This happens for situations where $K(s)G(s) = -1$. Typically, this happens when there is a 180 degree phase shift. Stability is guaranteed when $K(s)G(s) < 1$ for frequencies that suffer high phase shifts.

In order to achieve practical requirement, engineers have to adjust the parameters under different operating conditions and devise a means of obtaining complex transfer function. However, the robustness is limited to a small range. A mechanism to overcome this disadvantage is called the software-tuning mechanism. The parameter tuning at any

instance is usually based on a structurally fixed mathematical model produced by a software procedure [11]. Unfortunately, recent plants find it difficult to obtain their fixed mathematical models. This paper proposes a software-tuning mechanism for PID controller for an application in three phase induction motors. At the same time, the robustness will be expanded to a large range. In this paper, a practical high-order mechanism system with a PID controller is adopted to test the performance of the proposed software-tuning mechanism for PID controller. As compared with the other mechanisms such as the one proposed by [9][8] [7][6], it is found that the nominal values and tuning ranges of the PID parameters by the proposed software-tuning mechanism can be accurately determined. MatLab simulations and experimental results have shown that the proposed controller is most suitable and robust for PID controller.

II. MATERIALS AND METHODS

In this work the following materials were used: Software tools, PID Controller block in MATLAB package, Induction Motor and Voltage source.

2.1 PID Controller

PID controllers are widely used in industries for speed control purpose. A PID controller calculates an “error” value as the difference between the measured process value and the desired set point. The PID controller calculation involves three separate constants and is accordingly sometimes called three-term control i.e. the proportional, integral and the derivative value which is denoted by PID as show in figure 1 below.

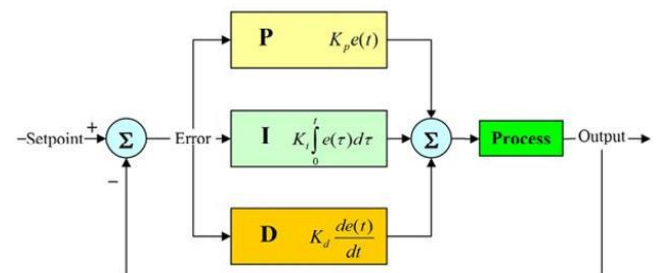


Fig. 1: Block diagram of PID controller [10]

Tuning a control loop is the adjustment of its control parameters (proportional band/gain, integral gain/reset, derivative gain/rate) to the optimum values for the desired control response [11]. Stability (no unbounded oscillation) is a basic requirement, but beyond that, different systems have different behavior, different applications have different requirements, and requirements may conflict with one another [4].

PID tuning is a difficult problem, even though there are only three parameters and in principle is simple to describe, because it must satisfy complex criteria within the limitations of PID control. There are accordingly various methods for loop tuning, and more sophisticated techniques are the subject of patents; this section describes some traditional manual methods for loop tuning. Figure 2 below shows the effect of tuning the PID parameters on the process response.

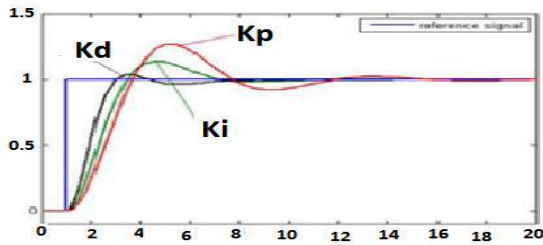


Fig. 2: Process variables for different Kp, Ki and Kd values [11].

Tuning the Proportional Term: Process variable for different Kp values (Ki and Kd held constant) is shown in Figure 2. The proportional term makes a change to the output that is proportional to the current error value. The proportional response can be adjusted by multiplying the error by a constant Kp, called the proportional gain [11]. The proportional term is given by the Equation (12)

$$P_{out} = K_p e^{(t)} \quad \dots (2)$$

$$e = G / K_p \quad \dots (3)$$

Integral Term: Process variable for different Ki values (Kp and Kd held constant) is shown in figure 2. The contribution of the integral term is proportional to both the magnitude of the error and the duration of the error. The integral in a PID controller is the sum of the instantaneous error over time and gives the accumulated offset that should have been corrected previously [12]. The accumulated error is then multiplied by the integral gain (Ki) and added to the controller output. The integral term is given by the Equation (4)

$$I_{out} = k_i \int e^{(\tau)} d\tau \quad \dots (4)$$

Derivative Term: Process variable for different Kd values (Ki and Kp held constant) is shown in Figure 2. The derivative of the process error is calculated by determining the slope of the error over time and multiplying this rate of change by the derivative gain Kd. The magnitude of the contribution of the derivative term to the overall control action is termed the derivative gain Kd [12]. The derivative term is given by the Equation (5)

$$D_{out} = K_d + \frac{d}{dt} c(t) \quad \dots (5)$$

2.2 PID Tuning Mechanisms

There are several methods for tuning a PID Controller. Tuning methods with its advantages and disadvantages are given in Table 1.

Table.1: PID Tuning Method [11]

Method	Advantage	Disadvantage
Manual Tuning	No maths required. On-line method	Require experience personnel
Ziegler-Nichols	Proven method. Online method	Process upset, some trial-and-error
Software tools	Consistent tuning. Online or offline method. Can support Non-Steady State Tuning	some cost and training involved
Cohen-Coon	Good process models	some math. Offline method only good for first order processes.

The most effective methods generally involve in the development of some form of the process model, and then choosing P, I, and D based on the dynamic model parameters. Manual tuning methods can be relatively inefficient, particularly if the loops have response times on the order of minutes or longer. The choice of method will depend largely on whether or not the loop can be taken "offline" for tuning, and the response time of the system. If the system can be taken offline, the best tuning method often involves subjecting the system to a step change in input,

measuring the output as a function of time, and using this response to determine the control parameters [11].

2.3 Software Tool

Most modern industrial facilities no longer tune loops using the manual calculation methods shown above. Instead, PID tuning and loop optimization software are used to ensure consistent results. These software packages will gather the data, develop process models, and suggest optimal tuning. Some software packages can even develop tuning by gathering data from reference changes [13].

Advances in automated PID Loop Tuning software also deliver algorithms for tuning PID Loops in a dynamic or Non-Steady State (NSS) scenario. The software will model the dynamics of a process, through a disturbance, and calculate PID control parameters in response.

2.4 Modelling of Induction Motor

In the control of any power electronics drive system, mathematical model of the plant is required [14]. From the objective equation (1), the Plant transfer function [8] is required to design the loop controller. To obtain the Induction Motor (Plant) transfer function and design any type of controller to control its speed, mathematical model is required. The Equivalent circuit of induction motor in d-q axis fig. (3) will be used to analyze the mathematical modeling of induction motor.

The induction motor can be analyzed as a three phase stator winding magnetically coupled with the rotors ones, independently on the rotor typology.

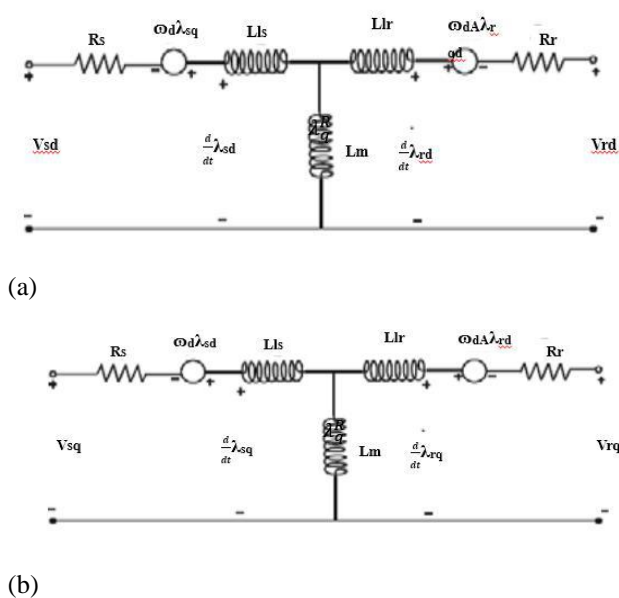


Fig. 3: Equivalent circuit of induction motor (a) d-axis and (b) q-axis [15]

The equivalent circuit used for obtaining the mathematical model of the induction motor is shown in the Fig. (3) The induction motor model is established using a rotating (d, q) field reference (without saturation) concept. An induction motor model is then used to predict the voltage required to drive the flux and torque to the demanded values within a fixed time period. This calculated voltage is then synthesized using the dynamic model of the motor in Simulink.

The induction motor can be analyzed as a three phase stator winding magnetically coupled with the rotors ones, independently on the rotor typology.

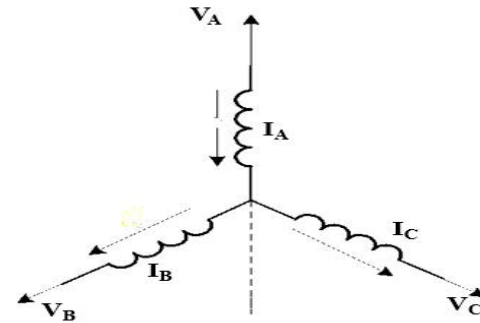


Fig. 4: Phasor diagram of Stator winding [10]

$$V_A = p\lambda_A + R_S I_A \quad \dots (6)$$

$$V_B = p\lambda_B + R_S I_B \quad \dots (7)$$

$$V_C = p\lambda_C + R_S I_C \quad \dots (8)$$

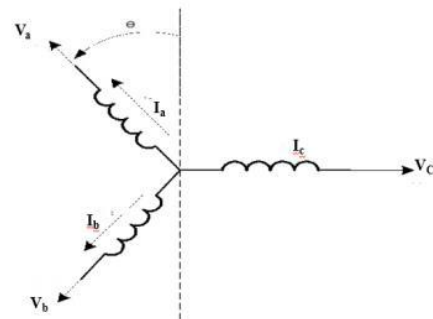


Fig. 5: Phasor diagram of Rotor winding [10]

$$V_a = p\lambda_a + R_S I_a \quad \dots (9)$$

$$V_b = p\lambda_b + R_S I_b \quad \dots (10)$$

$$V_c = p\lambda_c + R_S I_c \quad \dots (11)$$

When the dynamic model of the induction motors is determined, we can transform the three-phase machine into a two-phase machine using an orthonormal transformation matrix T:

$$T = \begin{bmatrix} \sqrt{\frac{2}{3}} & -\frac{1}{\sqrt{6}} & -\frac{1}{\sqrt{6}} \\ 0 & \frac{1}{\sqrt{2}} & -\frac{1}{\sqrt{2}} \\ \frac{1}{\sqrt{3}} & \frac{1}{\sqrt{3}} & \frac{1}{\sqrt{3}} \end{bmatrix} \quad \dots (12)$$

$$\begin{bmatrix} \lambda_{ABC} \\ \lambda_{abc} \end{bmatrix} = \begin{bmatrix} M_{ss} & M_{sr} \\ M_{rs} & M_{rr} \end{bmatrix} \begin{bmatrix} I_{ABC} \\ I_{abc} \end{bmatrix} \quad \dots (13)$$

$$M_{SS} = \begin{bmatrix} L_o + L_s ds & -\frac{L_o}{2} & -\frac{L_o}{2} \\ -\frac{L_o}{2} & L_o + L_s ds & -\frac{L_o}{2} \\ -\frac{L_o}{2} & -\frac{L_o}{2} & L_o + L_s ds \end{bmatrix} \quad \dots (14)$$

$$M_{rr} = \begin{bmatrix} Lo + Lrdr & -\frac{Lo}{2} & -\frac{Lo}{2} \\ -\frac{Lo}{2} & Lo + Lrdr & -\frac{Lo}{2} \\ -\frac{Lo}{2} & -\frac{Lo}{2} & Lo + Lrdr \end{bmatrix} \dots (15)$$

$$M_{sr} = \begin{bmatrix} Lo \cos \theta & Lo \cos(\theta + 120^\circ) & Lo \cos(\theta + 240^\circ) \\ Lo \cos(\theta + 240^\circ) & Lo \cos \theta & Lo \cos(\theta + 120^\circ) \\ Lo \cos(\theta + 120^\circ) & Lo \cos(\theta + 240^\circ) & Lo \cos \theta \end{bmatrix} \dots (16)$$

Where Mss, Mrr and Msr are the stator mutual inductance, rotor mutual inductance respectively. Lo is the no load inductance.

Below equations represent the equation of the equivalent two phase machine. For control purpose, another transformation is required.

$$V_\alpha^s = R_s i_\alpha^s + p\lambda_\alpha^s \dots (17)$$

$$V_\beta^s = R_s i_\beta^s + p\lambda_\beta^s \dots (18)$$

$$V_0^s = R_s i_0^s + p\lambda_0^s \dots (19)$$

$$V_\alpha^r = R_r i_\alpha^r + p\lambda_\alpha^r \dots (20)$$

$$V_\beta^r = R_r i_\beta^r + p\lambda_\beta^r \dots (21)$$

$$V_0^r = R_r i_0^r + p\lambda_0^r \dots (22)$$

If we want to move these equations in a reference frame fixed with the stator, we have to apply a rotation matrix around the Z axis [16].

$$\lambda_\alpha^s = (L_{ds} + \frac{3}{2}L_0)i_\alpha^s + \frac{3}{2}L_0 \cos(\theta) i_\alpha^r - \frac{3}{2}L_0 \sin(\theta) i_\beta^r \dots (23)$$

$$\lambda_\beta^s = (L_{ds} + \frac{3}{2}L_0)i_\beta^s + \frac{3}{2}L_0 \cos(\theta) i_\beta^r - \frac{3}{2}L_0 \sin(\theta) i_\alpha^r \dots (24)$$

$$\lambda_\alpha^r = (L_{dr} + \frac{3}{2}L_0)i_\alpha^r + \frac{3}{2}L_0 \cos(\theta) i_\alpha^s - \frac{3}{2}L_0 \sin(\theta) i_\beta^s \dots (25)$$

$$\lambda_\beta^r = (L_{dr} + \frac{3}{2}L_0)i_\beta^r + \frac{3}{2}L_0 \cos(\theta) i_\beta^s - \frac{3}{2}L_0 \sin(\theta) i_\alpha^s \dots (26)$$

With this transformation, the final equation in a reference system called ‘stator dq0 reference frame’ are:

$$\lambda_d^s = L_s i_d^s + L_m i_d^r \dots (27)$$

$$\lambda_q^s = L_s i_q^s + L_m i_q^r \dots (28)$$

$$\lambda_d^r = L_r i_d^r + L_m i_d^s \dots (29)$$

$$\lambda_q^r = L_r i_q^r + L_m i_q^s \dots (30)$$

$$V_d^s = R_s i_d^s + p\lambda_d^s \dots (31)$$

$$V_q^s = R_s i_q^s + p\lambda_q^s \dots (32)$$

$$0 = R_r i_d^r + p\lambda_d^r + w\lambda_q^r \dots (33)$$

$$0 = R_r i_q^r + p\lambda_q^r + w\lambda_d^r \dots (34)$$

$$\text{Torque (T)} = \lambda_q^r i_d^r - \lambda_d^r i_q^r \dots (35)$$

Where Ls and Lr are the respective stator and rotor inductance, Rs and Rr are the respective stator and rotor resistance. Id and Iq are the respective d and q axis of the stator and rotor winding.

Using these equations, it is possible to build the block scheme in order to simulate the machine. The blocks are: Stator Voltage Transformation, Fluxes, Currents, Electromagnetic Torque, and Mechanical Subsystem.

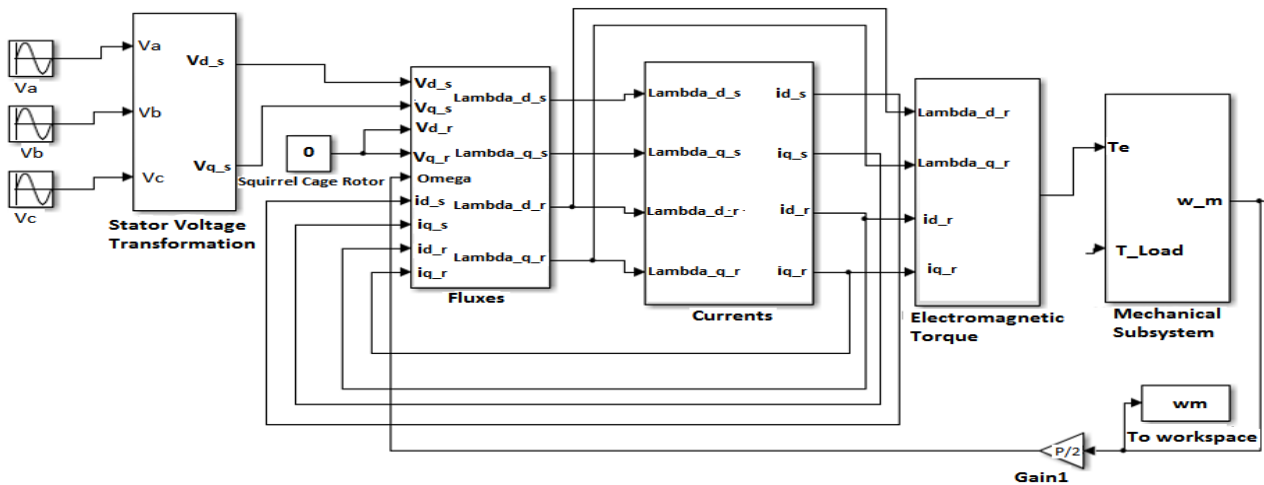


Fig. 6: Three Phase Induction Machine Asynchronous Motor Dynamic Model

2.5 Modelling PID Controller

Fig.(1) above shows the block diagram of PID Controller. The first term A proportional (TOP), an integral (CENTER) and A derivative (BOTTOM). A proportional controller may

not give steady state error performance which is needed in the system. An integral controller may give steady state error performance but it slows a system down. So the addition of a derivative term helps to cure both of these problems. The

proportional, integral and derivative outputs are added together. The PID controller can be thought of as having a transfer function. The PID transfer function can be obtained by adding the three terms together.

$$PID(s) = K_p + \frac{K_i}{s} + Sk_d \quad \dots (36)$$

The transfer function can be combined into a pole-zero form.

Hence, the equation becomes;

$$PID(s) = [sK_p + K_i + s^2K_d]/s \quad \dots (37)$$

From fig.(1) the output of PID controller $u(t)$, is equal to the sum of three signals: The signal obtained by multiplying the error signal by a constant proportional gain K_P , plus the signal obtained by differentiating and multiplying the error signal by constant derivative gain K_D and the signal obtained by integrating and multiplying the error signal by constant internal gain K_I . The output of PID controller is given by equation (38), taking Laplace transform, and solving for transfer function, gives ideal PID transfer function given by equation (39) [10]

$$u(t) = K_p e^{(t)} + K_p \frac{de(t)}{dt} + K_i \int e(t)dt \Leftrightarrow U(s) = K_p E(s)s + K_i E(s) \frac{1}{s} \quad \dots (38)$$

$$U(s) = E(s) \left[K_p + \frac{K_i}{s} + K_D s \right] \quad \dots (39)$$

$$G_{PID}(s) = K_p + \frac{K_i}{s} + K_D s = \frac{K_D s^2 + K_p s + K_i}{s} = \frac{K_D \left[s^2 + \frac{K_p}{K_D} s + \frac{K_i}{K_D} \right]}{s} \quad \dots (40)$$

Equation (40) is second order system, with two zeros and one pole at origin, and can be expressed to have the following form:

$$G_{PID} = \frac{K_D(S + Z_{PI})(S + Z_{PD})}{S} = K_D (S + Z_{PI}) \frac{(S + Z_{PD})}{S} = G_{PD}(S)G_{PI}(S) \quad \dots (41)$$

Which indicates that PID transfer function is the product of transfer functions PI and PD, Implementing these two controllers jointly and independently will take care of both controller design requirements? The transfer function given by Equation (40 and 41), can also be expressed to have the form:

$$G_{PID} = \frac{K_D(S + Z_{PI})(S + Z_{PD})}{S} = \frac{K_D s^2 + (Z_{PI} + Z_{PD})K_D s + (Z_{PI}Z_{PD}K_D)}{S} \quad \dots (42)$$

Rearranging the above equation (42) we have:

$$G_{PID} = \frac{K_D s^2}{s} + \frac{(Z_{PI} + Z_{PD})K_D s}{s} + \frac{(Z_{PI}Z_{PD}K_D)}{s} = (Z_{PI} + Z_{PD})K_D + \frac{(Z_{PI}Z_{PD}K_D)}{s} + K_D s \quad \dots (43)$$

Let, $K_1 = (Z_{PI} + Z_{PD})K_D$, $K_2 = (Z_{PI}Z_{PD}K_D)$, $K_3 = K_D$. Then, equation (43) becomes,

$$G_{PID} = K_1 + \frac{K_2}{s} + K_3 s \quad \dots (44)$$

Since PID transfer function is a second order system, it can be expressed in terms of damping ratio and undamped natural frequency to have the following form:

$$G_{PID} = K_p \left[1 + \frac{1}{T_I s} + T_D s \right] = K_p \frac{T_I T_D s^2 + T_I s + 1}{T_I s} \dots (45)$$

Where the integral time $T_I = \frac{K_p}{K_i}$, the derivative time $T_D =$

$$\frac{K_D}{K_p}, K_I = \frac{K_p}{T_I}, K_D = K_p T_D$$

2.6 Design of PID Tuning Software

The tuning mechanism used is the software tuning mechanism. The mechanism is designed using MatLab tools capable of deriving the transfer function of a complex Induction machine and varying the PID parameters to control the speed of the machine. Below is the various steps to designing the tuning mechanism.

Step 1. Modelling of the three phase induction motor in MatLab.

The three phase induction motor in MatLab is shown in fig.(6) and the model is converted to a block named Motor as shown in fig.(7) below

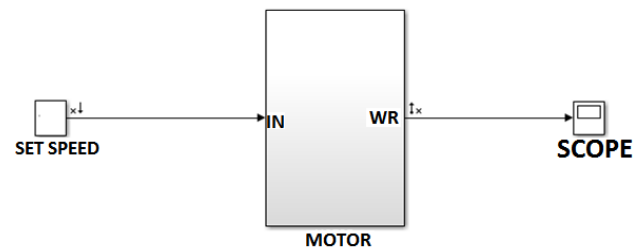


Fig. 7: Induction motor model block

Step 2. Obtain the transfer function of the Motor using MatLab script. The motor is run in MatLab and the step response is analyzed. The analysis further yields the step response of the motor as shown in figure 8 below.

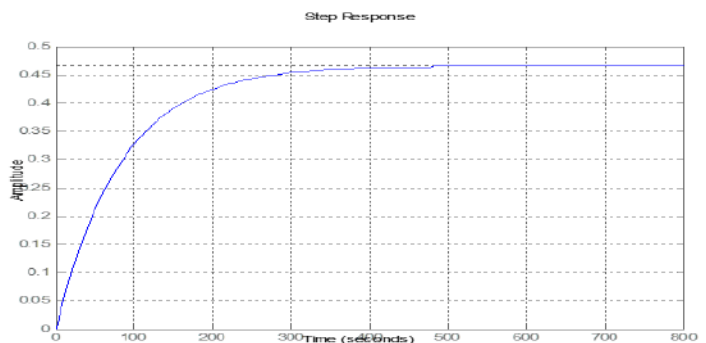


Fig. 8: step response of induction motor

And the transfer function of the step response in figure 8 above is obtained by taking the linear analysis in MatLab.

From input "Torque" to output "Subsystem":

$$G_s = \frac{-4.208e-12 s + 0.2598}{s^2 + 45.99 s + 0.2981} \quad \dots (46)$$

Linearization at model initial condition Continuous-time transfer function.

Equation 46 represent the transfer function of the three phase Asynchronous induction motor under analysis. This method can be used to obtain the transfer function of any system.

Step 3. Using this transfer function to design a PID controller in MatLab script and testing it on the step response in figure 8 above. Varying the PID parameter (Kp, Ki, Kd) on the script and running the script tunes the step response. This controller is then tuned for optimum response and the parameters are recorded for the actual controller design in the next step.

Step 4. Connect a PID controller to the Motor. Sequel to step 3 above, a PID controller block is connected with the motor block as show in fig.(9) below.

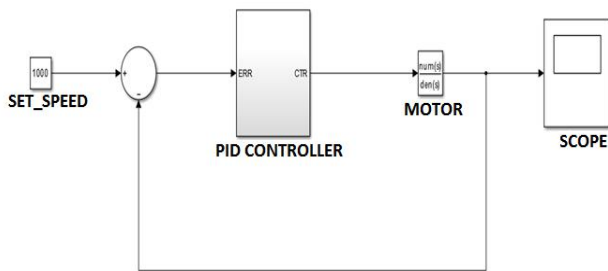


Fig. 9: Three Phase Induction Motor with PID Controller

As shown in figure 9, the output speed of the motor is feedback to the input and the summer computes the error value. This error is being fed to the PID controller and by tuning the PID using software script, the error is compensated. The value of the PID parameters and the motor parameters are programed into the system automatically. However, the script "IM_Initialization" can be run over the network from a remote location to the plant. With the availability of internet access, this tuning mechanism offers

the most advanced software tool for PID Controller in an application to three phase induction motors.

2.7 The Induction Motor Parameters

The induction motor used in this simulation is a 50 Hp, 420V, 60Hz, asynchronous motor having the parameters listed in table 2 below. The induction motor stator is fed by a current controlled three-phase source. The stator currents are regulated by hysteresis regulator which generates inverter drive signals for the inverter switches to control the induction motor. The motor torque is controlled by the quadrature-axis current component and the motor flux is controlled by direct-axis current component. The motor speed is regulated by a PID controller which produces the required torque current component signal.

Table 2. Induction motor parameters

S/No.	Parameter	Symbol	Value
1	Supply Frequency	f	60 Hz
2	Voltage	V	420 V
3	Stator Resistance	Rs	0.288Ω
4	Stator Inductance	Ls	0.0425 H
5	Rotor Resistance	Rr	0.158Ω
6	Rotor Inductance	Lr	0.0418 H
7	Magnetizing Inductance	Lm	0.0412 H
8	Inertia	J	0.4 Kg.m ²
9	No. of pole	P	2

2.8 Development of the Simulink Model Diagram

First of all, let us consider the development of a Simulink model for the speed performance or response of an induction motor without controller, the Simulink model for a proportional integral derivative (PID), and lastly, a developed Simulink model for a proportional integral derivative (PID) software tuning mechanism. The speed performance of the induction motor is checked first without any controller and then checked with the help of a proportional integral derivative (PID) controller tuned with software tool. The Simulink model is developed in the MATLAB which is shown in the following Fig.(10), and (11) respectively.

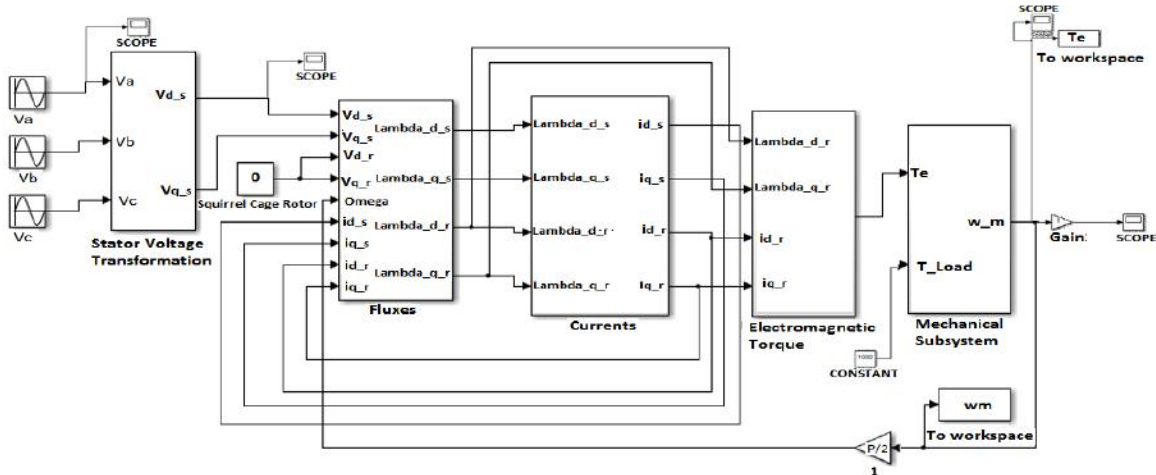


Fig. 10: Developed Simulink model to check speed response of Induction motor without any controller

Using the software tuning mechanism, we can obtain the parameters k_p , k_i , and k_d for optimal performance under the no-load and full-load conditions. In the open loop condition, we can determine the open loop transfer function of the plant by MATLAB program as

$$G_s = \frac{-4.208e-12 s + 0.2598}{s^2 + 45.99 s + 0.2981} \quad \dots (46)$$

Also, the closed-loop system with a PID controller has the following characteristic equation

$$M_c = \frac{-1.01e-10 s^3 + 6.235 s^2 + 15.85 s + 0.2598}{s^3 + 52.23 s^2 + 16.15 s + 0.2598} \quad \dots (47)$$

Equation 46 is obtained by running the MatLab script below and the PID parameters was tuned to give optimal step response as show in fig.(47). The response with controller has a steady state of 17 seconds while the open loop response steady state is 263 seconds.

The actual motor model “IM_Plant” is controlled using PID controller as shown in fig.(12) below. The parameters of the motor and PID controller are programmed into the system using the MatLab script. This script is used to tune the motor response in the same way as demonstrated in fig.(11) above. Below is the simulation of the motor with controller and the IM_Initialaization script.

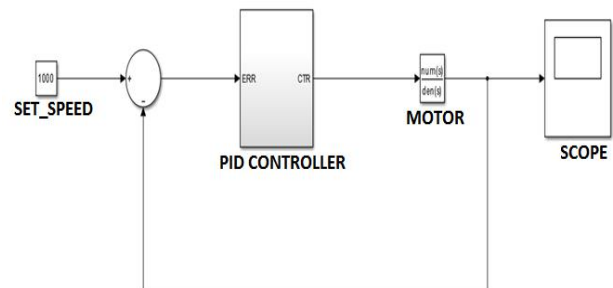


Fig. 12: Developed Simulink model to check speed response of Induction motor with PID controller

III. RESULT

Simulations were carried out in MATLAB environment and the results were verified for the set speed. The speed response of Induction motor is checked for without controller and with PID controller which is shown in Fig.(13) and (14)

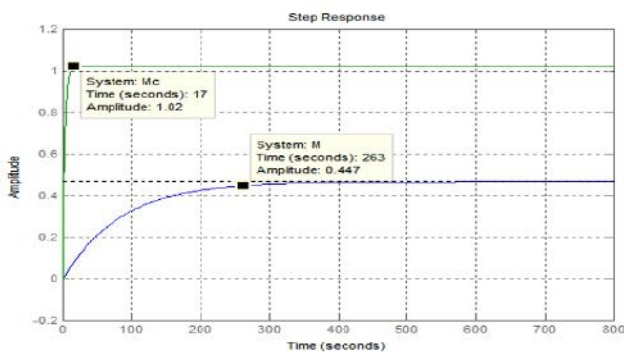


Fig.(11) Open loop and close loop step response of motor transfer function.

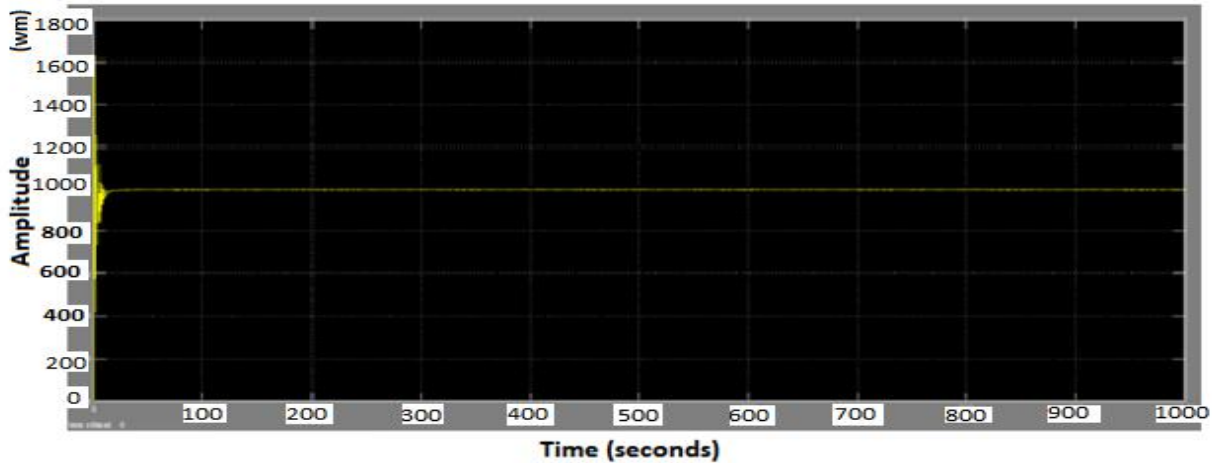


Fig. 13: Speed performance of Induction motor without any controller

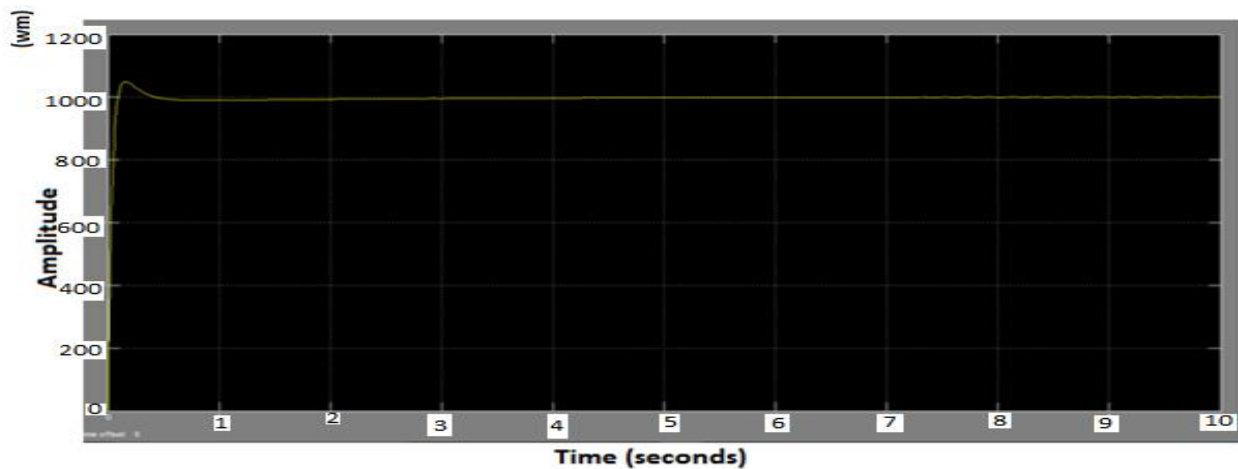


Fig. 14: Speed performance of Induction motor with PID controller

The speed performance of induction motor without any controller is shown in fig.(13). This is for full load condition. When we applied a full load the speed suddenly decreases and is not stable. So as to improve the speed performance, a PID controller tuned with software mechanism. Because of which the steady state error is eliminated and the rise time is improved in figure 4.6. Therefore the PID controller is used to improve the speed performance of Induction motor and the results is shown in fig.(14).

IV. DISCUSSION

The main purpose of this thesis is to control the speed of induction motor using software tuning mechanism of PID controller. From this we come to know that software tuning mechanism of PID controller is a good mechanism for controlling the speed of three phase induction motor. The speed of induction motor using PID controller settled early

when using software tuning than other tuning mechanism. As against Zigler – Nicole, the software tools is suitable for any complex system and it is not a trial by error method. It also add the advantage of remote management and flexibility.

V. CONCLUSION

The speed control of an induction motor by software tuning mechanism of PID controllers has led to the conservation of energy and the usage of high performance application such as hybrid vehicles, robotics, wind generation systems, paper and textile mills, and variable-torque centrifugal fan, pump and compressor load applications. Hence there is need to develop a software mechanism for effective speed control for induction motors.

REFERENCES

- [1] Singh, B. and G. Choudhuri, *Fuzzy Logic Based Speed Controllers For Vector Controlled Induction Motor Drive* IETE Journal of Research 2002. **48**: p. 6.
- [2] Z. Q. Zhu, Y.P., D. Howe, S. Iwasaki, R. Deodhar, and A. Pride, *Analysis of Electromagnetic Performance of Flux-Switching Permanent-Magnet Machines by Nonlinear Adaptive Lumped Parameter Magnetic Circuit Model*. IEEE TRANSACTIONS ON MAGNETICS, 2005. **41**(11): p. 11.
- [3] Chan, C.C. *The State of the Art of Electric, Hybrid, and Fuel Cell Vehicles*. in *Proceedings of the IEEE* 2007.
- [4] ZL, G., *A particle swarm optimization approach for optimum design of PID controller in AVR system*. IEEE Trans Energy Convers, 2004. **19**: p. 91-384.
- [5] Chih-Cheng Kao, C.-W.C., Rong-Fong Fung, *The self-tuning PID control in a slider–crank mechanism system by applying particle swarm optimization approach*. Mechatronics, 2006. **16**(8): p. 513-522.
- [6] Gaing, Z.-L., *A Particle Swarm Optimization Approach for Optimum Design of PID Controller in AVR System*. IEEE Transactions on Energy Conversion, 2004. **19**(2).
- [7] Ang, K.H., G. Chong, and Y. Li, *PID control system analysis, design, and technology* IEEE Transactions on Control Systems Technology, 2005. **13**(4): p. 559-576.
- [8] Rujisak Muangsong, D.K., Anak Khantachawana, Panadda Niranatlumpong, *A particle swarm optimization approach for optimal design of PID controller for position control using Shape Memory Alloys in Electrical Engineering / Electronics, Computer, Telecommunication and Information Technology* 2008, IEEE: Krabi Thailand.
- [9] Saghafinia, A., H. Ping, and M. Uddin, *Designing Self-Tuning Mechanism On Hybrid Fuzzy Controller For High Performance And Robust Induction Motor Drive*. International Journal of Advanced Technology & Engineering Research, 2013. **3**: p. 65-72.
- [10] R.Arulmozhiyal and K. Baskaran, *Space Vector pulse Width Modulation Based Speed Control of Induction Motor using Fuzzy PI Controller*. international Journal of Computer and Electrical Engineering 2009. **1**: p. 5-7.
- [11] Chih-Cheng Kao, C.-W.C., Rong-Fong Fung, *The self-tuning PID control in a slider–crank mechanism system by applying particle swarm optimization approach*, in *Mechanical and Automation Engineering* 2006, National Kaohsiung First University of Science and Technology, Taiwan. p. 513-522.
- [12] Liu Y, Z.J., Wang S. *Optimization design based on PSO algorithm for PID controller*. in *Proc Fifth World Congr on Intelligent Control and Automation*,. 2004. Instabul Turkey.
- [13] Shi, Y.H. and R.C. Eberthart, *A Modified Particle Swarm Optimizer*. IEEE International Conference on Evolutionary Computation, 1998: p. 7.
- [14] Noordin, M.A.B.M., *scaler control of three phase induction motor* 2007, University Teknikal: Malaysia.
- [15] Raji, C.T., S.P. Stivastava, and P. Agarwal, *Particle Swarm and Fuzzy Logic Based Optimal Energy control of Induction Motor for a Hoist Load Diagram*. International Journal of Computer Science, 2009. **36**: p. 17-25.
- [16] Pillay, P. and R. Krishnan, *Modeling, Simulation, and Analysis of Permanent-Magnet Motor Drives , Part I: The Permanent-Magnet Synchronous Motor Drive*. IEEE Transaction on Industry Application, 1989. **25**(2): p. 9.

Experimental analysis of the operation of a solar adsorption refrigerator under Sahelian climatic conditions: case of Burkina Faso

Guy Christian Tubreoumya^{1,2,3}, Eloi Salmwendé Tiendrebeogo¹, Ousmane Coulibaly¹,
Issoufou Ouarma¹, Kayaba Haro¹, Charles Didace Konseibo³, Alfa Oumar Dissa¹,
Belkacem Zeghmati²

¹Laboratoire de Physique et de Chimie de l'Environnement (L.P.C.E), Université Ouaga I, Pr Joseph KI ZERBO, Ouagadougou, Burkina Faso.

²Laboratoire de Mathématiques et Physique (L.A.M.P.S), Université de Perpignan Via Domitia (UPVD), Perpignan, France

³Centre Ecologique Albert Schweitzer (CEAS), Ouagadougou, Burkina Faso

Abstract—This work is an experimental analysis of the operation of a solar adsorption refrigerator designed for the conservation of pharmaceutical products. The experiment consisted to measure incident solar radiation on the collector-adsorber, temperature of all the components of the collector-adsorber, of the condenser, the evaporator and the storage tank. Experimental results indicated that the maximum temperature of the front face of the absorbent plate varied from 70 °C to 80 °C and that of the condenser varied from 45 °C to 53 °C. The minimum temperature reached by the evaporator was + 4 °C. With a total energy received of about 19 MJ/m², this solar adsorption refrigeration device can provide a SCOP ranging from 0.09 to 0.185. These results demonstrate the technical feasibility of the prototype solar adsorption refrigerator that we have experimented.

Keywords—Solar energy; Refrigeration; Adsorption; Experimentation; Zeolite / Water.

I. INTRODUCTION

The conservation of food and pharmaceutical products is a real problem in some regions of Burkina Faso. These different regions are not connected to the national electricity grid. This problem results from the lack of electrical energy to cover the whole country. However, Burkina Faso has a very important solar potential with an average irradiation between 5.5 kWh.m⁻².day⁻¹ and 6.5kWh.m⁻².day⁻¹ and an annual sunshine duration of 3000 hours running up to and 3500 hours [1]. Thus, solar adsorption refrigeration machines are an alternative to meet this energy problem. In fact, solar adsorption refrigeration units operate without moving parts and do not require another source of energy out of solar energy. The technology of these machines is simple, maintenance is easy and the materials used, are recyclable [2]. In

addition, they use refrigerants that have no effect on the environment such as water [3-5], methanol [6-8] and ammonia [9]. As a result, several researchers have focused their work on its machines because they have several advantages and the different demands of cold coincide in most of the time with the availability of the sun [10-15].

In this article, the solar adsorption refrigerator using the zeolite-water pair is presented, described and tested under the climatic conditions of Yako, Burkina Faso. The main objective of this study is to evaluate the behavior and overall performance of the prototype. Therefore, in the first part of our work, the operating principle and design criteria are described. Then, the experimental results of a few days of operation are presented.

II. OPERATIONAL PHASES OF THE SOLAR ADSORPTION REFRIGERATOR

A solar refrigerating adsorption machine operates in a cycle. It consists in a flat plate collector containing the zeolite/water mixture and plays a role of capturing and releasing the heat. It is connected to a condenser and an evaporator. The principle of operation of these machines is based on the phenomena of adsorption- desorption of a gas (water vapor) in a solid (zeolite). This chemical reaction is exo or endothermic according to its direction of unwinding. The basic adsorption cycle for refrigeration consists of four processes represented in Fig. 1. In the first one 1–2, the adsorbent is heated by solar energy until the pressure reaches a level that enables desorption of refrigerant (state 2). During process 2–3 addition of heat from solar energy results in desorption of vapor refrigerant, which condenses in an air-cooled condenser. At state 3, when the adsorbent rises up to its maximum temperature, solar irradiance starts to decrease. The

collector, cut off from the condenser, drops in temperature. Cooling of the adsorbent provokes a drop of pressure in the collector (process 3–4). Meanwhile, the liquid refrigerant is transferred into the evaporator. When the pressure reaches the value of the pressure at the evaporator temperature, the collector is connected to the evaporator (state 4). The adsorbent continues to decrease in temperature and pumps the liquid refrigerant, which evaporates and extracts out heat from the evaporator (process 4–1) generating a cooling process inside the chamber. The cycle is said intermittent because the evaporation–cooling process happens only during the night.

III. IMPLEMENTATION OF THE PROTOTYPE

The prototype of the solar adsorption refrigeration machine that we have experimented is installed in Yako, a village located in the province of Passoré, about 100 km far from Ouagadougou (Burkina Faso). It is located between latitudes $12^{\circ} 90$ and $12^{\circ} 96$ North and between longitudes $-2^{\circ} 17$ and $-2^{\circ} 26$ west. This prototype consists of a collector-adsorber, a condenser and a refrigerating enclosed containing the evaporator (Figure 2). The adsorbent / adsorbate pair used is the zeolite / water pair.

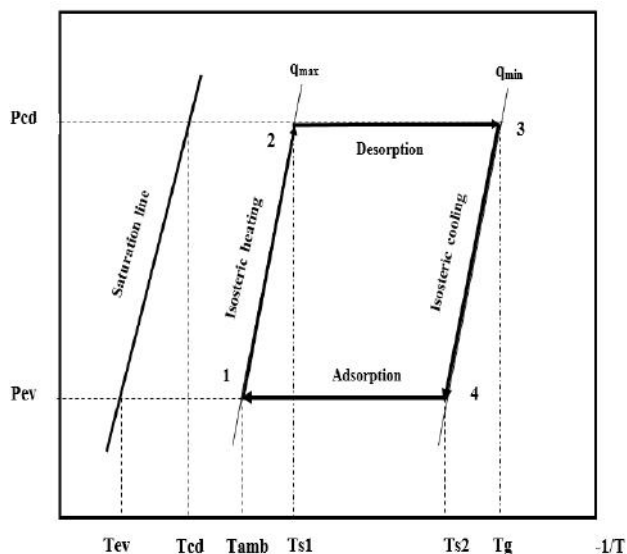


Fig.1. Theoretical cycle of an adsorption machine



Fig. 2. Photography of solar adsorption refrigerator

3.1 The collector-adsorber

The collector-adsorber is an essential element of the solar adsorption refrigerator. It is a parallelepipedic box of 1m^2 surface and 20 cm high, closed on its upper face by a 5 mm thick glass cover. The side faces and the back face are insulated by 10 cm thick of layer of glass wool. The adsorber, enclosed in the housing, is composed of:

- 8 cm of 32 kg of zeolite in contact with thirteen (13) fins provide heat transfer between the front face and the inside of the adsorber.
- a channel of rectangular section 2 cm high, arranged between the zeolite bed and the back plate of the adsorber with a grid to allow the water vapor desorbed from the bed of zeolite of flow to the condenser through the flexible tube.

The front face of the adsorber, intended to receive the solar flux, was previously coated with a black paint of low emissivity allowing good absorption of solar radiation. The absorbed solar flux is converted into heat for heating the adsorbent (the zeolite). The collector-adsorber assembly has a tilt angle of 13° to the horizontal (Fig.3).

3.2 The condenser

The condenser consists of an aluminum tube 65 cm long, 5 mm thick and 10 cm in diameter. It has 52 fins spaced 15 cm apart. Each aluminum fin has a square shape of 20 cm of coast and thickness 1 mm. The total exchange area of the condenser is 3.5m^2 . The condenser is cooled by natural convection generated by the difference between the temperature of the outer face of the condenser wall and that of the ambient air. It is positioned in the solar refrigeration plant so that the condensate flows through one of the orifices easily under the effect of gravity towards the evaporator.

3.3 The evaporator

It is installed in a thermally insulated cold chamber with internal dimensions 50x50x30 cm. It consists of a parallelepiped tank whose walls are insulated with 20 cm thick of layer of glass wool. It has two tubes 25 mm in diameter allowing the passage of water vapor during adsorption. The total exchange area of the evaporator is 0.7 m². A part of the evaporator contains a sufficient quantity of distilled water which does not participate in the cycle of the refrigerating machine. It is constantly present to form a mass of ice that serves as cold storage for the day and the periods without sun. The storage of cold latent form allows a constant evaporator temperature and very low.

3.4 Connecting accessories

The different components of the experimental prototype (the collector-adsorber, the condenser and the evaporator) are connected by connecting accessories namely: the flexible tube and the valves (Fig.4).



Fig.3. Detailed photograph of the collector-adsorber.

IV. MEASUREMENT PROCEDURE

To verify and evaluate the performance of our experimental device in a more realistic way, we tested it in the weather conditions of a city in Burkina Faso. This experimental study is based mainly on the measurements, over time, of the temperature of the components of the collector-adsorber, the condenser, the evaporator and the solar flux incident on the inclined plane of the collector-adsorber. The various tests on the solar refrigerator took place in Yako (Burkina Faso). We used (08) eight type K thermocouples placed on the various compartments of the refrigerator (glass, front and back side of the adsorber,

condenser, ...). We did not introduce a thermocouple inside the adsorber for the sake of sealing. These thermocouples are connected to a data logger of the Midi Logger GL220A type thus allowing the acquisition of measurements with an accuracy of $\pm 0,5\text{ }^{\circ}\text{C}$ (Fig.5). In addition, we measured the overall illumination on the inclined plane of the adsorber sensor with a KIMO brand solarimeter ($\pm 0.38\text{ W}/\text{m}^2\text{ }^{\circ}\text{C}$). Measurements were done all the day long with a timestep of fifteen (15) minutes.



Fig.4. Detailed photograph of the condenser and the refrigerating enclosure

V. EXPÉRIMENTAL RESULTS AND DISCUSSION

5.1 Evolution of solar irradiance and ambient temperature

Figs.6-8 present the hourly evolution of the ambient temperature and solar irradiance measured during the different days of experiments. We found that the global solar irradiance increases from 6:00 h and reaches a maximum value around 12:00 h, then gradually decreases until the end of the day. The maximum value of solar irradiance varies between 750 and 830 W / m². Moreover for the days considered, we observe a difference in the shape of evolution during the day of solar irradiance. This difference is due to the passage of clouds and the environment of the experimental site (the shadow of the building). The maximum value of the recorded ambient temperature was approximately 38 ° C and the minimum value was 21 ° C.



Fig.5. Acquisition of experimental data.

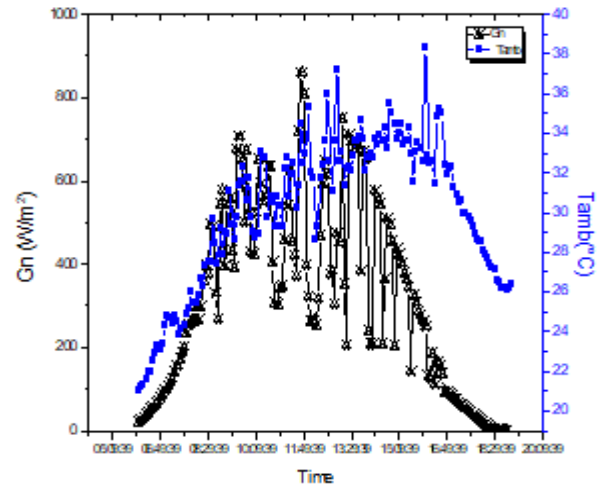


Fig.8. Evolution of solar irradiance and ambient temperature for 04/08/2016

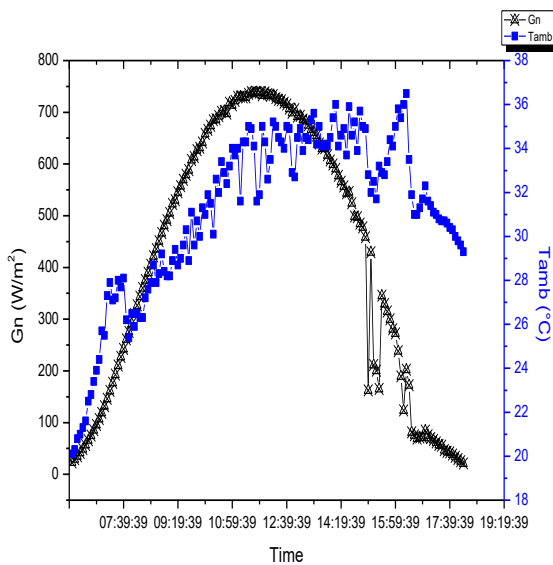


Fig.6. Evolution of solar irradiance and ambient temperature for 12/15/2016

5.2 Evolution of the temperature of the various components of the collector-adsorber

The hourly evolution of the temperature of the various components of the collector-adsorber (glass, front and back of the absorber plate, zeolite) are shown in Figs .9-11. Initially, the temperature of each of the components matches the ambient temperature, then they follow during the day the same shape as that of the solar irradiance. The hourly evolutions of the temperature of the front (T_{p-av}) and back (T_{p-ar}) of the absorber plate show that they reach a maximum value at 12:00 h, corresponding to the maximum solar irradiation of the day of 15/12/ 2016. Thus, the maximum temperature of the front face of the absorber plate is of the order of 80 °C and 40°C for the back face. The temperature of the zeolite is assumed equal to the average of the temperatures of the front and back of the absorber plate. Its maximum value is therefore 60 °C.

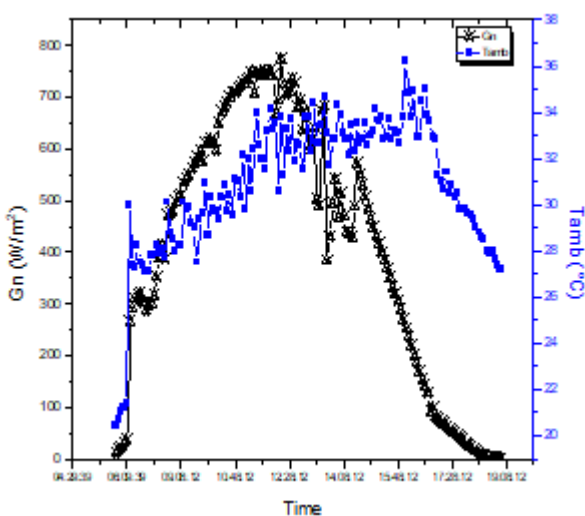


Fig.7. Evolution of solar irradiance and ambient temperature for 14/12/2016.

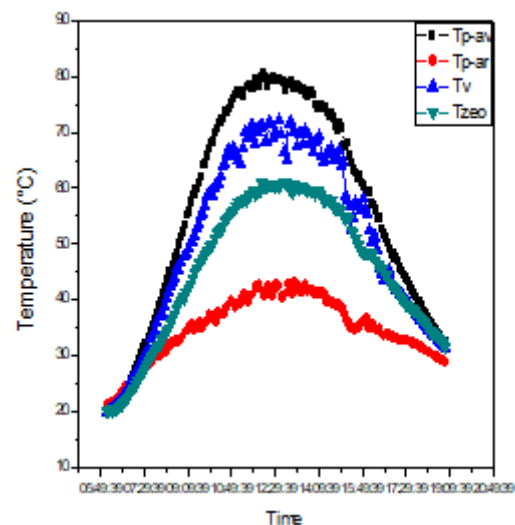


Fig.9. Evolution of the temperature of the various components of the collector-adsorber for 15/12/2016

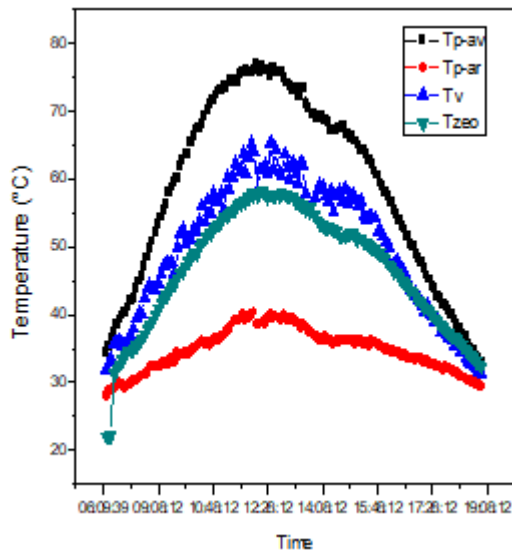


Fig.10. Hourly evolution of the temperature of the various components of the collector-adsorber during the day of 14/12/2016

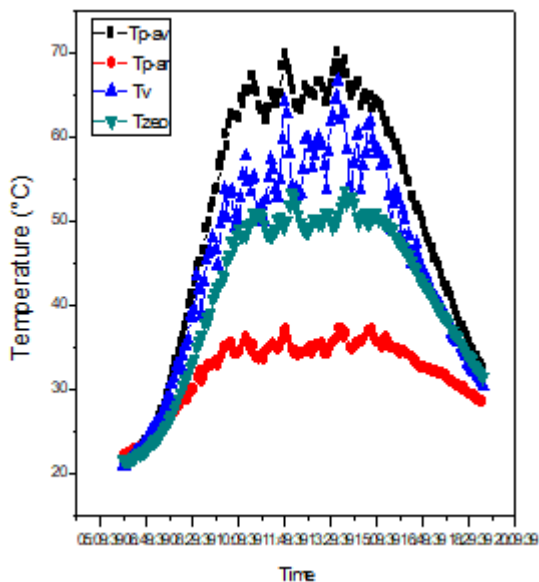


Fig.11. Evolution of the temperature of the various components of the collector-adsorber for 04/08/2016

5.3 Evolution of the condenser temperature

Figs. 12-14 show the hourly evolution of the condenser temperature during the different days of experimentation. It should be noted that the temperature of the condenser is equal to the ambient temperature up to 9h. Then, it gradually increases over time until the maximum difference with the ambient temperature is equal to 17 °C (15/12/2016). This increase of the temperature results mainly from the amount of heat released during the water vapor condensation on the walls of the condenser. The amount of water vapor desorbed is all the more important that the difference between the temperature of the condenser and that of the ambient is large. After 12:00 h,

the temperature of the condenser decreases along with the reduction of solar irradiance. It follows that the flow rate of the desorbed water vapor decreases with time, which causes a decrease in the temperature of the condenser. At approximately 16:00 h, the hourly evolution of the condenser temperature is similar to that of the ambient temperature.

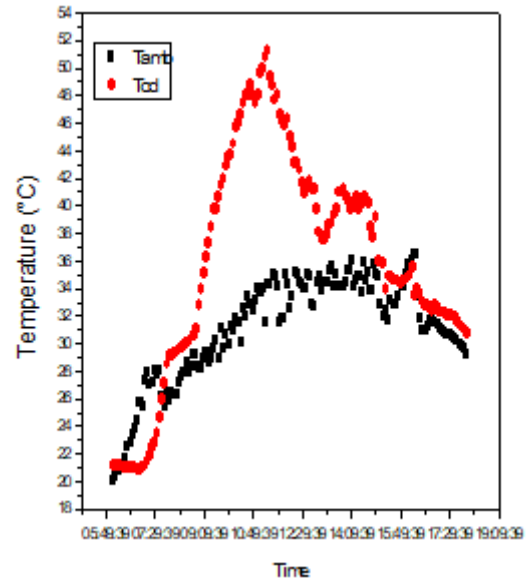


Fig.12 Evolution of the condenser and ambient temperature for 15/12/2016

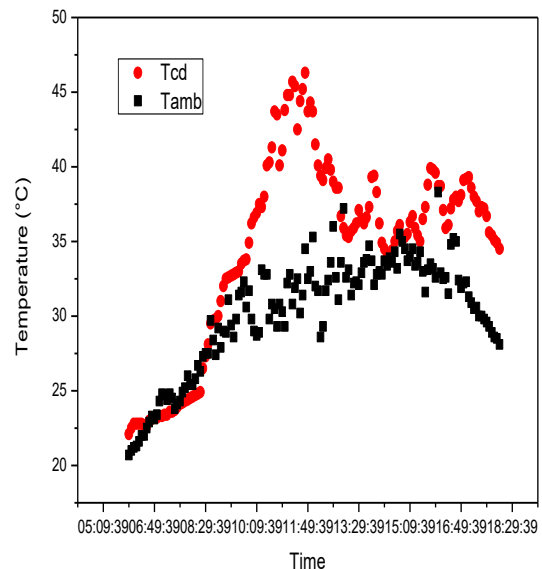


Fig.13 Evolution of the condenser and ambient temperature for 14/12/2016

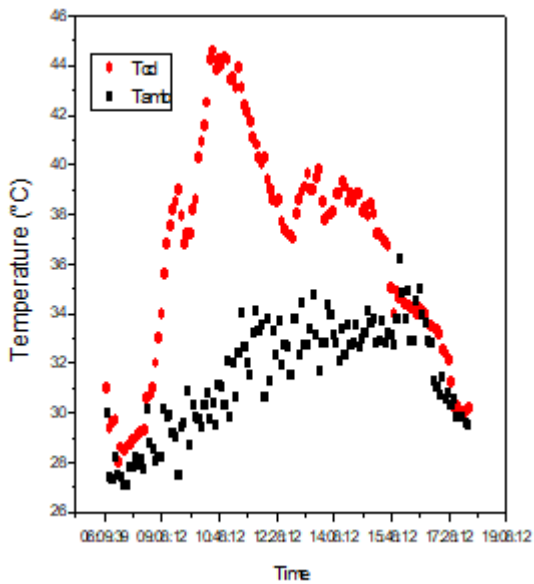


Fig.14 Evolution of the condenser and ambient temperature for 04/08/2016

5.4 Evolution of the evaporator and the storage tank temperature

We have shown in Fig. 15-17 the hourly evolution of the evaporator (T_{ev}) and the storage tank (T_{st}) temperatures. We note that the hourly evolution for these two temperatures, during the test days, is similar between 18:00 h to 6:00 h. During this period, the amount of cold is produced by the evaporation of water at low pressure. The high adsorption capacity of the zeolite makes it possible to adsorb large amounts of water vapor, which allows the continuation of the vaporization of the water and thus the production of cold in the refrigerating enclosure.

The evaporator temperature and that of the storage tank begin to decrease from 18:00 h until reaching a temperature about $+4^{\circ}\text{C}$ at about 6:00 h. However, during the day, the evaporator temperature and that of the storage tank gradually increase until reaching maximum values of 22°C (14/12/2016). This increase of the temperature is partly due to the infiltration of air into the refrigerating enclosure and also the energy losses and the climatic conditions.

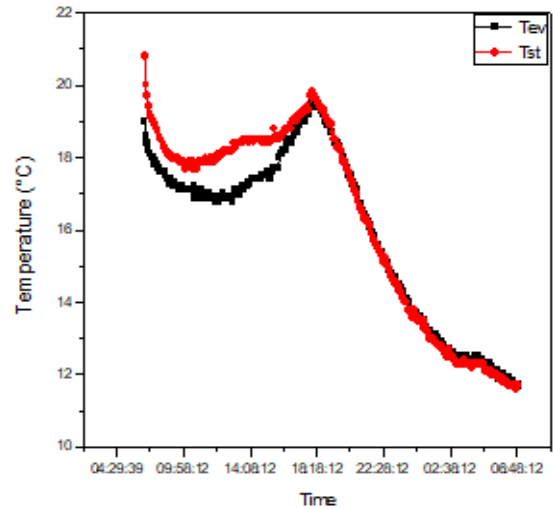


Fig.15 Evolution of the evaporator and the storage tank temperatures for 14/12/2016

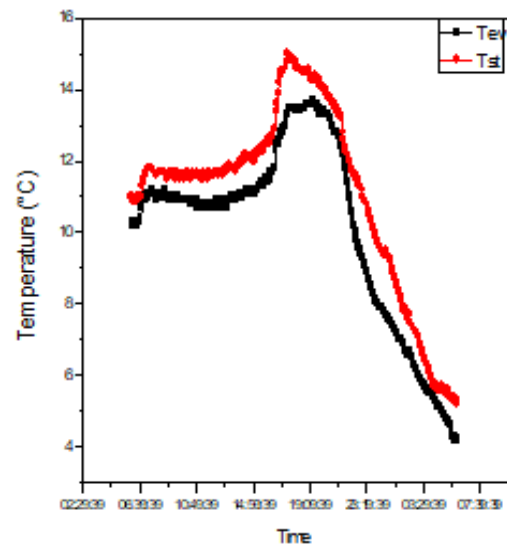


Fig.16 Evolution of the evaporator and the storage tank temperatures for 15/12/2016

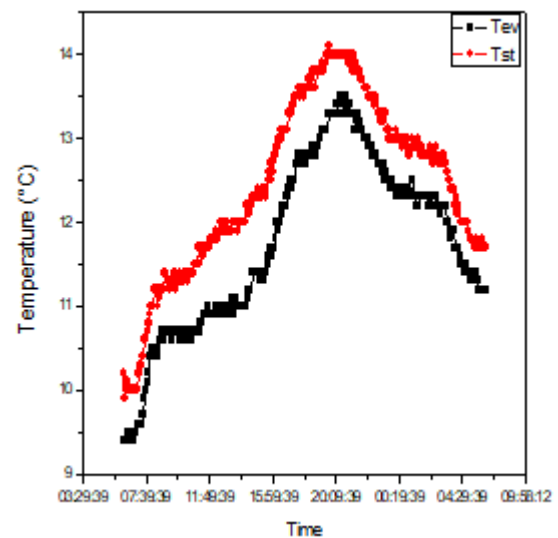


Fig.17 Evolution of the evaporator and the storage tank temperatures for 04/08/2016

VI. PERFORMANCE OF ADSORPTION REFRIGERATION SYSTEM

The thermal performance of the solar adsorption refrigerator is characterized by the solar performance coefficient (SCOP). This coefficient is the ratio between the amount of the cooling production to the heat input more precisely the total solar energy captured by the collector-adsorber during a day.

$$SCOP = \frac{Q_f}{\int_{t_{sr}}^{t_{ss}} A_s \cdot G_n \cdot dt} \quad (3.1)$$

Where A_s is the collecting surface and G_n is the solar irradiation

Q_f is the amount of cold product at the evaporator :

$$Q_f = m_{ad} \cdot [L(T_{ev}) - Cp_l (T_{cd} - T_{ev})] \quad (3.2)$$

The prototype that we have experimented is not equipped with a device for measuring the cycled condensate mass during a cycle of operation of the solar adsorption refrigerator. This quantity is an important parameter because it allows the calculation of the amount of cold

Q_f produced at the evaporator. Thus, we used the correlation of Errougani, A. (2007) [19] to estimate the mass of cycled condensate (m_{ad}) as a function of the ambient temperature and the incident daily solar irradiation. This correlation is given by equation (3.3):

$$\log(m_{ad}) = 2,44859 * \log\left(\frac{G_n}{T_{amb}}\right) - 4,0886 \quad (3.3)$$

Where G_n is kJ / m^2 and T_{amb} in (K).

Table 3.1 gives the solar performance coefficient (SCOP) estimates for the different days of experimentation. The experimental SCOP of our solar adsorption refrigeration system varies between 0.09 to 0.185 and the total energy received by the adsorber-collector varies between 15 and 19 MJ. The low SCOP value obtained can be explained by the small amount of cold produced due to the small amount of adsorbed refrigerant compared to the solar thermal energy received by the adsorber collector.

Table.1: Coefficient of performance of the solar adsorption refrigerator.

Day	Solar radiation energy (MJ)	Amount of cold produced(MJ)	Evaporator temperature (°C)		Condenser temperature (°C)		SCOP
			Max	Min	Max	Min	
03/08/2016	15,519	1,40	16	11	47	26	0,09
04/08/2016	21,86	2,21	14	9,5	44	28	0,101
05/08/2016	18,15	1.87	18	8	42	25	0,103
11/12/2016	15,77	2,69	16	11	47	26	0,171
12/12/2016	15,12	2,40	14	9,5	44	28	0,158
13/12/2016	19.66	3.30	18	8	42	25	0,167
14/12/2016	21,32	3,78	21	12	45	21	0,177
15/12/2016	19,60	3,63	15	4	52	20	0,185
16/12/2016	19,66	3,30	16	6	49	23	0,167

Table.2: Comparison SCOP of some solar refrigerator adsorption system

	adsorbent/adsorbate	SCOP	Total energy received
Present experimental study	Zeolithe/water	0.09-0.185	15-20 MJ/m ²
Hildbrand et al. (2004)	Silicagel/ water	0.12-0.23	> 20 MJ/m ² .
Philippe Dind et al. (2005)	Silicagel/ water	0.19	Artificial sunshine
A.Boubakri et al. (1992)	AC/methanol	0.12	19.54 MJ/m ²
Hildbrand et al. (2005)	AC/methanol	0.09-0.13	19-25 J/m ²

We compared the obtained results with those of the literature (Table 3.2). We found that these values are of the same order of magnitude as in the literature [16-18] using the zeolite-water or silica gel-water pair. This validates our experimental protocol and demonstrates the

technical feasibility of the solar adsorption refrigerator prototype that we used.

VII. CONCLUSION

In this paper, an experimental solar adsorption refrigerator, using the zeolite/water pair, is presented.

Designed for the conservation of pharmaceutical products, several experimental tests have been carried out in order to test the reliability of the solar adsorption refrigeration system. Thus, the hourly evolution of the temperature of the different components of the system was presented and discussed:

- The maximum value of solar irradiance varies between 750 and 830 W / m². The maximum value of the recorded ambient temperature was approximately 38 °C and the minimum value was 21 °C.
- The maximum temperature of the front face of the absorbent plate is of the order of 80 °C and that of the back face is 40°C. The temperature of the zeolite is maximum value is therefore 60 °C.
- The temperature of the condenser reaches a maximum temperature of 52 °C and that of the evaporator, a minimum temperature of 4 °C.

The SCOP of the solar adsorption refrigeration system varies between 0.09 to 0.185 and the total energy received by the adsorber-collector varies between 15 and 19 MJ.

Acknowledgements

The authors are grateful to the University Agency of the Francophonie (AUF) and the French Embassy (SCAC) for financial support which allowed the realization of this work.

Nomenclature

C _p	Specific heat (J/kg.K)
G _n	Solar radiation (W/m ²)
m	mass (kg)
Q _f	Cold production (J)
q	Water concentration inside the zeolithe (kg/kg)
A	Area (m ²)
L(T)	Latent heat of vaporization (J/kg)
T	Température (K)
P	Pressure (Pa)

Indexes

amb	ambient
zeo	zeolite
ev	evaporator
cd	condenser
v	glass
p	plaque
st	storage
t	Time (s)
g	generation
ad	adsorbent

REFERENCES

- [1] Ousmane, M., Dianda, B., Kam, S., Konfe, A., Ky, T. and Bathiebo, D. (2015) Experimental Study in Natural Convection. Global Journal of Pure and Applied Sciences, 21, 155-169. <https://doi.org/10.4314/gjpas.v21i2.8>
- [2] A. Chikouche, «Using solar energy for refrigeration purposes in Algeria,» chez 4th JIIRCAC Proceeding, 2012.
- [3] Marlinda, A. Uyun, T. Miyazaki, Y. Ueda et A. Akisawa, « Performance analysis of a double-effect adsorption refrigeration cycle with a silica gel/water working pair,» *Energies*, pp. 3,1704–1720., 2010.
- [4] Tubreoumya, G.C., Dissa, A.O., Tiendrebeogo, E.S., Chesneau, X., Compaore, A., Haro, K., Konseibo, C.D., Zeghmati, B. and Kouliadiati, J. (2017) Contribution to the Modeling of a Solar Adsorption Refrigerator under the Climatic Conditions of Burkina Faso. *Energy and PowerEngineering*, 9, 119-135. <https://doi.org/10.4236/epe.2017.92010>
- [5] Allouhi, A., Kousksou, T., Jamil, A. and Zeraouli, Y. (2014) Modeling of a Thermal Adsorber Powered by Solar Energy for Refrigeration Applications. *Energy*, 75, 589-596. <https://doi.org/10.1016/j.energy.2014.08.022>
- [6] H. Hassan, A. Mohamad et H. Al-Ansary, Development of a continuously operating solar-driven adsorption cooling system: Thermodynamic analysis and parametric study. *Appl. Therm. Eng.*, pp. 48, 332–341, 2012. <http://dx.doi.org/10.1016/j.applthermaleng.2012.04.040>
- [7] Boubakri, A., Guillemot, J. and Meunier, F. (2000) Adsorptive Solar Powered Ice Maker: Experiments and Model. *Solar Energy*, 69, 249-263. [https://doi.org/10.1016/S0038-092X\(00\)00063-3](https://doi.org/10.1016/S0038-092X(00)00063-3)
- [8] Lemmini, F. and Errougani, A. (2007) Experimentation of a Solar Adsorption Refrigerator in Morocco. *Renewable Energy*, 32, 2629-2641. <https://doi.org/10.1016/j.renene.2007.01.004>
- [9] M. Louajari, A. Mimet et A. Ouammi, «Study of the effect of finned tube adsorber on the performance of solar driven adsorption cooling machine using activated carbon-ammonia pair.» *Appl. Energy*, pp. 88, 690–698., 2011. <http://dx.doi.org/10.1016/j.apenergy.2010.08.032>
- [10] Muhammad, U., Atsushi, A. and Yuki, U. (2014) Performance Evaluation of a Solar Adsorption Refrigeration System with a Wing Type Compound Parabolic Concentrator. *Energies*, 7, 1448-1466. <https://doi.org/10.3390/en7031448>
- [11] Bakkas, M., Mada, M. and Tahri, M. (2001) Modelisation et Simulation du Transfert de Chaleur et de Masse a l'Interieur d'un Reacteur de Charbon Actif Reagissant avec de l'Ammoniac Couple a un Caloduc Annulaire a Eau. *Revue des Energies Renouvelables*, 19-24.

- [12] Allouhi, A., Kousksou, T., Jamil, A., El Rhafiki, T., Mourad, Y. and Zeraoui, Y.(2015) Optimal Working Pairs for Solar Adsorption Cooling Applications. *Energy*,79, 235-247.
<https://doi.org/10.1016/j.energy.2014.11.010>
- [13] Leite, A.D.M. (2000) Performance of a New Solid Adsorption Ice Maker with SolarEnergy Regeneration. *Energy Conversion and Management*, 41, 1625-1647.
[https://doi.org/10.1016/S0196-8904\(00\)00011-X](https://doi.org/10.1016/S0196-8904(00)00011-X)
- [14] Guilleminot, J.M.F. (1987) Heat and Mass Transfer in a Non Isothermal Fixed BedSolid Adsorbent Reactor a Uniform Pressure-Non Uniform Temperature. *International Journal of Heat and Mass Transfer*, 30, 1595-1606.
[https://doi.org/10.1016/0017-9310\(87\)90304-8](https://doi.org/10.1016/0017-9310(87)90304-8)
- [15] Mimet, A. (1991) Etude theorique et experimentale d'une machine frigorifique a adsorption d'ammoniac sur charbon actif. These de Doctorat, FPMS, Mons.
- [16] Boubakri, A., Arsalane, M., Yous, B., Alimoussa, L., Pons, M., Meunier, F., Guilleminot, J. (1992). Experimental study of adsorptive solar powered ice makers in Agadir (Morocco)-1.Performance in actual site. *Renew. Energ.*(2 (1), 7-13.), 2 (1), 7-13.
- [17] Dind, P., Catherine., H., Cherbuin, O., Mayor, J. (2005). La réfrigération solaire à adsorption. HES-SO: Projet Gerbert Rûf Stiftung.
- [18] Hildbrand, C., Dind, P., Pons, M., Buchter, F. (2004). A new solar powerd adsorption refrigerator with high performance. *Solar Energy*, vol 77, pp.311-318
<https://doi.org/10.1016/j.solener.2004.05.007>
- [19] Errougani, A. (2007). Fabrication et experimentation d'un refrigerateur solaire a adsorption utilisant le couple charbon actif- methanol. Agdal: Université Mohammed V.

General Pattern Search Applied to the Optimization of the Shell and Tube Heat Exchanger

Wagner H. Saldanha, Pedro A. A. M. Junior

Department of Mechanical Engineering, Pontifícia Universidade Católica de Minas Gerais, Belo Horizonte, Brasil

Abstract— The literature has different implementations and results for the mono-objective and multiobjective optimization of the shell and tube heat exchanger (STHE), most of them using evolutionary computation. However, there is a gap to find the optimal solution of this problem through direct search methods (numerical optimization). So, this paper uses the Pattern Search algorithm of MATLAB toolbox applied to this case study.

Keywords— Optimization, Pattern Search algorithm, Shell and Tube Heat Exchanger.

I. INTRODUCTION

Heat exchangers are used in process industries, steam generating plants, refrigeration systems, heating systems, air conditioning, petrochemical industries, among other applications. Its function is to provide the recovery and use of thermal energy efficiently and economically. There are different models of heat exchangers, such as spiral, plates, regenerators, compacts, shell and tube heat exchanger (STHE). During its design it is possible to obtain different configurations, however, it is desirable the optimal design, which starts from the modeling of the same.

The recent literature review [1] shows the trend in the use of Evolutionary Algorithms for the mono-objective optimization of STHE. The most commonly used technique is Genetic Algorithm (GA). Other algorithms are Particle Swarm Optimization (PSO), Harmony Search Algorithm, Differential Evolution, Cuckoo Search Algorithm, Imperialist Competitive Algorithm, Biogeography Base Algorithm, Simulated Annealing, Firefly algorithm, Bat Algorithm, and Jaya algorithm. In the multiobjective optimization are the Non-Dominated Sorting Genetic Algorithm II (NSGA II) and the Multi-Objective Particle Swarm Optimizer (MOPSO).

Considering the previous discussion, the objective of this article is to solve the mono-objective optimization of the STHE by minimizing the objective function total annual cost with the use of the algorithm General Pattern Search (GPS), which is implemented in the MATLAB toolbox.

II. OPTIMIZATION OF THE SHELL AND TUBE HEAT EXCHANGER

The problem considered is the minimization of the total annual cost (TC) of the shell and tube heat exchanger.

$$\text{Min } f(\mathbf{x}), f(\mathbf{x}) = TC, \quad (1)$$

The modeling and problem of the shell and tube heat exchange used in this article are the found in [1-3]. The variables used for the multiobjective optimization are presented in Table 1.

Table.1: Variables for optimization of the Shell and Tube Heat Exchanger

Var.	Symbol	Values
		triang. (30°); square (90°); rot. square (45°)
x ₁	a _p	(45°)
x ₂	n _p	1; 2; 4
x ₃	L _t	2.438 m to 11.58 m
x ₄	esp	0.002108 m to 0.004572 m
x ₅	d _o	0.01588 m to 0.0508 m
x ₆	L _b	0.0508 m to 29.5(x ₅) ^{0.75}
x ₇	bc	15% to 45%
x ₈	d _{tb}	0.01x ₅ to 0.1x ₅
x ₉	d _{sb}	0.0032 m to 0.011 m

Follow the description of the variables: a_p is the tube layout pattern, n_p is the number of tubes passes, L_t is the tube length, esp is the tube wall thickness, d_o is the tube outer diameter, L_b is the baffle spacing, bc is the baffle cut, d_{tb} is the tube-to-baffle diametrical clearance, d_{sb} is the shell-to-baffle diametrical clearance.

Considering the material of the tube (70%Cu, 30%Ni) and of the shell (carbon steel), the total annual cost estimation (TC) that includes direct and indirect costs

(C_{BM}) and operational costs (OC), was conducted in the same manner as in [1,2]:

$$TC = C_{BM} \frac{i(1+i)^n}{(1+i)^n - 1} + OC \quad (2)$$

Where i is the fractional interest rate per year, n is the lifetime in years estimated for the heat exchanger. Being that the operational costs are in function of the pressure

drop, and direct and indirect costs are in function of the thermal exchange area.

Three constraints was considered involve the limits of the shell side pressure drop, the tube side pressure drop, and the maximum area value of the heat exchanger. The formulation was the same as the one considered in [1,3,4].

III. EXPERIMENTS AND RESULTS

The optimization of shell and tube heat exchanger was performed by direct search [5,6], through the Pattern Search algorithm of the MATLAB toolbox, and the configuration of the *Poll* and *Search* methods used was the *General Pattern Search positive basis 2N* (GPS) [7-9], the other settings were the program standards.

The result obtained by the GPS was compared to the multiobjective optimization performed by the algorithm NSGA II and transformed to the minimum annual cost criterion used in [1]. The GPS algorithm was also compared to the result found for the genetic algorithm of MATLAB toolbox. In this case, a configuration used was 50 generations, uniform stochastic selection, scattered crossover, and mutation constraint dependent.

The Table 2 and Table 3 show the best results found for algorithm GPS. In Table 4 the results for the GA algorithm are presented and in Table 5 has the results for NSGA II algorithm.

Table.2: Results for optimization, GPS algorithm, triangular tube arrangement, one tube pass

Variable	Value
a_p	Triangular
n_p	1
L_t	2,438 m
esp	0,002108 m
d_o	0,01588 m
L_b	0,9925 m
bc	17,4 %
d_{tb}	0,0001588 m
d_{sb}	0,0032 m
Function objective	Value
	\$ 3335,45

Table.3: Results for optimization, GPS algorithm, rotated square tube arrangement, one tube pass

Variable	Value
a_p	rotated square
n_p	1
L_t	2,438 m
esp	0,002352 m
d_o	0,01863 m
L_b	0,711 m
bc	15,3 %

d_{tb}	0,0001588 m
d_{sb}	0,0032 m
Function objective	Value
	\$ 3346,77

Table.4: Results for optimization, GA algorithm

Variable	Value
a_p	rotated square
n_p	1
L_t	3,658 m
esp	0,002108 m
d_o	0,01905 m
L_b	0,8588 m
bc	18,6 %
d_{tb}	0,0003921 m
d_{sb}	0,0054 m
Function objective	Value
	\$ 3362,45

Table.5: Results for optimization, NSGA II algorithm

Variable	Value
a_p	Triangular
n_p	1
L_t	2,438 m
esp	0,002108 m
d_o	0,01588 m
L_b	1,6312 m
bc	17,4 %
d_{tb}	0,0004775 m
d_{sb}	0,0042 m
Function objective	Value
	\$ 3337,12

For the triangular tube arrangement configuration and one tube pass, the result was better than the obtained by the algorithm NSGA II. And for the arrangement square rotated and one tube pass the algorithm also obtained better performance than the GA.

During the experiment, GPS algorithm was applied for all combinations of discrete variables of the STHE, so nine results were obtained. However, it was chosen to present only the best results and that could be compared to other optimization algorithms.

It is understood that the configuration of the STHE with square tube arrangement, rotated square tube arrangement with two tube passes or four tube passes, and triangular tube arrangement with two tube passes or four tube passes, does not allow good results.

IV. CONCLUSION

The GPS algorithm was a viable alternative for the mono-objective optimization of the shell and tubes heat exchanger, being that it found better results than the

popular algorithms like NSGA II and GA.

This result is important and interesting because most paper that apply optimization of the heat exchanger use heuristic methods, especially with the use of genetic algorithm (GA). However, when a competitive result is found with a direct search algorithm, one must extend the use of numerical optimization applied to other real problems. In addition, it is suggested that it encourages its use in hybrid algorithms.

REFERENCES

- [1] Saldanha, W. H. et al., (2017). Choosing the best evolutionary algorithm to optimize the multiobjective shell and tube heat exchanger design problem using PROMETHEE. *Applied Thermal Engineering*, vol. 127, pp. 1049-1061.
- [2] Fettaka, S.; Thibault, J.; Gupta, Y., (2013). Design of shell and tube heat exchangers using multiobjective optimization. *International Journal of Heat and Mass Transfer*, vol. 60, n. 1, pp. 343-354.
- [3] Shah, R. K.; Sekulic, D. P., (2003). *Fundamentals of heat exchanger design*. John Wiley Sons
- [4] Wildi-Tremblay, P. and Gosselin, L., (2007). Minimizing shell and tube heat exchanger cost with genetic algorithms and considering maintenance. *International Journal of Energy Research*, vol. 31, n. 9, pp. 867-885.
- [5] Hooke, R. and Jeeves, T. A., (1961). Direct search solution of numerical and statistical problems. *Journal of the ACM*, vol. 8, n. 2, pp. 212-229.
- [6] Kolda, T. G.; Lewis, R. M.; Torczon, V., (2003). Optimization by direct search: new perspectives on some classical and modern methods. *SIAM review*, vol. 45, n. 3, pp. 385-482.
- [7] Torczon, V., (1997). On the convergence of pattern search algorithms. *Journal on Optimization*, vol. 7, pp. 1-25.
- [8] Lewis, R. M.; Torczon, V., (1997). Pattern search algorithms for bound constrained minimization. *SIAM Journal on Optimization*, vol. 9, n. 4, pp. 1082-1099.
- [9] Audet, C.; JR, J.E.D., (2002). Analysis of generalized pattern searches. *SIAM Journal on optimization*, vol. 13, n. 3, pp. 889-903.

Study the Dynamic Response of the Stiffened Shallow Shell Subjected to Multiple Layers of Shock Waves

Le Xuan Thuy

Department of Solid Mechanics, Le Quy Don Technical University, Ha Noi, Viet Nam

Abstract— The ANSYS APDL programming and the results of calculating the stiffened shallow shell on elastic supports subjected to multiple layers of shock waves presented in the study. The program set up allows for the survey and evaluation of structural parameter and loads to the dynamic response of different types of shallow shell.

Keywords— Dynamic, Shell, shock wave, Elastic supports.

I. INTRODUCTION

The shell is used in many areas due to its good coverage and light weight. Some structures can be mentioned as: roof of the building, cover tunnel, engine cover, ... Calculation of shell structure is influenced by different types of load are many scientists concerned. One of the types of high destructive load mentioned is the shock wave load [1,2,3,4,5]. In fact, when exposed to multiple layers of shock waves, the structural response is complex. To avoid the impact of impulse load, in some cases the elastic supports is used. In this paper, the problem of shallow shell structure with (or without) elastic supports subjected to multi layers of shock waves is investigated. The study results may give the readers a more complete vision on the response of the mentioned shell structure and may be used for reference in the its design.

II. PROBLEM MODELING

The Considering an eccentrically stiffened singly (or doubly) curved shell that is simply supported at the edges by elastic springs with stiffness k (Fig. 1). The shell is affected by multiple layers of shock waves $p(t)$.

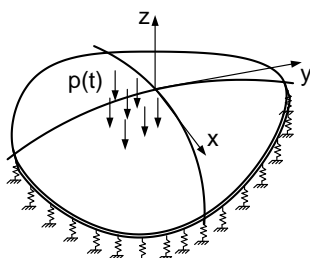


Fig. 1: Problem Model

For establishing an algorithm for the problem the following assumptions are used:

- The ribs and the shell material are homogeneous and isotropic;
- The shock-wave pressure is uniformly distributed on the shell surface.

III. TYPES OF ELEMENTS USED IN THE PROGRAM

To describe the bending shell, the SHELL63 element is used. The element has six degrees of freedom at each node: translations in the nodal x, y, and z directions and rotations about the nodal x, y, and z-axes. Stress stiffening and large deflection capabilities are included [8].

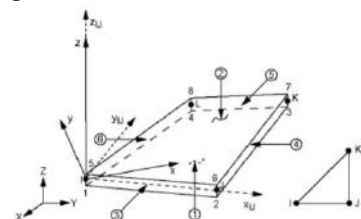


Fig. 2: SHELL63 Geometry

To describe the stiffener, 3-D Linear Finite Strain Beam (BEAM188) is used. BEAM188 is a linear (2-node) or a quadratic beam element in 3-D. It has six or seven degrees of freedom at each node, with the number of degrees of freedom depending on the value of KEYOPT(1). When KEYOPT(1) = 0 (the default), six degrees of freedom occur at each node. The eccentricity of the stiffener is described by the SECOFFSET command [8].

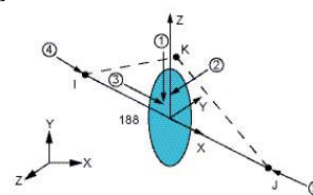


Fig. 3: BEAM188 Geometry

Elastic springs are described by the COMBIN14 element. With this type of element, the computational power of the

program is extended to other types of viscoelastic pillows. In this case, the damping coefficient should be added when declaring the constants of the COMBIN14 element.

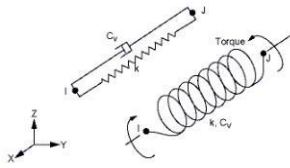


Fig. 4: COMBIN14 Geometry [8]

COMBIN14 has longitudinal or torsional capability in 1-D, 2-D, or 3-D applications. The longitudinal spring-damper option is a uniaxial tension-compression element with up to three degrees of freedom at each node: translations in the nodal x, y, and z directions. No bending or torsion is considered. The torsional spring-damper option is a purely rotational element with three degrees of freedom at each node: rotations about the nodal x, y, and z axes. No bending or axial loads are considered [8].

IV. GOVERNING EQUATIONS AND CALCULATION PROGRAM

The connection of the rib and the support elements into the flat shell elements is implemented by the direct stiffness method and the Skyline diagram is established by using the general algorithm of the FEM [6, 7, 8]. After connecting the element matrices and the element vectors in to the global ones the differential equation describing the oscillation of the stiffened shell may be written in the form:

$$[M]\{\ddot{q}\} + [C]\{\dot{q}\} + [K]\{q\} = \{F\}, \quad (*)$$

where:

$[M] = \sum_e [M_s^e] + \sum_e [M_b^e]$ - the overall mass matrix ($[M_s^e]$ - the element mass matrix of shell element, $[M_b^e]$ - the element mass matrix of beam element);

$[K] = \sum_e [K_s^e] + \sum_e [K_b^e] + \sum_e [K_{sp}^e]$ - the overall stiffness matrix ($[K_s^e]$, $[K_b^e]$, $[K_{sp}^e]$ - the element stiffness matrix of shell element, beam element and combin14 element respectively);

$\{F\} = \sum_e \{F_s^e\} + \sum_e \{F_b^e\}$ - the overall load vector;

$[C] = \alpha_R [M] + \beta_R [K]$ - the overall damping matrix, where α_R , β_R are Rayleigh damping coefficients [7,8].

Solution of equation (*) provided by the algorithm of calculator in ANSYS software. Depending on the choice of linear or nonlinear solvers, the Newmark's direct integration algorithm is used or combined using the Newton-Raphson iteration method.

A program to calculate the stiffened shallow shell subjected to multiple layers of shock waves on ANSYS APDL language written called *Shallow_shell_multishock_waves* (SSMW). The program includes the following modules:

- Modul 1: Import_data.mac;
- Modul 2: Model_building.mac;
- Modul 3: Loading_and_solving.mac;
- Modul 4: Export_result.mac.

Within the scope of the study, the calculation program was designed to calculate two types of shell: shallow cylindrical shell and doubly curved shell.

V. NUMERICAL RESULTS AND DISCUSSION

1. Problem 1

Consider an eccentrically stiffened shallow cylindrical shell whose plan view is a rectangular, $a = 2.0\text{m}$, $b = 1.0\text{m}$, the radius of curvature $R = 1.6\text{m}$, the thickness $h = 0.025\text{m}$. Shell material has an elastic modulus $E_s = 2.1 \times 10^{11} \text{N/m}^2$, poisson coefficient $\nu_s = 0.3$, specific weight $\rho_s = 7850 \text{kg/m}^3$. Four edges of shell are supported by elastic springs with stiffness $k = 3.10^4 \text{ kN/m}$. The eccentric ribs of the shell has $h_r = 0.03\text{m}$, $b_r = 0.01\text{m}$, the ribs in the directions are 6 (6 ribs parallel to the generating line, 6 ribs perpendicular to the generating line). The ribbed material has $E_r = 2.5 \times 10^{11} \text{N/m}^2$, $\nu_r = 0.3$, $\rho_r = 7500 \text{kg/m}^3$.

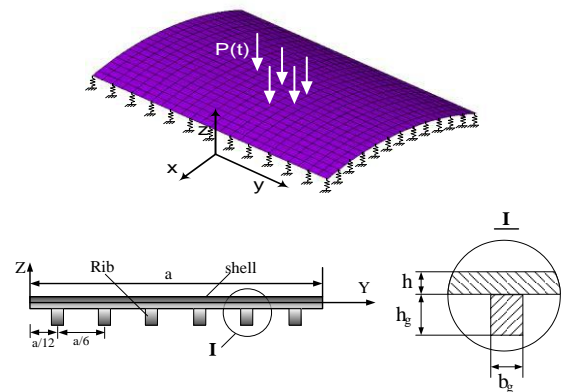


Fig. 5: Model of problem 1

The working load is two shock waves acting on the shell $p(t) = p_{\max} F(t)$, with: $p_{\max 1} = p_{\max 2} = 3.10^4 \text{ N/m}^2$,

$$F(t) = \begin{cases} 1 - \frac{t}{\tau} & 0 \leq t \leq \tau \\ 0 & t > \tau \end{cases}, \quad \tau_1 = \tau_2 = 0.05\text{s}, \text{ time difference}$$

between wave layers: $\Delta\tau = 0.02\text{s}$.

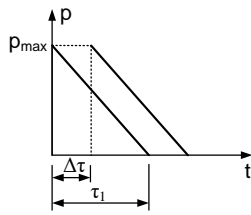


Fig. 6: Variation law of the load

Using the SSMW program, the author solved the problem with the calculating time $t_{cal} = 0.16s$, integral time step $\Delta t = 0.0005s$. Resulting in stress and vertical displacement at the center of the shell, as shown in Table 1 and Figures 7, 8, 9.

Table.1: The maximum value of the quantity calculated in problem 1

	w_{max} [cm]	σ_x^{max} [N/m ²]	σ_y^{max} [N/m ²]
SSMW	0.0115	3.5977×10^6	1.5273×10^6

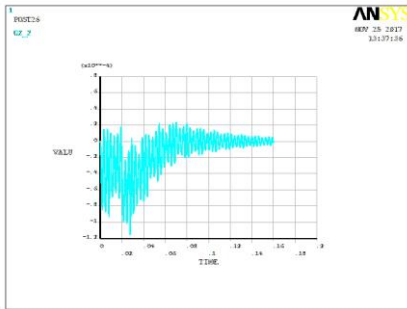


Fig. 7: Vertical displacement response w at center point

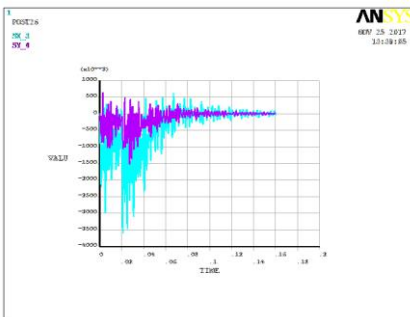


Fig. 8: Stress response σ_x, σ_y at center point

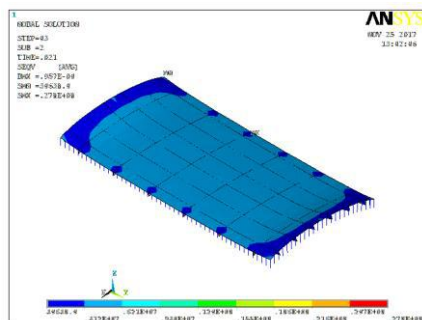


Fig. 9: Field of von mises stress of the shell at time $t = 0.021s$

Comment: With the given set of data, the maximum dynamic response values of the system reached at the time of two waves of simultaneous effects (time $t = 0.021s$). At center point, the stress σ_x^{max} is greater than the stress σ_y^{max} .

2. Problem 2

Considering the shallow cylindrical shell whose plan view is a rectangular, generating line's length $a = 2.0m$, opening angle of the shell $\theta = 40^\circ$, the radius of curvature is $R = 2.0m$, $h = 0.02m$, $E_s = 2.2 \times 10^{11} N/m^2$, $\nu_s = 0.31$, $\rho_s = 7800 kg/m^3$. The eccentrically ribbed shell with $h_r = 0.03m$, $b_r = 0.01m$, the shell with 4 ribs is parallel to the generating line, 6 ribs is perpendicular to the generating line, the ribs are equispaced. $E_r = 2.4 \times 10^{11} N/m^2$, $\nu_r = 0.3$, $\rho_r = 7000 kg/m^3$. The mentioned shell has a round hole in the middle position, with $d = 0.2 m$ (fig. 10). The load acting and the boundary are the same as Problem 1.

Vertical displacement and stress at point A, field of von mises stress of the shell and the overall transposition field of the structure at time $t = 0.021s$ are shown in Figure 11, 12, 13, 14 and table 2.

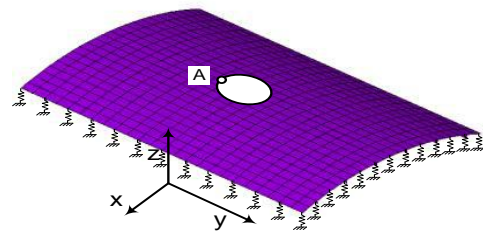


Fig. 10: Model of problem 2

Table.2: The maximum value of the quantity calculated in problem 2

	w^{Amax} [cm]	σ_x^{Amax} [N/m ²]	σ_y^{Amax} [N/m ²]
SSMW	0.0178	24.502×10^6	3.669×10^6

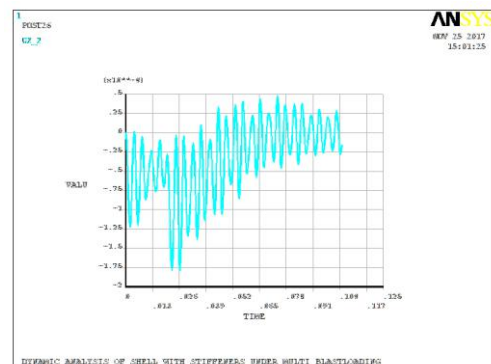


Fig. 11: Vertical displacement response w at point A

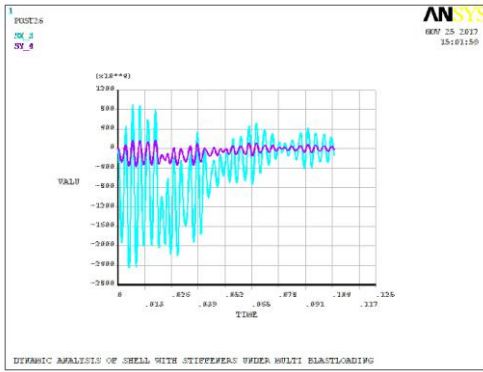


Fig. 12: Stress response σ_x , σ_y at point A

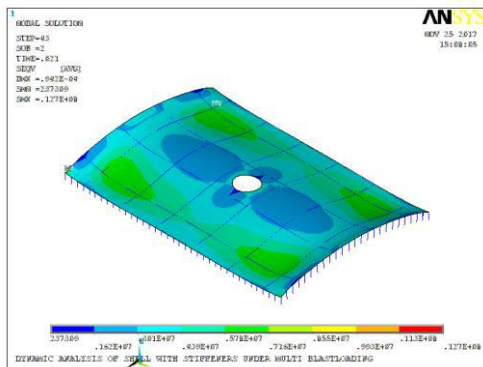


Fig. 13: Field of von mises stress of the shell at time $t = 0.021s$

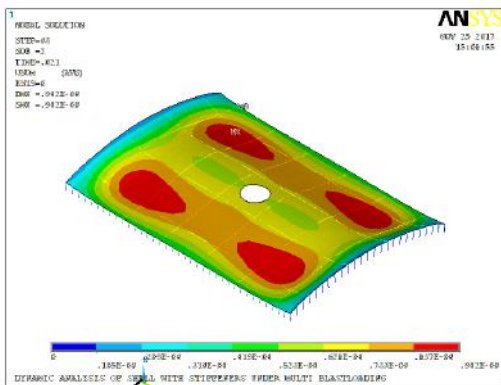


Fig. 14: The overall transposition field of the structure at time $t = 0.021s$

Comment: Immediately after the second wave appeared, the vertical displacement of the point A increases quite a lot, which represents the great influence of the second wave on the structure. At the time $t = 0.021s$, the shell appeared four symmetrical areas through the center with relatively large stress and displacement responses compared to the other positions. This is due to the reduction in the pressure applied to the position at the center of the cover.

3. Problem 3

Considering the doubly curved shell whose plan view is a rectangular, $a = 1.5m$, $b = 1.0m$, $R_1 = 2.0m$, $R_2 = -4.0m$, the thickness $h = 0.005m$. Shell material has $E_s = 2.1 \times 10^{11}$

N/m^2 , $\nu_s = 0.31$, $\rho_s = 7800kg/m^3$ (fig. 15). The load acting is the same as Problem 1.

Vertical displacement and stress at center point, field of von mises stress of the shell and the overall transposition field of the structure at time $t = 0.025s$ are shown in Figure 16, 17, 18, 19 and table 3.

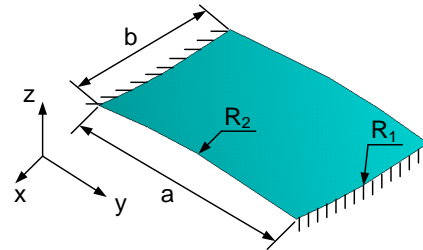


Fig. 15: Model of problem 3

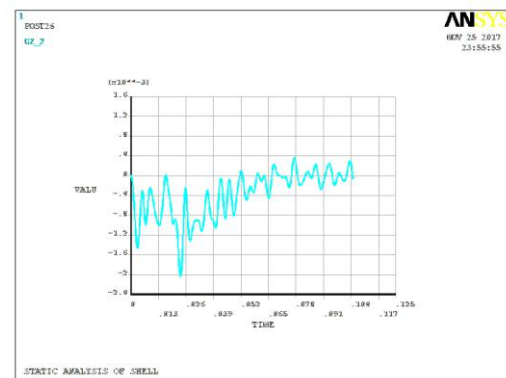


Fig. 16: Vertical displacement response w at center point

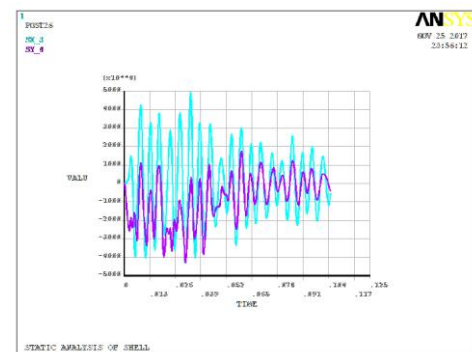


Fig. 17: Stress response σ_x , σ_y at center point

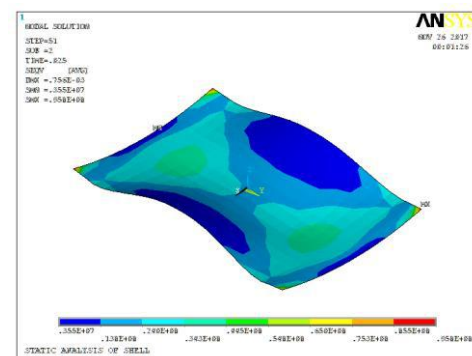


Fig. 18: Field of von mises stress of the shell at time $t = 0.025s$

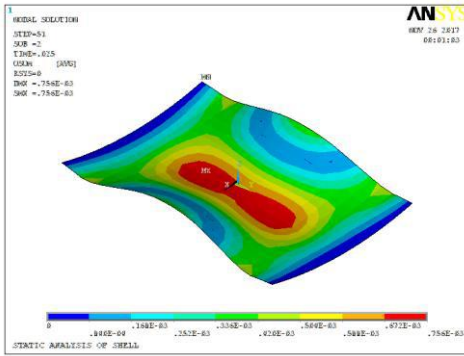


Fig. 19: The overall transposition field of the structure at time $t = 0.025s$

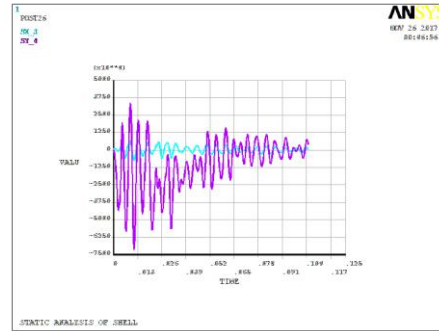


Fig. 22: Stress response σ_x, σ_y at point A

Table.3: The maximum value of the quantity calculated in problem 3

	w^{\max} [cm]	σ_x^{\max} [N/m ²]	σ_y^{\max} [N/m ²]
SSMW	0.0204	49.535×10^6	42.782×10^6

Comment: Like the results of the problem 1 and problem 2, the maximum dynamic response values at point A of the structure reached at the time of two waves of simultaneous effects.

4. Problem 4

The parameters of the model are similar to the parameters in problem 3. The difference is that the shell has a square hole ($a_1 \times a_1$) in the middle position, with $a_1 = 0.2$ m.

Table.4: The maximum value of the quantity calculated in problem 4

	w^{\max} [cm]	σ_x^{\max} [N/m ²]	σ_y^{\max} [N/m ²]
SSMW	0.0126	7.348×10^6	71.405×10^6

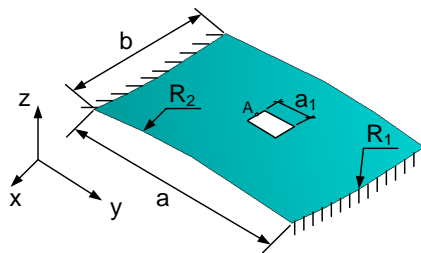


Fig. 20: Model of problem 4

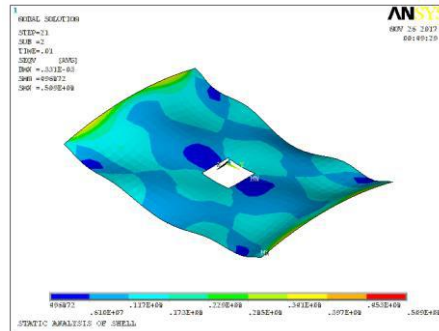


Fig. 23: Field of von mises stress of the shell at time $t = 0.01s$

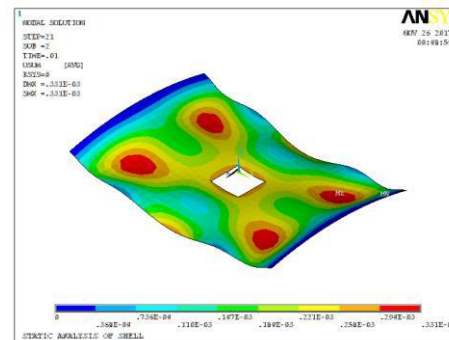


Fig. 24: The overall transposition field of the structure at time $t = 0.01s$

Comment: Compared to the result at the midpoint of the shell in Problem 3, the maximum value of the stress response at point A (σ_y^{\max}) is much greater, this shows that the more susceptible to damage of the structure when there is a defect on its.

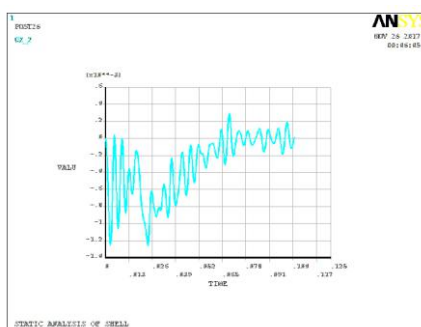


Fig. 21: Vertical displacement response w at point A

VI. CONCLUSION

In this study, using the ANSYS APDL programming language, a program has been established that allows for solving many different problem classes. The paper focuses on solving the problem of calculating the shell structure with one or two curvature with or without holes, which is affected by the impulse load system. The results show the complex response of the structure when multiple layers of shock wave load are applied. Solving different problem classes demonstrates the ability of the program.

The results of the study may be good references when calculating, designing the same structural.

REFERENCES

- [1] Ioannis G. Raftoyiannis, Constantine C. Spyrakos, George T. Michaltsos (2007). Behavior of suspended roofs under blast loading. *Engineering Structures* 29 (ISSN: 0141-0296) 88–100, doi:10.1016/j.engstruct.2006.04.006.
- [2] A. Ghani Razaqpur, Ahmed Tolba, Ettore Contestabile (2007). Blast loading response of reinforced concrete panels reinforced with externally bonded GFRP laminates. *Composites: Part B* 38, 535–546, doi:10.1016/j.compositesb.2006.06.016.
- [3] Zhenyu Xue, John W. Hutchinson (2003). Preliminary assessment of sandwich plates subject to blast loads. *International Journal of Mechanical Sciences* 45, 687–705, doi:10.1016/S0020-7403(03)00108-5.
- [4] H. S. Türkmén (2002). Structural Response of Laminated Composite Shells Subjected to Blast Loading: Comparison of Experimental and Theoretical Methods. *Journal of Sound and Vibration* 249(4), 663-678, doi:10.1006/jsvi.2001.3861.
- [5] Yonghui Wang, Ximei Zhai, Siew Chin Lee, Wei Wang (2016). Responses of curved steel-concrete-steel sandwich shells subjected to blast loading. *Thin-Walled Structures* 108, 185–192, <http://dx.doi.org/10.1016/j.tws.2016.08.018>.
- [6] Saeed Moaveni (2008). *Finite element analysis: theory and application with ANSYS*. Pearson Prentice Hall., Pearson Education.Inc.
- [7] Erdogan Madenci, Ibrahim Guven (2015). *The finite element method and applications in engineering using ANSYS*. Springer International Publishing.
- [8] Release 11.0 Documentation for ANSYS.

Theoretical investigation of series of diazafluorene-functionalized TTFs by using density functional method

Tahar Abbaz^{1*}, Amel Bendjeddou¹, Didier Villemin²

¹Laboratory of Aquatic and Terrestrial Ecosystems. Org. and Bioorg. Chem. Group, University of Mohamed-Cherif Messaadia, Souk Ahras, 41000, Algeria

²Laboratory of Molecular and Thio-Organic Chemistry, UMR CNRS 6507, INC3M, FR 3038, Labex EMC3, ensicaen & University of Caen, Caen 14050, France

Abstract— Quantum chemical calculations of energies, geometrical structure and electronic parameters of diazafluorene-functionalized TTFs **1-4** were carried out by using density functional (DFT/B3LYP) method with 6-31G(d,p) as basis set. Stability of the molecule arising from hyper conjugative interactions, charge delocalization has been analyzed using natural bond orbital (NBO) analysis. The calculated HOMO and LUMO energies show that chemical activity of the molecule. The local reactivity descriptor analysis is performed to find the reactive sites within molecule.

Keywords— Computational chemistry, Density functional theory, Electronic structure, Quantum chemical calculations

I. INTRODUCTION

The chemistry of heterocyclic compounds has a key role in the discovery of new drugs. This study field have gathered great attention over the past years, and a number of paper constructed by experimental techniques and theoretical methods have appeared in the literature. Various compounds such as alkaloids, essential amino acids, vitamins, hemoglobin, hormones, large number of synthetic drugs and dyes contain heterocyclic ring systems. There are large numbers of synthetic heterocyclic compounds, like pyrimidine, pyridine, pyrrole, pyrrolidine, diazafluorene, furan and thiophene. Heterocyclic compounds exhibits wide range of synthetic and biological activities, especially nitrogen and sulfur containing heterocyclic moieties were found to be vital for a number of biologically active compounds [1]. Density functional theory (DFT) has become the dominant tool in chemistry and physics for calculations of electronic structure as it demands less time for inclusion of electron correlation. Detailed analysis on the applicability of different methods of DFT has been performed, particularly for equilibrium structure properties of geometry, vibrational frequency, etc [2]. The

general conclusion from these studies was that DFT methods, particularly with the use of nonlocal exchange-correlation functions, can predict accurate equilibrium structure properties. NBOs provide an accurate method for studying intramolecular interactions and give an efficient basis to investigate charge transfer or conjugative interaction in various molecular systems [3]. Molecular electrostatic potential (MEP) is used to map and understand the dimeric sites within the molecules. MEP is very much required for predicting structure–activity relationship and drug–receptor interactions of biomolecules.

The present work aims to investigate the molecular structure, electronic and non-linear optical properties of series of diazafluorene-functionalized TTFs **1-4** described in literature [4] and to predict their activities, we give a global study of the molecular geometry, natural bond orbital (NBO) analysis, nonlinear optical (NLO) properties, and chemical reactivity as HOMO-LUMO energy gap, chemical hardness, chemical potential and local reactivity descriptors.

II. MATERIALS AND METHODS

All parameters and properties of diazafluorene-functionalized TTFs **1-4** were calculated using the Gaussian 09 software package on a personal computer [5]. The computations were performed at B3LYP/6-31G(d,p) level of theory to get the optimized geometries shown in Fig 1 of the title compound. DFT calculations were carried out with Becke's three-parameter hybrid model using the Lee-Yang-Parr correlation functional (B3LYP) method.

III. RESULTS AND DISCUSSION

3.1. Molecular Geometry

The molecular structure along with numbering of atoms of diazafluorene-functionalized TTFs molecules are as shown in Fig 1. The calculated global minimum energy of

diazafluorene-functionalized TTFs **1-4** in C₁ point group symmetries are between -3189.3021 and -4064.3090 a.u. by 6-31G(d,p) basis set. The optimized bond lengths,

bond angles and dihedral angles of the title compound which calculated using B3LYP method are with 6-31G(d,p) basis set are shown in Tables 1-4.

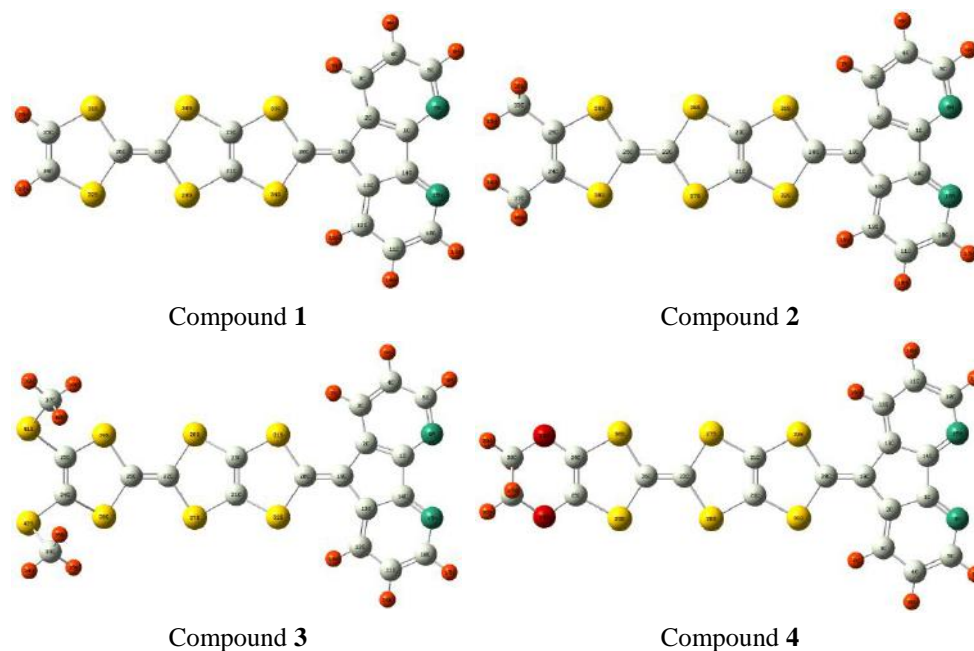


Fig.1: Optimized molecular structure of diazafluorene-functionalized TTFs 1-4

Table.1: Optimized geometric parameters of compound 1

Bond Length(Å)		Bond Angles (°)		Dihedral Angles (°)	
R(25,28)	1.082	A(27,24,32)	117.002	D(6,1,2,19)	179.999
R(24,25)	1.336	A(24,25,28)	124.925	D(1,2,3,7)	179.999
R(25,31)	1.762	A(24,32,26)	94.977	D(16,12,13,14)	179.999
R(26,31)	1.786	A(22,26,32)	123.049	D(2,19,20,34)	179.998
R(22,26)	1.349	A(29,22,30)	115.248	D(13,19,20,33)	179.999
R(22,30)	1.795	A(21,34,20)	95.537	D(33,23,30,20)	179.999
R(5,9)	1.088	A(15,10,17)	116.124	D(27,24,25,31)	180.000
R(1,2)	1.421	A(2,3,7)	122.964	D(22,26,31,25)	179.999
R(5,6)	1.340	A(3,4,8)	120.291	D(6,1,2,3)	53.175
R(3,4)	1.396	A(2,1,6)	125.556	D(6,1,14,15)	64.203
R(21,34)	1.757	A(1,14,15)	126.229	D(23,21,29,22)	47.100
R(13,19)	1.476	A(12,13,19)	134.005	D(29,22,30,23)	59.001
R(14,15)	1.330	A(1,2,19)	108.848	D(24,25,31,26)	96.023
R(19,20)	1.366	A(33,20,34)	113.311	D(31,26,32,24)	83.000
R(2,3)	1.397	A(11,12,16)	119.169	D(27,24,32,26)	179.999

Table.2: Optimized geometric parameters of compound 2

Bond Length(Å)		Bond Angles (°)		Dihedral Angles (°)	
R(1,2)	1.421	A(5,4,8)	119.949	D(6,1,2,19)	179.999
R(1,14)	1.467	A(2,1,6)	125.559	D(1,2,3,7)	179.998
R(5,6)	1.340	A(1,2,19)	108.858	D(3,2,19,13)	179.998
R(5,9)	1.088	A(3,2,19)	134.004	D(1,2,19,20)	180.000
R(4,8)	1.085	A(2,19,13)	105.870	D(9,5,6,1)	179.999
R(2,19)	1.476	A(10,15,14)	115.917	D(1,14,15,10)	179.999
R(19,20)	1.366	A(1,14,15)	126.234	D(2,19,20,32)	179.993
R(20,31)	1.784	A(31,20,32)	113.288	D(13,19,20,31)	179.993

R(21,23)	1.342	A(23,21,27)	118.675	D(19,20,31,23)	179.999
R(22,26)	1.349	A(26,22,27)	122.380	D(32,21,23,28)	179.998
R(24,37)	1.502	A(25,24,30)	117.158	D(32,21,27,22)	179.998
R(33,34)	1.095	A(28,25,33)	127.158	D(27,21,32,20)	179.999
R(33,35)	1.090	A(22,26,29)	123.302	D(28,22,27,21)	70.003
R(26,29)	1.777	A(25,33,35)	111.269	D(25,24,37,39)	120.247
R(25,29)	1.781	A(38,37,39)	107.930	D(30,24,37,40)	59.752

Table.3: Optimized geometric parameters of compound 3

Bond Length(Å)		Bond Angles (°)		Dihedral Angles (°)	
R(5,9)	1.088	A(4,5,9)	120.126	D(39,37,41,25)	178.120
R(4,5)	1.397	A(5,4,8)	119.932	D(22,26,30,24)	160.466
R(5,6)	1.339	A(2,3,4)	117.870	D(24,,25,41,37)	123.928
R(1,2)	1.421	A(3,2,19)	133.998	D(41,25,29,26)	173.253
R(1,14)	1.467	A(2,19,20)	127.075	D(30,24,25,41)	172.808
R(19,20)	1.366	A(1,14,13)	108.225	D(26,22,28,23)	161.774
R(20,31)	1.785	A(19,20,31)	123.408	D(28,22,26,30)	177.695
R(23,31)	1.756	A(31,20,32)	113.157	D(27,21,32,20)	174.248
R(21,23)	1.342	A(27,22,28)	114.204	D(32,21,27,22)	170.939
R(23,28)	1.769	A(38,37,40)	110.352	D(32,21,23,28)	176.999
R(22,28)	1.791	A(27,21,32)	124.071	D(13,19,20,31)	178.998
R(22,26)	1.349	A(26,22,27)	122.881	D(12,13,14,1)	179.869
R(25,29)	1.789	A(25,24,42)	125.702	D(6,1,2,19)	179.912
R(24,25)	1.355	A(34,33,42)	105.492	D(9,5,6,1)	179.994
R(33,42)	1.837	A(29,26,30)	112.357	D(10,11,12,16)	179.972

Table.4: Optimized geometric parameters of compound 4

Bond Length(Å)		Bond Angles (°)		Dihedral Angles (°)	
R(4,5)	1.397	A(3,4,5)	119.751	D(6,1,2,19)	179.973
R(4,8)	1.085	A(4,5,6)	123.760	D(14,1,6,5)	179.984
R(19,20)	1.366	A(6,1,14)	126.235	D(2,3,4,8)	179.996
R(2,19)	1.476	A(1,2,19)	108.855	D(9,5,6,1)	180.000
R(19,20)	1.366	A(10,15,14)	115.920	D(2,19,20,32)	179.887
R(20,31)	1.784	A(2,19,13)	105.854	D(27,21,32,20)	179.978
R(23,31)	1.757	A(2,19,20)	127.073	D(27,22,26,29)	179.745
R(21,23)	1.342	A(19,20,31)	123.349	D(30,24,34,38)	164.277
R(23,28)	1.763	A(31,20,32)	113.303	D(29,25,33,35)	164.251
R(26,29)	1.788	A(28,23,31)	123.555	D(25,33,35,36)	165.327
R(25,29)	1.771	A(22,28,23)	93.722	D(25,33,35,38)	44.664
R(33,35)	1.436	A(27,22,28)	115.268	D(24,34,38,39)	165.316
R(35,36)	1.091	A(21,23,28)	118.643	D(33,35,38,40)	58.105
R(35,38)	1.528	A(29,25,33)	116.933	D(37,35,38,40)	178.864
R(38,40)	1.097	A(33,35,36)	106.298	D(36,35,38,39)	61.869

3.2. Molecular Electrostatic Potential (MEP)

The MEP is related to the electronic density and is a very useful descriptor for determining the sites for electrophilic and nucleophilic reactions as well as hydrogen bonding interactions [6]. The electrostatic potential $V(r)$ is also well suited for analyzing processes based on the "recognition" of one molecule by another, as in drug-receptor, and enzyme-substrate interactions, because it is through their potentials that the two species first "see"

each other [7,8]. For the system studied the $V(r)$ values were calculated as described previously using the equation [9].

$$V(r) = \sum Z_A / |R_A - r| - \int \rho(r') / |r' - r| d^3 r'$$

The different values of the electrostatic potential at the surface are represented by different colors. Potential increases in the ordered (most negative) < orange < yellow < green < blue (most positive). To predict reactive

sites of electrophilic or nucleophilic attack for the investigated molecule, the MEP at the B3LYP/6-31G(d,p) optimized geometry was calculated. The negative (red and yellow) regions of the MEP are related to

electrophilic reactivity and the positive (blue) regions to nucleophilic reactivity, as shown in Fig 2. As can be seen from the figure, this molecule has several possible sites for electrophilic and nucleophilic attacks.

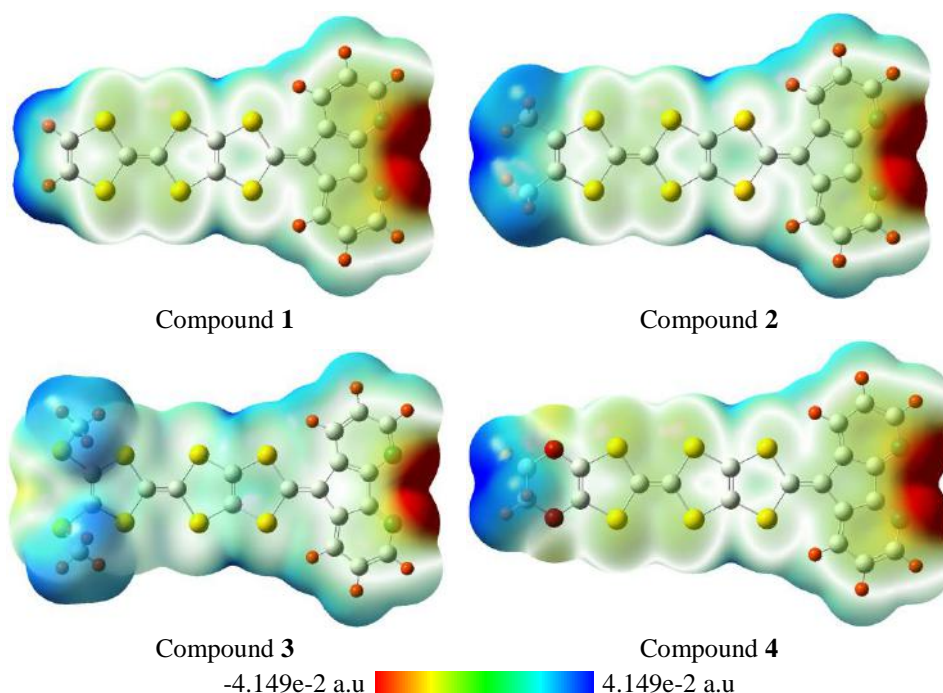


Fig.2: Molecular electrostatic potential surface of diazafluorene-functionalized TTFs 1-4

According to these calculated results, the MEP map shows that in all molecules, the regions exhibiting the negative electrostatic potential are localized near the nitrogen atoms while the regions presenting the positive potential are localized vicinity of the hydrogen atoms of alkyl and cyclic groups. These sites give information about the region from where the compound can have intermolecular interactions.

3.3. Frontier Molecular Orbitals (FMOs)

Frontier molecular orbitals i.e. the highest occupied molecular orbital (HOMO) and lowest unoccupied molecular orbital (LUMO) are very popular quantum chemical parameters. They determine the molecular reactivity and light absorption ability. The vicinal orbitals of HOMO and LUMO play the role of electron donor and electron acceptor, respectively. The HOMO-LUMO

energy gap (ΔE_{gap}) is an important stability index. The conjugated molecules are characterized by HOMO-LUMO separation, which is the result of a significant degree of intramolecular charge transfer (ICT) from the end-capping electron donor groups to the efficient electron-acceptor groups through π -conjugated path. Therefore, an electron density (ED) transfer occurs from the aromatic part of the π -conjugated system in the electron donor side to its electron-withdrawing part [10]. The HOMO-LUMO energy gap that reflects the chemical reactivity of the molecule, calculated at B3LYP/6-31G(d,p) level. The HOMO- LUMO plots of compound 4 are given in Figure 3. According to Figure 3, the positive phase is shown as green color region whereas the negative one is provided as red color region. Table 5 illustrates the change of $\Delta E_{\text{LUMO} - \text{HOMO}}$ (E_{gap}) energy gap value of title compound.

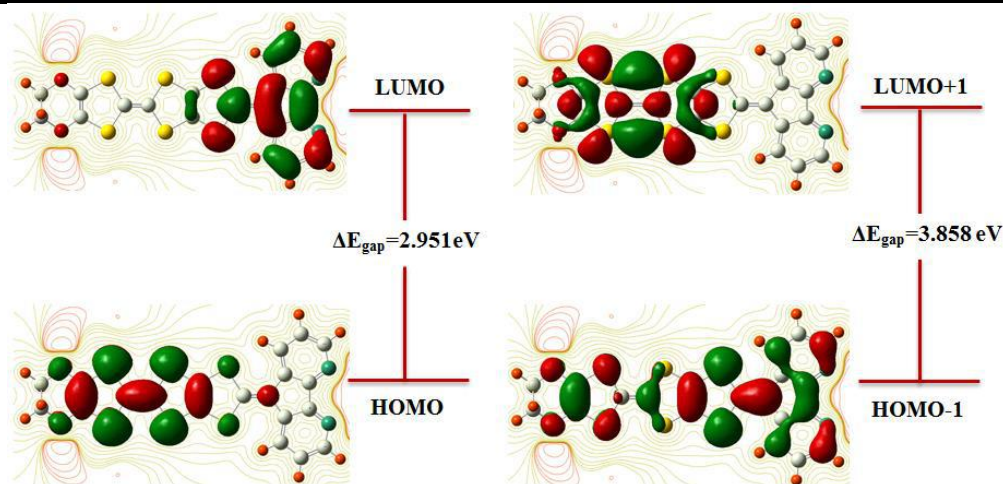


Fig.3: HOMO-LUMO Structure with the energy level diagram of compound 4

3.4. Global Reactivity Descriptors

By using HOMO and LUMO energy values of a molecule, the global chemical reactivity descriptor of molecules such as hardness, chemical potential, softness, electronegativity and electrophilicity index as well as local reactivity have been defined [11-15]. The HOMO and LUMO energies, the energy gap (ΔE), ionization potential (I), electron affinity (A), absolute electronegativity (χ) absolute hardness (η) and softness (S) of the diazafluorene-functionalized TTFs **1-4** molecules have been computed by DFT/B3LYP/6-31G(d,p) method are listed in Table 5. The chemical potential [13] provide a global reactivity index and related to charge transfer from a system of higher chemical potential to lower chemical potential. The reactivity index is the measure of stabilization in energy when the system acquires an additional electronic charge (ΔN). A molecule or atom that has a positive electron affinity is often called an electron acceptor and may undergo charge transfer reactions. The electron donating power of a donor molecule is measured by its ionization potential which is the energy required to remove an electron from the highest occupied molecular orbital. The overall energy balance (ΔE), i.e., energy gained or lost, in an electron donor-acceptor transfer is determined by the difference between the acceptor's electron affinity (EA) and the ionization potential (IP) as $\Delta E = EA - IP$. Electronegativity is a chemical property that describes the ability of an atom or a functional group to attract electrons or electron density towards itself. Parr et al. [13, 14] have defined a new descriptor to quantify the global electrophilic power of the compound as electrophilicity index (ω) which defines a quantitative classification of global electrophilic nature of a compound. Parr et al. [13, 14] have proposed electrophilicity index (ω) as a measure of energy lowering

due to maximal electron flow between donor and acceptor. The usefulness of this new reactivity quantity has been recently demonstrated understanding the toxicity of various pollutants in terms of their reactivity and site selectivity. The electrophilicity index is positive, definite quantity and direction of the charge transfer is fully determined by the chemical potential (μ) of the molecule. Because an electrophile is a chemical species, it has an electron accepting capability from the environment and its energy must decrease upon accepting electronic charge, therefore, its electronic chemical potential must be negative. The chemical hardness [14-17] is the second derivative of the electronic energy with respect to the number of electrons for a constant external potential. Pauling introduced the concept of electronegativity as the power of an atom in a compound to attract electrons to it. Using Koopman's theorem for closed shell compounds the electronegativity and chemical hardness can be calculated as follow:

$$\chi = (E_{HOMO} - E_{LUMO}) / 2$$

$$\mu = -(IE + EA) / 2 = (E_{N+1} - E_{N-1}) / 2 = -\chi$$

$$\eta = (IE - EA) / 2 = (E_{N-1} - E_{N+1} - 2E_N) / 2$$

$$S = 1 / 2\eta$$

$$\omega = \mu^2 / 2\eta$$

Where I and A are ionization potential and electron affinity, $I = E_{HOMO}$ and $A = E_{LUMO}$ respectively as shown in Table 5. The large HOMO-LUMO gap means a hard molecule and small HOMO-LUMO gap means a soft molecule. One can also relate the stability of the molecule to hardness, which means that the molecule with least HOMO-LUMO gap means it is more reactive.

Table.5: Quantum chemical descriptors of diazafluorene-functionalized TTFs 1-4

Parameters	Compound 1	Compound 2	Compound 3	Compound 4
E_{HOMO} (eV)	-4.969	-4.846	-5.205	-4.837
E_{LUMO} (eV)	-1.900	-1.853	-1.929	-1.886
ΔE_{gap} (eV)	3.068	2.993	3.277	2.951
I (eV)	4.969	4.846	5.205	4.837
A (eV)	1.900	1.853	1.929	1.886
μ (eV)	-3.435	-3.349	-3.567	-3.362
χ (eV)	3.435	3.349	3.569	3.362
η (eV)	1.534	1.496	1.638	1.475
S (eV)	0.326	0.334	0.305	0.339
ω (eV)	3.845	3.748	3.830	3.830

As presented in table 5, the compound which have the lowest energetic gap is the compound **4** ($\Delta E_{\text{gap}} = 2.951$ eV). This lower gap allows it to be the softest molecule. The compound that have the highest energy gap is the compound **3** ($\Delta E_{\text{gap}} = 3.277$ eV). The compound that has the highest HOMO energy is the compound **4** ($E_{\text{HOMO}} = -4.837$ eV). This higher energy allows it to be the best electron donor. The compound that has the lowest LUMO energy is the compound **3** ($E_{\text{LUMO}} = -1.929$ eV) which signifies that it can be the best electron acceptor. The two properties like I (potential ionization) and A (affinity) are so important, the determination of these two properties allow us to calculate the absolute electronegativity (χ) and the absolute hardness (η). These two parameters are related to the one-electron orbital energies of the HOMO and LUMO respectively. Compound **4** has lowest value of the potential ionization ($I = 4.837$ eV), so that will be the better electron donor. Compound **3** has the largest value of the affinity ($A = 1.929$ eV), so it is the better electron acceptor. The chemical reactivity varies with the structural of molecules. Chemical hardness (softness) value of compound **4** ($\eta = 1.475$ eV, $S = 0.339$ eV) is lesser (greater) among all the molecules. Thus, compound **4** is found to be more reactive than all the compounds. Compound **3** possesses higher electronegativity value ($\chi = 3.569$ eV) than all compounds so; it is the best electron acceptor. The value of ω for compound **1** ($\omega = 3.845$ eV) indicates that it is the stronger electrophiles than all

compounds. Compound **4** has the smaller frontier orbital gap so, it is more polarizable and is associated with a high chemical reactivity, low kinetic stability and is also termed as soft molecule.

3.5. Local Reactivity Descriptors

To describe the chemical reactivity of an atom in a molecule, it is necessary to obtain the values of condensed Fukui function (FF) around each atomic site. Thus, for an atom k in a molecule, three kinds of condensed FF, namely, f_k^+ , f_k^- and f_k^0 can be used to describe the electrophilic, nucleophilic and radical reactivity, respectively, which are defined by Eqs. (5)-(7) in a finite difference approximation [18]. The higher FF values indicate more reactivity of this atom than other ones.

$$\text{For nucleophilic attack } f^+ = [q(N+1) - q(N)]$$

$$\text{For electrophilic attack } f^- = [q(N) - q(N-1)]$$

$$\text{For radical attack } f^0 = [q(N+1) - q(N-1)]/2$$

where, q is the gross charge of atom k in the molecule and N , $N+1$, $N-1$ are electron systems containing neutral, anion, cation form of molecule respectively. Where +, -, 0 signs show nucleophilic, electrophilic and radical attack respectively. Fukui functions for selected atomic sites in diazafluorene-functionalized TTFs **1-4** are shown in Tables 6-7.

Table.6: Order of the reactive sites on compounds 1 and 2

	Compound 1				Compound 2				
Atom	23 C	21 C	22 C	26 C	Atom	21 C	23 C	22 C	24 C
f^+	0.030	0.030	0.022	-0.003	f^+	0.026	0.026	0.025	0.003
Atom	14 C	1 C	19 C	2 C	Atom	1 C	2 C	20 C	22 C
f^-	0.143	0.143	0.103	0.091	f^-	0.143	0.091	0.029	0.010
Atom	14 C	1 C	19 C	2 C	Atom	1 C	2 C	22 C	21 C
f^0	0.059	0.059	0.048	0.029	f^0	0.059	0.029	0.017	0.013

Table.7: Order of the reactive sites on compounds 3 and 4

Compound 3				Compound 4					
Atom	15 N	6 N	20 C	22 C	Atom	21 C	22 C	23 C	34 O
f^+	0.248	0.248	0.205	0.085	f^+	0.034	0.030	0.019	-0.001
Atom	14 C	1 C	19 C	2 C	Atom	20 C	26 C	22 C	21 C
f^-	0.146	0.146	0.114	0.091	f^-	0.027	0.008	0.001	0.000
Atom	24 C	25 C	26 C	22 C	Atom	21 C	22 C	23 C	26 C
f^0	-0.007	-0.007	-0.009	-0.010	f^0	0.017	0.015	0.010	-0.001

From the tables 6-7, the parameters of local reactivity descriptors show that 21C is the more reactive site in compounds 2 and 4 and 23C, 15N are the more reactive sites in compounds 1 and 3 respectively for nucleophilic attacks. The more reactive sites in radical attacks are 14C, 1C, 24C and 21C for compounds 1, 2, 3 and 4 respectively. The more reactive sites for electrophilic attacks are 14C for compounds 1, 3 and 1C, 20C for compounds 2 and 4 respectively.

3.6. Natural Bond Orbital Analysis (NBO)

Weak occupancies of the valence anti-bonds signal irreducible withdraw from an idealized localized Lewis structure which means true “delocalization effects” [19]. NBO analysis provides the most accurate possible natural Lewis structure picture of orbits because all the orbital details are mathematically selected to include the highest possible percentage of the electron density. The NBO method gives information about interactions in both completed and virtual orbital spaces that could improve the analysis of intra and inter-molecular interactions. In NBO analysis the donor-acceptor interactions are computed by carrying out the second order Fock matrix [20]. The interactions consequence is the loss of occupancy from the localized natural bond orbital of the idealized Lewis structure into a vacant non- Lewis orbital. For each donor (i) and acceptor (j) the stabilization energy $E_{(2)}$ related with the delocalization i - j is approximated as

$$E(2) = \Delta E_{ij} = q_i \frac{F^2(i, j)}{E_j - E_i}$$

Where $F(i,j)$ is the off diagonal NBO Fock matrix element and q_i is the donor orbital occupancy, $2j$ and $2i$ are diagonal elements. NBO analysis provides a suitable basis for investigating conjugative interaction or charge transfer in molecular systems. This is a powerful method for studying inter and intra molecular bonding and interaction among bonds. As a result of some electron donor orbital, acceptor orbital and the interacting stabilization energy, the second order micro disturbance theory is reported [21, 22]. If the values $E_{(2)}$ is larger, the interaction between electron donors and electron acceptors becomes more intensive i.e., the more donating propensity from electron donors to electron acceptors and larger the amount of conjugation of the whole molecular system. The stabilizing donor-acceptor interaction arises due to delocalization of electron density between occupied Lewis-type (lone pair or bond) and properly unoccupied (Rydberg or anti-bond) non Lewis NBO orbitals. NBO analysis has been performed on the diazafluorene-functionalized TTFs molecules at the B3LYP/6-31G (d,p) level for the sake of elucidate the re-hybridization, intramolecular and delocalization of electron density within the molecule.

Table.8: Second order perturbation theory analysis of Fock matrix on NBO of compound 1

Donor(i)	ED/e	Acceptor(j)	ED/e	E(2) Kcal/mol	E(j)-E(i) a.u	F(i,j) a.u
$\pi(C5-N6)$	1.70308	$\pi^*(C1-C2)$	0.42259	27.22	0.32	0.085
$\pi(C14-N15)$	1.69674	$\pi^*(C10-C11)$	0.31921	26.17	0.32	0.081
$\pi(C3-C4)$	1.65658	$\pi^*(C5-N6)$	0.37754	26.13	0.27	0.076
$\pi(C12-C13)$	1.63552	$\pi^*(C14-N15)$	0.39725	24.65	0.28	0.075
$\pi(C1-C2)$	1.55690	$\pi^*(C3-C4)$	0.32855	22.56	0.27	0.072
$\pi(C1-C2)$	1.55690	$\pi^*(C19-C20)$	0.35069	22.27	0.24	0.067
LP(2) S31	1.77785	$\pi^*(C24-C25)$	0.21458	22.17	0.26	0.067
LP(2) S32	1.77785	$\pi^*(C24-C25)$	0.21458	22.17	0.26	0.067
LP(2) S33	1.75038	$\pi^*(C21-C23)$	0.38475	22.00	0.24	0.067
LP(2) S34	1.75038	$\pi^*(C21-C23)$	0.38475	22.00	0.24	0.067
$\pi(C10-C11)$	1.63494	$\pi^*(C12-C13)$	0.36158	21.99	0.28	0.070
LP(2) S29	1.80130	$\pi^*(C21-C23)$	0.38475	21.68	0.23	0.066

LP(2) S30	1.80130	$\pi^*(C21-C23)$	0.38475	21.68	0.23	0.066
LP(2) S31	1.77785	$\pi^*(C22-C26)$	0.41752	20.82	0.24	0.066
LP(2) S32	1.55690	$\pi^*(C22-C26)$	0.41752	20.82	0.24	0.066
$\pi(C1-C2)$	1.55690	$\pi^*(C14-N15)$	0.39725	20.60	0.27	0.067
LP(2) S33	1.75038	$\pi^*(C19-C20)$	0.35069	18.41	0.28	0.066
LP(2) S29	1.80130	$\pi^*(C22-C26)$	0.35069	18.31	0.24	0.063
$\pi(C12-C13)$	1.63552	$\pi^*(C10-C11)$	0.31921	17.82	0.28	0.064
$\pi(C1-C2)$	1.55690	$\pi^*(C5-N6)$	0.37754	17.75	0.26	0.062

Table.9: Second order perturbation theory analysis of Fock matrix on NBO of compound 2

Donor(i)	ED/e	Acceptor(j)	ED/e	E(2) Kcal/mol	E(j)-E(i) a.u	F(i,j) a.u
$\pi(C10-N15)$	1.70363	$\pi^*(C13-C14)$	0.42287	27.16	0.32	0.085
$\pi(C1-N6)$	1.69685	$\pi^*(C4-C5)$	0.31988	26.16	0.32	0.081
$\pi(C11-C12)$	1.65694	$\pi^*(C10-N15)$	0.37798	26.12	0.27	0.076
$\pi(C2-C3)$	1.63513	$\pi^*(C1-N6)$	0.39770	24.64	0.28	0.075
$\pi(C13-C14)$	1.55654	$\pi^*(C11-C12)$	0.32870	22.55	0.27	0.072
$\pi(C13-C14)$	1.55654	$\pi^*(C19-C20)$	0.35229	22.24	0.24	0.067
$\pi(C4-C5)$	1.63537	$\pi^*(C2-C3)$	0.36172	21.96	0.28	0.070
LP(2) S31	1.74975	$\pi^*(C21-C23)$	0.38500	21.91	0.24	0.067
LP(2) S29	1.79135	$\pi^*(C22-C26)$	0.41598	21.53	0.23	0.067
$\pi(C13-C14)$	1.55654	$\pi^*(C1-N6)$	0.39770	20.64	0.27	0.067
LP(2) S32	1.74975	$\pi^*(C19-C20)$	0.35229	18.50	0.28	0.066
$\pi(C2-C3)$	1.63513	$\pi^*(C4-C5)$	0.31988	17.86	0.28	0.064
$\pi(C11-C12)$	1.65694	$\pi^*(C13-C14)$	0.42287	17.51	0.29	0.064
$\pi(C4-C5)$	1.63537	$\pi^*(C1-N6)$	0.39770	16.08	0.28	0.060
$\pi(C1-N6)$	1.69685	$\pi^*(C2-C3)$	0.36172	12.57	0.32	0.057
LP(1) N6	1.91890	$\sigma^*(C1-C2)$	0.03865	11.92	0.87	0.092
LP(1) N15	1.91890	$\sigma^*(C13-C14)$	0.03865	11.92	0.87	0.092
$\pi(C19-C20)$	1.84851	$\pi^*(C2-C3)$	0.36172	11.00	0.33	0.057
$\pi(C1-N6)$	1.69685	$\pi^*(C13-C14)$	0.42287	10.12	0.32	0.052
LP(1) N6	1.91890	$\sigma^*(C4-C5)$	0.02577	9.66	0.90	0.084

Table.10: Second order perturbation theory analysis of Fock matrix on NBO of compound 3

Donor(i)	ED/e	Acceptor(j)	ED/e	E(2) Kcal/mol	E(j)-E(i) a.u	F(i,j) a.u
$\pi(C10-N15)$	1.70320	$\pi^*(C13-C14)$	0.42225	27.21	0.32	0.085
$\pi(C1-N6)$	1.69642	$\pi^*(C4-C5)$	0.31928	26.19	0.32	0.081
$\pi(C11-C12)$	1.65666	$\pi^*(C10-N15)$	0.37712	26.13	0.27	0.076
$\pi(C2-C3)$	1.63540	$\pi^*(C1-N6)$	0.39750	24.67	0.28	0.075
$\pi(C13-C14)$	1.55725	$\pi^*(C11-C12)$	0.32827	22.55	0.27	0.072
$\pi(C13-C14)$	1.55725	$\pi^*(C19-C20)$	0.34935	22.21	0.24	0.067
$\pi(C4-C5)$	1.63460	$\pi^*(C2-C3)$	0.36154	22.01	0.28	0.070
LP(2) S31	1.74885	$\pi^*(C21-C23)$	0.38033	21.79	0.24	0.067
LP(2) S32	1.74885	$\pi^*(C21-C23)$	0.38033	21.79	0.24	0.067
LP(2) S27	1.79859	$\pi^*(C21-C23)$	0.38033	20.84	0.23	0.065
LP(2) S28	1.79859	$\pi^*(C21-C23)$	0.38033	20.84	0.23	0.065
$\pi(C13-C14)$	1.55725	$\pi^*(C1-N6)$	0.39750	20.61	0.27	0.067
LP(2) S29	1.77996	$\pi^*(C24-C25)$	0.31190	19.26	0.25	0.063
LP(2) S30	1.77996	$\pi^*(C24-C25)$	0.31190	19.26	0.25	0.063
LP(2) S31	1.74885	$\pi^*(C19-C20)$	0.34935	18.34	0.28	0.065
LP(2) S32	1.74885	$\pi^*(C19-C20)$	0.34935	18.34	0.28	0.065

$\pi(\text{C13-C14})$	1.55654	$\pi^*(\text{C4-C5})$	0.31928	17.81	0.28	0.064
$\pi(\text{C13-C14})$	1.55654	$\pi^*(\text{C10-N15})$	0.37712	17.72	0.26	0.061
$\pi(\text{C11-C12})$	1.65666	$\pi^*(\text{C13-C14})$	0.42225	17.52	0.29	0.064
$\pi(\text{C2-C3})$	1.63540	$\pi^*(\text{C19-C20})$	0.34935	16.94	0.26	0.059

Table.11: Second order perturbation theory analysis of Fock matrix on NBO of compound 4

Donor(i)	ED/e	Acceptor(j)	ED/e	E(2) Kcal/mol	E(j)-E(i) a.u	F(i,j) a.u
LP(2) O33	1.86696	$\pi^*(\text{C24-C25})$	0.35091	27.62	0.33	0.090
LP(2) O34	1.86696	$\pi^*(\text{C24-C25})$	0.35091	27.62	0.33	0.090
$\pi(\text{C1-N6})$	1.69649	$\pi^*(\text{C4-C5})$	0.31948	26.19	0.32	0.081
$\pi(\text{C14-N15})$	1.69649	$\pi^*(\text{C10-C11})$	0.31948	26.19	0.32	0.081
$\pi(\text{C2-C3})$	1.63530	$\pi^*(\text{C1-N6})$	0.39766	24.67	0.28	0.075
$\pi(\text{C12-C13})$	1.63530	$\pi^*(\text{C14-N15})$	0.39766	24.67	0.28	0.075
LP(2) S31	1.75021	$\pi^*(\text{C21-C23})$	0.38546	22.01	0.24	0.067
LP(2) S32	1.75021	$\pi^*(\text{C21-C23})$	0.38546	22.01	0.24	0.067
$\pi(\text{C4-C5})$	1.63473	$\pi^*(\text{C2-C3})$	0.36171	22.00	0.28	0.070
$\pi(\text{C10-C11})$	1.63473	$\pi^*(\text{C12-C13})$	0.36171	22.00	0.28	0.070
LP(2) S27	1.80007	$\pi^*(\text{C21-C23})$	0.38546	21.75	0.23	0.067
LP(2) S28	1.80007	$\pi^*(\text{C21-C23})$	0.38546	21.75	0.23	0.067
LP(2) S29	1.80795	$\pi^*(\text{C22-C26})$	0.41778	20.33	0.23	0.065
LP(2) S30	1.80795	$\pi^*(\text{C22-C26})$	0.41778	20.33	0.23	0.065
LP(2) S29	1.80795	$\pi^*(\text{C24-C25})$	0.35091	19.39	0.26	0.066
LP(2) S30	1.80795	$\pi^*(\text{C24-C25})$	0.35091	19.39	0.26	0.066
LP(2) S27	1.80007	$\pi^*(\text{C22-C26})$	0.41778	18.44	0.24	0.063
LP(2) S28	1.80007	$\pi^*(\text{C22-C26})$	0.41778	18.44	0.24	0.063
LP(2) S31	1.75021	$\pi^*(\text{C19-C20})$	0.35079	18.42	0.28	0.066
LP(2) O33	1.86696	$\pi^*(\text{C24-C25})$	0.35091	27.62	0.33	0.090

The intra molecular interaction for the title compounds is formed by the orbital overlap between: $\pi(\text{C5-N6})$ and $\pi^*(\text{C1-C2})$ for compound **1**, $\pi(\text{C10-N15})$ and $\pi^*(\text{C13-C14})$ for compound **2**, $\pi(\text{C10-N15})$ and $\pi^*(\text{C13-C14})$ for compound **3** and $\pi(\text{C1-N6})$ and $\pi^*(\text{C4-C5})$ for compound **4** respectively, which result into intermolecular charge transfer (ICT) causing stabilization of the system. The intra molecular hyper conjugative interactions of $\pi(\text{C5-N6})$ to $\pi^*(\text{C1-C2})$ for compound **1**, $\pi(\text{C10-N15})$ to $\pi^*(\text{C13-C14})$ for compound **2**, $\pi(\text{C10-N15})$ to $\pi^*(\text{C13-C14})$ for compound **3** and $\pi(\text{C1-N6})$ to $\pi^*(\text{C4-C5})$ for compound **4** lead to highest stabilization of 27.22, 27.16, 27.21 and 26.19 kJ mol⁻¹ respectively. In case of LP(2) S31orbital to the $\pi^*(\text{C24-C25})$ for compound **1**, LP(2) S31 orbital to $\pi^*(\text{C21-C23})$ for compound **2**, LP(2) S31orbital to $\pi^*(\text{C21-C23})$ for compound **3**, LP(2) O33 orbital to $\pi^*(\text{C24-C25})$ for compound **4** respectively, show the stabilization energy of 22.17, 21.91, 21.79 and 27.62 kJ mol⁻¹ respectively.

3.7. Nonlinear Optical Properties (NLO)

The first hyperpolarizabilities (β_{total}) of this novel molecular system, and related properties (β , α_0 and α) of diazafluorene-functionalized TTFs molecules were

calculated using B3LYP/6-31G(d,p) basis set, based on the finite-field approach. In the presence of an applied electric field, the energy of a system is a function of the electric field. Polarizabilities and hyperpolarizabilities characterize the response of a system in an applied electric field [23]. They determine not only the strength of molecular interactions (long-range inter induction, dispersion force, etc.) as well as the cross sections of different scattering and collision process and also the nonlinear optical properties (NLO) of the system [23, 24]. First hyperpolarizability is a third rank tensor that can be described by $3 \times 3 \times 3$ matrix. The 27 components of the 3D matrix can be reduced to μ_0 components due to the Kleinman symmetry [24]. The components of first hyperpolarizability (β_{total}) are defined as the coefficients in the Taylor series expansion of the energy in the external electric field. When the external electric field is weak and homogeneous, this expansion becomes:

$$E = E^0 - \mu_i F_i - 1/2\alpha_{ij} F_i F_j - 1/6\beta_{ijk} F_i F_j F_k + \dots$$

Where E^0 is the energy of the unperturbed molecules, F_α the field at the origin μ_α , $\alpha_{\alpha\beta}$ and $\beta_{\alpha\beta\gamma}$ are the components of dipole moments, polarizability and the first hyperpolarizabilities, respectively. The total static dipole

moments μ , the mean polarizabilities α_0 , the anisotropy of the polarizabilities $\Delta\alpha$ and the mean first hyperpolarizabilities β_{total} , using the x, y and z components they are defined as: [25, 26].

The total static dipole moment is

$$\mu_{\text{tot}} = [\mu_x^2 + \mu_y^2 + \mu_z^2]^{1/2}$$

The isotropic polarizability is

$$\alpha = (\alpha_{xx} + \alpha_{yy} + \alpha_{zz})/3$$

The polarizability anisotropy invariant is

$$\Delta\alpha = 2^{-1/2} [(\alpha_{xx} - \alpha_{yy})^2 + (\alpha_{yy} - \alpha_{zz})^2 + (\alpha_{zz} - \alpha_{xx})^2 + 6\alpha_{xy}^2 + 6\alpha_{yz}^2 + 6\alpha_{xz}^2]^{1/2}$$

and the average hyperpolarizability is

$$\beta_{\text{tot}} = (\beta_x^2 + \beta_y^2 + \beta_z^2)^{1/2}$$

and

$$\beta_x = \beta_{xxx} + \beta_{xyz} + \beta_{xzz}$$

$$\beta_y = \beta_{yyy} + \beta_{xyy} + \beta_{yzz}$$

$$\beta_z = \beta_{zzz} + \beta_{xxz} + \beta_{yyz}$$

The total molecular dipole moment (μ), mean polarizability (α_0) and anisotropy polarizability ($\Delta\alpha$) and first hyperpolarizability (β_{total}) of diazafluorene-functionalized TTFs 1-4 are computed and are depicted in Table 12.

Table.12: The dipole moments μ (D), polarizability α , the average polarizability α (esu), the anisotropy of the polarizability $\Delta\alpha$ (esu), and the first hyperpolarizability β (esu) of diazafluorene-functionalized TTFs 1-4 calculated by B3LYP/6-31G(d,p) method

Parameters	Compound 1	Compound 2	Compound 3	Compound 4
β_{xxx}	677.1939	-830.9894	-432.3042	1135.9456
β_{yyy}	0.0000	0.0006	0.0563	0.0015
β_{zzz}	0.0000	0.0013	22.0873	0.0097
β_{xyy}	-63.1921	62.7291	35.8198	-99.9727
β_{xxy}	-0.0001	-0.0045	0.1253	-0.0073
β_{xxz}	0.0026	0.0070	67.5898	0.0369
β_{xzz}	-4.4989	-8.8737	-61.1122	41.3088
β_{yzz}	0.0000	0.0000	-0.0078	0.0011
β_{yyz}	0.0004	0.0017	34.0753	0.0013
β_{xyz}	-0.0010	-0.0110	-0.0041	6.3277
$\beta_{\text{tot}}(\text{esu}) \times 10^{-33}$	672.694	839.8741	138.0195	1138.5821
μ_x	7.2251	-8.5208	-5.0318	8.5982
μ_y	0.0000	0.0000	0.0033	0.0000
μ_z	0.0000	0.0001	2.0817	0.0002
$\mu_{\text{tot}}(\text{D})$	7.2251	8.5208	5.4454	8.5982
α_{xx}	-186.9905	-195.8329	-274.7100	-198.0445
α_{yy}	-168.9288	-181.5590	-200.1455	-196.1587
α_{zz}	-196.7445	-209.0996	-228.7712	-217.0407
α_{xy}	0.0000	-0.0006	-0.0205	0.0019
α_{xz}	0.0006	-0.0028	-21.2170	0.0068
α_{yz}	0.0000	-0.0017	-0.0011	0.5477
$\alpha(\text{esu}) \times 10^{-24}$	25.2388	23.8561	74.8018	20.0058
$\Delta\alpha(\text{esu}) \times 10^{-24}$	3.7403	3.5354	11.0856	2.9648

Since the values of the polarizabilities ($\Delta\alpha$) and the hyperpolarizabilities (β_{tot}) of the GAUSSIAN 09 output are obtained in atomic units (a.u.), the calculated values have been converted into electrostatic units (e.s.u.) (for α ; 1 a.u. = 0.1482 x 10⁻²⁴ e.s.u., for β ; 1 a.u. = 8.6393 x 10⁻³³ e.s.u.). The calculated values of dipole moment (μ) for the title compounds were found to be 7.2251, 8.5208, 5.4454 and 8.5982 D respectively, which are approximately eight times than to the value for urea ($\mu=1.3732$ D). Urea is one of the prototypical molecules used in the study of the

NLO properties of molecular systems. Therefore, it has been used frequently as a threshold value for comparative purposes. The calculated values of polarizability are 25.2388 x 10⁻²⁴, 23.8561 x 10⁻²⁴, 74.8018 x 10⁻²⁴ and 20.0058 x 10⁻²⁴ esu respectively; the values of anisotropy of the polarizability are 3.7403, 3.5354, 11.0856 and 2.9648 esu, respectively. The magnitude of the molecular hyperpolarizability (β) is one of important key factors in a NLO system. The DFT/6-31G(d,p) calculated first hyperpolarizability value (β) of diazafluorene-

functionalized TTFs molecules are equal to 672.694×10^{-33} , 839.8741×10^{-33} , 138.0195×10^{-33} and $1138.5821 \times 10^{-33}$ esu. The first hyperpolarizability of title molecules is approximately 1.96, 2.45, 0.40 and 3.32 times than those of urea (β of urea is 343.272×10^{-33} esu obtained by B3LYP/6-311G (d,p) method). This result indicates the non-linearity of the diazafluorene-functionalized TTFs **1-4**.

IV. CONCLUSION

The investigation of the present work is illuminate about computational study of series of diazafluorene-functionalized TTFs molecules by using (DFT/B3LYP) method with 6-31G(d,p) as basis set. The study of global reactivity descriptors confirmed that compound **4** has the smaller frontier orbital gap so; it is more polarizable and has a high chemical reactivity. The MEP map shows that the negative potential sites are on electronegative atoms (nitrogen atoms) while the positive potential sites are around the hydrogen atoms of alkyl and cycled groups. These sites give information about the region from where the compound can undergo non-covalent interactions. NBO analysis revealed that the $\pi(C5-N6) \rightarrow \pi^*(C1-C2)$ interaction gives the strongest stabilization to the system. The predicted nonlinear optical (NLO) properties of the title compound are much greater than those of urea.

ACKNOWLEDGMENTS

This work was generously supported by the (General Directorate for Scientific Research and Technological Development, DGRS-DT) and Algerian Ministry of Scientific Research.

REFERENCES

- [1] M. H. Jamroz (2004). Vibrational Energy Distribution Analysis VEDA 4.0 Program, Warsaw.
- [2] D. C. Young (2001). Computational Chemistry: A Practical Guide for Applying Techniques to Real-world Problems, Wiley, New York pp. 42–56.
- [3] A. E. Reed, L. A. Curtiss, F. Weinhold (1988). Intermolecular interactions from a natural bond orbital, donor-acceptor viewpoint. Chem. Rev. Vol. 88, pp. 899–926.
- [4] D. Lorcy, N. Bellec, M. Fourmigué, N. Avarvari (2009). Tetrathiafulvalene-based group XV ligands: Synthesis, coordination chemistry and radical cation salts. Coordination Chemistry Reviews Vol. 253, pp. 1398–1438.
- [5] M. J. Frisch, G.W. Trucks, H.B. Schlegel, G.E. Scuseria, M.A. Robb, J.R. Cheeseman, G. Scalmani, V. Barone, B. Mennucci, G.A. Petersson, H. Nakatsuji, M. Caricato, X. Li (2010). Gaussian 09, Revision B.01, Gaussian, Inc., Wallingford CT.
- [6] N. Okulik, A. H. Jubert (2005). Theoretical Analysis of the Reactive Sites of Non-steroidal Anti-inflammatory Drugs. Internet Electron. J. Mol. Des. Vol. 4, pp. 17-30.
- [7] P. Politzer, P. R. Laurence, K. Jayasuriya, J. Mc Kinney (1985). Molecular electrostatic potentials: an effective tool for the elucidation of biochemical phenomena. Environ. Health Perspect. Vol. 61, pp. 191-202.
- [8] E. Scrocco, J. Tomasi, Topics in Current Chemistry, vol.7, Springer, Berlin, (1973).
- [9] P. Politzer, J. S. Murray (2002). The fundamental nature and role of the electrostatic potential in atoms and molecules. Theor. Chem. Acc. Vol. 108, pp. 134-142.
- [10] K. Fukui (1982). Role of Frontier Orbitals in Chemical Reactions. Science Vol. 218, pp. 747-754.
- [11] R.G. Parr, L. Szentpaly, S. Liu (1999). Electrophilicity Index. J. Am. Chem. Soc. Vol. 121, pp. 1922-1924.
- [12] P. Chattaraj, B. Maiti, U (2003). Sarkar. Philicity: A Unified Treatment of Chemical Reactivity and Selectivity. J. Phys. Chem. Vol. A107, pp. 4973-4975.
- [13] R. G. Parr, R. A. Donnelly, M. Levy, W. E. Palke (1978). Electronegativity: The density functional viewpoint. J. Chem. Phys. Vol. 68, pp. 3801-3807.
- [14] R. G. Parr, R. G. Pearson (1983). Absolute hardness: companion parameter to absolute electronegativity. J. Am. Chem. Soc. Vol. 105, pp. 7512-7516.
- [15] P. K. Chattaraj, H. Lee, R. G. Parr (1991). HSAB principle. J. Am. Chem. Soc. Vol. 113, 1855-1856.
- [16] R. G. Pearson (1963). Hard and Soft acids and bases, J. Am. Chem. Soc. Vol. 85, 3533-3539.
- [17] P. K. Chattaraj, P. V. R. Scheleye (1994) r. An ab initio study resulting in a greater understanding of the HSAB principle. J. Am. Chem. Soc. Vol. 116, pp. 1067-1071.
- [18] R. G. Parr, W. Yang (1989). Density Functional Theory of Atoms and Molecules, Oxford University Press, New York.
- [19] http://www.en.wikipedia.org/wiki/Natural_bond_orbital.
- [20] M. Szafran, A. Komasa, E. B. Admska (2007). Crystal and molecular structure of 4-carboxypiperidinium chloride (4-piperidinecarboxylic acid hydrochloride). J. Mol. Struct. Theochem. Vol. 827, pp. 101-107.
- [21] C. James, A. Amal Raj, R. Reghunathan, I. Hubert Joe, V. S. Jayakumar (2006). Structural conformation and vibrational spectroscopic studies of 2, 6-bis (p-N,N-dimethyl benzylidene)

- cyclohexanone using density functional theory. *J. Raman Spectrosc.* Vol. 37, pp. 1381-1392.
- [22] J. N. Liu, Z. R. Chen, S. F. Yuan, J. Zhejiang (2005). Study on the prediction of visible absorption maxima of azobenzene compounds. *Univ. Sci.* Vol. B6, pp. 584-589.
- [23] Y. Sun, X. Chen, L. Sun, X. Guo, W. Lu (2003). Nano ring structure and optical properties of Ga₈As₈. *J. Chem. Phys. Lett.* Vol. 381, pp. 397-403.
- [24] O. Christiansen, J. Gauss, J. F. Stanton (1999). Frequency-dependent polarizabilities and first hyperpolarizabilities of CO and H₂O from coupled cluster calculations. *J. Chem. Phys. Lett.* 305, pp. 147-155.
- [25] A. Kleinman (1962). Nonlinear Dielectric Polarization in Optical Media. *J. Phys. Rev.* Vol. 126, pp. 1977-1979.
- [26] V. P. Gupta, A. Sharma, V. Viridi (2006). Structural and spectroscopic studies on some chloropyrimidine derivatives by experimental and quantum chemical methods. *J. Ram, Spectrochim. Acta Part A* Vol. 64, pp. 57-67.

Is the EM-Drive a Closed System?

Carmine Cataldo

Independent Researcher, PhD in Mechanical Engineering, Battipaglia (SA), Italy
Email: catcataldo@hotmail.it

Abstract—Since its disclosure, the so-called EM-Drive, an apparently reactionless electromagnetic thruster conceived by Roger Shawyer, has simultaneously caused wide scepticism, related to the physical principles that may allow its functioning, and understandable enthusiasm, by virtue of the astonishing scenarios potentially offered by such a device. On the one hand, thrust without exhaust is de facto impossible, unless we deny the Law of Action-Reaction, whose evident violation would result in acknowledging the concrete need for a new Physics; on the other hand, it would appear that opportunely shaped resonant cavities, when fuelled with microwaves, deliver a certain thrust, apparently without a detectable exhaust. In this paper, instead of discussing the validity of the various tests to date independently carried out, speculating about misleading side-effects or inadequate instrumental precision, we simply suppose that the thrust may be an actual phenomenon. Therefore, we try to provide a qualitative explanation to the functioning of the alleged reactionless device, by resorting to a theory elsewhere proposed and herein briefly discussed.

Keywords—EM-Drive, Closed System, Resonant Cavity Thruster, Hidden Coordinate, Reflectors Temperature.

I. INTRODUCTION

Very qualitatively, the EM-Drive is nothing but a resonant cavity fuelled by microwaves, basically consisting of a hollow conical frustum and a magnetron. According to Shawyer [1], the principle of operation of his revolutionary contraption is essentially based on the radiation pressure: in a few words, the alleged thrust would arise from the difference between the forces exerted upon the reflectors (the bases of the frustum). In spite of the fact that such a device, as long as it is considered as being a closed system, explicitly violates the conservation of momentum and Newton's well-known third law, it would appear, according to several tests to date carried out, that the EM-Drive can concretely deliver a certain thrust without a detectable exhaust [2]. As implicitly suggested in the foregoing sentence, the easiest way to solve the paradox may consist in demonstrating, first and foremost, that the device in question cannot be properly regarded as a closed system.

For the sake of clarity, we reveal in advance that the detectability of the exhaust [3], a term that actually will turn out not to be entirely suitable for the hypothesized scenario, is not herein addressed.

II. THE CONSERVATION OF ENERGY

We hypothesize a closed Universe, globally flat, characterized by four spatial dimensions, belonging to the so-called oscillatory class [4] [5] (“O Type” in Harrison’s classification) [6]. Time is postulated as being absolute [7]. The Universe is modelled as a 4-Ball whose radius is herein denoted by R . On the contrary, the Universe we are allowed to perceive is identified with a hypersphere whose radius of curvature, herein denoted by z (with z not null and not greater than R), depends on the state of motion. Net of the symmetry [8], what we perceive as being a material point may actually be a material straight-line segment, whose (four-dimensional) mass is herein denoted by M , bordered by the centre of the Universe and the point itself. If a material point is at rest, the radial extension of the corresponding material segment is equal to the radius of the Universe. If a point starts moving with a constant tangential speed, denoted by v , the radial extension of the corresponding material segment undergoes a reduction. Similarly, the mass (of the segment) in motion, herein denoted by M_z , is less than the one at rest, even though the linear density remains the same. Denoting with c , as usual, the speed of light, the conservation of energy (for a free particle-segment) can be written as follows [9]:

$$E = Mc^2 = E' + E'' + E''' \quad (1)$$

Let’s now make explicit the three energetic components:

$$E' = M_z v^2 \quad (2)$$

$$E'' = \left(\frac{z}{R}\right)^2 M_z c^2 \quad (3)$$

$$E''' = (M - M_z)c^2 = \left(\frac{M}{M_z} - 1\right) M_z c^2 \quad (4)$$

For the reduced mass, since the linear density is considered as being constant, we banally have:

$$M_z = \frac{z}{R} M \quad (5)$$

By virtue of (2), (3) and (4), taking into account (5), we can evidently write (1) as follows:

$$Mc^2 = M_z v^2 + \left(\frac{z}{R}\right)^2 M_z c^2 + \left(\frac{R}{z} - 1\right) M_z c^2 \quad (6)$$

From the previous equation we immediately deduce the underlying identity:

$$M_z c^2 = M_z v^2 + \left(\frac{z}{R}\right)^2 M_z c^2 \quad (7)$$

If we introduce the Lorentz factor [10] [11], we have:

$$\gamma = \frac{1}{\sqrt{1 - \left(\frac{v}{c}\right)^2}} \quad (8)$$

$$\left(\frac{v}{c}\right)^2 = \beta^2 = 1 - \frac{1}{\gamma^2} \quad (9)$$

From (7), exploiting the definition of the Lorentz factor, we immediately obtain:

$$z = R \sqrt{1 - \left(\frac{v}{c}\right)^2} = \frac{R}{\gamma} \quad (10)$$

Taking into account (5), the linear density can be defined as follows:

$$\bar{M} = \frac{M}{R} = \frac{M_z}{z} \quad (11)$$

As for the specific energies (the energies per unit of length), we consequently have:

$$\bar{E} = \bar{E}' + \bar{E}'' + \bar{E}''' = \frac{Mc^2}{z} = \frac{\bar{M}}{R} c^2 = \frac{\bar{M}c^2}{\sqrt{1 - \left(\frac{v}{c}\right)^2}} = \gamma \bar{M}c^2 \quad (12)$$

$$\bar{E}' = \frac{M_z}{z} v^2 = \bar{M} \beta^2 c^2 = \left(1 - \frac{1}{\gamma^2}\right) \bar{M}c^2 \quad (13)$$

$$\bar{E}'' = \left(\frac{z}{R}\right)^2 \frac{M_z}{z} c^2 = \frac{\bar{M}c^2}{\gamma^2} \quad (14)$$

$$\bar{E}''' = \left(\frac{R}{z} - 1\right) \frac{M_z}{z} c^2 = (\gamma - 1) \bar{M}c^2 \quad (15)$$

By virtue of (13), (14) and (15), taking into account (12), we immediately obtain:

$$\gamma \bar{M}c^2 = \left(1 - \frac{1}{\gamma^2}\right) \bar{M}c^2 + \frac{\bar{M}c^2}{\gamma^2} + (\gamma - 1) \bar{M}c^2 \quad (16)$$

Denoting with E_0 the energy at rest, we can banally write:

$$\bar{E}_0 = \frac{Mc^2}{R} = \bar{M}c^2 \quad (17)$$

$$\bar{E} = \gamma \bar{M}c^2 = \bar{E}_0 + (\gamma - 1) \bar{M}c^2 \quad (18)$$

By dividing both members of (7) by z , making explicit the Lorentz factor, we immediately obtain:

$$\bar{M}c^2 = \bar{M}v^2 + \frac{\bar{M}c^2}{\gamma^2} \quad (19)$$

By multiplying both members of the foregoing equation by the Lorentz factor, we have:

$$\gamma \bar{M}c^2 = \gamma \bar{M}v^2 + \frac{\bar{M}c^2}{\gamma} \quad (20)$$

$$\bar{E} = \frac{\bar{M}c^2}{\sqrt{1 - \left(\frac{v}{c}\right)^2}} = \frac{\bar{M}v^2}{\sqrt{1 - \left(\frac{v}{c}\right)^2}} + \sqrt{1 - \left(\frac{v}{c}\right)^2} \bar{M}c^2 \quad (21)$$

The concept of dimensional thickness has been elsewhere expounded [9]. Very briefly, the three-dimensional curved space we are allowed to perceive may be characterized by a thickness, denoted by Δz_{min} , that may represent nothing but the “quantum of space”. Consequently, the mass we perceive, denoted by m , may be provided by the underlying banal relation:

$$m = \bar{M} \Delta z_{min} \quad (22)$$

As for the energy we perceive, with obvious meaning of the notation, we can write:

$$E_m = \bar{E} \Delta z_{min} = (\bar{E}' + \bar{E}'' + \bar{E}''') \Delta z_{min} \quad (23)$$

$$E_m = E'_m + E''_m + E'''_m \quad (24)$$

By multiplying both members of (16) by Δz_{min} , we have:

$$E_m = \gamma mc^2 = \left(1 - \frac{1}{\gamma^2}\right) mc^2 + \frac{mc^2}{\gamma^2} + (\gamma - 1) mc^2 \quad (25)$$

By multiplying all the members of (21) by Δz_{min} , we immediately obtain the well-known underlying equation

$$E_m = \frac{mc^2}{\sqrt{1 - \left(\frac{v}{c}\right)^2}} = \frac{mv^2}{\sqrt{1 - \left(\frac{v}{c}\right)^2}} + \sqrt{1 - \left(\frac{v}{c}\right)^2} mc^2 \quad (26)$$

Denoting with p the momentum, with L the (relativistic) Lagrangian, and with H the Hamiltonian, we have:

$$p = \frac{mv}{\sqrt{1 - \left(\frac{v}{c}\right)^2}} \quad (27)$$

$$L = -\sqrt{1 - \left(\frac{v}{c}\right)^2} mc^2 \quad (28)$$

$$E_m = H = pv - L \quad (29)$$

III. REFLECTORS TEMPERATURE

If something can be heated, it is surely characterized by a microstructure. Obviously, this intuitive concept also applies to the *EM-Drive* reflectors. Very approximately, when a solid is heated, its atoms start vibrating faster (around points that can be considered as being fixed). In other terms, as the temperature increases, the average kinetic energy increases (and vice versa). Several thermal analyses of the *EM-Drive* have shown how the bases of the above-mentioned device (when in operation) reach different temperatures [12]. For the sake of simplicity, we ignore how the temperature is distributed (in other terms, two generic points belonging to the same base are regarded as characterized by the same temperature). Consequently, let's denote with T_1 and T_2 the average temperatures reached by the bases (with T_2 greater than T_1).

The scenario is qualitatively depicted in *Figure 1*.

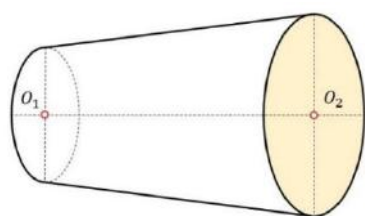


Figure 1. Hollow Conical Frustum

According to the model briefly expounded in the previous paragraph, O_1 and O_2 , the centres of the bases, are not the endpoints of an ideal (the cavity is empty) straight line segment. When the device is completely at rest, O_1 and O_2 can be approximately considered as being the endpoints of an (ideal) arc of circumference whose radius is equal to R . Moreover, bearing in mind the four-dimensional model herein exploited, the above-mentioned points are actually straight line segments whose radial extension, at rest, equates the radius (of curvature) of the Universe.

IV. IS THE EMDRIVE A CLOSED SYSTEM?

At the beginning, when the device is not in operation, the bases are characterized by the same temperature, and the *EM-Drive* can be obviously regarded as a closed system. When the device is in operation, the bases, after a certain time, reach the temperatures T_1 and T_2 . Consequently, we can (statistically) state that the average kinetic energy (and, consequently, the average vibrational speed) of the points belonging to *Surface 1* is less than the average kinetic energy of the points belonging to *Surface 2*. According to the theory we have being resorting to, this means that the radial extension of the material segment that corresponds to O_1 , denoted by z_1 , is greater than the one that corresponds to O_2 , denoted by z_2 .

The scenario is qualitatively depicted in *Figure 2*.

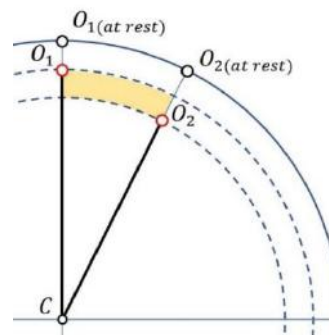


Figure 2. The "Hidden" Exhaust

In other terms, we have:

$$\overline{CO_2} = z_2 < z_1 = \overline{CO_1} \quad (30)$$

Since the electromagnetic radiation can propagate at any level [8] (for any value of z less than or equal to R), photons are allowed to leave the cavity if z is greater than z_2 (and the thrust is so legitimized). On balance, notwithstanding our perception of reality, the *EM-Drive* can be considered as being a closed system only for z less than z_2 .

V. FINAL REMARKS AND CONCLUSIONS

Firstly, it is worth highlighting how the dissertation in its entirety has been carried out by introducing several heavy approximations and intentionally ignoring a great deal of subjects, among which the detectability of the alleged exhaust and a more accurate description of the device stand out. In particular, as far as the principle of operation of the *EM-Drive* is concerned, we have evidently avoided discussing Shawyer's explanation [1] (who, among other things, explicitly resorts to Special Relativity) [13], as well as further interesting theories [14] [15], limiting ourselves to referring to the contents of the official *EM-Drive* page. However, as implicitly suggested by the title, the aim of this paper fundamentally lies in providing an alternative explanation, expounded as qualitatively and understandably as possible, to the alleged functioning of the device. According to our theory, if a material point (actually a material segment) is provided with a certain kinetic energy, its radial coordinate (the radial extension of the material segment) is different from R : on this subject, we underline that if z^* is the value taken by the radial (de facto hidden) coordinate, there is no mass for z greater than z^* . Consequently, radiation (but not mass) can, as it were, pass through the point (the segment). The third addend in the second member of (1), that represents the energy needed to produce the motion (in this specific case vibrational), is clearly related to the non-material component of the particle. In this regard, although the

wave-particle duality is not herein addressed, we would like to simply highlight how the above-mentioned energetic component is somehow connected to the well-known concept of quantum potential [16] [17] [18]. Ultimately, returning to the title of this paper, the answer is: the *EM-Drive* can be simultaneously a closed and an open system. More precisely, the device is completely closed when it is concretely at rest (actually, this is an ideal condition), and partially closed when it is in operation. Moreover, the opening of the (hidden) exhaust basically depends on the difference between the reflectors temperatures.

REFERENCES

- [1] Shawyer, R. (2006). A Theory of Microwave Propulsion for Spacecraft. (Theory Paper, V 9.4). [Online exclusive]. Retrieved from: <http://www.emdrive.com/theorypaper9-4.pdf>
- [2] White, H., March, P., Lawrence, J., Vera, J., Sylvester, A., Brady, D., Bailey, P. (2017). Measurement of Impulsive Thrust from a Closed Radio-Frequency Cavity in Vacuum. *Journal of Propulsion and Power* 33 (4), 830-841. <https://doi.org/10.2514/1.B36120>
- [3] Grahn, P., Annala, A., Kolehmainen, E. (2016). On the exhaust of electromagnetic drive. *AIP Advances* 6, 065205. <http://dx.doi.org/10.1063/1.4953807>
- [4] Cataldo, C. (2017). From General Relativity to A Simple-Harmonically Oscillating Universe, and Vice-Versa: a Review. *Applied Physics. Research*, 9(1), 86-92. <http://dx.doi.org/10.5539/apr.v9n1p86>
- [5] Cataldo, C. (2017). A short discussion on the Gravitational Redshift in the light of an alleged local variability of the Planck Constant. *Journal of Applied Mathematics and Physics*, 5, 1001-1008. <https://doi.org/10.4236/jamp.2017.55087>
- [6] Harrison, E.R. (1967). Classification of Uniform Cosmological Models. *Monthly Notices of the Royal Astronomical Society*, 137, 69-79. <https://doi.org/10.1093/mnras/137.1.69>
- [7] Cataldo, C. (2017). Gravity and the Absoluteness of Time: a simple qualitative model. *App. Phys. Res.*, 9(2), 42-52. <http://dx.doi.org/10.5539/apr.v9n2p46>
- [8] Cataldo, C. (2016). Faster than Light: again on the Lorentz Transformations. *Applied Physics Research*, 8(6), 17-24. <http://dx.doi.org/10.5539/apr.v8n6p17>
- [9] Cataldo, C. (2017). From the Oscillating Universe to Relativistic Energy: a Review. *Journal of High Energy Physics, Gravitation and Cosmology*, 3, 68-77. <http://dx.doi.org/10.4236/jhepgc.2017.31010>
- [10] Lorentz, H. A. (1904). Electromagnetic Phenomena in a System Moving with Any Velocity Smaller than That of Light. *Proceed. of the Roy. Netherlands Acad. of Arts and Sciences*, 6, 809-831. Retrieved from <http://www.dwc.knaw.nl/DL/publications/PU00014148.pdf>
- [11] Cataldo, C. (2017). The "Light Clocks" Thought Experiment and the "Fake" Lorentz Transformations. *International Journal of Advanced Engineering Research and Science*, 4(9), 10-13. <https://dx.doi.org/10.22161/ijaers.4.9.3>
- [12] Vera, J. (2015, January 4). Thermal analysis of the EmDrive (by Jerry Vera, NASA Eagleworks Lab) [Online exclusive]. Retrieved from: <https://drive.google.com/file/d/0Bx2cC35KJTwsdGY1X2kyRXJOQTA/view>
- [13] Einstein, A. (1916). *Relativity: The Special and General Theory* (translated by R. W. Lawson, 1920). Henry Holt and Company, New York. Retrieved from <https://archive.org/details/cu31924011804774>
- [14] McCulloch, M. E. (2013). Can the flyby anomalies be explained by a modification of inertia? Retrieved from: <https://arxiv.org/abs/0712.3022>
- [15] McCulloch, M. E. (2015). Testing quantised inertia on the EmDrive. *Europhysics Letters* 111, 60005. <https://doi.org/10.1209/0295-5075/111/60005> (Also available on <https://arxiv.org/abs/1604.03449>)
- [16] de Broglie, L. (1970). The reinterpretation of wave mechanics, *Foundations of Physics* 1(1), 5-15. <https://doi.org/10.1007/BF00708650>
- [17] Bohm, D. (1952). A Suggested Interpretation of the Quantum Theory in Terms of "Hidden Variables" I. *Physical Review*. 85: 166–179. <https://doi.org/10.1103/PhysRev.85.166>
- [18] Bohm, D. (1952). A Suggested Interpretation of the Quantum Theory in Terms of "Hidden Variables", II. *Physical Review*. 85: 180–193. <https://doi.org/10.1103/PhysRev.85.180>

3D Seismic Study to Investigate the Structural and Stratigraphy of Mishrif Formation in Kumiya Oil Field, Southern Eastern Iraq

Kamal K. Ali¹, Ghazi H. Alsharaa², Ansam H. Rasheed³

¹Department of Geology, College of Science, University of Baghdad, Iraq.

²Oil Exploration Company, Iraqi Oil Ministry, Baghdad, Iraq.

Abstract— This thesis is a reflection seismic study (structural and stratigraphic) of a (1200) km² area located in the eastern south of Iraq within the administrative border of the province of Maysan province. The study area was interpreted by using 3-D seismic data from Oil Exploration company. The reflector is detected within Mishrif Formation which is deposited during the Cretaceous age. The seismic interpretation of the area approves the presence of some stratigraphic features in the studied Formation. Some distributary mound and flatspot were observed within the study area, but they are not continuous due to the tectonic effects. These activities elements give reasonable explanation for the hydrocarbon distribution in the area of study and explain why in Kt-2 is wildcat. The study of seismic facies of the picked reflectors distinction type of seismic configuration is progressive seismic facies characterized by Mishrif Formation. Using seismic attribute techniques including instantaneous frequency showed low frequency in areas of hydrocarbon accumulations. Instantaneous phase attribute was detected seismic sequence boundaries, sedimentary layer patterns and regions of onlap and top lap patterns. Amplitude attribute showed that low amplitude value which probably the area of hydrocarbon reservoir.

Keywords—Flat spot, Dim spot, Muond, Seismic Attribute.

I. INTRODUCTION

The geophysical research history for a bout hydrocarbon accumulations returns to the beginning of the last century and a seismic reflection exploration applied to detection of that accumulations. (Berg, O., 1982). The seismic method is the most important geophysical technique in terms of expenditures and number of geophysicists involved. The predominance of the seismic method over the geophysical methods is due to various factors, the most important of which are the high accuracy, high resolution and great penetration of which the method is capable. The seismic methods are the most widely used of all geophysical methods used in petroleum

exploration. (Hart, Bruce S., 2004). The role of seismic in the petroleum studies is to provide the most accurate graphic representation of the earth's subsurface and its geological structures, where it gives a seismic section, velocity & time contour maps to determination of a structural traps, as well as, a seismic stratigraphy and seismic facies to determination of an internal stratigraphic geometry interpretation in terms of environmental deposition pale-geography, in addition to sedimentary basin analysis. (Milson, John, 2003). Seismic reflection gives more direct and detailed picture of the subsurface geological structures. It is more suitable in areas where the oil is in structural traps, but it is also useful for locating and detailing certain types of stratigraphic features (AL-Sinawi, 1981). The seismic reflection exploration method passed through numerous development stages from mid last century to a present time included the field survey, data processing & interpretation. With reflection methods one can locate and map such features as anticlines, faults, salt domes, and reefs where many of these are associated with the accumulation of oil and gas. Major convergences caused by depositional thinning can be detected, but the resolution of the method is not as favorable as we would usually like for finding stratigraphic traps (Dobrin, 1976).

II. LOCATION OF STUDY AREA

The study area which represent Kumiya oil field is located at the eastern parts of southern Iraq as part of the administrative border of the province of Maysan, to the East of the Tigris River, near the city of Kumait (Figure 1) (Al-Shuhail and Abdullatif, 2012). Kumiya oil field lies within the Universal Transversal Market (U.T.M) coordinates as given in Table (1)

Table.1: Coordinates of the study area.

Point	Northern	Eastern
A	356000	655000
B	354000	695000
C	3530000	680000
D	3545000	650000

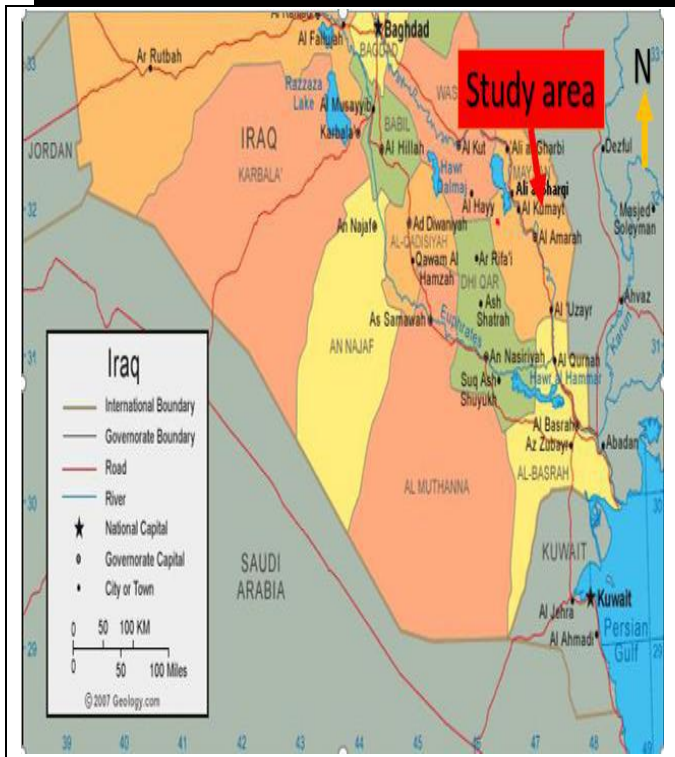


Fig.1: Location of study area (Al-Shuhail and Abdullatif, 2012).

III. PROCESSING

The seismic data were processed at the Processing Center of Oil Exploration Company. The primary objective is to enhance the quality of the 3-D recorded data. Basically, this improvement is essential to facilitate the structural & stratigraphic seismic interpretation.

Noise attenuation process leads to improve reflection continuity and enhance ability to compute seismic attributes. The main steps in processing are: 1-Editing and muting.

2- Gain recovery static correction.

3-Deconvolution of source.

The order in which these steps are applied is variable.

IV. DATA BASE

The data base includes 3D survey which was carried out by the Company De General Geophysics French (CGG-05) and Iraqi seismic party no.2, there are two wells to the area have been drilled in this study, they are Kumiat_1 and Kumiat-2. Marker, check shot and sonic logs information were available for Kumiat_1 and Kumiat-2 wells.

V. REFLECTION DATA PROCESSING

To convert the field recording into a usable seismic section requires a good deal of data manipulation. The purpose of seismic processing is to manipulate the acquired data into an image that can be used to infer the sub-surface structure. Only minimal processing would be required if we had a perfect acquisition system.

Processing consists of the application of a series of computer routines to the acquired data guided by the hand of the processing geophysicist. Processing routines generally fall into one of the following categories:

- 1- enhancing signal at the expense of noise
- 2- Correction CDP gather for normal move out and stack them.
- 3- Correction for effect of near-surface time delays (static correction).
- 4- Filtering processes.
- 5- Providing velocity information
- 6- Increasing resolution
- 7- Collapsing diffractions and placing dipping events in their true subsurface locations (migration).

This processes are achieved using Geoframe system, they include many mathematical processes depend on physical fundamentals. There are three main processes in seismic data processing: deconvolution, stacking and migration. The processing stages are divided into pre-stack and post-stack processing (Yilmaz, 1987).

VI. VELOCITY SURVEY

Figures (2) and (3) show a check-shot of well Kumiat_1 and Kumiat_2.

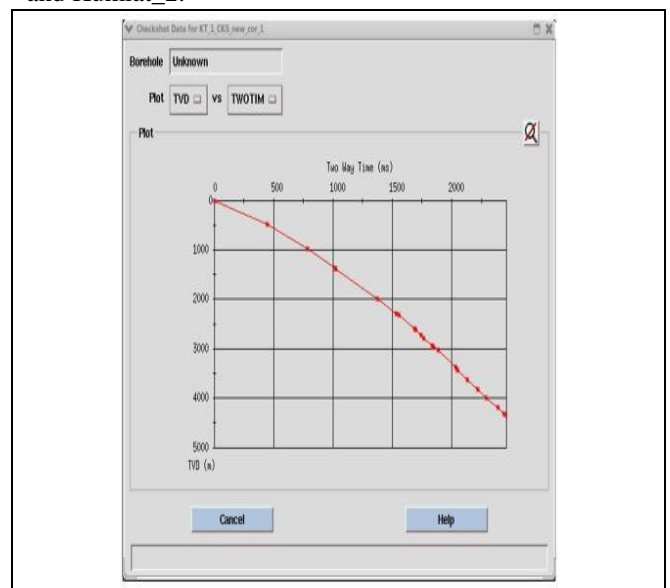


Fig.2: Illustrates the check shot curve for Kt-1 well.

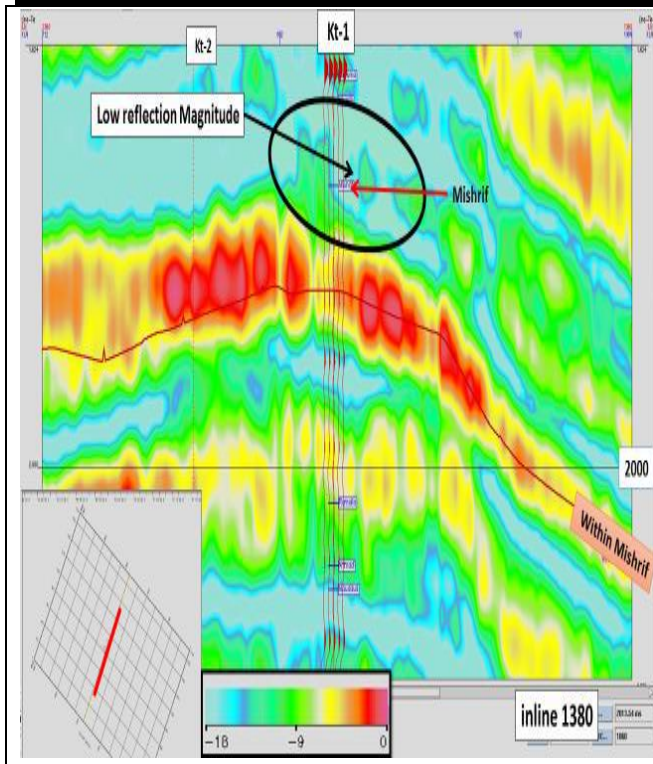


Fig.5: Seismic section display the variation in reflection magnitude of studied reflectors.

Instantaneous Phase Sections

Instantaneous Phase Section refer to a phase display the continuity of seismic event (Taner&Shariff, 1977). It is very important to study the faults, discontinuity of reflectors, angular unconformity, pinchout and onlap. The information of instantaneous phase is very important in showing and distinguishing the ends of continuity of reflective surfaces (khorshid and khadhm, 2015). The downlap in seismic section were noted by the application of Instantaneous Phase Section (Figure 6)

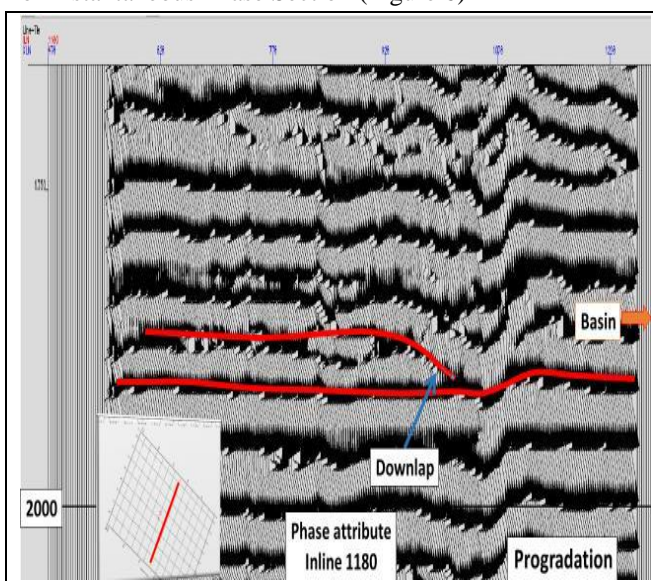


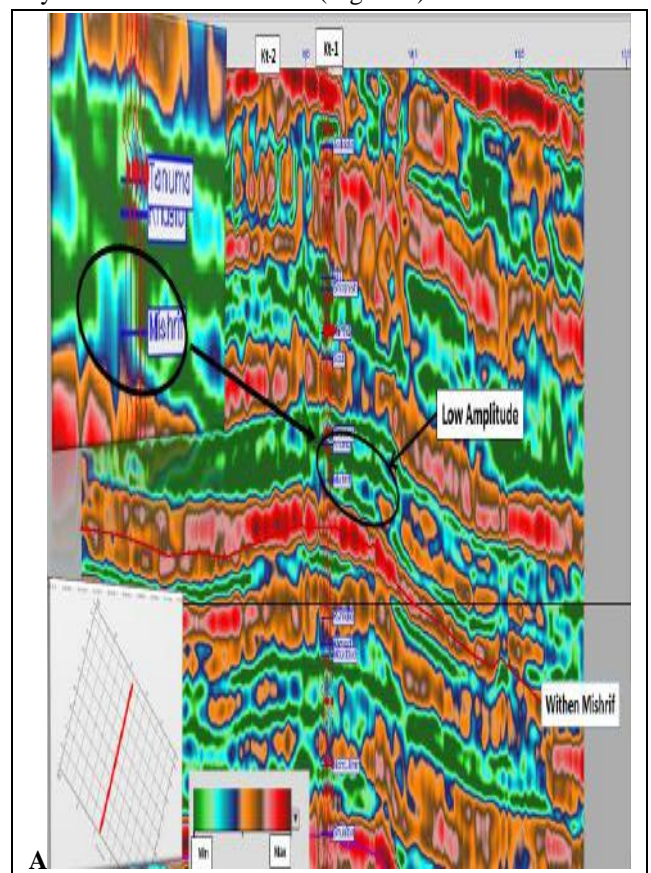
Fig.6: Seismic section display the variation in instantaneous phase of studied reflectors.

Instantaneous Amplitude Sections:

A seismic reflection is strong or weak depending on difference in velocities and densities between the rock layers above the reflection and the one below it , the greater the difference the stronger the reflection (Al-Ridha and Ali, 2015).This attribute which measured in time is primarily used to visualize regional characteristics such as structure, sequence boundaries, thickness and lithology variations. In some cases, bright and dim spots phenomena are related to gas accumulations. Low amplitude values are observed in study area, which are probably area of hydrocarbon reservoirs,(figure7).Region that rounded with KT-1 and KT-2 has decreases of seismic amplitude which indicate to absorption of seismic wave energy due to presence the hydrocarbon accumulation. Also low amplitude value in time slice view in the same area were noted (Mitchum and Vail, 1977). . Low amplitude in KT-1 Within Mishrif is noted which is consider as hydrocarbon accumulation.

Instantaneous Frequency Sections:

The results of the application of attribute assist to determine sites changes Instantaneous frequency and their relationship to changes in petro-physical qualities, is linked frequencies of low-lying areas to zones communities of hydrocarbon (Al-Ridha and Muhsin, 2015) .Low frequency signals were noted within this section which indicates of hydrocarbon accumulation, while high frequency which indicate weak probability of hydrocarbon accumulation (Figure 8) .



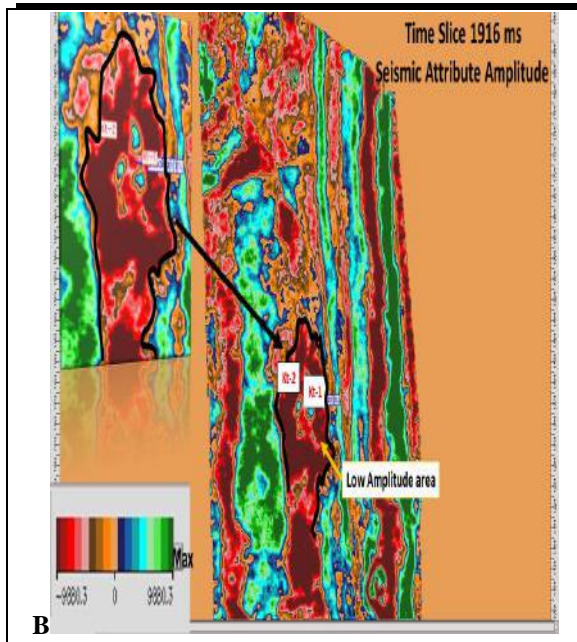


Fig.7: Shows the low amplitude in KT-1

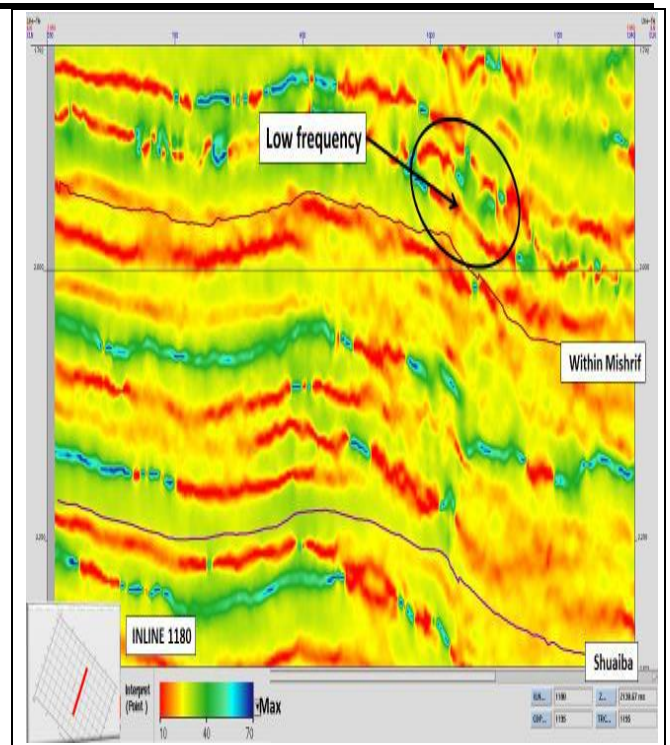


Fig.9: Seismic section for seismic attributes (Instantaneous Frequency)

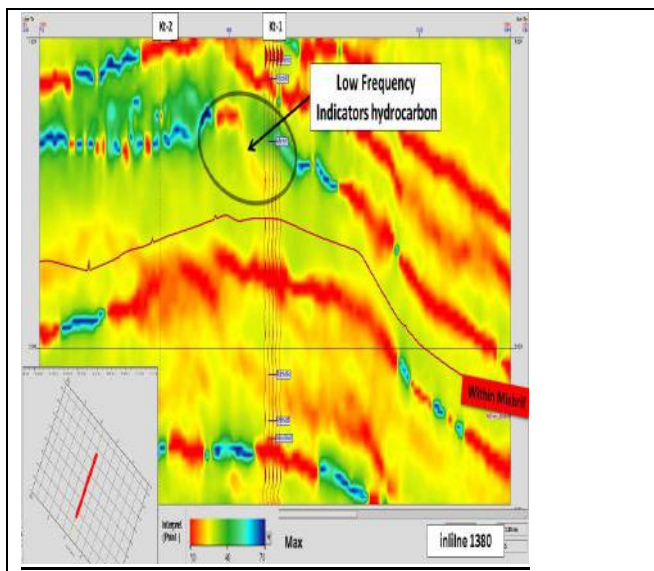


Fig.8: Shows seismic section display the variation in instantaneous frequency of studied reflectors.

It is noted that Frequency decreases in shelf margin (Figure 9) and that is indicator to presence of hydrocarbon accumulation.

X. CONCLUSIONS

1. The reflector which is picked in this study (Within Mishrif) show that Within Mishrif wavelet appeared on synthetic seismogram as peak , with different intensity. This is because they have higher density than the densities of the above and under reflector.
2. The seismic interpretation of the area approves the presence of some stratigraphic features in the studied formations. Some distributary mound and flat spot were observed within the study area, but they are not continuous due to the tectonic effects. These activities elements give reasonable explanation for the hydrocarbon distribution in the area of study and explain why in Kt-2 is wildcat.
3. The study of seismic facies of the picked reflector distinction type of seismic configuration is progressive seismic facies characterized by Mishrif Formation.
4. Using seismic attribute techniques showed stratigraphic feature such as mound and flat spot which indicate hydrocarbon accumulations. Instantaneous Amplitude attribute showed that the low amplitude values are observed in study area, which are probably the area of hydrocarbon reservoir.

REFERENCES

- [1] Alridha N. A. and Muhsin S. U., (2015). Seismic attributes analysis in Balad oil field – center of Iraq, Arabian Journal of Geosciences ISSN 1866-7511, Volume 8 . Number 5 , p2785-2798.

- [2] Al-Ridha N.A. and Ali H. M. , (2015). Study the Image of Wasit Subsurface Structure Using 3D Seismic Data Center of Iraq . Iraqi Journal of Science .V.56 , No.4C , P3513-3523.
- [3] Al-Shuhail, Abdullatif A., 2012.Reflection Seismology. King Fahd University of petroleum and minerals, GEOP 501.
- [4] Al-Sinawi, 1981, Introduction to Applied Geophysics, first ed., 142 p.
- [5] Berg, O.,1982 ,(Seismic Detection and Evaluation of Delta and turbidities sequences :Their Application to exploration for the subtle trap) ,AAPG,Vol,66,No.9,PP.(1271- 1288) .
- [6] Dobrine, M., 1976. Introduction to Geophysical Prospecting, 3rd ed., McGraw Hill. Int. co., International Student Edition 386 p.
- [7] Gadallah,M.,R.,andFisher,R.,2009.(ExplorationGeo physics), Springer-Verlag Berlin Heidelberg.262 p.
- [8] Hart, Bruce S., 2004 , Principle of 2D and 3D seismic interpretation , McGill University.
- [9] Khorshid S. Z. and Kadhm A.D. , 2015. Subsurface Investigation of Oligocene Geologic Formations Age , East Baghdad Oil Field .Iraqi Journal of Science .V.56 , No.4C , P3441-3451.
- [10] Milsom , John, 2003. Field Geophysics, 3rd Ed. University College London, 232 p.
- [11] Mitchum Jr., R. M.P.R. Vail 1977. Seismic Stratigraphy and Global Changes of Sea Level: Part 11. Glossary of Terms used in Seismic Stratigraphy: Section 2. Application of Seismic Reflection Configuration to Stratigraphic Interpretation, Memoir 26 Pages 205 - 212. No.7, p. 854-886.
- [12] Sheriff, R.E., 1980. Seismic Stratigraphy, IHRDC, Boston, 277 p.
- [13] Taner, M.T., Sheriff R.E., 1977. Application of amplitude, frequency and other attributes to stratigraphic and hydrocarbon exploration. AAPG Memoir 26, p.301-327
- [14] Yilmaz,O., 1987. seismic data processing, SEG series: Investigation Geophysics, V.2 526 p.

Hydraulic jump on smooth and uneven bottom

A. Mammadov

Doctor of technical sciences, Baku State University, Baku, Azerbaijan

Abstract— The mechanism of absorption of excess power of the flow within hydraulic jump has been studied in the article based on theoretical manner. Mathematic model of hydraulic jump has been investigated by taking additional water body (mass) in hydraulic jump zone as basic. Theoretical research has shown that main part of excess power is discharge for rotation of additional water mass and a formula has been obtained to make calculation thereof. The article also has provided a formula for calculating the portion of flow energy needed for overcoming friction resistance emerged in bed bottom. Because of conducted studies, formulas have been suggested for calculating hydraulic jump length occurred in flat and uneven beds. Obtained formulas have been mutually analyzed with results found by other researchers.

Keywords— hydraulic jump, variable mass, motion quantity, additional discharge, critical section, jump length.

I. INTRODUCTION

It is obvious that process of absorption of excess flow energy in tailraces of hydro-technical facilities happen by hydraulic jump. One of the main parameters when designing tailraces of hydro-technical facilities is accurate and proper calculation of length of emerged hydraulic jump. Study of energy losses in the jump zone bears great importance when analyzing flow structure. Number of studies have been devoted to the given problem

□ 1,2,3,4,5,6,7,8,9,10,11,14,15,16,17,18,19,20,21,22,23 □.

Results of these studies indicate that intensive turbulent agitation takes place in the area of hydraulic jumping, which causes penetration of large vortex structures in the form of additional discrete liquid masses from the turbulent (stormy) zone into transit (tranquil) one.

An analysis of the existing assignments on this issue suggests that most of them are devoted to a flow with a constant mass.

Currently, several empirical formulas are used in practice to determine the length of hydraulic jump □ 1, 5 □.

a) The formula of N.N.Pavlovsky:

$$l=2,5 (1,9 \square h_2-h_1)$$

b) The formula of M.O. Chertausov:

$$l = 10,3h_1 (\sqrt{Fr} - 1)^{0,81}$$

c) The formula of Safrenech:

$$L = 4,5 \square h_2$$

r) The formula of Bakhmetov-Matchick:

$$L= 5 (h_2-h_1)$$

Great majority of these formulas have been proposed considering analysis of the results of studies conducted in various laboratories globally that carry out hydraulic investigations. Results derived from the calculation formulas sometimes vary from each other up to 50-80%. Proper design of water stilling wells constructed in tailraces of hydro-technical facilities depends on accurate calculation of hydraulic jump length. Studies regarding hydromechanical analysis of energy absorption within hydraulic jump have not been conducted in known formulas. All calculation formulas have been empirically suggested based on the results of laboratory tests performed within a given range.

Theoretical research.

Unlike existing tasks and works, we consider a hydraulic jump in which the motion of a liquid occurs with a variable mass with decreasing number of motions. With a sudden transition of the flow from a turbulent state to a calm one between sections I-I and II-II, a hydraulic jump is generated within which highly complex hydrodynamic process takes place (Fig. 1).

Both connection to the main flow (between sections I-I and K-K) and separation of the additional flow (between sections K-K and II-II) from it happens within the limits of hydraulic jump. In this case, specific water discharge in the range of I-I will be q_0 , it will increase in the range of K-K and become (q_0+q_d) , where q_d is the specific flow rate of the connected flow. Separation of connected discharge $-q_d$ from main stream takes place in the area between the ranges of K-K and II-II.

As a result, specific discharges of main stream in sections of I-I and II-II are the same and equal to $-q_0$.

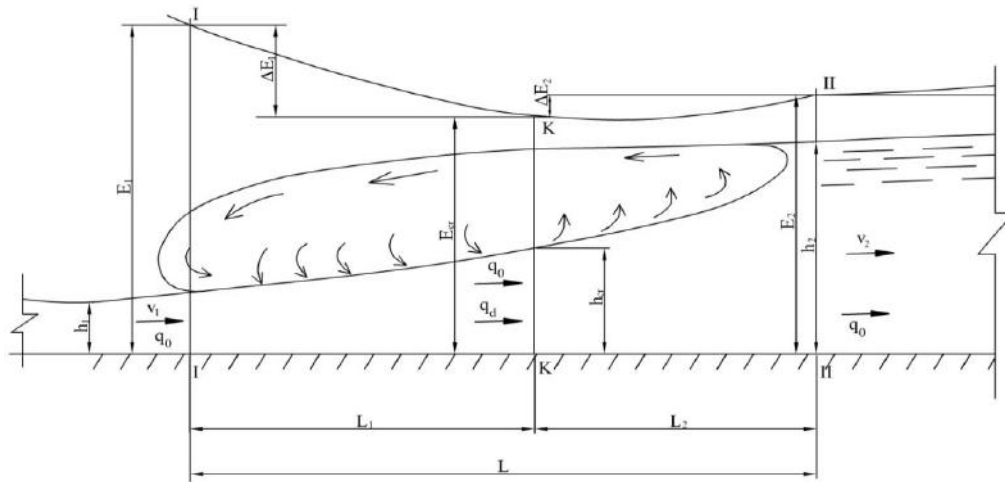


Fig.1: Calculation diagram

It has been established according to available studies that energy of the stream within the hydraulic jump is getting decreased. However, according to results of the studies we have conducted it becomes obvious that the nature of the change in energy of the stream between sections I-I and II-II differs to some extent from existing similar studies. When processing the data of numerous studies it is confirmed that specific energy of the stream decreases to a minimum - E_{cr} in section K-K along the length of the hydraulic jump, and then, it increases somewhat due to restoration of the pressure and equals to E_2 in section II-II.

We reviewed G.A. Petrov equation in the following form [10,11,12,13,14], to study pressure loss in hydraulic jump:

$$d\left(\frac{\alpha_0 v^2}{2g}\right) + \frac{dP}{\gamma} + dz + i_f dx + \frac{\alpha_0(v-\theta)}{g} \cdot \frac{v dQ}{Q} = 0 \quad (1)$$

where: Q - is discharge along the flow; α -average flow velocity along the flow; P -hydrodynamic pressure; i_f - hydraulic slope of the friction; θ -projection of velocities of attached particles on the direction of main stream velocity. Accepting bed bottom as horizontal and integrating equation (1) between the sections I-I and II-II along the flow length and after not complicated transformation, we get:

$$\frac{\alpha_1 v_1^2}{2g} + h_1 = \frac{\alpha_2 v_2^2}{2g} + h_2 + \int_1^2 i_f dx + \int_1^2 \frac{\alpha_0(v-\theta)}{g} \cdot \frac{v}{Q} \cdot dQ \quad (2)$$

Supposing that energy loss during the jump is equal to difference in energy of E_1 and E_2 in sections I-I and II-II, instead of (2) we find out:

$$E_1 - E_2 = \left(\frac{\alpha_1 v_1^2}{2g} + h_1\right) - \left(\frac{\alpha_2 v_2^2}{2g} + h_2\right) = \int_1^2 i_f dx + \frac{\alpha_0}{g} \int_1^2 \frac{v \cdot (v-\theta)}{Q} dQ \quad (3)$$

Equation (3) reminds the Bernoulli equation, but with new term on the right side. During flow movement with variable discharge along the path, we determine the pressure loss on the friction against the bottom and the side walls of the channel bed by the formula of the same kind as with constant discharge, i.e.:

$$h_f = \int_1^2 i_f dx = \frac{v_{av}^2}{C_{av}^2 R_{av}} \quad (4)$$

where C_{med} - is average value of Chezy coefficient between the sections; R_{med} - average value of hydraulic radius between the sections.

Another integral in (3) expresses mainly the pressure loss caused by the variability of the flow discharge:

$$h_{mix} = \frac{\alpha_0}{g} \int_1^2 \frac{v \cdot (v-\theta)}{Q} dQ \quad (5)$$

where: θ -means the ratio of the projection of the velocity of the attached flow to the main one.

We will assume in future studies that $\alpha_1 = \alpha_2 = 1$ and $\theta = 0$ (meeting of two streams happens at an angle of 90°).

Taking into account assumptions and considering that $b = 1.0$ m, $dQ = q_x dx$, we determine the value of the pressure loss by formula (5) as follows:

$$h_{mix} = \frac{\alpha}{g} \int_1^2 \frac{v \cdot (v-\theta)}{Q} dQ = \frac{1}{g} \int_1^2 \frac{v^2 q_x}{bhv} dx = \frac{1}{g} \int_1^2 \frac{\tilde{v}_x q_x}{\tilde{h}_x} dx \quad (6)$$

\tilde{v}_x and \tilde{h}_x in expression (6) are variable values and depend on the length of the jump.

We determine the value of q_x , for running value of separable or connected value from the expression.

$$q_x = \frac{q_d}{l_x} \quad (7)$$

Where: l_x is the length of connection and separation section; q_d is additional discharge.

By integrating the dependence (6) within the boundaries of I-I and K-K sections, we determine pressure loss for mixing additional discharge with main discharge:

$$\Delta h_{mix} = \frac{1}{g} \int_1^K \frac{\tilde{v}_{x_1}}{\tilde{h}_{x_1}} \cdot \frac{q_d}{l_1} dx \quad (8)$$

We apply change of \tilde{v}_x and \tilde{h}_x in these sections according to straightforward principle:

$$\tilde{v}_{x_1} = v_1 - (v_1 - v_{cr}) \frac{x}{l_1} \quad (9)$$

$$\tilde{h}_{x_1} = h_1 + (h_{cr} - h_1) \frac{x}{l_1} \quad (10)$$

Considering (9) and (10), equation (8) obtains the following form:

$$\Delta h_{mix} = \int_0^{l_1} \frac{v_1 - (v_1 - v_{cr}) \frac{x}{l_1}}{h_1 + (h_{cr} - h_1) \frac{x}{l_1}} \cdot \left(\frac{q_d}{gl_1} \right) dx \quad (11)$$

For hydraulic jump area between I-I and K-K sections with water depth h_1 and h_{cr} , expression (11) can be presented in the following form after minor transformations:

$$dh_{mix} = \frac{\alpha q_d}{gl} \int_0^l \frac{v_1 - \frac{v_1 - v_{cr}}{l} x}{h_1 + \frac{h_{cr} - h_1}{l} x} dx \quad (12)$$

By integrating and transforming expression (12), we find out dependence of pressure loss on the mixing of the additional discharge with the primary one during the jump in the form below:

$$\Delta h_{mix} = \frac{\alpha q_d}{g(h_{cr} - h_1)} \left[\frac{(v_1 h_{cr} - v_{cr} h_1)}{h_{cr} - h_1} \ln \frac{h_{cr}}{h_1} + (v_{cr} - v_1) \right] \quad (13)$$

By integrating the dependence (8) within the limits of K-K – II-II sections, we determine pressure loss on separation of the additional discharge from the primary one:

$$\Delta h_{sec} = \frac{1}{g} \int_K^{II} \frac{\tilde{v}_{x_2}}{\tilde{h}_{x_2}} \cdot \frac{q_d}{l_2} dx \quad (14)$$

We accept the change of \tilde{v}_x and \tilde{h}_x according to straightforward principle in the following manner:

$$\tilde{v}_{x_2} = v_{cr} - (v_{cr} - v_2) \frac{x}{l_2} \quad (15)$$

$$\tilde{h}_{x_2} = h_{cr} + (h_2 - h_{cr}) \frac{x}{l_2} \quad (16)$$

Considering (15) and (16), equation (14) obtains the following form:

$$\Delta h_{sec} = \int_0^{l_2} \frac{v_{cr} - (v_{cr} - v_2) \frac{x}{l_2}}{h_{cr} + (h_2 - h_{cr}) \frac{x}{l_2}} \cdot \left(\frac{q_d}{gl_2} \right) dx \quad (17)$$

Expanding the integral in expression (17) and conducting certain transformations, we get the formula for pressure loss on separation of additional discharge during the jump:

$$\Delta h_{sec} = \frac{\alpha q_d}{g(h_2 - h_{cr})} \left[\frac{(v_{cr} h_2 - v_2 h_{cr})}{h_2 - h_{cr}} \ln \frac{h_2}{h_{cr}} + (v_2 - v_{cr}) \right] \quad (18)$$

Thus, two expressions (13) and (18) were obtained for determining pressure loss during hydraulic jump on connection and separation of additional discharge.

It should be mentioned that, according to the adopted scheme, the energy of the stream gets decreased before the critical section. Arriving at minimum value in the critical section, and further due to separation of additional discharge, the flow partially recovers its energy. This condition indicates that pressure restoration happens in the section K-K – II-II. Pressure restoration value is determined by the expression (18).

The values q_d and h_{cr} can be determined from the following expression (13) with known magnitudes of hydraulic parameters of the jump:

$$h_{cr} = \sqrt{\frac{1}{3} [h_2 (h_1 + h_2) + h_1^2]} \quad (19)$$

$$q_d = \sqrt{g} \left[\sqrt{\frac{h_{cr}^3}{\alpha_0}} - \sqrt{\frac{h_1 h_2}{2\alpha_0} (h_1 + h_2)} \right] \quad (20)$$

Being aware of parameters on hydraulic jump elements, it is possible to determine pressure loss due to the connection and separation of the additional discharge along the length of the jump according to formulas (13) and (18) with great accuracy.

Proposed dependencies (13) and (18) enables for determining energy loss in hydraulic jumping. These energy losses are formed under the influence of a surface roller. On the other hand, part of the flow energy is spent

on overcoming the resistance of the bed bottom. Specific energies E_1 , E_2 and E_c in sections I-I, II-II and K-K of the hydraulic jump are identified by using hydraulic flow parameters. At the same time, energy losses between the sections I-I and K-K constitute $\Delta E_1 = E_1 - E_{cr}$, and between the sections of K-K and II-II they become $\Delta E_2 = E_{cr} - E_2$. In all cases, terms of $E_{cr} \geq E_2$, and at the same time $\Delta E_2 \geq 0$ are satisfied. Hence it is obvious that during flow movement within the boundaries between the sections K-K and II-II, the specific flow energy increases additionally from the minimum (section K-K) to E_2 (section II-II) by an amount of ΔE_2 . While calculating for (13) and (18) of values Δh_1 and Δh_2 you can determine energy loss to overcome resistance along a segment of length L_1 from the expression $\Delta H_1 = \Delta E_2 - \Delta h_1$ and along the length of section L_2 from the expression $\Delta H_2 = \Delta h_2 + \Delta E_2$. It becomes obvious from the presented material that, in hydraulic jump, energy loss necessary for overcoming bottom resistance of the bed will be equal to $\Delta H_1 + \Delta H_2 = \Delta E$.

It should be mentioned that in order to determine hydraulic parameters of the stream and to find the magnitude of value of the pressure loss in the hydraulic jump according to (13), (18) and other expressions we recommended, the data of laboratory studies by D.A. Akhutin [2] were processed, the results of which are

presented in table 1. It is obvious from this table that experiments were carried out at the values of the conjugate depths $h_1 = 1,30 \dots 7,35$ cm and $h_2 = 10,60 \dots 32,80$ cm, and the length of the hydraulic jump fluctuated within the range of 35 ... 185 cm.

Pressure losses in the hydraulic jump calculated by (13) and (18) are respectively $\Delta h_1 = 1,01 \dots 36,0$ cm and $\Delta h_2 = 0,85 \dots 3,87$ cm. The total pressure loss along the length of the hydraulic jump varied from 0.15 to 11.81 cm. Furthermore, according to the data in the table, it is obvious that for all the experiments ΔE_2 is negative and the conditions of $\Delta E_1 > \Delta h_1$ and $\Delta E_2 \geq \Delta h_2$ are satisfied. This statement fully confirms the recommendations we made on the assessment of hydraulic jumps.

To determine the magnitude of pressure loss for overcoming the bottom resistance of the channel, bypassing formulas (13) and (18), after processing numerous data, a dependence was obtained in the form:

$$\Delta E = E_1 \left[0,78 - 0,89 \left(\frac{h_1}{h_2} \right)^{0,15} \right], \quad (21)$$

where h_1 , h_2 – are first and second conjugate depths in hydraulic jumping; E_1 – is specific flow energy within initial section of hydraulic jump.

Elements of hydraulic jump and energy loss in it

Table 1.

Water depth in section I-I, h_1 , sm	Water depth in section II-II, h_2 , sm	Length of hydraulic jump, L_j , sm	Froude number	Flow velocity in section I-I, v_1 , sm/s	Flow velocity in section II-II, v_2 , sm/s	Flow energy in section I-I, E_1 , sm	Flow energy in section II-II, E_2 , sm	Critical depth, h_{cr} , sm	Additional water discharge, q_{ad} , sm ² /s	Critical velocity, v_{cr} , sm/s	Critical flow energy, E_{cr} , sm	$\Delta E_1 = E_1 - E_{cr}$	$\Delta E_2 = E_{cr} - E_2$	Δh_1 for (4.27), sm	Δh_2 for (4.32), m	$\Delta H_1 = \Delta E_2 - \Delta h_1$, sm	$\Delta H_2 = \Delta E_2 + \Delta h_2$, sm	$\Delta E = \Delta H_1 + \Delta H_2$, sm
1	2	3	4	5	6	7	8	9	10	11	12	13	14	15	16	17	18	19
1,3	10,9	55	39,3	224	26,7	26,9	11,26	6,7	251,99	81,07	10,05	16,82	-1,21	13,36	1,3	3,47	0,08	3,55
1,3	16,0	82	81,9	323,2	26,3	54,5	16,35	9,63	516,58	97,22	14,45	40,08	-1,90	31,08	2,07	9,0	0,17	9,17
1,9	8,80	35	13,0	155,9	33,7	14,3	9,38	5,71	130,99	74,84	8,56	5,73	-0,81	4,73	0,85	1,0	0,03	1,03
1,9	14,7	72	33,8	251,0	32,4	34,0	15,24	9,09	380,84	94,41	13,63	20,38	-1,61	16,26	1,71	4,12	0,10	4,22

1,9	21,0	107	66,6	352,3	31,9	65,2	21,52	12,71	749,50	111,66	19,06	46,11	-2,46	36,00	2,67	10,1	0,21	10,3 1
2,52	6,20	15	4,30	102,6	41,7	7,9	7,090	4,49	39,240	66,35	6,730	1,15	-0,35	1,01	0,36	0,14	0,00	0,15
2,52	13,7	63	17,5	208,0	38,3	24,6	14,45	8,73	283,61	92,54	13,09	11,47	-1,35	9,37	1,42	2,11	0,06	2,17
2,52	19,1	104	32,5	283,5	37,4	43,5	19,81	11,82	558,72	107,69	17,73	25,75	-2,08	20,57	2,21	5,18	0,13	5,31
2,52	24,4	127	51,7	357,6	36,9	67,7	25,10	14,87	894,61	120,77	22,30	45,38	-2,79	35,72	3,01	9,66	0,22	9,88
3,11	12,6	48	10,2	176,7	43,6	19,0	13,57	8,32	202,02	90,34	12,48	6,54	-1,09	5,46	1,13	1,08	0,03	1,11
3,08	18,5	90	21,0	252,1	42,0	35,5	19,4	11,7	472,40	107,0	17,5	18,0	-1,89	14,58	1,99	3,40	0,10	3,50
3,06	23,0	120	32,0	310,0	41,2	52,0	23,9	14,2	735,40	118,2	21,4	30,7	-2,50	24,51	2,66	6,15	0,16	6,31
3,07	29,5	160	51,0	391,8	40,8	81,3	30,3	18,0	1185,6	132,8	27,0	54,3	-3,37	42,79	3,63	11,6	0,26	11,8 6
3,72	16,0	65	11,4	204,0	47,4	24,9	17,1	10,5	303,50	101,4	15,7	9,2	-1,43	7,65	1,48	1,56	0,05	1,61
3,68	23,1	123	22,8	287,1	45,7	45,7	24,2	14,5	675,6	119,3	21,8	23,9	-2,39	19,35	2,52	4,58	0,13	4,71
3,70	26,7	140	29,6	328,0	45,5	58,5	27,8	16,6	902,1	127,6	24,9	33,7	-2,87	26,98	3,05	6,69	0,18	6,86
3,72	32,2	170	41,8	390,5	45,1	81,5	33,2	19,8	1296,8	139,2	29,6	51,8	-3,61	41,06	3,87	10,7 6	0,26	11,0 2
4,42	15,4	48	7,8	184,0	52,8	21,7	16,8	10,4	237,7	101,0	15,6	6,1	-1,22	5,14	1,25	0,93	0,03	0,96
4,40	20,1	95	12,7	234,3	51,3	32,4	21,4	13,1	447,6	113,2	19,6	12,8	-1,85	10,58	1,92	2,21	0,07	2,28
4,40	24,2	128	17,9	277,8	50,5	43,7	25,5	15,4	670,7	122,9	23,1	20,6	-2,40	16,83	2,51	3,80	0,11	3,91
4,42	30,5	160	27,3	343,8	49,8	64,7	31,8	19,0	1077,3	136,6	28,5	36,1	-3,24	29,04	3,43	7,10	0,19	7,29
4,40	33,7	185	33,2	378,3	49,4	77,4	34,9	20,8	1315,8	143,0	31,3	46,1	-3,68	36,80	3,92	9,29	0,24	9,53
4,93	12,8	30	4,7	150,3	57,9	16,4	14,5	9,2	126,3	94,8	13,7	2,7	-0,78	2,36	0,79	0,35	0,01	0,36
4,93	18,0	70	8,5	202,6	55,5	25,9	19,6	12,1	314,3	108,8	18,1	7,8	-1,47	6,54	1,51	1,22	0,04	1,26
4,94	23,2	110	13,4	254,6	54,2	38,0	24,7	15,0	566,4	121,4	22,5	15,4	-2,16	12,74	2,24	2,70	0,08	2,78
4,97	27,4	135	18,0	295,9	53,7	49,6	28,9	17,4	809,2	130,8	26,1	23,4	-2,72	19,12	2,85	4,32	0,13	4,45

4,97	31,6	160	23,4	337,7	53,1	63,1	33,0	19,8	1088,5	139,5	29,8	33,3	-3,29	26,94	3,46	6,41	0,18	6,59
5,62	16,5	65	5,8	178,5	60,8	21,9	18,4	11,5	218,0	106,2	17,2	4,6	-1,14	3,97	1,16	0,64	0,02	0,66
5,67	21,5	100	9,1	224,8	59,3	31,4	23,3	14,3	425,0	118,6	21,5	9,9	-1,79	8,34	1,84	1,59	0,05	1,64
5,65	25,8	130	12,7	265,4	58,1	41,6	27,5	16,8	650,7	128,2	25,1	16,4	-2,37	13,57	2,46	2,84	0,09	2,93
5,65	31,2	190	18,0	315,9	57,2	56,5	32,9	19,8	984,2	139,5	29,8	26,8	-3,10	21,82	3,24	4,93	0,15	5,08
6,27	15,0	35	4,1	158,0	66,0	19,0	17,2	10,9	141,1	103,5	16,4	2,6	-0,83	2,29	0,84	0,31	0,01	0,32
6,27	19,8	80	6,6	201,0	63,6	26,9	21,9	13,6	312,2	115,5	20,4	6,4	-1,45	5,50	1,48	0,94	0,03	0,97
6,27	23,9	115	9,2	237,5	62,3	35,0	25,9	15,9	500,4	125,0	23,9	11,1	-2,00	9,35	2,06	1,79	0,06	1,85
6,27	28,9	150	12,9	282,0	61,2	46,8	30,8	18,8	776,8	135,7	28,1	18,7	-2,67	15,42	2,77	3,24	0,10	3,34
6,25	32,6	185	16,2	315,3	60,4	56,9	34,5	20,9	1013,9	143,1	31,3	25,6	-3,17	20,98	3,31	4,64	0,14	4,78
7,35	16,5	30	3,6	162,1	72,2	20,7	19,2	12,2	145,9	109,5	18,3	2,4	-0,83	2,14	0,84	0,27	0,01	0,28
7,25	21,5	70	5,9	204,5	69,0	28,6	23,9	15,0	328,2	121,1	22,4	6,1	-1,50	5,28	1,52	0,86	0,03	0,89

Hence, energy loss in in hydraulic jumps will be:

$$E_1 - E_2 = \Delta h_f + \Delta h_{mix} + \Delta h_{sec}, \quad (22)$$

It is obvious from the equation (22) that for hydraulic jumps, following conditions must be necessarily fulfilled:

$$\Delta E = E_1 - E_2 - (\Delta h_{mix} - \Delta h_{sec}). \quad (23)$$

We use Darcy-Weisbach formula for critical section form to determine length of hydraulic jump:

$$\Delta E = (\lambda_p + \lambda_f) \frac{L_{jmp} \cdot v_{cr}^2}{h_{cr} \cdot 2g}, \quad (24)$$

where: ΔE - is the energy for overcoming frictional resistance;

λ_p - coefficient of hydraulic friction from the slopeof the gradient of pressure λ_p ;

λ_f - coefficient of hydraulic friction from the slopeof the friction λ_f ;

L_{jmp} - length of jump; v_{cr} - critical flow velocity; h_{cr} - critical flow depth.

We define the following from (24) for length of hydraulic jump:

$$L_{jmp} = \frac{2g}{v_{cr}^2} \cdot \frac{\Delta E h_{cr}}{\lambda_p + \lambda_f} \quad (25)$$

For determining λ_p and λ_f we processed data of laboratory studies by several authors [2,3,6,8,9,14,15,16,17,20,21,22,23]. Based on results of these studies an expression was found for determining λ_p in the following form:

$$\lambda_p = 0,0021 Fr^{0,84} \quad (26)$$

In this case, the value of λ_f is determined both for smooth and uneven bed separately. Coefficient of hydraulic friction λ_f for smooth bed is determined by the formula:

$$\lambda_{f.smo.} = 0,08 \cdot \lambda_0^{0,42} \left(\frac{h_{cr}}{h_1} \right)^{1,6} \quad (27)$$

λ_0 is determined by formula (15) in dependency (27).

$$\lambda_0 = \frac{0,035}{Re^{0,25}}$$

where: Re- is Reynolds number and determined by the formula:

$$Re = \frac{v_1 \cdot h_1}{\nu} \quad (28)$$

For uneven bed, hydraulic friction coefficient is determined from the expression:

$$\lambda_{f(frict.)} = 0,033\lambda_f^{0,34} \left(\frac{h_{cr}}{h_1} \right)^{1,6} \quad (29)$$

In dependency (29) the magnitude of λ_f value is determined from (30).

$$\lambda_f = \frac{1}{\left(3,9 \lg \frac{h}{k} + 4 \right)^2} \quad (30)$$

where: K- is determined by A.P.Zegjda methodology (1,5,15).

It should be mentioned that comparison of these dependencies was carried out with the data of experimental studies by M.D. Chertausov (table 2). By using presented data, the length of the hydraulic jump is calculated both with the dependences we proposed, and according to the recommendations of N.N. Pavlovsky and M.D. Chertausov, which are given in table 2. Comparison of the obtained dependences with the results of M.D.Chertausov's experimental data indicated their satisfactory convergence (16). At that time discrepancy between the experimental and calculated lengths of the hydraulic jump changed: 0,4...22% according to the dependencies recommended by us, 1,0...36,0% by N.N.Pavlovsky formula, 2,1...29% according to M.D.Chertausov expression.

Results of the comparison of length of the hydraulic jump according to the experimental data of M.D. Chertausov

Table 2.

h_1 -first conjugate depth, cm	h_2 -second conjugate depth, cm	q_0 -specific discharge, cm ² /c on 1 p.sm	Experimental length of hydraulic jump, L_0 , cm	Jump length according to the author, L_a , cm	Difference between L_0 and L_a , %	Jump length according to N.N.Pavlovsky, L_n , cm	Difference between L_0 and L_n , %	Jump length according to M.D.Chertausov, L_r , cm	Difference between L_0 and L_r , %
1	2	3	4	5	6	7	8	9	10
0,24	2,92	33,0	11,5	11,6	-0,4	13	-15	13	-16,9
3,75	33,8	1527,9	180,0	178,9	0,6	151	16	161	10,4
2,20	15,5	544,1	70,0	74,7	-6,7	68	3	77	-10,1
1,95	15,02	493,8	60,0	73,2	-22,0	66	-11	73	-21,0
1,96	14,93	492,4	67,0	72,6	-8,2	66	1	73	-9,0
2,25	17,64	622,3	87,0	87,7	-0,9	78	10	85	2,1
1,94	15,85	518,0	70,0	78,1	-11,5	70	-1	76	-8,9
0,34	2,980	40,6	13,0	12,2	6,1	13	-2	14	-10,1
1,01	9,22	216,2	41,5	42,6	-2,6	41	1	44	-6,5
0,24	2,54	28,8	10,5	10,1	3,8	11	-9	12	-13,1
0,22	2,67	28,9	11,5	10,5	9,1	12	-6	12	-7,0
0,24	2,92	33,0	11,5	11,6	-0,4	13	-15	13	-16,9

0,17	2,18	20,7	10,0	8,3	17,1	10	1	10	0,8
0,35	4,5	61,2	19,0	18,4	3,0	21	-8	21	-9,0
0,21	2,72	28,7	12,0	10,5	12,2	12	-3	12	-3,9
0,25	3,55	40,7	14,0	13,8	1,1	16	-16	16	-15,9
0,21	3,11	32,6	12,0	11,9	1,1	14	-19	14	-17,3
0,23	3,79	41,5	17,0	14,6	14,4	17	-3	17	2,0
0,18	3,34	32,2	13,0	12,1	7,1	15	-19	15	-14,4
0,11	2,45	18,4	10,0	8,3	17,0	11	-14	10	-2,9
0,19	4,16	41,1	19,0	14,9	21,6	19	-2	18	6,4
0,18	4,10	39,40	14,0	14,2	-1,3	19	-36	18	-29,0
0,10	2,63	18,80	9,0	8,5	5,8	12	-36	11	-22,0
3,35	13,64	617,1	61,5	54,9	10,8	56	8	65	-5,6
3,23	13,88	613,4	59,0	56,9	3,5	58	2	69	-16,6
3,29	14,42	642,0	62,0	60,3	2,7	60	3	71	-14,5
3,14	15,27	658,0	79,5	68,7	13,5	65	19	73	7,9
3,03	14,60	618,5	65,0	64,2	1,3	62	5	72	-10,9
2,68	15,5	608,6	65,0	72,4	-11,4	67	-3	78	-19,4
2,68	15,89	622,8	78,0	75,1	3,7	69	12	79	-1,3
2,16	14,35	501,0	67,0	69,4	-3,6	63	6	69	-3,5
2,50	16,62	624,2	98,5	81,3	17,5	73	26	81	17,9
0,40	2,750	41,20	14,0	11,2	20,2	12	14	13	5,3
2,10	14,51	498,3	66,0	70,4	-6,6	64	4	70	-6,6
0,51	3,68	62,1	16,5	15,5	5,9	16	2	18	-7,0

Extensive research activities have been carried out under the leadership of academician M. Vyzgo regarding the impact of bed roughness on hydraulic jump length [4]. The length of hydraulic jump has been studied under laboratory conditions within same hydraulic parameters in smooth and uneven beds. Results of carried studies are summarized and presented in Figure 2. As it is obvious from this graph, obtained results are subject to parabolic functioning appropriateness.

The results of the calculation done by formulas (25), (29), (29) and (30) that we obtained through theoretical method for the length of hydraulic jump occurring in uneven beds have been compared to research results by academician M. Vyzgo (Figure 2).

When comparing the parameters of the hydraulic jump according to the recommendations developed by us for the uneven bottom, the data of M.S. Vyzgo and Y.A. Kuzminova were used [4], results of which are presented in Figure 2. According to data of this figure,

hydraulic jump parameters determined according to our recommendations, as well as by M.S. Vyzgo expression $L_{frik}=L_0$ almost coincide, which is confirmed by graphics

$$\frac{L_{frik}}{L_0} = f\left(\frac{\Delta}{h_2}\right).$$

Furthermore, according to recommendations made by us, a schedule of changes was developed

$$\frac{L}{(h_2 - h_1)} = f\left(\frac{v_1}{\sqrt{gh_1}}\right)$$

for hydraulic jump and (figure 3) where it was given together with similar graphs of US Bureau of Reclamation, N.N. Pavlovsky and M.D. Chertausov [14]. The analysis of materials of figure 3 indicate that schedule of change for length of hydraulic jump developed according to the methodology suggested by us is satisfactorily compliant with the graph of US Bureau of Reclamation [18,19] and well confirmed by experimental data of A.N.Akhutin and

A.N.Rakhmanov. When determining the length of hydraulic jump according to the schedules of the US Bureau of Reclamation, the discrepancy does not exceed

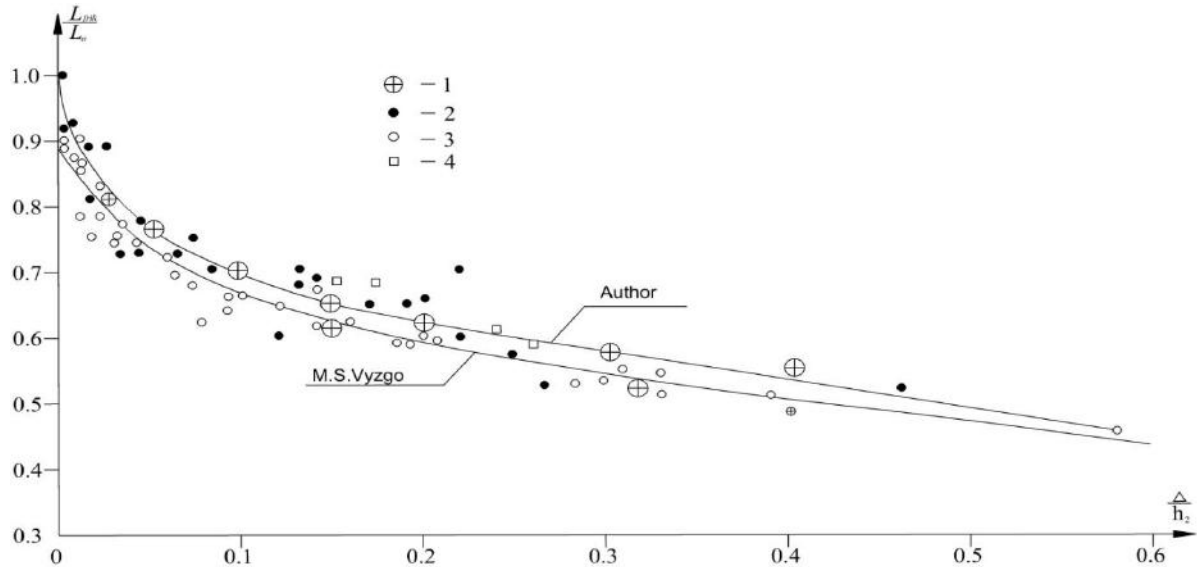
$$\frac{v_1}{\sqrt{gh_1}} < 4$$

□ 9,5...15,6%. However, in case of these graphs significantly differ from the graphs of N.N. Pavlovsky and M.D. Chertausov. Significant deviations of all these graphs descend from the experimental data of

Pistrovsky and Bradley. It should be noted that at a value

$$\frac{v_1}{\sqrt{gh_1}} > 4$$

of the convergence of the lengths of the hydraulic jump determined by different, including dependencies recommended by us are satisfactory.



$$\frac{L_{frik}}{L_0} = f\left(\frac{\Delta}{h_2}\right)$$

Fig.2: Diagram

1- K.A. Suleymanova; 2; 3; 4 – Y.M.Kuzminova

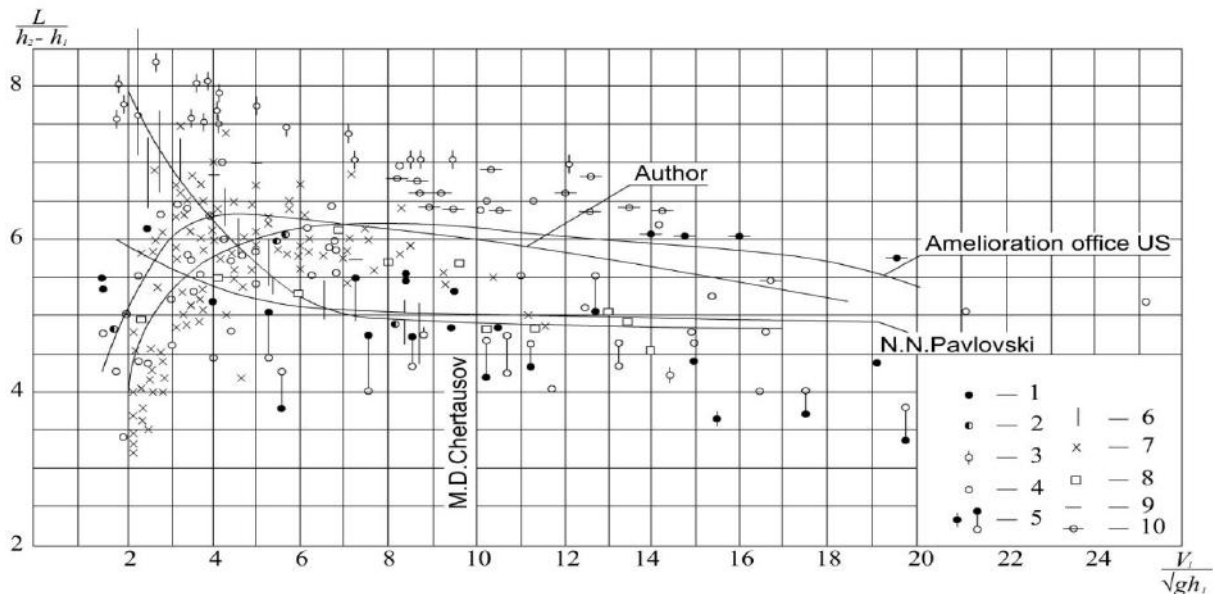


Fig.3: Jump length: 1- according to experiments of Safranch; 2 - according to experiments of Einwachter; 3 - according to experiments of Voychiska; 4 - according to experiments of Smetana; 5 - according to experiments of Pistrovsky; 6 - according to experiments of Bakhmetyev and Matchsko; 7 - according to experiments of Akhutin; 8 - according to experiments of Rakhmanov; 9 - according to experiments of Mur; 10 - according to experiments of Bradley and Peterky.

Main outcomes

1. The mechanism of flow energy absorption within hydraulic jump zone has been explained by the model for the rotation of q_d - additional water body on the mainstream and overcoming the resistance emerged in bed bottom against the flow. According to this selected mathematical model, the maximum flow energy - E_1 within I-I section in the hydraulic jump zone falls to minimum - E_{cr} value while decreasing to the critical depth located in K-K cross section and then increases to - E_2 value within section of II-II.
2. Within the hydraulic jump zone, q_d - additional water body is connected to mainstream between the section of I-I and K-K and the process of energy loss occurs, the formula (13) is developed to calculate the same. Between the cross sections K-K and II-II the process of separation of q_d - additional water body from the mainstream happens; the formula f to computed. Among the K-K and II-II fragments, the main stream is the q_d - separation of the water mass, which is composed of the formula (18) has been developed to calculate the additional energy generated at that time.
3. A proposal has been made for using the formula (19) to calculate the critical depth in the hydraulic jump zone and using the formula (20) to calculate the discharge of q_d - additional water body.
4. Formulas (21) and (23) have been developed to calculate the energy used by the flow bed for overcoming the bed bottom resistance.
5. It is recommended to use formulas of (25), (26), (27), (28), (29) and (30) obtained by theoretical method for calculating the length of hydraulic jump formed in smooth and rough beds.

REFERENCES

- [1] Agroskin I.I., Dmitriev G.T., Pikalov Ph.I. Hydraulics. M.-L.: Energy, 1964, 351 pages.
- [2] Akhutin D.A. On the determination of certain parameters of complete hydraulic jump // Proceedings of the hydro project, No. 10, 1963, pages 323-327.
- [3] Belshyayevskiy N.N., Pivovarov N.G., Kalantynenko I.I. Calculation of the tailrace for spillway structures on non-scalloped grounds: Kiev: Naukova Dumka, 1973, 290 pages.
- [4] Vyzgo M.S. Operational measures, forecasts and ways to reduce local erosion behind hydraulic structures. T.: Science, 1966, 257 pages.
- [5] Hydraulic calculations of spillway hydraulic structures: Reference manual. Moscow: Energoatomizdat, 1988, 624 pages.
- [6] Gratsiansky M.N. Application of the laws of change in the amount of movement and living forces in the conjugation of the flow with the tailrace // Construction and Architecture, 1959, No. 10, pages 44 ... 58.
- [7] Gritsyuk A.V. Mechanism and theory of fluid flow jump. M: Selkolkhozgiz, 1932, 38 pages.
- [8] Dmitriev A.F., Khlapuk N.N. Investigation of regimes of unflooded and submerged bottom hydraulic jumping // Hydraulics and Hydrotechnics, Issue 2, 1975, No. 2, p. 8 ... 15.
- [9] Kuznetsov S.K. Theory and hydraulic calculations of the tail water. Lviv: Vishcha school, 1983, 172 pages.
- [10] Mamedov A.Sh. Loss of energy of the open flow in the jump zone // Collection of scientific works on mechanics Az. ISU. Baku, 1999, No. 9, pages 237 ... 245.
- [11] Mamedov A.Sh. Hydraulic jump // Agrarian Science of Azerbaijan, 2007, No. 1-3, pages 191 ... 192.
- [12] Mamedov A.Sh. Loss of pressure in hydraulic jumping / Water supply, water disposal, hydraulic engineering, engineering hydro geo-ecology (collection of abstracts dedicated to the 70th anniversary of the FSUE Scientific-Research Institute VODGEO), Moscow, 2004, pages 167 ... 168.
- [13] Petrov G.A. Hydraulics of variable mass. Kharkov: Publishing house of Kharkov University, 1964, 224 pages.
- [14] Russo G.A. On vortex motions in liquids // Proceedings of the hydro project. Thirteenth collection, pages 218 ... 303.
- [15] Khapaeva A.K. Hydraulic jump on a smooth and dirty bottom like a wall jet // Transaction of All-Union Scientific Research Institute of Hydraulic Engineering, Vol. 92, 1970, p. 234 ... 245.
- [16] Chertausov M.D. Hydraulics, special course. L-M: Gosenergoizdat, 1949, 407 pages.
- [17] Ernest Razvan. Studiu asupra disipării energiei cu aplicare la baraje. R: București, 1969, pp. 412.
- [18] James F. Cruise, Mohsen M. Sherif, Vijay P. Singh. Elementary hydraulics. Not for Sale in America, Thomson, 2007, p. 560.
- [19] Novak P., Moffat A. Í. B., Nalluri C., Narayanan R. Hydraulic structures. L: Ciria, 1992, p. 532.
- [20] Resh F.J., Leutheusser H.J. Mesures des tensions de reynolds dans le ressaut hydraulique // Journal of hydraulic research de recherches hydrauliques, vol. 10, 1972, №4, pp. 409...429.
- [21] Resh F.J., Leutheusser H.J., Coantic M. Etude de la structure cinematique et dynamique du ressaut hydraulique // Journal of hydraulic research de

recherches hydrauliques, vol. 14, 1976, №4, pp. 293...319.

[22] Vischer D.L., W.H. Hager, Energy dissipators, Rotterdam, 1995, p. 1...181.

[23] Willi H. Hager, Roger Bremen. Classical hydraulic jump: sequent depths. Le ressaut hydraulique classique: etude des hauteurs conjuguees // Journal of hydraulic research de recherches hydrauliques, vol. 27, 1989, №5, pp. 565...586.